Efficient and Accurate Gust Loads Simulations

Carmine Valente

Department of Aerospace Engineering

University of Bristol

A dissertation submitted to the University of Bristol in accordance with the requirements of the degree of Doctor of Philosophy in the Faculty of Engineering.

April 2018

Abstract

Gust loads simulations are important loads cases that must be investigated during the design and development of an aircraft. Since a very high number of simulations have to be performed to clear the flight envelope (a reasonable estimation would be of the order of hundreds of thousands), an efficient and accurate methodology is essential to complete this task. Traditionally potential methods are used to estimate the aerodynamic loads interacting with the structure. Specifically, the Doublet-Lattice Method is the industrial standard for gust loads simulations. However, the simplifying assumptions on which it is based do not allow accurate estimations of the aero loads in the transonic regime, where thickness and nonlinear effects become relevant. The present work presents a new approach to evaluate a correction matrix to post multiply the Aerodynamic Influence Coefficient matrix in the Doublet-Lattice Method. This overcomes the limitations when used to investigate those flight conditions characterised by nonlinear aerodynamic effects. The correction approach has been formulated in the frequency domain to fit with the DLM formulation and the correction coefficients computed are complex numbers, which are intended to capture the unsteady aerodynamic effects associated with shock movement and nonlinearities. In order to reduce the computational cost necessary to compute the reference aerodynamic loads used to correct the DLM, time domain CFD simulations have been replaced with the more time efficient linear frequency domain LFD analysis. Additionally to reduce the number of discrete reduced frequencies at which the corrections have to be evaluated, an interpolation method has been used to compute the correction factors for the entire spectrum of reduced frequencies. The aerodynamic gust loads evaluated using the correction method presented in this thesis have been compared to the high fidelity results obtained from a strongly coupled method that couples the CFD TAU-Code and the finite element model solver MSC Nastran, through the AlpesFSI defined in this work. The correction method proposed is used to evaluate the aerodynamic loads due to a one minus cosine gust shape as prescribed by the CS-25 regulations. Very good results have been obtained both for an Euler CFD model of the FFAST wing and for a RANS model of the NASA Common Research Model.

Acknowledgements

Firstly, I would like to thank my supervisors, Dr. Ann Gaitonde and Dr. Dorian Jones, for their support, advice and guidance during all these years.

I also thank Prof. Jonathan Cooper and Dr. Yves Lemmens and all the people involved in the ALPES Project.

My gratitude goes also to all my friends and colleagues who shared with me technical discussions and opinions.

A special thanks goes to my lovely wife Aurora and our son Matteo for being by my side along this long journey. Without their support this would not have been possible.

My thoughts are also for my family who always supported me throughout my studies.

I express my gratitude to the European Community for funding this research through the European Community's Marie Curie Initial Training Network (ITN) on Aircraft Loads Prediction using Enhanced Simulation (ALPES) FP7-PEOPLE-ITN-GA-2013-607911. The partners in the ALPES ITN are the University of Bristol, Siemens and Airbus Operations Ltd.

Lastly, I acknowledge that this work was carried out using the computational facilities of the Advanced Computing Research Centre, University of Bristol - http://www.bris.ac.uk/acrc/.

Author's Declaration

I declare that the work in this dissertation was carried out in accordance with the requirements of the University's Regulations and Code of Practice for Research Degree Programmes and that it has not been submitted for any other academic award. Except where indicated by specific reference in the text, the work is the candidate's own work. Work done in collaboration with, or with the assistance of, others, is indicated as such. Any views expressed in the dissertation are those of the author.

SIGNED: ..... DATE: .....

Publications

This research has resulted in the conference papers listed below:

- C. Valente, D. Jones, A. Gaitonde, J. E. Cooper, and Y. Lemmens. OpenFSI Interface For Strongly Coupled Steady And Unsteady Aeroelasticity. In *IFASD 2015 International Forum on Aeroelasticity and Structural Dynamics*, Saint Petersburg, Russia, 2015.

- C. Valente, D. Jones, A. Gaitonde, J. E. Cooper, and Y. Lemmens. Doublet-Lattice Method Correction by Means of Linearised Frequency Domain Solver Analysis. In *15th Dynamics Specialists Conference*, 4-8 January 2016, San Diego, California, USA, 2016.

- C. Valente, C. Wales, D. Jones, A. Gaitonde, J. E. Cooper, and Y. Lemmens. A Doublet-Lattice Method Correction Approach for High Fidelity Gust Loads Analysis. In 58*th AIAA/ASCE/AHS/ASC Structures, Structural Dynamics, and Materials Conference*, 9 -13 January 2017, Grapevine, Texas, USA, 2017.

- C. Valente, C. Wales, D. Jones, A. Gaitonde, J. E. Cooper, and Y. Lemmens. An Optimized Doublet-Lattice Method Correction Approach for a Large Civil Aircraft. In *IFASD 2017 International Forum on Aeroelasticity and Structural Dynamics*, Como, Italy, 2017.

Contents

List of Figures

List of Tables

Nomenclature

Variables

$\bar{a}_j$	*j-th* DLM panel box area
$\bar{q}$	Dynamic pressure
$\boldsymbol{\epsilon}^w$	Corrections factor vector
$\mathbf{\Phi}$	Matrix of mode shapes
Δx_j	*j-th* DLM panel box dimension in the free streem direction
γ_j	Dihedral angle
κ	Reduced frequency
$\hat{\mathbf{q}}$	Vector of modal coordinates
$\mathbf{A}_{jj}^{-1}$	Aerodynamic influence coefficient matrix
$\mathbf{B}$	Damping matrix
$\mathbf{c}_{p_j}$	Pressure coefficient vector
$\mathbf{D}_{jk}^1$	Matrix relating the deformation to a local angle of attack
$\mathbf{D}_{jk}^2$	Matrix relating the rate of deformation to a local angle of attack
$\mathbf{f_n}$	Vector of element nodal forces
$\mathbf{f_p}$	Vector of applied loads
$\mathbf{f_q}$	Vector of constraint forces
$\mathbf{f}$	External force vector
$\mathbf{F}_a$	Aerodynamic load vector over the structural grid
$\mathbf{G}_{ka}$	Transformation matrix relating structural and aerodynamic grid points
$\mathbf{G}_{kr}$	Integration matrix over the aerodynamic monitor point
$\mathbf{K}$	Stiffness matrix
$\mathbf{K}^d$	Differential stiffness
$\mathbf{K}^m$	Material stiffness
$\mathbf{K}_T$	Tangential stiffness matrix
$\mathbf{M}$	Mass matrix

$\mathbf{P}_k$ Vectors of the vertical forces, and pitching moments for each of the panels

$\mathbf{P}_P$ Gust disturbance Fourier transform

$\mathbf{p}_j$ Pressure on lifting surface j

$\mathbf{Q}_{ARJ}^T$ Generalised aerodynamic influence coefficient matrix relating the downwash to the aerodynamic loads on the monitor points

$\mathbf{Q}_{kj}$ Generalised aerodynamic force matrix due to flow unsteadiness

$\mathbf{Q}_{kk}$ Generalised aerodynamic force matrix due to the structural motion

$\mathbf{S}_{kj}$ Aerodynamic integration matrix, which relates the pressures to the loads

$\mathbf{u}_e$ Extra point displacement vector

$\mathbf{W}_{jj}^w$ Downwash correction coefficient matrix

γ_{hcr} Heat capacity ratio

$\mathbf{v}$ Flow velocity vector

$\mathbf{w}_j$ Downwash vector

ω Angular speed of the harmonic oscillation of the panels

ω_i Excitation frequency

ρ Air density

ζ Damping ration

a_0 Speed of sound

b_cr Critical damping

f Frequency

l_{ref} Reference length

M Free stream Mach number

U_∞ x velocity component of the uniform mean flow

w_g Gust scaling factor

x_0 Reference coordinate for the gust

x_j Aerodynamic element's location in the aerodynamic coordinate system

$\mathbf{w}_j^g$ Downwash vector arising from air stream motion.

Symbols

Δ Variation or finite difference

$\Im$ Imaginary part

$\int(\,)$ Integral

$\nabla(\,)$ Gradient

$\nabla \cdot (\,)$ Divergence

∂ Partial derivative

$\Re$ Real part

i Imaginary unit

Superscripts

$(\,)^{S_1}$ Flight shape 1

$(\,)^{S_2}$ Flight shape 2

$(\,)^{CFD_G}$ Gust CFD aerodynamic forces

$(\,)^{CFD_S}$ Steady CFD aerodynamic forces

$(\,)^{DLM_G}$ Gust DLM aerodynamic forces

$(\,)^{DLM_S}$ Steady DLM aerodynamic forces

$(\,)^{G}$ Gust contribution

$(\,)^{I}$ Imaginary part

$(\,)^{MS}$ Mode shape contribution

$(\,)^{R}$ Real part

$\bar{(\,)}$ Fourier transform

$\hat{(\,)}$ Modal generalized quantity

Subscripts

a Set of the structural degree of freedom.

E Elastic

e Set of the aerodynamic extra points.

i Set of the normal models degree of freedom

j Set of the aerodynamic control points located at the panel's $3/4$ chord.

k Set of the aerodynamic box degree of freedom consisting of both the translational and rotational degrees of freedom.

R Rigid

r Set of the monitor points degree of freedom

Acronyms

AIC Aerodynamic Influence Coefficients Matrix

CFD Computational Fluid Dynamic

DLM Doublet-Lattice Method

DLR German Aerospace Center

FEM Finite Element Model

GAF Generalised Aerodynamic Forces

LFD Linearized Frequency Domain

NCRM NASA Common Research Model

ROM Reduced Order Model

UVLM Unsteady Vortex Lattice Method

VLM Vortex Lattice Method

CHAPTER 1

Introduction

The aeronautics industry is a key and strategic sector in the economy of the European Union, which plays a leading role in embracing new technologies and efficiency challenges. The Advisory Council for Aeronautics Research and Innovation in Europe (ACARE) has set very ambitious technology goals, with its vision for the future of aeronautics in the document Flightpath 2050 [1]. In order to meet these goals a big step forward is required from all the stake holders of the sector: not only aircraft and engine manufactures, but from airlines and air traffic management as well. Present forecasts highlight a constant growth in terms of the number of passengers per year, with a big expansion of new markets in the Middle East and Asia. At the same time even more demanding requirements in terms of environmental regulation: from CO_2 emission reduction, to NO_X cutting and a relevant reduction in noise pollution must be met.

Aircraft manufacturers are rising to these challenges by identifying new configurations and solutions which can bring improved performance and higher efficiency. Two areas which have been a focus for research are structural design and aerodynamic optimization. In structural design this has led to the introduction of new and lighter materials (e.g. up to 50% of structural weight is composites materials in the B787 and up to 53% for the A350 [2]) and aerodynamicists have focussed on design optimization in order to reduce drag and hence to obtain the optimum performance of conventional aircraft designs.

At a research level, innovative design solutions have been presented, introducing new devices

which could contribute to reduced drag. These include folding wing tip devices to reduce aerodynamic drag [3] or to reduce gust loads [4]. Additionally, great emphasis has been dedicated to investigating high aspect ratio configurations [5, 6] that could drive the design for the wings of the next generation of aircraft.

In order to achieve an efficient design it is essential that during the entire aircraft development phase, accurate and robust methodologies are implemented to predict the loads acting on the structure. Designing a safe structure while minimizing the weight is the aim of the aircraft designer. It has to be ensured that no failure occurs due to excessive stresses during the operational life of the aircraft, both in flight and on the ground. This is the reason why an accurate loads estimation is essential during the development and certification phases of a new aircraft. They, in fact, have a large impact on the structural sizing and weight. Therefore it is evident that gust loads modelling is an essential prerequisite for an optimal structural design.

The present thesis addresses the need to accurately estimate the aerodynamic loads acting on an aircraft structure, using methods that are computationally efficient enough to allow the analysis of the very high number of simulations necessary to cover the entire spectrum of load cases to accomplish aircraft certification. To achieve this goal a new hybrid approach is considered, where a potential method is used to compute the aerodynamic loads and a correction technique is implemented to increase the accuracy at higher Mach numbers where transonic effects become important.

1.1 Aeroelastic Loads Analysis

During its operational life, an aircraft is subject to a broad range of loads cases. These include both ground loads such as taxiing, steering, towing and landing or taking off manoeuvres, and flight loads due to steady and unsteady manoeuvres and atmospheric turbulence. An accurate estimation of the aircraft loading condition is achievable only if the interaction between elastic, aerodynamic and inertial loads is taken into account. The science that studies this problem is called Aeroelasticity, and it provides an understanding of how the mutual interaction of these loads affects the static and dynamic response of the aircraft, Figure 1.1. A graphical representation of this interaction is given by Collar's Aeroelastic Triangle shown in Figure 1.2.

Figure 1.1: Coupling of atmospheric loads and structural effects (Credit: DLR Fully coupled aeroelastic gust and manoeuvre simulations [7]).

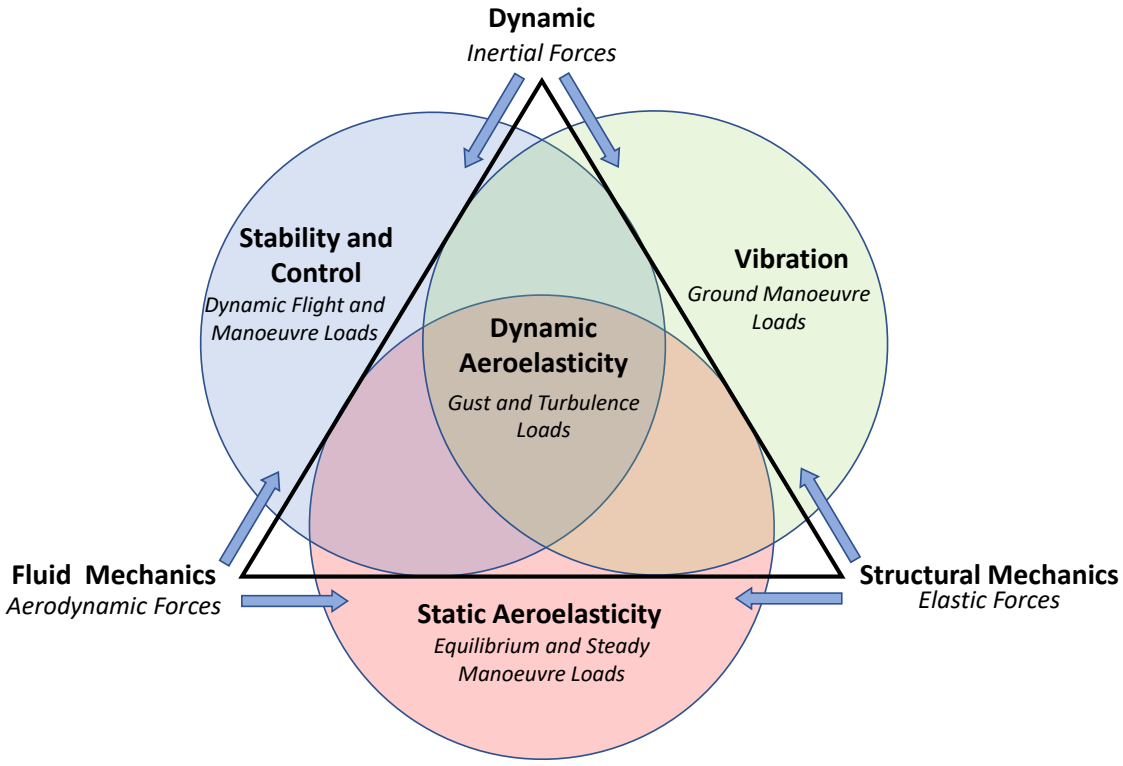

Figure 1.2: Collar's Aeroelastic Triangle [8].

It shows how the interaction of two of the three types of forces mentioned, define a discipline such as static aeroelasticity, structural dynamics and stability and control. Traditionally aeroelastic phenomena are classified into two groups: static aeroelasticity and dynamic aeroelasticity. Static aeroelasticity takes into consideration the effect of non oscillatory aerodynamic loads acting on the flexible aircraft structure. As a consequence of the wing flexibility, the shape of the wing will be modified, and with it the lift distribution, in cruise or during a steady manoeuvre. No matter how accurate the aerodynamic simulation is, if the structure is not modelled accurately, the final flight shape could be in error. Dynamic aeroelasticity refers to the oscillatory effect of the aeroelastic interactions, with specific attention to the flutter phenomenon. In this case the interaction of aerodynamic, inertia and elastic forces couples together with one or two modes of vibration, with the consequence that the structure can extract energy from the air stream. The flexibility of the structure has an influence on the dynamic stability modes of the rigid aircraft, and consequently influences the flight dynamics. If additionally the interaction of the flexible aircraft with the flight control system is investigated then this is called aeroservoelasticity.

The design of an aircraft is strongly influenced by aeroelasticity, which is needed to identify the critical load cases as well as the static and dynamic stability boundaries. Structural sizing depends on this essential information and the accurate prediction of aeroelastic behaviour becomes essential for an optimal design. The in flight wing shape is optimized to reduce drag in the cruise condition, with this configuration obtained by the equilibrium of the aerodynamic forces acting on the flexible wing structure. Knowing the aeroelastic loads is fundamental to identifying the corresponding "jig-shape" which is the geometry with which the wing is manufactured. Returning to Collar's triangle, equilibrium manoeuvres result from the interaction between aerodynamic and elastic effects, with aircraft experiencing steady manoeuvres (longitudinal or lateral). The interaction of inertia and aerodynamic effects define the area of dynamic manoeuvres: aircraft dynamic response to transient control inputs. Ground manoeuvres see the interaction of inertia and elastic effects, it includes steady and dynamic loads conditions when the aircraft is operating on the ground with the landing gear deployed. The response to gust disturbance is given by the interaction of elastic, aerodynamic and inertia effects: the response of the aircraft to encounters with discrete gusts or continuous turbulence are considered.

1.2 Aircraft Loads Modelling

During the design phase of an aircraft, and in order to achieve its certification, manufacturers have to ensure that no structural damage will be experienced by the structure due to excessive loads, both in flight and on the ground. No flutter or divergence must occur at any point of the flight envelope. Numerical simulations and flight tests are essential to accomplish these requirements. A loads envelope, accounting the combination of flight condition (defined by altitude, Mach number, angle of attack), different mass configurations and excitations (such as gusts, manoeuvres or dynamic landing), needs to be computed. The Certification Authorities (e.g. EASA, FAA) prescribe the type of unsteady loads that the aircraft have to withstand in their regulations (CS-25 for large commercial aircraft [9] , JAR/FAR 25 [10]). EASA certification specification for large aeroplanes, CS-25, explicitly requires the loads prediction to take into account: airframe flexibility, unsteady aerodynamics and interaction of systems and structure; leading to computationally expensive numerical models. Among the unsteady loads, gust loads are critical for strength design. In particular because they are a major source of fatigue loads [8]. Therefore, an accurate evaluation of the aerodynamic loads interacting with the structure become essential for the structural design.

To perform loads simulation it is necessary to represent:

- structural inertial properties: a Finite Element Model FEM including stiffness and mass data for each mass case;
- aerodynamic properties: steady or/and unsteady loading at a specific flight point;
- flight dynamic properties: including the Flight Control System control laws influencing control surface deflection;
- external disturbances: accounting for external disturbances, which include both gust and pilot prescribed inputs.

1.3 Aerodynamic Loads Modelling for Aircraft Design

A wide range of aerodynamic models are available to evaluate the aero loads interacting with the structure. From very simple lifting line to high fidelity Navier-Stokes Computational Fluid Dynamics (CFD) analysis. Hence a range of approaches with increasing level of accuracy and complexity can be adopted. Steady approaches are used to investigate trim configurations and define the optimized flight shape. Unsteady methods are necessary to investigate stability problems or the response to gust disturbance.

In the first initial stages of the design, driven by the need to explore several design variations, often simplified unsteady approaches are favoured. Among these it is possible to use modified 2D strip theory where the unsteadiness of the flow field is modelled using transfer functions. The Indicial Functions Method (IFM), uses the so called Wagner function to account for sudden variation of angle of attack, while the Küssner function accounts for intrusion in a sharp edge gust [11, 12]. Whilst these methods are quick and computationally efficient, they are of low fidelity and neglect tip effects and wake-aerofoil interaction.

For low subsonic speeds the Doublet-Lattice Method (DLM) is widely used in industry. This is a three dimensional unsteady potential method, which solves the acceleration potential equations using a harmonic approach, resulting in a solution in the frequency domain [13]. The DLM is a finite element method for the determination of the oscillatory subsonic loading on configurations of interfering nonplanar surfaces with arbitrary planforms, dihedral and control surfaces [14]. It is an oscillatory extension of the steady Vortex Lattice Method (VLM). The modification is oriented to take in consideration the oscillatory motion by adding a line of incremental oscillatory doublets of constant strength to the bound vortex along the quarter-chord of each box. The steady doublets singularity is equivalent to the horseshoe vortex, so the sum of the vortex and the incremental doublet singularities represents the total loading caused by the oscillatory motion and acts at the box quarter-chord. This preserves the accuracy of the VLM at low reduced frequencies [14]. It is a linear method, therefore its accuracy is drastically reduced in the transonic regime, when non linear phenomena become relevant.

High fidelity results can be obtained using Computation Fluid Dynamics (CFD) simulations, where the unsteady, three-dimensional, Navier-Stokes equation can be implemented [15]. The main disadvantage of this methodology is the increased computational cost necessary to solve

the problem.

Additionally to account for the flexibility of the structure it is necessary to consider the coupling of the CFD model with the flexible structural dynamics equation of motion. Whilst fully coupled Fluid Structure Interaction analysis can provide the highest level of accuracy, the results are very computationally expensive.

1.4 Gust Load Analysis for Aircraft Design

As prescribed by the certification regulations EASA CS 25 [9], a large range of loads cases has to be verified for an aircraft before it enters service. Each of those is represented by a combination of flow parameters (altitude, Mach number, angle of attack, etc), mass configuration, control surface angles, manoeuvre conditions and external loads (such as gust) [16]. Accounting for all the variable combinations means that the number of loads cases to be examined is of the order of the hundreds of thousand.

Although great advances have been made on the field of computational fluid dynamics (CFD), the very high number of cases to be investigated requires the application of cheaper computational methods. For this reason the industrial standard is to rely on linear lifting surface potential methods, such as the Doublet-Lattice Method (DLM) to model the unsteady aerodynamic lifting surface and bodies. Despite being very computationally efficient, these methods are based on simplifying assumptions which do not allow to capture transonic, viscous or thickness effects.

In order to overcome these limitations, it is common practice to correct the aerodynamic lifting pressure based on steady aerodynamics and leave the computation of the phase lag between the surface motion and the aerodynamic forces to lower order methods. An overview of existing DLM correction methods is provided in [17, 18]. However, these methods do not permit accurate estimation of the aeroloads due to unsteady phenomena, such as the response to gust disturbance. In particular none of them has shown the capability to account for the structural flexible deformation induced by the atmospheric perturbation.

To answer the need of balancing computational efficiency and accuracy in flight regimes of interest for civil transport aircraft, a novel fully unsteady correction method for the DLM is proposed in this thesis.

1.5 The ALPES Project

The research activity resulting in this thesis has been performed within the "Aircraft Loads Prediction Using Enhanced Simulation (ALPES) Project", an EC FP7 Marie Curie European Industrial Doctorate Training Network. This project involved a network of five Early Stage Researchers (ESRs) who were registered for PhDs at the University of Bristol and which ran from 1 October 2013 to 30 September 2017. The research performed in the project contributed towards two key aspects of the ACARE2020 and FLIGHTPATH2050: design an environmentally friendly aircraft and achieve a faster design and certification process. The main academic and industrial partners for ALPES were the University of Bristol (UK) and Siemens Industry Software NV (Leuven, BE); while Airbus Operations Ltd (UK) was involved as an Associate Partner.

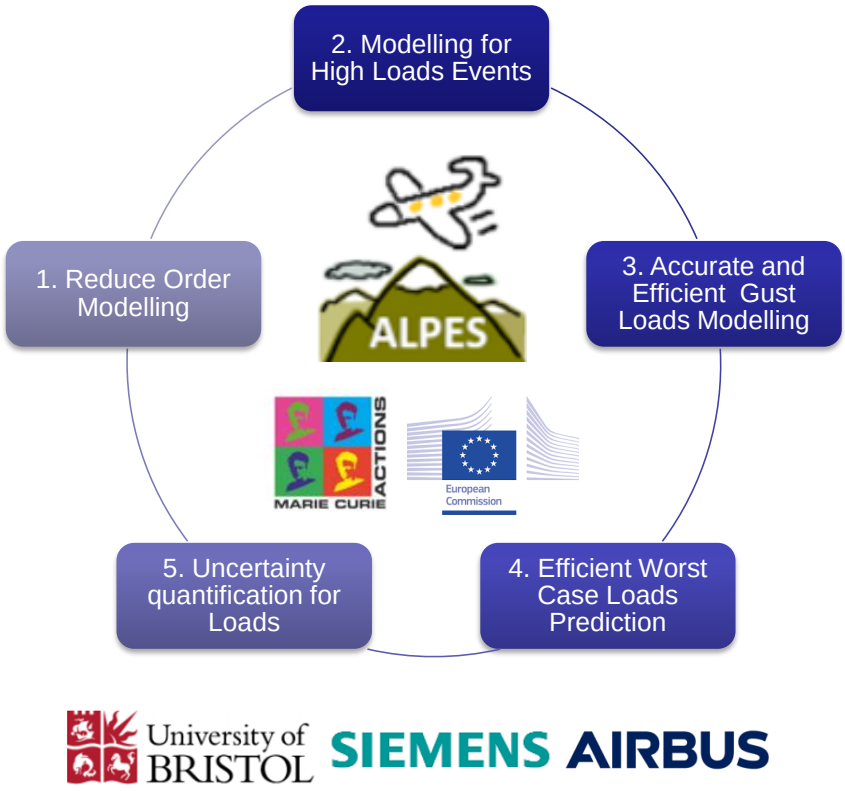

Figure 1.3: ALPES Project research topics.

The project aimed to develop novel methods and procedure for accurate and efficient aircraft loads prediction, while providing an industrially focused training regime for the researchers in order to facilitate their movement into the European aerospace industry. The five research top-

ics focused on different aspects of the loads modelling and evaluation as described in Figure 1.3. The present work is the result of the work package 3 which investigated new methodologies to improve the accuracy of present-days gust loads modelling approaches adopted in the aeronautics industrial context.

1.6 Contribution of this thesis

This thesis focuses on the definition of a novel approach to integrate high fidelity unsteady data with the aerodynamic loads computed by means of a potential method. Since experimental results were not available, a dedicated Fluid Structure Interaction methodology has been developed to compute reference aeroelastic loads. This allows the CFD DLR TAU-Code to be coupled with the FEM solver MSC Nastran, with the capability to investigate steady and unsteady aeroelastic problems.

The major novel scientific contributions of this study are:

- A mathematical formulation of a fully unsteady Aerodynamic Influence Coefficient factor correction technique, for the doublet-lattice method.
- Development and implementation of a framework to allow the integration of a limited number of high fidelity analyses to compute the correction factors used to correct the doublet-lattice method available in the commercial FEM solver.
- The validation of the presented methodology for two reference cases. This includes comparison with fully coupled analysis.

1.7 Aerodynamic methods and their application in this thesis

In the following chapters a series of different methods are presented and used to evaluate the aerodynamic loads interacting with the structure.

- Aeroelastic high fidelity fluid structure interaction analysis, where the aerodynamic loads computed using the DLR TAU-Code are coupled with a structural finite element model,

solved in MSC Nastran.

- Rigid Computational Fluid Dynamics, DLR TAU-Code.
- Unsteady time domain CFD simulation, DLR TAU-Code.
- Linearised Frequency Domain (LFD) analysis for prescribed mode deformation and gust, DLR TAU-Code.
- Uncorrected Doublet-Lattice Method (DLM), MSC Nastran.
- Corrected DLM using rigid data: reference data obtained from unsteady time domain CFD data or LFD simulation.
- Corrected DLM using rigid data and imposed mode deformation: reference data obtained by means of unsteady time domain CFD or LFD simulation.

1.8 Thesis outline

The research activity presented in this thesis builds on the theoretical background of correction techniques for an Aerodynamic Influence Coefficient matrix, which represent the kernel of many potential methods. It implements for the first time a fully unsteady correction approach, and defines a strategy to reduce the computational time necessary to evaluate high fidelity aerodynamic loads.

Chapter 2 provides an overview of the Doublet-Lattice Method formulation and its implementation in the commercial software MSC Nastran. A literature review of correction approaches is presented.

Chapter 3 presents the CFD code used in this thesis to provide a high fidelity reference aero loads case data, the DLR TAU-Code.

Chapter 4 introduces a fluid structure analysis environment, the AlpesFSI, developed to perform fully coupled CFD-FEM aeroelastic simulations. This chapter builds upon a conference paper presented at the IFASD 2015 International Forum on Aeroelasticity and Structural Dynamics [19].

Chapter 5 provides the formulation of the novel correction approach presented in this thesis. An unsteady AIC correction methodology is presented to increase the accuracy of the doublet-lattice method.

Chapter 6 exploits the correction method proposed and presents the numerical results of its application for an aircraft wing. An initial Euler model is used to solve the CFD. This chapter in an extension of the conference paper presented at the AIAA SciTech 2017 [20].

Chapter 7 provides the results of the correction method on a civil aircraft model, the NASA Common Research Model. In this case the corrected DLM method is compared with the high fidelity results obtained from a RANS CFD aeroelastic simulation. This chapter is an extension of a conference paper presented at the IFASD 2017 International Forum on Aeroelasticity and Structural Dynamics [21].

Finally, Chapter 8 presents the conclusions reached in this work and makes suggestions on areas for future research.

CHAPTER 2

The Doublet-Lattice Method

This chapter provides an overview of the Doublet-Lattice Method used to account for unsteady aerodynamic loads in the linear aeroelastic analysis throughout this thesis. The DLM is a potential method formulated in the frequency domain. This method has been integrated within the aeroelastic solution available in the commercial software MSC Nastran, where it is coupled with the structural Finite Element Method (FEM) model to provide a framework to evaluate steady aeroelastic analysis, flutter analysis and unsteady response to gust disturbance. The main focus is to present the formulation of the DLM for gust response analysis, which will be used as the starting point in Chapter 5 to define the correction method developed in this work. A review of some methodologies to correct the DLM is presented, outlining the limitation of such approaches and the need to define a specific more efficient correction technique for gust response analysis.

2.1 Introduction to the Doublet-Lattice Method

The Doublet-Lattice Method (DLM) [13, 22] is a linear potential unsteady aerodynamic theory for thin lifting bodies. It is based on the assumption of inviscid, attached, irrotational flow and a perfect isentropic gas. From these the Navier-Stokes equations can be simplified leading first to Euler's equations for an inviscid flow:

$$\frac{\partial \rho}{\partial t} + \nabla \cdot (\rho \mathbf{v}) = 0 \tag{2.1}$$

$$\rho \left[\frac{\partial \mathbf{v}}{\partial t} + (\mathbf{v} \cdot \nabla) \mathbf{v} \right] = -\nabla p \tag{2.2}$$

$$\frac{p}{\rho^{\gamma_{hcr}}} = const \tag{2.3}$$

This system of equations consists of the equation of conservation of mass, three equations for the conservation of momentum and the equation of state for a perfect isentropic gas. The unknowns are the three components of the flow velocity $\mathbf{v}$, the pressure p and the density ρ. γ_{hcr} is the heat capacity ratio of the fluid. From the assumption of inviscid fluid follow there is no shear force component in the equation of momentum, consequently no vorticity can be generated. Nevertheless the Euler equations allow vorticity to be convected in cases where vorticity exist due to boundary or initial conditions (e.g. a starting vortex). Since the fluid is inviscid the no-slip boundary condition can not be applied. Because the only consideration that can be applied is the impermeability of the body, the fluid velocity at the boundary is made parallel to the local boundary tangent. The Kutta condition specifies a smooth and finite flow off the sharp trailing edge of a lifting surface in incompressible flow. The velocity vector is not allowed to deflect as the flow passes over the trailing edge. If it does deflect, the velocity become locally infinite. This trailing edge and wake are completely characterized for incompressible flow.

As shown by Blair in [22] the Euler's formulation can be rearranged to give the full potential equation:

$$\nabla^2 \chi - \frac{1}{a^2} \left[\frac{\partial^2 \chi}{\partial t^2} + \frac{\partial}{\partial t} \mathbf{v}^2 + \nabla \chi \cdot \nabla \left(\frac{\mathbf{v}^2}{2} \right) \right] = 0 \tag{2.4}$$

Following the assumption of irrotational flow, it is possible to define a velocity potential χ as

$$\mathbf{v} = \nabla \cdot \chi = \left\{ \frac{\partial \chi}{\partial x}, \frac{\partial \chi}{\partial y}, \frac{\partial \chi}{\partial z} \right\} = \{\chi_x, \chi_y, \chi_z\} \tag{2.5}$$

Eq. (2.4) can be expanded, using subscript to indicate differentiation:

$$\begin{aligned} \nabla^2 \chi - \frac{1}{a^2} \chi_{tt} - \frac{2}{a^2} \left(\chi_x \chi_{xt} + \chi_y \chi_{yt} + \chi_z \chi_{zt} \right) - \frac{1}{a^2} \left(\chi_x^2 \chi_{xx} + \chi_y^2 \chi_{yy} + \chi_z^2 \chi_{zz} \right) - \\ \frac{1}{a^2} \left(2\chi_x \chi_y \chi_{xy} + 2\chi_x \chi_z \chi_{xz} + 2\chi_y \chi_z \chi_{yz} \right) = 0 \end{aligned} \tag{2.6}$$

The steady state form of Eq. (2.6) can be obtained setting to zero the derivatives respect to time t. Assuming that a steady state solution to this non linear equation exists, it is possible to express the term of the equations as given by two contribution. The first ia a steady state component and the second is a small disturbance component which is time dependent:

$$\chi(x, y, z, t) = \bar{\chi}(x, y, z) + \Delta\chi(x, y, z, t) \tag{2.7}$$

In this linearization process, the speed of sound is considered time invariant:

$$a(x, y, z, t) = \bar{a}(x, y, z) \tag{2.8}$$

The speed of sound will be considered constant in the linearized formulation. To proceed with the linearization it is necessary to replace Eq. (2.7) and (2.8) in Eq. (2.6). Additionally, it is necessary to delete any nonlinear term in χ and it's derivatives. Furthermore the steady state condition is removed. At this point it is possible to express the time linear partial differential equation as:

$$\begin{aligned}(\Delta\chi_{xx} &+\Delta\chi_{yy} + \Delta\chi_{zz}) - \frac{1}{\bar{a}^2}\left[\Delta\chi_{tt} + 2\bar{\chi}_x\Delta\chi_{xt} + 2\bar{\chi}_y\Delta\chi_{yt} + 2\bar{\chi}_z\Delta\chi_{zt} + \right.\\ &\bar{\chi}_x^2\Delta\chi_{xx} + \bar{\chi}_y^2\Delta\chi_{yy} + \bar{\chi}_z^2\Delta\chi_{zz} + 2\left(\bar{\chi}_x\bar{\chi}_y\Delta\chi_{xy} + \bar{\chi}_y\bar{\chi}_{xy}\Delta\chi_x + \bar{\chi}_x\bar{\chi}_{xy}\Delta\chi_y\right) + \\ &2\left(\bar{\chi}_x\bar{\chi}_z\Delta\chi_{xz} + \bar{\chi}_z\bar{\chi}_{xz}\Delta\chi_x + \bar{\chi}_x\bar{\chi}_{xz}\Delta\chi_z\right) + \\ &\left.2\left(\bar{\chi}_y\bar{\chi}_z\Delta\chi_{yz} + \bar{\chi}_z\bar{\chi}_{yz}\Delta\chi_y + \bar{\chi}_y\bar{\chi}_{yz}\Delta\chi_z\right)\right] = 0\end{aligned} \tag{2.9}$$

Even if the speed of sound would have been considered of an higher order, the higher order terms would have dropped out when the non linear terms have been dropped to get to the above expression. Despite the Euler equation has been expressed in terms of a partial differential equation linear in $\Delta\chi$, the solution for $\Delta\chi$ is still difficult to analyse for any general description of the steady state field $\bar{\chi}(x, y, z)$. Since there are no elementary solution available for the entire flow field described in Eq. (2.9), it is possible to restrict this partial differential equation to simple steady mean flows. Considering the assumptions of a time invariant speed of sound, small perturbations around a mean uniform steady flow with a velocity U_∞, aligned with the x direction with respect to the aerodynamic reference system, for the entire flow field the coefficients

are simply:

$$\bar{\chi}(x, y, z) = U_\infty x \tag{2.10}$$

$$\bar{a}(x, y, z) = a_0 \tag{2.11}$$

where a_0 is the constant value of the speed of sound in the far field. Replacing these in Eq. (2.9) it is possible to obtain the classical linear small disturbance velocity potential partial differential equation give by:

$$\left(1 - M^2\right) \Delta\chi_{xx} + \Delta\chi_{yy} + \Delta\chi_{zz} - \left(\frac{2U_\infty}{a_0^2}\right) \Delta\chi_{xt} - \left(\frac{1}{a_0^2}\right) \Delta\chi_{tt} = 0 \tag{2.12}$$

where $M = U_\infty/a$ is the free stream Mach number. Both the steady velocity U_∞ and the steady speed of sound a are assumed to be constant in the entire flow field to formulate this linear equation. So for the linear small disturbance theory, the Mach number is assumed constant for the entire flow field. Since all the coefficient of Eq. (2.12) are now constant, it is possible to identify elementary solutions of the linearized problem.

The linearised velocity potential assumes a constant uniform velocity in the x direction. Under a Gaussian transform in x:

$$x \;\rightarrow\; x - U_\infty t \tag{2.13}$$

we get the acoustic potential equations:

$$\varphi_{xx} + \varphi_{yy} + \varphi_{zz} - \frac{1}{a_0^2}\varphi_{tt} = 0 \tag{2.14}$$

This highlights the relationship between aerodynamics and acoustics, and to understand the relationships we must understand the time delay between a signal at a point arriving at some other point in the domain. The fundamental analysis outlined by Landahl and Blair [23, 22] considers a moving source and arrives at a fundamental solution of the form

$$\varphi = \frac{1}{R} F(t - \tau) \tag{2.15}$$

with

$$\tau = \frac{M\Delta x + R}{a_0\sqrt{1 - M^2}} \tag{2.16}$$

where $F(t)$ is the source strength, R is a transformed distance and Δx is the distance in the x direction between the source point and the receiver position. A doublet solution for an infinitely thin wing can be found by bringing a source and sink together between the upper and lower surfaces. However to increase efficiency, further steps are taken so that the pressure can be found directly, rather than solving for the velocity potential, and then using a 1D Euler equation to find the pressure. Taking derivatives of the velocity potential equations and using the definition of the unsteady pressure leads to the definition of the pressure potential (or acceleration potential) as:

$$(1 - M^2)p_{xx} + p_{yy} + p_{zz} - \frac{2U_\infty}{a_0^2}p_{xt} - \frac{1}{a_0^2}p_{tt} = 0 \tag{2.17}$$

As this is the same form as the velocity potential the fundamental doublet solution is unchanged. Further manipulation of this solution means that the upwash, w, at a point (x, y, z) from a "pressure doublet" sheet of strength Δp oscillating around a $z = const$ plane can be written as:

$$w(x, y, z) = \frac{-1}{4\pi\rho U_\infty} \int\int_{sheet} \Delta p \; K[(x - \xi), (y - \eta), z] d\xi d\eta \tag{2.18}$$

where K is the kernel function. The full equations are rather lengthy [23] and need not be restricted to the $z = const$ plane, only planes parallel to the x axis. With this upwash basis defined we can proceed in a manner similar to standard incompressible doublet panel potential solvers, as will now be outlined. The fundamental solutions found can be linearly superimposed such that the boundary conditions are satisfied. So for the assumption of potential flow the problem can be solved using a spatial discretisation of the body wetted surface and the wake, without considering the entire aerodynamic domain. The solution of the unsteady aerodynamic problem is reduced to solving a boundary problem.

The solution of the problem is based on the definition of an aerodynamic lifting surface given by flat panels aligned to the free stream direction, see Figure 2.1. For each panel, a horseshoe shaped doublet distribution is located at the quarter chord. The intensity of this distribution is unknown, but it is evaluated assigning the boundary condition on a control point located at the three quarter chord. The potential and the pressure are considered as uniformly distributed within each panel.

The unknown pressure on each panel is assumed to be lumped on one single point positioned on the $1/4$ of the panel's chord (where the doublet line lies as well) and centred with respect

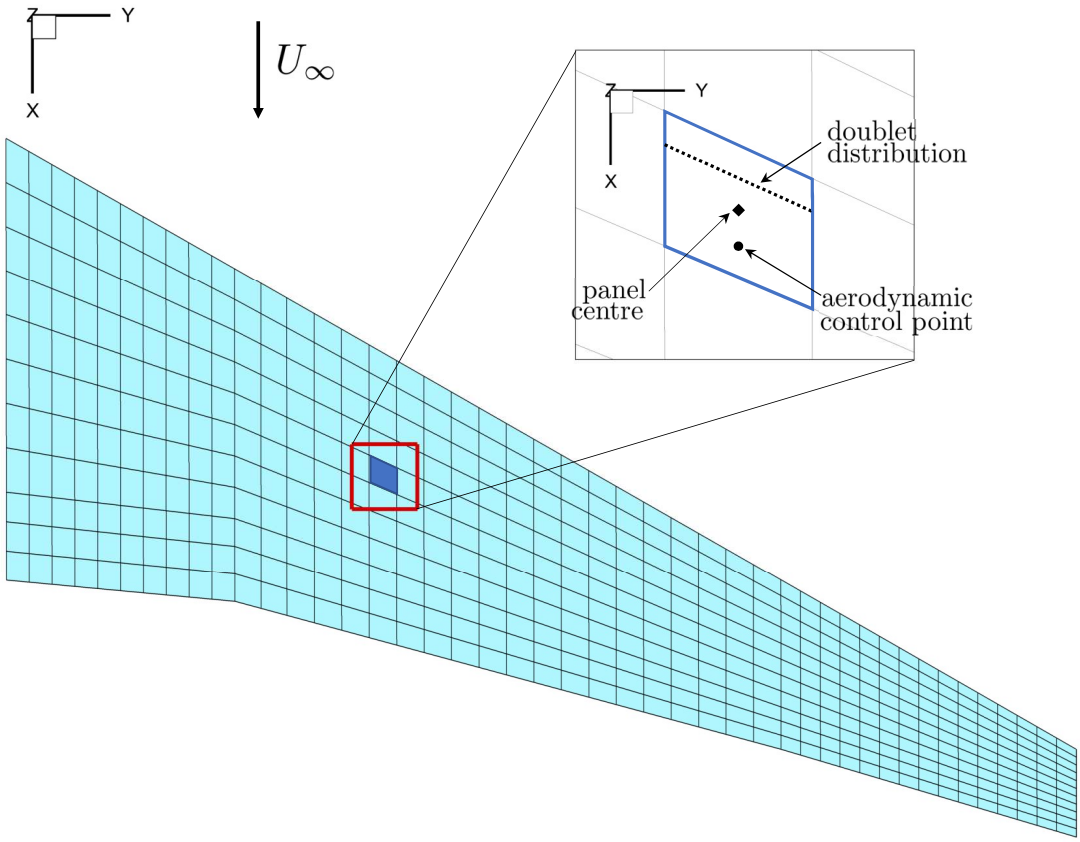

Figure 2.1: DLM Panel Discretisation

to the spanwise direction, while the impermeability boundary condition is satisfied only in one point, the control point, which is placed at the $3/4$ of the panel's chord midspan. Applying the boundary condition to all the panels it is possible to define the Aerodynamic Influence Coefficient matrix (AIC), whose generic element A_{mn} relates the downwash on the m^{th} panel to the aerodynamic pressure coefficient on the n^{th} panel as follows:

$$w_m = A_{mn} c_{p_n} \tag{2.19}$$

The modelling and discretisation of the aerodynamic wake, released from the trailing edge, is an important aspect of DLM for unsteady aerodynamics simulation. The Doublet Lattice Method is based on the assumption of pure harmonic motion of the aerodynamic panels leading to a pure harmonic aerodynamic wake. The transient effects due to the development of a free wake can therefore not be accounted for and the aerodynamic forces on the body that arise due to lifting body motion or atmospheric turbulence are evaluated through the linear superimposition of basic harmonic solutions. Furthermore if one makes the assumption of a constant pressure

through the wake (force free condition valid for the released wake) then there is no acceleration potential associated with the wake sheet.

The wake aerodynamic forces are thus fully defined by the motion of the aerodynamic panels of the lifting body only. This permits unsteady aerodynamic effects to be included without the need to evaluate the free development of the wake [24, 22]. Consequently the aerodynamic panels need only be defined on the lifting body and no mesh is needed to discretise the wake. The unsteady aerodynamic effects are modelled through the use of complex coefficients within the AIC matrices. These define the harmonic unsteady aerodynamic forces due to the harmonic motion of the aerodynamic panels, and also the phase delay between the motion and the related forces. For a given aerodynamic mesh geometry, the AIC matrices are functions of the Mach number and of the reduced frequency κ, defined as

$$\kappa = \frac{\omega}{U_\infty}\frac{l_{ref}}{2} \tag{2.20}$$

where ω is the angular speed of the harmonic oscillation of the panels given by $\omega = 2\pi f$ where f is the frequency, and l_{ref} is a reference length (e.g. the wing mean chord).

2.2 The Doublet-Lattice Method in MSC Nastran

The commercial finite element software MSC Nastran is the aeronautic industry standard for structural load analysis. Within its wide range of solution methods, it includes aeroelastic analysis capability to investigate steady aeroelastic problems, stability or flutter analysis and the unsteady gust response. As well as the structural solver it integrates finite element approaches with the evaluation of aerodynamic loads. Among these, MSC Nastran implements the Doublet-Lattice Method (DLM), developed by Albano and Rodden [24] in the late sixties, for unsteady aerodynamic modelling.

Many other software companies during the past decades have produced solutions dedicated to the design and analysis of aircraft loads. Among those, Zona Technology, since its foundation in 1985, has developed dedicated application for steady and unsteady aeroelasticity. In their commercial solutions, ZAERO [25] and ZONAIR [26], an higher-order panel formulation for lifting surface has been implemented [27] [28].

Since MSC Nastran is the reference finite element solver used in Airbus for structural dynamic analysis and most of the aeroelastic methods used for loads analysis are based on Nastran models, it has been decided to adopt MSC Nastran and the DLM method implemented in its aeroelastic solution as reference method for steady aeroelasticity and gust response investigation.

In order to formulate the expression that leads to the DLM method, the following degree of freedom sets are introduced:

- *a-set*: is the set of the structural degree of freedom;
- *j-set*: is the set of the aerodynamic control points located at the panel's $3/4$ chord. These correspond to the points where the downwash vectors are computed.
- *k-set*: is the set of the aerodynamic box degree of freedom consisting of both the translational, in z direction, and rotational, around the y-axis, degrees of freedom. This set is twice the size of the *j-set*.
- *e-set*: set of the aerodynamic extra points, used to describe aerodynamic control surface deflections and rigid body motions, such as angle of attack or roll acceleration.
- *i-set*: set of normal modes.
- *h-set*: combination of normal modes and extras point set.

Note that in this analysis, the set introduced above will be used at the matrices and vectors subscript, to indicate the set of the quantity considered rather than identifying the indices of the matrix elements. All the matrices and vectors are indicated with a bold style. As discussed in the the previous section, in the DLM the pressure is assumed to act at the quarter chord location of each element and the downwash is matched at the three-quarter chord on the centreline of each element. A representation of the generic aerodynamic panel is shown in Figure 2.2(a).

To be able to express the aerodynamic forces evaluated by the DLM it is necessary to introduce the matrix formulation which relates the lifting pressure and normal velocity induced by the inclination of the surface to the airstream, defined as downwash:

$$\mathbf{c}_{p_j} = \mathbf{A}_{jj}^{-1}\, \mathbf{w}_j \tag{2.21}$$

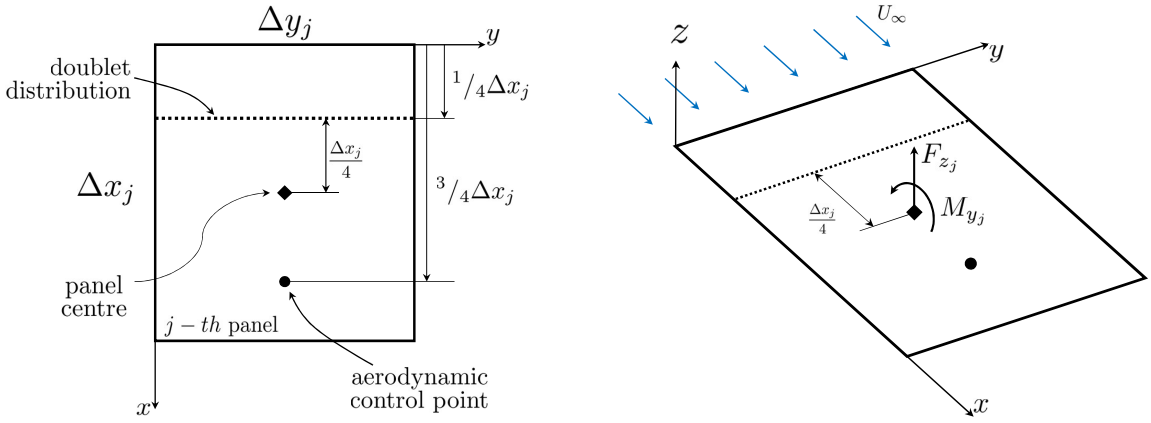

(a) DLM panel geometry.

(b) DLM panel loads orientation.

Figure 2.2: DLM panel

where $\mathbf{w}_j$ is the downwash vector, $\mathbf{A}_{jj}^{-1}(M,\kappa)$ is the aerodynamic influence coefficient matrix, function of Mach number and reduced frequency, and $\mathbf{c}_{p_j}$ is the vector of pressure coefficients. Integrating the pressure on the panels, $\mathbf{p}_j$, it is possible to obtain the aerodynamic forces and moments acting on them as:

$$\mathbf{P}_k = \mathbf{S}_{kj}\ \mathbf{p}_j \tag{2.22}$$

where $\mathbf{P}_k$ is the vector of the vertical force, and pitching moments for each of the panels, $\mathbf{S}_{kj}$ is the aerodynamic integration matrix, which relates the pressures to the loads. Considering that the resulting forces are acting at the quarter point location of each box, but the loads are then computed at the panel centre, the vertical force is obtained by multiplying the pressure by the panel area $\bar{a}_j$, while the pitching moment is evaluated by multiplying the pressure by the panel area and the moment arm $\Delta x_j/4$ for each box [29]:

$$S_{kj} = \begin{bmatrix} \bar{a}_j \\ \bar{a}_j \frac{\Delta x_j}{4} \end{bmatrix} \tag{2.23}$$

In terms of pressure coefficient Eq. (2.22) becomes:

$$\mathbf{P}_k = \bar{q}\ \mathbf{S}_{kj}\ \mathbf{c}_{p_j} \tag{2.24}$$

where $\bar{q} = \frac{1}{2}\rho U_\infty^2$ is the dynamic pressure.

For deforming cases the motion of the *k-set* is related to the *j-set* by the $\mathbf{D}_{jk}^1$ and $\mathbf{D}_{jk}^2$ matrices.

The first relates the deformation to a local angle of attack u_j by transferring the rotational degree of freedom from the *k-set*, u_k:

$$u_j = D^1_{jk} u_k \tag{2.25}$$

$$D^1_{jk} = \begin{bmatrix} 0 \\ 1 \end{bmatrix} \tag{2.26}$$

The matrix $\mathbf{D}^2_{jk}$ relates the rate of deformation $\dot{u}_k$ to a local angle of attack u_j. The lever arm $\Delta x_j/4$ is the distance between the panel centre, in the *k-set*, and the control point, of the *j-set* so that:

$$u_j = D^2_{jk} \frac{\dot{u}_k}{U_\infty} \tag{2.27}$$

$$D^2_{jk} = \begin{bmatrix} 1 \\ \frac{\Delta x_j}{4} \end{bmatrix} \tag{2.28}$$

Considering a transient motion, normal to the xy-plane, the collocation point downwash is given by:

$$\mathbf{w}_j(x, y, t) = \mathbf{D}^1_{jk} \mathbf{u}_k + \mathbf{D}^2_{jk} \frac{\dot{\mathbf{u}}_k}{U_\infty} + \mathbf{w}^g_j(x, y, t) \tag{2.29}$$

where $\mathbf{w}^g_j(x, y, t)$ is the downwash arising from the motion of the airstream, e.g. a gust. In the case of harmonic motion with frequency ω, Eq. (2.29) can be written in the frequency domain, and by considering the definition of reduced frequency κ given in Eq. (2.20), this equation becomes:

$$\mathbf{w}_j(x, y) = (\mathbf{D}^1_{jk} + i\kappa \mathbf{D}^2_{jk}) \mathbf{u}_k + \mathbf{w}^g_j(x, y) \tag{2.30}$$

At this point from Eqs. (2.21), (2.24) and (2.30) it is possible to express the aerodynamic forces, acting on the aerodynamic panels, as a function of the deflection and the external downwash:

$$\mathbf{P}_k = \bar{q}\, \mathbf{S}_{kj} \mathbf{A}^{-1}_{jj} \left(\left(\mathbf{D}^1_{jk} + i\kappa \mathbf{D}^2_{jk} \right) \mathbf{u}_k + \mathbf{w}^g_j \right) \tag{2.31}$$

Introducing the matrices which provide the aerodynamic forces due to the structural motion, $\mathbf{Q}_{kk}$:

$$\mathbf{Q}_{kk} = \mathbf{S}_{kj} \mathbf{A}^{-1}_{jj} \left(\mathbf{D}^1_{jk} + i\kappa \mathbf{D}^2_{jk} \right) \tag{2.32}$$

and $\mathbf{Q}_{kj}$ as the matrix which provides the aerodynamic forces due to flow unsteadiness:

$$\mathbf{Q}_{kj} = \mathbf{S}_{kj}\mathbf{A}_{jj}^{-1} \tag{2.33}$$

Eq. (2.31) can be rearranged as:

$$\mathbf{P}_k = \bar{q}\,\mathbf{Q}_{kk}\,\mathbf{u}_k + \bar{q}\,\mathbf{Q}_{kj}\,\mathbf{w}_j^g \tag{2.34}$$

Considering the limit at zero frequency ($\kappa = 0$) of Eq. (2.32) it is possible to obtain the rigid aerodynamic forces as:

$$\mathbf{Q}_{kk}^R = \mathbf{S}_{kj}\mathbf{A}_{jj}^{-1}(\kappa = 0)\mathbf{D}_{jk}^1 \tag{2.35}$$

The aerodynamic loads evaluated as described above need to transferred to the structural model. Since the structural and aerodynamic surfaces of the aircraft use different discretisation, an interpolation matrix is used to connect them. A splining method is used to define a matrix of coupling, $\mathbf{G}_{ka}$, that relates the component of the structural grids point deflections to the deflections of the aerodynamic grid points:

$$\mathbf{u}_k = \mathbf{G}_{ka}\mathbf{u}_a \tag{2.36}$$

Similarly the aerodynamic loads obtained from Eq. (2.34), have to be transformed to the structural grid points. By using the transpose of the spline matrix to define the transfer of forces between aerodynamic and structural points ensures a conservation of works between the two meshes [30]:

$$\mathbf{F}_a = \mathbf{G}_{ka}^T\mathbf{P}_k \tag{2.37}$$

2.3 Finite Element Method

The behaviour of a dynamic structural system can be studied by means of the Finite Element Method solving the equation of motion expressed in a matrix form as:

$$\mathbf{M}\ddot{\mathbf{u}}(t) + \mathbf{B}\dot{\mathbf{u}}(t) + \mathbf{K}\mathbf{u}(t) = \mathbf{f}(t) \tag{2.38}$$

where $\mathbf{M}$, $\mathbf{B}$ and $\mathbf{K}$ are respectively the mass, damping and stiffness matrices. $\mathbf{f}$ is the vector of the external forces, and $\mathbf{u}(t)$ is the structural displacement. In the case of a direct transient response analysis, this equation can be solved using direct numerical integration. In this case the structural response (displacement) is solved at discrete times [31]. This approach is used in the present work to solve the Fluid Structure Interaction problem presented in Chapter 4, where at each time step the external forces will be provided by the fluid solver and the structural solver will evaluate the displacement.

An alternative approach to study the response of a dynamic system is to analyse the modal frequency response of the structure. This method uses the mode shapes of the structure to reduce the size, uncouple the equation of motion (in case modal or no damping is defined), and make the numerical solution more efficient. Since modal shapes are typically computed as part of the characterization of the structure, modal frequency response is a natural extension of a normal modes analysis. Considering the Fourier transform Eq. (2.38) can be expressed in frequency domain as:

$$-\omega^2\mathbf{M}\mathbf{u}(\omega) + i\omega\mathbf{B}\mathbf{u}(\omega) + \mathbf{K}\mathbf{u}(\omega) = \bar{\mathbf{f}}(\omega) \tag{2.39}$$

In order to obtain a modal formulation of the equation of motion, it is necessary to transform the physical variables $\mathbf{u}$ to modal coordinates $\hat{\mathbf{q}}$ by assuming:

$$\mathbf{u}\,(\omega) = \mathbf{\Phi}\hat{\mathbf{q}}(\omega)e^{i\omega t} \tag{2.40}$$

where $\mathbf{\Phi}$ is the matrix of mode shapes $\phi^{(n)}$ used to transform the problem in terms of the behaviour of the modes as opposed to the grid points:

$$\mathbf{\Phi} = \left[\phi^{(1)}\phi^{(2)}\dots\phi^{(n)}\right] \quad \text{with } n = 1, .., N_{Modes} \tag{2.41}$$

Eq. (2.40) represent an equality in the case all modes are used to reconstruct the structural response; since often not all the modes are used it represents an approximation. Substituting Eq. (2.40) in Eq. (2.39) and dividing by $e^{i\omega t}$ it is possible to obtain:

$$-\omega^2\mathbf{M}\mathbf{\Phi}\hat{\mathbf{q}}(\omega) + i\omega\mathbf{B}\mathbf{\Phi}\hat{\mathbf{q}}(\omega) + \mathbf{K}\mathbf{\Phi}\hat{\mathbf{q}}(\omega) = \bar{\mathbf{f}}(\omega) \tag{2.42}$$

At this point the equation of motion is expressed in modal coordinates, but the equations are still coupled. To uncouple the equations it is possible to premultiply by $\mathbf{\Phi}^T$ to obtain:

$$-\omega^2\mathbf{\Phi}^T\mathbf{M}\mathbf{\Phi}\hat{\mathbf{q}}(\omega)+i\omega\mathbf{\Phi}^T\mathbf{B}\mathbf{\Phi}\hat{\mathbf{q}}(\omega)+\mathbf{\Phi}^T\mathbf{K}\mathbf{\Phi}\hat{\mathbf{q}}(\omega)=\mathbf{\Phi}^T\overline{\mathbf{f}}(\omega) \tag{2.43}$$

where for the orthogonality property of the mode shapes it is possible to introduce the generalized mass, damping and stiffness matrices:

$\mathbf{\Phi}^T\mathbf{M}\mathbf{\Phi}=\hat{\mathbf{M}}$ is the modal generalized mass matrix
$\mathbf{\Phi}^T\mathbf{B}\mathbf{\Phi}=\hat{\mathbf{B}}$ is the modal generalized damping matrix
$\mathbf{\Phi}^T\mathbf{K}\mathbf{\Phi}=\hat{\mathbf{K}}$ is the modal generalized stiffness matrix
$\mathbf{\Phi}^T\overline{\mathbf{f}}=\hat{\mathbf{f}}$ is the modal force vector.

It is important to notice that the decoupling of the damping matrix is achieved only considering modal damping, which is applied to each mode separately. In this case each mode has damping b_i where $b_i=2\ m_i\ \omega_i\ \zeta_i$, with ζ_i that is the damping ratio $\zeta_i=b_i/b_{i_{cr}}$, having introduced the critical damping $b_{i_{cr}}=2\sqrt{k_i m_i}$. At this point it is possible to write the decoupled equation of motion in modal coordinates in the frequency domain as:

$$-\omega^2\hat{\mathbf{M}}\hat{\mathbf{q}}(\omega)+i\omega\hat{\mathbf{B}}\hat{\mathbf{q}}(\omega)+\hat{\mathbf{K}}\hat{\mathbf{q}}(\omega)=\hat{\mathbf{f}}(\omega) \tag{2.44}$$

where the generic equation of motion has the form:

$$-\omega^2 m_i\hat{q}_i(\omega)+i\omega b_i\hat{q}_i(\omega)+k_i\hat{q}_i(\omega)=\hat{f}_i(\omega) \tag{2.45}$$

The modal form of the equation of motion is much faster to solve than the direct method because it consist of a series of uncoupled single degree of freedom systems. Once the individual modal responses $\hat{q}_i(\omega)$ are computed the physical responses are recovered as the summation of the modal responses using:

$$\mathbf{u}\left(\mathbf{x},\omega\right)\cong\sum_{n=1}^{N_{Modes}}\phi^{(n)}\left(\mathbf{x}\right)\hat{q}_i\left(\omega\right)e^{i\omega t} \tag{2.46}$$

2.3.1 Aeroelastic frequency response analysis

In the commercial software MSC Nastran the response problem to gust disturbance is solved in the frequency domain in modal coordinates. The system described at Eq. (2.44), can be expressed in Nastran notation as:

$$\left[-\omega^2 \mathbf{M}_{hh} + i\omega \mathbf{B}_{hh} + (1+ig)\mathbf{K}_{hh}\right] \hat{\mathbf{q}} = \mathbf{Q}^a(\omega) + \mathbf{Q}^e(\omega) \tag{2.47}$$

where $\mathbf{M}_{hh}$, $\mathbf{B}_{hh}$ and $\mathbf{K}_{hh}$ are the modal generalized mass, damping and stiffness matrices; g represents an artificial hysteretic damping (associated with the structure). $\mathbf{Q}^a(\omega)$ is the aerodynamic generalised force dependent on the structural motion, while $\mathbf{Q}^e(\omega)$ is the generalised force of the prescribed external loads. Since the aerodynamic loads are only known in the frequency domain it is possible to obtain the transient response of a flight vehicle to time-dependent loads by means of Fourier Transform techniques. In the DLM, the lifting surface theory is used to calculate the aerodynamic loads due to the motion and to the gust. To obtain the governing equation, used by the finite element code MSC Nastran, it is necessary to express the dependencies of the generalised aerodynamic force terms on the aerodynamic force computed by the DLM presented in Section 2.2. The generalised aerodynamic forces due to motion can be written as:

$$\mathbf{Q}^a(\omega) = \bar{q}\, \mathbf{Q}_{hh}(M, \kappa)\, \mathbf{u}_h \tag{2.48}$$

where:

$$\mathbf{Q}_{hh} = \begin{bmatrix} \mathbf{Q}_{ii} & \mathbf{Q}_{ie} \\ 0 & 0 \end{bmatrix} \tag{2.49}$$

Where a new set of degree of freedom has been introduced: the *h-set* is a combination of normal mode (*i-set*) and extra points (*e-set*). The fact that the lower *e-set* rows in the matrix are null, indicates that the normal modes deflection do not produce aerodynamic forces on the extra points ($\mathbf{Q}_{ei} = 0$) and the extra point deflection do not produce aerodynamic loads on the extra points ($\mathbf{Q}_{ee} = 0$).

The generalised aerodynamic loads due to the aerodynamic gust can be written, instead, as:

$$\mathbf{Q}^e(\omega) = \bar{q} w_g \mathbf{P}_P(\omega) \mathbf{Q}_{hj}(M, \kappa) \mathbf{w}_j(\omega) \tag{2.50}$$

where w_g is the gust scalar factor, $\mathbf{P}_P(\omega)$ is the user-supplied frequency variation of the gust, which can be obtained from a Fourier transform of the user-supplied discrete gust. The gust scalar factor can be used to linearly scale the gust input provided in $\mathbf{P}_P(\omega)$. $\mathbf{Q}_{hj}$ is the matrix supplying the generalised aerodynamic forces (in the modal *h-set*) due to the downwash vector and $\mathbf{w}_j(\omega)$ is the downwash vector applied at the collocation points. The gust downwash matrix, presented in Eq. (2.50), is a function of frequency and the geometry of the aerodynamic model:

$$\mathbf{w}_j(\omega_i) = \cos\gamma_j e^{-i\omega_i(x_j - x_0)/U_\infty} \tag{2.51}$$

where ω_i is the excitation frequency, γ_j is dihedral angle of the *j-th* aerodynamic panel, x_j is the x-location of the *j-th* aerodynamic element in the aerodynamic coordinate system and x_0 is the reference coordinate for the gust.

Considering Eqs. (2.48) and (2.50) the governing equation (2.47) assumes the form:

$$\left[-\omega^2\mathbf{M}_{hh} + i\omega\mathbf{B}_{hh} + (1+ig)\,\mathbf{K}_{hh} - \bar{q}\mathbf{Q}_{hh}(M,\kappa)\right]\mathbf{u}_h = \bar{q}w_g\mathbf{P}_P(\omega)\mathbf{Q}_{hj}(M,\kappa)\mathbf{w}_j \tag{2.52}$$

Both $\mathbf{Q}_{hh}$ and $\mathbf{Q}_{hj}$ are evaluated in correspondence to the discrete number of reduced frequencies κ (used to calculate the aerodynamic loads) and then extended to the entire range of frequency required in the analysis by means of a linear interpolation technique.

From Eq. (2.32) it is possible to define the AIC matrix that provides the forces at the structural grid points due to the structural deformation:

$$\mathbf{Q}_{aa}(M,\kappa) = \mathbf{G}_{ka}^T\mathbf{S}_{kj}\mathbf{A}_{jj}^{-1}\mathbf{D}_{jk}\mathbf{G}_{ka} \tag{2.53}$$

where $\mathbf{D}_{jk} = \mathbf{D}_{jk}^1 + i\kappa\mathbf{D}_{jk}^2$. Considering a modal reduction, the matrices can be expressed in the generalised form:

$$\mathbf{Q}_{ii}(M,\kappa) = \mathbf{\Phi}_{ai}^T\mathbf{Q}_{aa}\mathbf{\Phi}_{ai} = \mathbf{\Phi}_{ai}^T\mathbf{G}_{ka}^T\mathbf{S}_{kj}\mathbf{A}_{jj}^{-1}\mathbf{D}_{jk}\mathbf{G}_{ka}\mathbf{\Phi}_{ai} \tag{2.54}$$

where $\mathbf{\Phi}_{ai}$ is the matrix of *i-set* normal mode vectors in the physical *a-set*.

The use of the extra points is necessary for the representation of the control system and are required in aeroservoelastic analysis. If the extra point deflection results in displacement of the

aerodynamic model, the user is required to provide the downwash information.

$$\mathbf{w}_j^e = \left(\mathbf{D}_{je}^1 + i\kappa\mathbf{D}_{je}^2\right)\mathbf{u}_e \tag{2.55}$$

where $\mathbf{u}_e$ is the vector of extra point displacements. At this point it is possible to express the forces due to extra point as:

$$\mathbf{F}_{ae} = \bar{q}\mathbf{G}_{ka}^T\mathbf{Q}_{ke}\mathbf{u}_e \tag{2.56}$$

$$\mathbf{Q}_{ie}(M,\kappa) = \mathbf{\Phi}_{ai}^T\mathbf{G}_{ka}^T\mathbf{S}_{kj}\mathbf{A}_{jj}^{-1}\left(\mathbf{D}_{je}^1 + i\kappa\mathbf{D}_{je}^2\right) \tag{2.57}$$

From Eq. (2.52), it is evident that to perform an aerodynamic gust analysis it is necessary to know the aerodynamic matrix that provides the forces on the aerodynamic elements due to an applied downwash at any other point:

$$\mathbf{Q}_{kj}(M,\kappa) = \mathbf{S}_{kj}\ \mathbf{A}_{jj}^{-1} \tag{2.58}$$

which can be expressed in terms of modal coordinates as:

$$\mathbf{Q}_{ij}(M,\kappa) = \mathbf{\Phi}_{ai}^T\mathbf{G}_{ka}^T\mathbf{Q}_{kj} = \mathbf{\Phi}_{ai}^T\mathbf{G}_{ka}^T\mathbf{S}_{kj}\ \mathbf{A}_{jj}^{-1} \tag{2.59}$$

Since extra points cannot affect the gust loading, there is no generalised loading associated with them, so the matrix which provides the generalised loadings in the modal set, $\mathbf{Q}_{hj}$ is obtained by adding a null matrix onto the bottom of $\mathbf{Q}_{ij}$:

$$\mathbf{Q}_{hj} = \begin{bmatrix} \mathbf{Q}_{ij} \\ 0 \end{bmatrix} \tag{2.60}$$

2.4 Correction Methods for Unsteady Aerodynamics and Aeroelastic Analysis

For many years the Doublet-Lattice Method has been used as the reference in the aerospace industry to compute unsteady aerodynamics. One of the main advantages that it offers is the low computational cost and the fact that it can easily be integrated into the commercial aeroelastic

solver MSC Nastran.

However being based on the linearised potential equations, it does not allow the description of effects related to thickness, shock wave formation or viscosity.

Linear aeroelastic solutions, under the assumption of small perturbations about a fixed point, allow the steady characteristics to be decoupled from the unsteady response. According to Lyapunov's first criterion, the stability analysis around a point of equilibrium for a non linear system, can be reduced to the stability analysis of the corresponding linearized system around the equilibrium point. While this assumption remains valid in case of flutter analysis or small gust disturbance, where we study the effect of small perturbation around an equilibrium point, it lose its validity in presence of large gust perturbations which produce large structure deformation.

Additionally, Tijdeman in [32] highlighted how the principle of superposition inherent in linear systems is not valid in the transonic regime, thus is not possible to consider the steady and unsteady characteristics separately. In fact the unsteady aerodynamics depends explicitly upon the steady part.

Due to the fact that the DLM method cannot properly predict the aerodynamics in the transonic regime, where nonlinear effects become important, several techniques have been presented during the last decades to correct the aerodynamic influence coefficient matrix. In particular, the industrial approach has been to match the steady results at frequency zero [33]. The common idea, at the base of most of these correction methods, is the use of nonlinear pressure distributions, measured on an experimental model or computed with CFD analysis, to correct the result obtained from linear theories.

Combining the small computational cost of a lower order method, with the information obtained with a higher order method, it is possible to achieve a good compromise between performance and accuracy. This makes possible the investigation of the thousands of load cases, necessary for flutter and dynamic flight loads, approximating the complex flow effects.

2.4.1 A classification of different correction techniques

Many attempts have been made to solve the transonic aeroelastic problem using procedures that relate linear aerodynamic models to measured data to calculate corrections. These corrections have been carried out by the multiplication, addition, or complete replacement of the AIC matrix.

The correction techniques, applied to unsteady loading calculation for static or dynamic stability analysis, can be classified in four major groups according to Silva [18]:

- Force-matching methods: the integrated loads in terms of lift and pitching moments, from experiments or CFD analysis, are matched. The aerodynamic nonlinearities are accounted for in the provided forces and moments [33].
- Pressure-matching methods: the pressure distributions are matched from wind tunnel test or simulations [18, 34].
- Dau-Garner type: starting from steady nonlinear results, it is possible to predict the result of the unsteady nonlinear corrected pressure, using semi-empirical methods [35, 36].
- Modal aerodynamic influence coefficient matrix replacement: the nonlinear pressure or loads due to the modal response of the lifting surface are used to compute the AIC matrices [37, 38, 39].

The present work has defined a novel force-matching method presented in Chapter 5, where the integrated forces and moments over wing strips defined in the spanwise direction are matched. The reference data are the results of CFD rigid deformation, of fully coupled fluid structure interaction to consider the effects of the structure flexibility. The correction of AIC matrices is achieved considering a post multiplication correction matrix.

2.4.2 AIC based correction of Doublet-Lattice Method

In 1976, Giesing, Kalman and Rodden [33], published a report describing methods to correct lifting surface theory so it reflects known experimental data. The work presented two

approaches to account for thickness effects and for camber induced by boundary-layer displacement effects. The first focused on correcting the pressure distribution on the DLM panels. The second, instead, concentrated on the downwash generated by the aero boxes. Both methods made use of a matrix of correction factors in order to better match experimental data while minimising the change to the theoretical pressure distribution. However, in order to correct the pressure distribution the matrix of correction factor needs to pre-multiply the AIC matrices, while to achieve the correction on the downwash, the correction coefficient need to post-multiply the AIC matrices.

2.4.2.1 Pressure correction approach

Considering the pre-multiplying approach, if $\mathbf{A}_{jj}$ is the matrix of theoretical aerodynamic influence coefficients that relates the theoretical pressures $\mathbf{C}_{p_j}^{th}$ on a set of aerodynamic panels to the dimensionless downwashes, $\mathbf{w}_j$, at the same aerodynamic elements by:

$$\mathbf{c}_{p_j}^{th} = \mathbf{A}_{jj}^{-1}\, \mathbf{w}_j \tag{2.61}$$

the diagonal matrix of correction coefficients $\mathbf{W}_p$ is applied to the pressure of the DLM in order that the experimental/CFD pressure vector can be obtained from the theoretical one as:

$$\mathbf{c}_p^{exp} = \mathbf{W}_p\, \mathbf{c}_p^{th} \tag{2.62}$$

Considering that the experimental/CFD pressure distribution is usually not known but only the integrated force and moment coefficient $\mathbf{C}_e$ are available, they can be related to the pressure using an integration matrix:

$$\mathbf{C}_e^{exp} = \mathbf{S}\, \mathbf{c}_p^{exp} = \mathbf{S}\mathbf{W}_p\, \mathbf{c}_p^{th} \tag{2.63}$$

This yields:

$$\mathbf{C}_e^{exp} = \mathbf{S}\, \mathbf{W}_p\, \mathbf{A}^{-1}\, \mathbf{w} \tag{2.64}$$

where $\mathbf{S}$ and $\mathbf{w}$ are known from the aerodynamic model, and $\mathbf{C}_e^{exp}$ is known from the experiment or CFD data. This leads to an under determined system when trying to solve for $\mathbf{W}_p$. It can be solved using a least square approach, so that changes to the DLM loads distribution will be as small as possible. This means minimising the change in the DLM loads distribution, where the

deviation $\mathbf{W}_p$ is defined as the difference between the correction factor and unity:

$$\epsilon_p = \mathbf{W}_p - \mathbf{I} \tag{2.65}$$

Including a weighting function denoted by $\mathbf{T}_p$ which respects

$$\sum \mathbf{T}_p \epsilon_p^2 = \epsilon_p^H \mathbf{T}_p \epsilon_p \tag{2.66}$$

where H denotes a Hermitian (complex conjugate) transpose.

$$\mathbf{C}_e^{exp} = \mathbf{S}\left[\mathbf{I} + \epsilon_p\right]\mathbf{P}_t \tag{2.67}$$

$$\mathbf{C}_e^{exp} = \mathbf{S}\mathbf{P}_t + \mathbf{S}\epsilon_p\mathbf{P}_t \tag{2.68}$$

$$\mathbf{C}_t = \mathbf{S}\mathbf{P}_t \tag{2.69}$$

$$\mathbf{S}_p = \mathbf{S}\mathbf{I}\mathbf{P}_t \tag{2.70}$$

$$\Delta\mathbf{C}_e = \mathbf{C}_e^{exp} - \mathbf{C}_t \tag{2.71}$$

$$\Delta\mathbf{C}_e = \mathbf{S}_p\epsilon_p \tag{2.72}$$

which can be solved by means of a Lagrangian multiplier [40], leading to the definition of the correction matrix.

2.4.2.2 Downwash correction factor matrix

Another approach is to modify the downwash, using a multiplying matrix of correction factors (otherwise the same approach as previously) or using an incremental downwash. It is possible to define an experimental downwash:

$$\mathbf{w}^{exp} = \mathbf{W}_w\mathbf{w} \tag{2.73}$$

where $\mathbf{W}_w$ is the downwash correction matrix. The estimate of the experimental pressure distribution becomes:

$$\mathbf{c}_p^{exp} = \mathbf{A}^{-1}\,\mathbf{w}^{exp} \tag{2.74}$$

$$\mathbf{c}_p^{exp} = \mathbf{A}^{-1}\,\mathbf{W}_w\mathbf{w} \tag{2.75}$$

Alternatively the integrated loads can be matched instead of the pressure data and so

$$\mathbf{C}_e^{exp} = \mathbf{S}\mathbf{A}^{-1}\,\mathbf{W}_w\mathbf{w} \tag{2.76}$$

As before $\mathbf{S}$ and $\mathbf{w}$ are known from the aerodynamic model, and $\mathbf{C}_e^{exp}$ is know from experiment or CFD data. This leads to an under determined system to solve for $\mathbf{W}_p$. This can be solved using a least squares approach following a similar process, as described in the previous section.

2.4.3 Other correction methods

In 1997 Baker [41] proposed a correction of linear aerodynamics introducing the local equivalence concept. Defining a representative deflection shape function φ, any arbitrary deformation of the plane u is approximated by the scaled dominant reference mode defined by φ, for which the CFD pressure distribution is known:

$$u = \varphi\eta + \delta u \tag{2.77}$$

where $\varphi\eta$ is a suitable projection of u, obtained with a local equivalent concept. From the original linear AIC^L it is possible to define a corrected AIC^C by replacing the linear effect of the projection $\varphi\eta$ by its nonlinear effect and adding the linear results for the residual δu. To relate the nonlinear unsteady pressure field with those derived from the wing deformation, a subdivision into spanwise strips of the wing is operated, and the local equivalence of aerodynamic quantities such as lift and pitching moment is imposed. This provides a local equivalence factor, that at each strip and modal shape, corrects the linear pressures.

In 1999 Jadic, Dayton and Giri [42], presented an Enhanced Correction Factor Technique where the diagonal correction matrix is replaced by full matrices. With respect to the diagonal correction it allows multiple modes to be considered simultaneously, allowing a correction capability that includes any interference effects. It also allows the definition of several correction matrices that account for nonlinearities for a fixed Mach number.

In 2000 Brink-Spalink and Bruns [43], presented an AIC correction method, which generalizes the least square approach of [33]. Using an additive approach the method enabled weighted least squares correction of AIC matrices with component totals or detailed pressure measurements using several downwash modes simultaneously.

In 2008 Silva et al. [18] presented a correction method designed to match the pressure distribution. In this work, one of the main criticisms raised with respect to the force-matching methods is that the updated AIC matrix will produce a new pressure distribution that is not guaranteed to be the same as that from the reference data (experimental or CFD). Consequently the information related to shock waves could not be captured well, and hence the ability to represent aeroelastic phenomena such as flutter would be degraded. The conservation of the integrated loads does not guarantee that the nonlinear quasi-steady pressure distribution is restored. To prevent these problems, Silva proposed a weighting process focused on matching the pressure distribution, and trying to avoid numerical problems using a post-multiplying approach. This method, developed in collaboration with P.C. Chen, has been integrated in the commercial software ZAERO by Zona Technology [25].

Downwash correction methodology approaches where already presented in the past by Pitt and Goodman [44] and McCain [45]. Both these methodologies were based on a post multiplication of the AIC matrix, where the strip's integrated loads were matched with the reference ones.

In [44] the downwash correction was carried out on the basis of the consideration made by McCain [45]. According to him the post multiplication approach allowed modification of the real and imaginary parts of the downwash, resulting in a variation of the pressure amplitude and phase.

2.4.3.1 Downwash Weighting Correction Method, DWM

The aim of the pressure-matching downwash correction method of Pitt and Goodman and McCain is to use the steady nonlinear pressure distribution to compute the correction matrix $\mathbf{W}^{DWM}$. At zero reduced frequency ($\kappa = 0$) the nonlinear reference pressure distribution can be expressed as:

$$\Delta\mathbf{C}_{p_j}^{nl}(\kappa = 0) = \mathbf{A}_{jj}^{-1}(\kappa = 0)\mathbf{W}^{DWM}(\kappa = 0)\mathbf{w}_j(\kappa = 0) \tag{2.78}$$

Luber and Schmid [46] suggested the computation of the correction matrix using quasi-steady pressures. Silva made use of the pressure rate instead of the absolute values in order to have weighting factors independent from the displacement. This method allows the recovery of the mean steady nonlinear flow, the pressure being fully restored in the steady state condition. However, it does not consider any unsteady reference data, so it is not able to predict unsteady pressure.

Silva proposed an extension to this method in [18] for reduced frequency greater than zero:

$$\Delta\mathbf{C}_p^{nl}(\kappa_r) = \mathbf{A}_{jj}^{-1}(\kappa_r)\mathbf{W}^{DWM}(\kappa_r)\mathbf{w}(\kappa_r) \tag{2.79}$$

which can be rewritten as:

$$\mathbf{A}_{jj}(\kappa_r)\Delta\mathbf{C}_p^{nl}(\kappa_r) = \mathbf{W}^{DWM}(\kappa_r)\mathbf{w}(\kappa_r) \;\Rightarrow\; \bar{\mathbf{w}}^{nl}(\kappa_r) = \mathbf{W}^{DWM}(\kappa_r)\mathbf{w}(\kappa_r) \tag{2.80}$$

where κ_r is the reduced frequency of the reference unsteady transonic flow, and $\bar{\mathbf{w}}^{nl}(k_r)$ is the modified downwash obtained multiplying the aerodynamic influence coefficient matrix for the reference pressure. It is now possible to compute the correction factors as the ratio between the prescribed and the modified downwash for both the methods considering steady or unsteady pressure as reference conditions:

$$\mathbf{W}_{ii}(\kappa = 0) = \frac{\bar{\mathbf{w}}_i^{nl}(\kappa = 0)}{\bar{\mathbf{w}}_i(\kappa = 0)} \qquad \mathbf{W}_{ii}(\kappa_r) = \frac{\bar{\mathbf{w}}_i^{nl}(\kappa_r)}{\bar{\mathbf{w}}_i(\kappa_r)} \tag{2.81}$$

The diagonal weighting operator can then be included in the relation that allows the computation of the aerodynamic loading:

$$\begin{aligned} \mathbf{P}_k^{nl} &= \bar{q}\,\mathbf{S}_{kj}\,\mathbf{A}_{jj}^{-1}(\kappa)\,\mathbf{W}_{jj}(\kappa_0)\mathbf{w}_j \\ &= \bar{q}\,\mathbf{S}_{kj}\,\mathbf{A}_{jj}^{-1}(\kappa)\,\mathbf{W}_{jj}(\kappa_r)\mathbf{w}_j \end{aligned} \tag{2.82}$$

Comparing the pressure-matching versus the force-matching approach presented by Giesing et al. [33], Silva pointed out the better results achieved from the first method in the case of a transonic aeroelastic stability analysis.

Even though Giesing's approach is able to compute a weighting matrix that exactly reproduces

the nonlinear reference loading condition, it is not able to restore the pressure distribution because the force matching is a least-squares based procedure. Silva observed how the method based on force matching over predicted the flutter stability margin in terms of the dynamic pressure. He associated this effect with the poor capability that this method has to manage unsteady effects due to transonic aerodynamic nonlinearities.

2.4.3.2 DWM enhancement: SKEM

One of the main assumptions on which linear unsteady aerodynamic theories are based is that of a small perturbation around the mean angle of attack of the lifting surface. During his linear-nonlinear investigation, Silva proved how the unsteady flow behaviour is strongly dependent on the amplitude of the motion.

For this reason, considering aeroelastic analysis in a small-disturbance sense, the unsteady transonic flow presented linear behaviour (with respect to the aerodynamic derivatives and shock behaviour) if the amplitude of lifting surfaces in unsteady motion is below a linear limit.

The investigation performed by Silva in [47], showed that unsteady aerodynamic pressure behaves linearly around a steady nonlinear mean flow for small perturbation. In the validity region of the superposition principle, the pressure of an unsteady flow, around a mean steady state, can be computed as the sum of the contribution predicted by the small-disturbance linear aerodynamic model and a nonlinear steady state. The unsteady contribution is computed by the linearised potential flow equation in a steady nonlinear mean flow.

The presented successive kernel expansion method, SKEM [18], allows the nonlinear steady pressure to be input into the frequency-based integral equation, using an algorithm based on successive kernel expansion. The main objective is to be able to recover the information from the pressure's imaginary part.

Considering the integral equation of the lifting-surface formulation:

$$\mathbf{w}(x, y, 0, i\kappa) = -\frac{1}{8\pi} \int \int_A \Delta \mathbf{C}_p(\xi, \eta)\, \mathbf{K}(x - \xi, y - \eta, 0, i\kappa, M)\, d\xi d\eta \tag{2.83}$$

where $K(i\kappa)$ is the kernel function of the acceleration potential, the downwash $\mathrm{w}(i\kappa) = h_x + i\kappa h$, and h is the normal mode. It is assumed possible that the subsonic kernel function can

be expanded as an asymptotic series about a small reduced frequency. So expanding the kernel about $\kappa = 0$ (for $\kappa < 1.0$), the pressure downwash can be rewritten in terms of a reduced frequency expansion. Expanding $\Delta\mathbf{C}_p(i\kappa)$ and $\mathbf{K}(i\kappa)$ in term of $(i\kappa)^n$:

$$h_x + i\kappa h = (i\kappa)^0 \int\int_A (\Delta\mathbf{C}_p^0 + i\kappa\Delta\mathbf{C}_p^1 + (i\kappa)^2\Delta\mathbf{C}_p^2 + \cdots) \times (\mathbf{K}^0 + i\kappa\mathbf{K}^1 + (i\kappa)^2\mathbf{K}^2 + \cdots)dA \tag{2.84}$$

Reorganizing the $(i\kappa)^n$ order terms $(n = 0, 1, 2, \ldots)$, it is possible to write n equations:

$$\begin{aligned} \mathcal{O}(i\kappa)^0 : \mathbf{h}_x = \mathbf{K}^0\Delta\mathbf{C}_p &\rightarrow \Delta\mathbf{C}_p^0 = \mathbf{A}^0\mathbf{h}_x \\ \mathcal{O}(i\kappa)^1 : \mathbf{h} = \mathbf{K}^1\Delta\mathbf{C}_p^0 + \mathbf{K}^0\Delta\mathbf{C}_p^1 &\rightarrow \Delta\mathbf{C}_p^1 = \mathbf{A}^0\mathbf{h}_x - \mathbf{K}^1\Delta\mathbf{C}_p^0 \\ \mathcal{O}(i\kappa)^2 : 0 = \mathbf{K}^0\Delta\mathbf{C}_p^2 + \mathbf{K}^1\Delta\mathbf{C}_p^1 + \mathbf{K}^2\Delta\mathbf{C}_p^0 &\rightarrow \Delta\mathbf{C}_p^2 = \mathbf{A}^0\mathbf{K}^1\Delta\mathbf{C}_p^1 + \mathbf{K}^2\Delta\mathbf{C}_p^0 \\ &\vdots \end{aligned} \tag{2.85}$$

where $\mathbf{A}^0$ is the AIC matrix at $\kappa = 0$. This matrix is then replaced with the corrected one obtained using the DWM at $\kappa = 0$, while Eq. (2.83) allows the computation of the unsteady contribution. With this improved downwash correction approach the unsteady solution is obtained starting from the transonic steady analysis.

The numerical application of the SKEM method involves the computation of the $\mathbf{A}^0$ corrected using the DWM method, while the unsteady pressure coefficients are then computed by the successive kernel expansion method. A CFD solver is used to evaluate the steady pressure coefficient $\Delta\mathbf{C}_p$ at two different flight conditions: α_1 and α_2, and the reference quasi steady pressure is obtained as the ratio between the change in pressure coefficient and the motion amplitude:

$$\Delta\mathbf{C}_p^{qs} = \frac{\Delta\mathbf{C}_p(\alpha_2) - \Delta\mathbf{C}_p(\alpha_1)}{\Delta\alpha} \tag{2.86}$$

Test cases are presented in order to show the matching of the unsteady pressure coefficient computed by the SKEM method and measured data. One of the main improvements of the SKEM method is the better prediction of the imaginary part of the pressure distribution. The SKEM method shows an improvement compared to the DWM, in particular for the out-of-phase pressure distribution. It shows even some improvement with respect to the flutter solution.

No results for gust analysis have been presented in [18].

2.4.4 Further refinements with iSKEM and CREAM Methods

An improvement to the SKEM method has been presented by Thormann and Dimitrov [34] in the "improved Successive Kernel Expansion Method" iSKEM, where an automatic differentiation is used to derive the Taylor coefficients. The iSKEM is therefore not restricted in the number of Taylor coefficients, while in the SKEM only two Taylor coefficients are used.

The basic idea is to introduce additional data around the zero reduced frequency and obtain the correction for higher frequencies using the DLM's higher order Taylor coefficients. The zero-th order Taylor coefficient can then be corrected by means of quasi-steady CFD simulation or experimental results.

In order to compute the corrected AIC matrix, a Taylor expansion of the AIC is considered with respect to $i\kappa$. The corrected AIC matrix can be expressed as:

$$\mathbf{AIC}^*(i\kappa) = \mathbf{C} \cdot \mathbf{AIC}^0 + \sum_n \mathbf{AIC}^n \, (i\kappa)^n \tag{2.87}$$

The zero-th order term represents the quasi-steady part of the AIC matrix, and is modified by a diagonal matrix $\mathbf{C}$. This matrix can be obtained by considering the downwash expression:

$$\mathbf{w}^{DLM} = \mathbf{C} \cdot \mathbf{AIC}_0^{DLM} \cdot \Delta\mathbf{C}_{p0}^{CFD} \tag{2.88}$$

where

$$\Delta\mathbf{C}_{p0}^{CFD} = \frac{\Delta\mathbf{C}_p(\alpha + \Delta\alpha) - \Delta\mathbf{C}_p(\alpha - \Delta\alpha)}{2\Delta\alpha} \tag{2.89}$$

is the quasi-steady pressure difference computed with CFD methods. The results obtained from the CFD model then have to be projected into the DLM panel discretisation. In this case a local approach has been used with linear basis functions over every CFD surface element for the interpolation of the pressure coefficient to the mid-points of every single DLM box. Making the assumption that $\mathbf{C}$ is a diagonal matrix, for each DLM box it is possible to define:

$$c_i = \frac{w_{0i}^{DLM}}{AIC_0^{DLM} \cdot \Delta C_{p0}^{CFD}} \tag{2.90}$$

Comparison of the results for gust analysis using DLM, CFD and iSKEM, for different gust lengths and amplitudes has been presented. The iSKEM method has shown a good capability

to match the CFD results in the presence of a range of gust disturbances. For small and medium gust lengths, and a vertical gust speed that produced an equivalent $\alpha_g = 1.79°$ the DLM is not very far from the CFD results. For a higher gust amplitude a difference of 10% in the magnitude of the lift and moment coefficient was observed. In this case the quasi steady corrections were able to close the gap. Regarding the influence of the gust vertical speed (for different gust lengths), it has been observed that the DLM results are in agreement with the CFD for small and medium gust lengths, but the differences increase when the length of the gust is larger and is equivalent to a higher angle of attack.

In fact, in these cases the results of DLM and iSKEM tend to increase linearly with the gust amplitude, while the CFD results show some nonlinear effects in the $C_L(t)$ curve, with an anticipated reduction in the lift, indicating flow separation. This effect named "Dynamic Overshoot", seen in Figure 2.3, is characterised by early maximum loads.

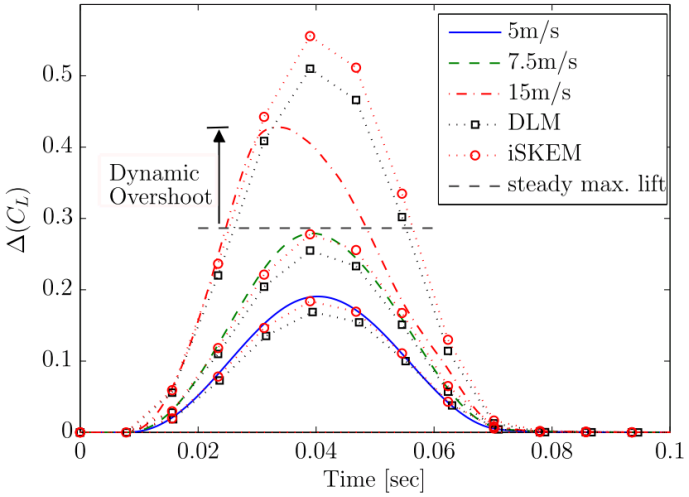

Figure 2.3: Lift response for long gust length *(From Thormann and Dimitrov[34] page 9)*.

Such phenomena cannot be predicted by iSKEM, which is obtained from quasi-steady calculations at zero angle of attack. Moreover, all the correction approaches presented so far have no information about a possible onset of flow separation or even shock movement.

In Figure 2.4 the lift Frequency Response Function (FRF) [48] is depicted, predicted by the nonlinear CFD analysis: in the case of higher gust amplitudes a non zero response exists for a reduced frequency where no input is assigned. This is an indication that in that condition the superposition of effects is not valid any more. So as observed in [34], the gust response for higher gust amplitudes can not be predicted with linear methods. Neither DLM-correction

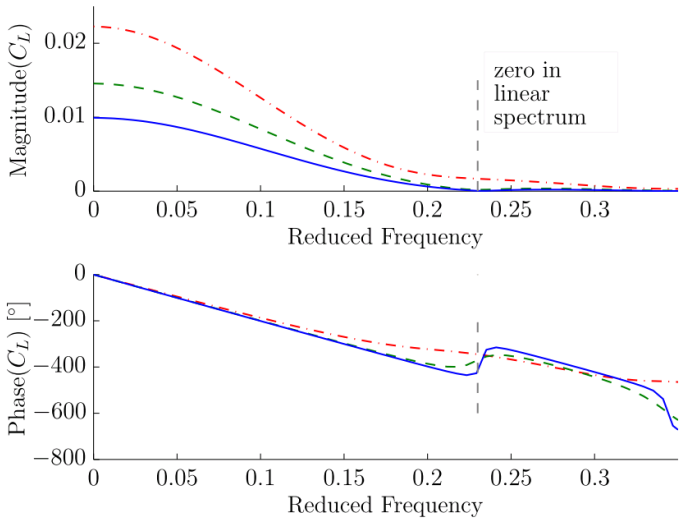

Figure 2.4: Lift response for long gust length *(From Thormann and Dimitrov[34] page 9)*.

method based on constant correction coefficient will be able to predict such results, whether they are quasi-steady or unsteady.

In 2014 Thormann and Dimitrov [49], published a new pressure-matching correction method based on the Taylor series expansion of the AIC matrices. The method named "CorREction of Aerodynamic Matrices" (CREAM) avoids an explicit Taylor series expansion of the AIC matrix, but instead makes use of an appropriate subtraction of two AIC matrices to obtain the higher order terms. To correct the zero-th order term only one CFD analysis is necessary, at $\kappa_0 = 0$, and is obtained using the linear frequency domain (LFD) solution method in the DLR TAU Code [50].

A comparison between the results obtained with the CREAM-0 (using only one steady CFD analysis at $\kappa_0 = 0$) or CREAM-1 (using an additional LFD-TAU analysis at $\kappa > 0$) were presented. The CREAM-0 based corrections improves the magnitude response whereas the effect of the phase response is small. In fact the derivative of the phase response with respect to the reduced frequency at $\kappa_0 = 0$ is not corrected. This has been justified considering an extension of the method including a first order correction, which is able to account for the phase derivative. Comparison of the results in terms of lift FRF, for DLM, LFD TAU, zero-th order and first order correction methods have been presented in [49]. It has been observed that the DLM tends to under-predict the magnitude of the lift derivative compared to the LFD-TAU, because it can not capture the recompression shock. This difference is corrected using a zero-th

order method, CREAM-0, based on quasi-steady correction. Even though the corrections are introduced on a local level, they work well also on the global loads. Being based on the quasi steady approach this kind of correction only scales the original DLM results by an offset. There are minor changes to the phase.

Introducing the first order correction the deviation from the LFD-TAU results can be delayed until $\kappa = 0.4$. But in this case CREAM-1 is only capable to improve the phase of the AIC matrix, since the real part of the derivative is equal to zero. Since the lift is an integrated value, the magnitude of the lift is also slightly modified by CREAM-1. For the pitching moment, the phase is quite well predicted by CREAM-1, while a bigger difference is present in the magnitude. This effect is associated with the incorrect prediction of the shock movement. CREAM-1 continues to improve the quality of the phase, while the magnitude is worse for this case.

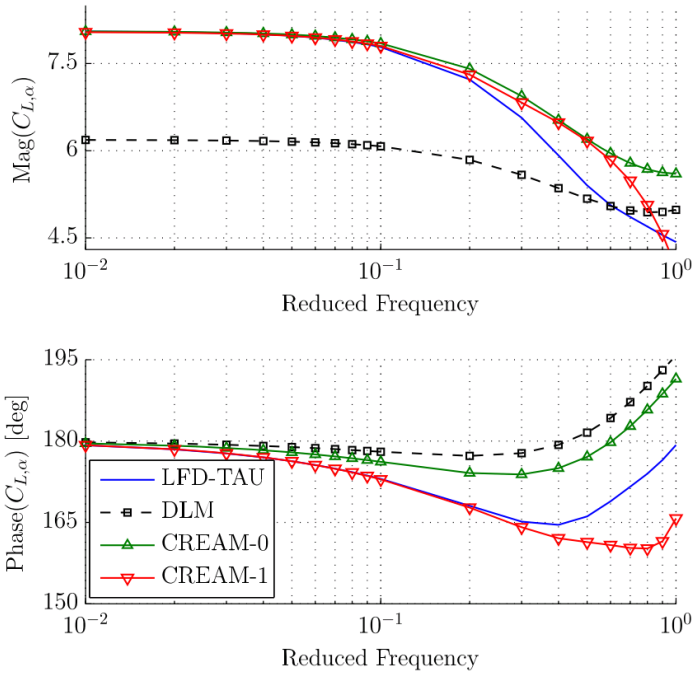

Figure 2.5: Lift FRF *(From Thormann and Dimitrov [49] page 442)*.

Comparing the results in terms of chordwise pressure distribution for two different reduced frequencies, $\kappa = 0.2$ and $\kappa = 0.7$, two different behaviours have been identified as shown in figure 2.5 and 2.6.

Keeping in mind that the CREAM-1 method is obtained by correcting the AIC matrix using data at $\kappa = 0$ and $\kappa = 0.01$, a good behaviour is shown by CREAM-1 versus LFD-TAU, with an

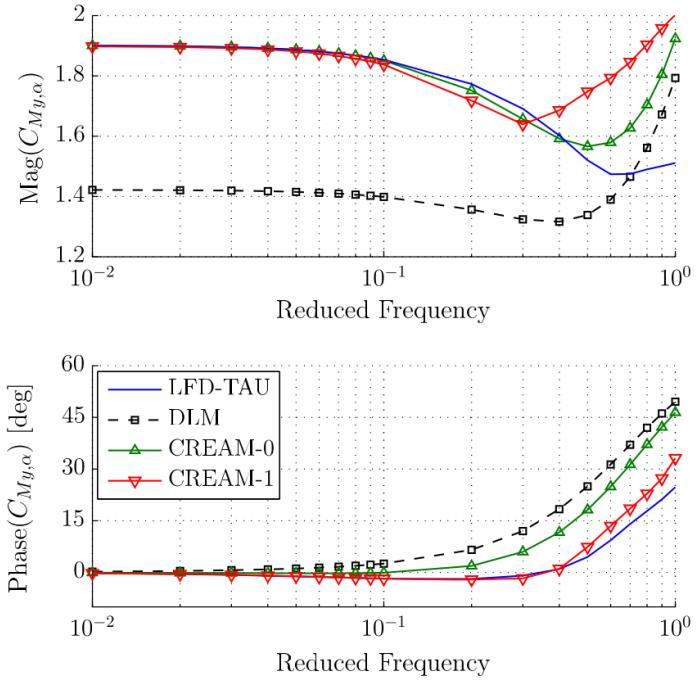

Figure 2.6: Pitching moment FRF *(From Thormann and Dimitrov [49] page 442).*

evident improvement over the DLM for the first case. Analysing the condition at higher reduced frequencies, the wing presents a lambda shock , with two weak shocks in the inner span and a strong shock in the outer part. The LFD-TAU response of the two shocks is very different at higher reduced frequencies. In this condition the CREAM curves show similar trends as they did for the lower frequency, so there is a higher discrepancy between the corrected method and the LFD TAU.

By introducing an additional correction for unsteady flow the CREAM method is able to improve the phase-lag of the pressure distribution for transonic unsteady flow. However it is still not able to provide good results in the presence of nonlinear behaviour due to shock motion and flow separation. This approach could, in principal, be extended to higher order DLM corrections by taking an larger number of unsteady CFD samples. However higher derivatives become inaccurate when using finite differences due to the limited machine precision. If several unsteady sample points are considered then a direct polynomial approximation might be numerically more efficient and robust.

One of the main limitations of the CREAM-0 and CREAM-1 methods is related to the limited capability to correct the unsteady behaviour associated with higher reduced frequencies. In fact, they relay only on a steady CFD and a steady CFD plus a low frequency LFD analysis.

However, to have a good representation of the response of a flexible aircraft to a gust disturbance it is necessary to account for a much larger range of reduced frequency, as will be shown in Chapter 6.

2.4.5 Recent Updates on DLM Correction for Gust Analysis.

In 2014 Quero Martin [51] presented a correction method for DLM based on a reduced order model, which allows the correction in the frequency domain to be applied at all frequencies. This method is based on a force-matching approach, developing the idea presented by Brink-Spalink and Bruns in [43]. The latter method allows matching the lift and pitching moment coefficient at each strip solving a linear square optimization (LSQ) problem. The quantities that have to be matched are transformed into the frequency domain, via Fourier transformation (numerically DFT), and the LSQ problem is solved for each frequency. In this approach a Reduced Order Model (ROM) is built in the frequency domain, using CFD time domain analysis computed for different gust lengths. Due to the low frequency content considering the higher gust length, it has been necessary to interpolate the data in the frequency domain for a gust length value not included in the original set.

Comparing the results for different gust lengths and amplitudes, it has been shown how for lower gust amplitudes, when the unsteady problem can be linearised, it is possible to define a transfer function independent of the gust length. For higher gust amplitudes, when the nonlinear effects are present, the transfer function is strongly dependent on the gust amplitude. In this case a concept of a describing function has been introduced to underline the fact that there is not a unique transfer function per flightpoint. The transfer function in the nonlinear regime depends on the gust amplitude and the gust length.

This kind of nonlinear effect can not be predicted by the DLM, where the transfer function depends on the Mach number and the reduced frequency alone. But as the DLM problem has been linearised, there is no dependency upon the gust amplitude or gust length.

In [51] the results obtained with the corrected ROM including the dependency with the gust length are presented. In this case a correction has to be done per gust length, as imposing all gust lengths simultaneously would lead to a singular LSQ problem.

In 2015 Quero Martin [52] presented further development on his work, showing how the ROM is able to compute the loads due by a discrete gust acting on an aircraft and to account for nonlinear aerodynamics effects as predicted by CFD. To identify the region where the linear assumption can still be accepted, a linear/nonlinear boundary has been identified using a lift coefficient criterion [53]. The definition of the linear-nonlinear region is necessary to know when it is possible to use a constant transfer function or when a nonlinear approach has to be implemented (by considering a describing function dependent on gust amplitude, gust length and initial angle of attack). One of the main disadvantages of such approach consists in building the Reduced Order Model. This operation requires a high number of unsteady simulations and is very time consuming. In 2018 Friedewald et al. [54] presented an application of the quasi-steady AIC correction approach introduced with CREAM [49], where the correction is applied to the local pressure coefficient. In this case only a single quasi-steady CFD input is used for the correction. Results are presented for gust loads analysis. However, the work is limited to comparison of rigid gust response and no flexible effects are considered.

2.5 Final considerations on the correction methods

Following the review of the correction methods carried out in the previous section, it has been decided to formulate a new DLM correction method with the following requirements:

- Define a method in the frequency domain for a straight forward integration with the gust frequency response analysis available in MSC Nastran.
- Provide a correction in the entire range of reduced frequency used for the gust analysis.
- Define a load based correction approach, where the reference data are the integral loads over a wing section. The main consideration driving this decision is that the low refinement in the DLM aerodynamic mesh can not allow a good representation of the shock position and movement.
- make use of a down wash correction method to avoid numerical problem, as described in Section 2.4.2.1.

The formulation of this correction approach will be presented in Chapter 5.

CHAPTER 3

Computational Fluid Dynamics

Computational Fluid Dynamics (CFD) is now mature and is widely accepted as a tool to provide essential data to integrate with results from wind tunnel and flight tests. Thanks to the continuous improvement in high power computing, it is now possible to provide highly efficient, reliable and accurate predictions for new configurations. Recent aircraft developments have relied more than ever on multi physics simulations, trying to reduce as much as possible expensive wind tunnel tests. This has focussed mainly on steady simulations, but the use of CFD for unsteady flows is increasing. However it is still too expensive when large numbers of unsteady simulations are required. The European aircraft manufacture Airbus has employed the DLR TAU-Code as the CFD-tool for complex configurations simulated using hybrid unstructured grids [55].

3.1 The DLR TAU-Code

The DLR TAU-Code has been developed since the middle nineties at the German research institute DLR in Gottingen and Braunschweig [56, 57] , thanks to a series of national and European projects. Today, the Numerical Methods Department of the DLR Institute of Aerodynamic and Flow Technologies continues to develop the DLR TAU-Code and supports numerous users in universities and industrial partners in the aerospace industry who contribute to the validation

and implementation of new capabilities in the DLR TAU-Code ecosystem. The DLR TAU-Code does not include a grid generation tool, however it has the capability to perform grid modification via adaptation and deformation. Grids can be generated using various software packages and imported into TAU. DLR use the unstructured hybrid grid generator CENTAUR from the company CentaurSoft [58]. In this project the hybrid mesh generator SOLAR [59] was used to produce the unstructured meshes for the test cases investigated. TAU can be used with both (block-) structured and unstructured grids composed of

- *hexahedrons*, *prisms*: generally used for a better representation of the boundary layer in a semi-structured configuration above the surface;
- *tetrahedrons*: generally used to fill the computational domain;
- *pyramids*: used to create a transition between cells with quadrilateral faces and cells with triangular faces.

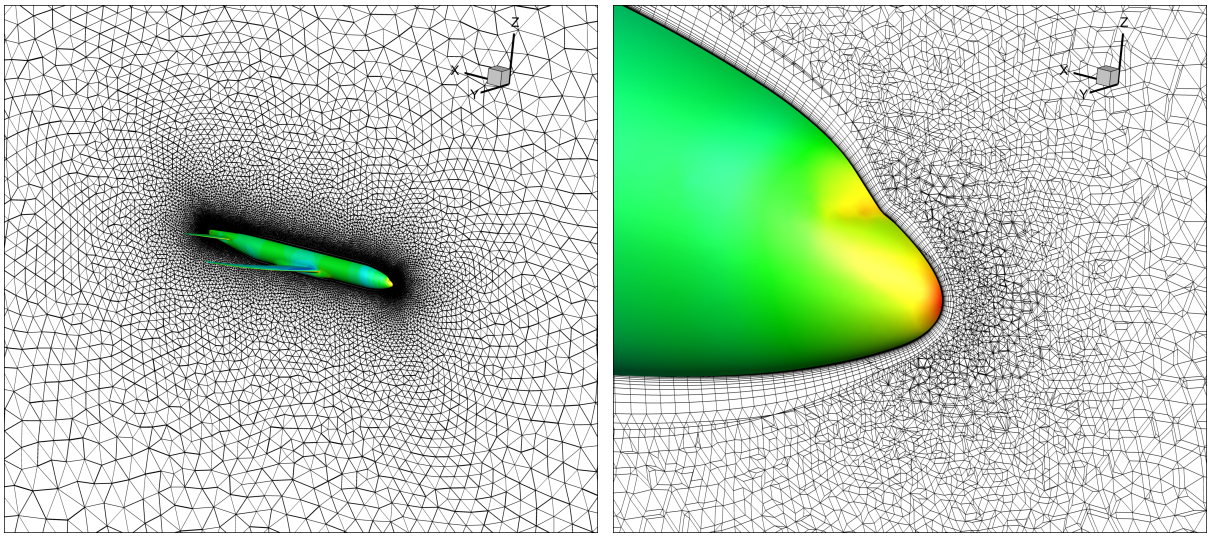

(a) Global view of a CFD mesh. (b) Boundary layer example.

Figure 3.1: DLR TAU-Code mesh examples

The DLR TAU-Code consists of a system of modules and libraries for the prediction of viscous and inviscid flows about complex geometries from low subsonic to hypersonic flow regimes. TAU modules can be used independently or wrapped in a Python environment. TAU is characterised by an efficient parallization based on domain decomposition with MPI communication [60, 61, 62]. In the last decades TAU has been employed for a variety of complex aircraft-type

configuration studies, including rigid CFD simulations, fluid-structure interactions via coupling to structural solvers [63, 64] and flight mechanics investigations [65].

The standard TAU solver uses an edge-based dual-cell approach, where inviscid terms are computed employing either a second-order central scheme or a variety of upwind schemes using linear reconstruction for second-order accuracy. For the computation of the viscous terms a second-order central scheme is used. The user can choose between a scalar or matrix artificial dissipation. To permit the use of the code in the incompressible flow regime a low Mach number preconditioning has been implemented. For the time integration several explicit Runge-Kutta schemes are available, with the possibility of implementing a multi-grid algorithm using coarse grids generated at a pre-processing level. Additionally an implicit LU-SGS (Lower-Upper Symmetric Gauss-Seidel) scheme is available allowing better performance and robustness.

A grid deformation capability is available and represents an important tool in aerodynamic shape optimization or unsteady aeroelastic simulations [66]. This allows modification of the model geometry to be accounted for without the need to perform a re-meshing of the entire grid. This method, based on the radial basis function (RBF) interpolation approach [66], is independent from the mesh type and flow solver used. This mesh deformation technique is based on geometrical consideration of the grid node locations, with no information about the volume cells which constitute the fluid mesh. In fact, this methodology uses only information about arbitrary point clouds, neglecting any connectivity data. This can lead to situations where the resulting deformed fluid mesh possesses cells with negative volume. Such cells cannot be used for finite volume based methods such as the CFD TAU-Code, which require cells with positive volumes. It is therefore necessary to adopt specific techniques to correct the affected cells [67]. The application of this approach in TAU has been enhanced by the capability to specify separate interpolation and blending functions in different regions of the grid. This allows the deformation to be restricted to a specified zone around the boundaries. Thus, it is possible to adopt a weighting approach to ensure an independent movement of the different model parts, without influencing other boundaries. The shape of the body is preserved using a separated interpolation for each group. Consequently, the boundary layer is preserved using a deformation-blending technique [66].

An hybrid mesh deformation capability has also been integrated into TAU, by means of a Chimera technique [68]. This represents an important feature for accurate simulation of ma-

noeuvring aircraft. It allows an efficient handling of complex configurations which have movable control surfaces.

3.2 Fluid-Structure coupling simulation using TAU

Whilst CFD simulations that consider the solid surface as rigid are often performed, the aircraft flexibility is an essential characteristic which needs to be accounted for to obtain an accurate loads estimation. The aerodynamic loads acting on the aircraft surface will produce a deformation of its flexible structure, with a consequent modification of the fluid flow and of the evaluated loads. Therefore, for an accurate prediction of the aerodynamic performance, it is imperative to consider multi-physics (fluid-structure) simulations.

In a fluid structure interaction analysis it is essential that the aero loads, computed by the CFD code, are accurately transferred to the solid model. The structural equations are typically solved by means of a FEM solver, which computes the deformation due to the external load prescribed. Then the computed solid surface deformation has to be transferred back to the fluid domain. Often the fluid and solid model are characterised by a different resolution on the interface. The surface grid for the first can be of several order of magnitude higher that the second. For this reason implementing a proper strategy for accurate and efficient transfer of information, is key for loads prediction. The mapping of forces and displacements is achieved by means of interpolating functions, also known as splining methodology [69, 70, 71]. Fluids structural interaction analysis have been adopted in industry to provide high fidelity results for static aeroelastic simulations [72]. Additionally, in the recent years, the growing interest in large structural deformations and nonlinearities, has driven the coupling of CFD codes with multibody software [73, 74].

There are many aircraft design issue, where aeroelastic predictions are essential. For example, a more accurate prediction of the wing root bending moment can help to reduce structural weight and consequently improve aircraft performance (reducing fuel consumption). For these reasons fluid structure interaction capabilities within the DLR TAU-Code have been developed and investigated at DLR [75].

3.3 Gust modelling in CFD

Using CFD for unsteady load calculations permits simulations involving wake modelling and atmospheric disturbance such as gusts and vortices.

One methodology to include disturbances in the fluid domain due to gusts is to apply unsteady boundary conditions at the far field boundary. One of the main advantages of this approach is the possibility of capturing the mutual interaction of atmospheric disturbances and an aircraft [76]. However, their application is limited by problems related to numerical dissipation and stability constraints [77]. Generally, a CFD mesh is characterised by a grid resolution which decreases moving further away from the aircraft. The farfield region is therefore affected by numerical dissipation, with a rapid diffusion of any disturbances. Using such an approach for gusts would require a fine mesh throughout the domain [15], with a consequent large increase in computational cost. Therefore, this solution approach becomes impracticable for early stage design. A solution would be to use local mesh refinement or mesh adaptation [78], but these would introduce added complexity and cost.

These problems can be solved using a prescribed velocity approach such as the so called Field Velocity Method (FVM) [79] or the Split Velocity Method (SVM) [80], which do not require fine meshes in the farfield in order to prevent numerical dissipation of the gust as it convects through the domain. In these methods the velocity components in the Euler equations are decomposed into a prescribed gust velocity and the remaining velocity components. In SVM the Euler equations are just rearranged with no simplifications allowing the capture of the full interaction between the body and the gust. In contrast, FVM does not capture the influence of the body on the gust. This could produce some inaccuracy in particular for short wavelength gusts. Both the FVM and SVM can be applied to any moving mesh unsteady CFD code with only small modifications. Additionally it can be noted that prescribed velocity approaches can be used to calculate the response to a step gust, from which it is possible to calculate the force due to an arbitrary gust by applying convolution methods.

In the present work, the field velocity method already implemented in DLR TAU-Code is used to study the response to gusts.

3.4 Time Linearised Analysis in the DLR TAU-Code

CFD can produce high fidelity results for complex unsteady flows such as unsteady gust response. Its application, to study large aircraft configuration gust interaction by solving the governing equations in an unsteady time-marching approach within the TAU-Code has been demonstrated by Reimer et al in [16]. However, despite the continuing increase in computation power offered by high performance computing (HPC) systems, unsteady time domain simulations are still too expensive to be used in an industrial design context.

To overcome this problem, linearised frequency domain methods which offer increased efficiency have been developed to widen the potential application of computational fluid dynamics. This approach considers a linearisation of the Euler equations around a nonlinear steady state solution with the assumption of small amplitude harmonic motion. This linearity assumption has been shown to be reasonable for many interesting flows e.g. flutter, since flutter onset will be captured in the limit of infinitesimally small displacement and some gust responses. The efficiency gains come from the fact that the system is solved in the frequency domain and no time integration is necessary. Thus, an unsteady periodic problem is effectively transformed into the equivalent of a single steady state simulation with consequential significant decrease in computational cost. Further, the mesh motion is also assumed periodic so that the need to move the mesh in the time domain and the associated costs are avoided.

The method was originally applied to model oscillatory blade motion inside a cascade in turbomachinery [81, 82, 83]. Comparing the first harmonic of the perturbation with unsteady time domain methods, a good agreement has been found in [84, 85] for turbomachinery applications with a significant reduction in computational cost. Early results for the response due to forced-motion of an aerofoil, wing and aircraft using this method were presented in [86] and the analysis of a delta wing subject to small harmonic oscillation of elastic modes and control surface was presented in [87]. All of these studies highlighted the benefit in terms of computational cost of the linearised Euler frequency domain approach with respect to the equivalent Euler nonlinear time domain solutions.

The first implementation of the linear frequency domain approach for the Reynolds-Averaged Navier-Stokes equations [88] was again in the field of turbomachinery. This study of separation and stall flutter in a blade cascade showed a good agreement with the experimental data. Appli-

cation to forced-motion response for aerofoils and wings have been presented from a number of studies [89, 90].

The detail of the LFD method implemented in the DLR TAU-Code for external flow is presented with results for an aerofoil and wing flutter in [50] and results for a full civil aircraft at cruise condition are given in [91]. The LFD method in TAU has been extended to investigate gust responses both in [92] and in [93]. In [94], a direct complex valued superposition of the frequency-domain response has been introduced allowing the analysis of aerodynamic gust response independently of structural dynamics. Further relevant developments using LFD within TAU include: reduced-order modelling based on linearised frequency domain solutions and a proper orthogonal decomposition method, applied to a three-dimensional industry relevant test case for gust response simulation [95]; the recent application for gust loads analysis in an industrial context [96]. LFD simulations are also useful for calculating aeroelastic stability in the transonic regime [97].

CHAPTER 4

The Alpes Fluid Structure Interaction Interface: "AlpesFSI"

The need for a high fidelity analysis environment, capable of capturing the interaction of aerodynamic loads with a flexible structure, has driven the decision to make use of a fluid structure interaction analysis environment for aeroelastic simulations. Moreover, to make possible the coupling of aerodynamic loads evaluated with the DLR TAU-Code acting on a flexible structure represented with an FEM model, solved with the structural solver MSC Nastran, has required the development of a dedicated interface called AlpesFSI (Alpes Fluid Structure Interaction) interface. This interface, developed during the ALPES project, has used the capability offered by the MSC Software Open Fluid Structure Interface (OpenFSI). Providing a simulation environment where the finite element code MSC Nastran can exchange interaction data with an external code, it allows the performance of multi-physics analysis. The OpenFSI interface provides an access to structural variables hard coded in the MSC Nastran solver. In particular it allows a communication in input to provide forces at each time step and in output to extract displacements. However, this access is provided as a series of empty functions and requires the implementation of all the communication and translation of information between structural and aerodynamic parameters.

Previously application of the OpenFSI interface have been focussed on investigating static aeroelastic and flutter problems. These involved the coupling with Unsteady Vortex Lattice Method [98] or CFD codes such as ANSYS Fluent [99]: in this last case by means of dedicated third party interfaces such as the MpCCI coupling environment developed by the Fraunhofer Institute for Algorithms and Scientific Computing SCAI [100]. A dedicated project from Technische Universitat Braunschweig named “Aerostruct” [101] has focussed on developing an interface between the simulation environment FlowSimulator and MSC Nastran using the OpenFSI interface [102]. However, at the moment when this work was been produced, no applications for coupling MSC Nastran and DLR Tau code for gust analysis was available at the University of Bristol, therefore the necessity to develop this capability within the ALPES project.

This chapter gives an overview of how the AlpesFSI interface has been created and customised in order to allow the coupling with the CFD code TAU.

The accuracy of the DLM correction method is assessed against the AlpesFSI coupled solution in this work. It is this requirement for a solution to compare with that necessitated the development of the coupling interface for this project. In the comparison between DLM and AlpesFSI presented in the rest of the work, the structural FEM model is in common between the two methodologies and only the aerodynamic modelling is different.

At the time when the present work has been produced, the AlpesFSI did not include the capability to account for rigid body motion of the structural model. Therefore, the test cases analysed in the next chapters have been considered constrained at a point on the fuselage or the wing root.

4.1 Fluid Structure Interaction Simulation

Fluid structure interaction refers to the situation where a fluid is interacting with a solid structure, exerting force on its surface which may cause displacement of the structure, and as a consequence alter the flow of the fluid itself. The aim of the FSI developed here using the Application Program Interface (API) available in MSC Nastran, is to provide a means to create an interface with a CFD code to allow for fluid structure interaction simulations. The struc-

tural and aerodynamic codes will execute simultaneously and exchange information through the interface during the simulation. MSC Nastran reads nodal forces from the external solver and sends structural displacement, velocity and acceleration back to it. The exchange of information is performed on a set of the structural nodes, defined as "wetted nodes", typically much lower than the number of nodes characteristic of the CFD mesh. An appropriate spline method is required to ensure the correct transfer of the relevant quantities between the different mesh discretisations.

In the fluid structure simulation, the CFD code computes viscous and pressure forces, and the relative forces acting on the wetted surface are provided to the FEM code through the FSI interface. On the other side, MSC Nastran will compute the displacement, inertial forces and accelerations based on the driving aerodynamics forces. These computed quantities on the wetted surface are then provided back to the CFD code.

The FSI allows the transfer of the following information to the FEM code in INPUT: forces and moment, and obtain in OUTPUT: displacement, velocity and acceleration.

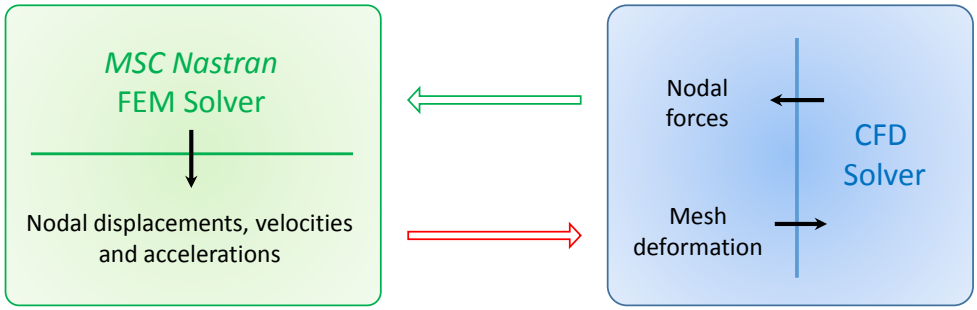

Figure 4.1: Data exchange in an Fluid Structure Interaction simulation.

4.1.1 Coupling schemes

The AlpesFSI interface supports two types of FSI simulations: explicit staggered time steps and implicit coincident time steps. The latter is the focus of this study and is presented in this section. To describe the solution scheme the notation introduced in Table 4.1 is used.

The implemented method considers coincident time stepping from t^k to t^{k+1} and the time step in the two codes are equal, $\Delta t_F = \Delta t_S$. The FE code solves for convergence within each time step, and the data is communicated between the codes, possibly multiple times per time

Notation		***Subscripts***	
f	Force vector	F	Fluid
Δt	Time steps	S	Structure
t	Time	W	Nodal quantity on wetted surface
u	Displacement	i	Iteration index
v	Velocity	***Superscript***	
a	Acceleration	k	Time step index

Table 4.1: AlpesFSI solution scheme's notation.

step. Each set of calculation and communication forms a single iteration; note that a criterion for maximum iterations may be specified. The implicit numerical scheme implemented is described by Figure 4.2.

The minimum number of inner iterations per time step can be fixed at the beginning of the simulation. Additional inner iterations can be considered if a convergence criterion on the displacement of a reference grid point of the structural model is not satisfied. In this case the maximum allowed displacement between two following inner iterations has to be specified.

If the numerical scheme performs multiple iterations (index i) for each time step, it is referred to as "strongly coupled". Otherwise if there is just one inner step, it is called a "loosely coupled" method.

To synchronise the time step between the two codes, to allow a strongly coupled analysis, it has been necessary to modify the solution stream management in TAU. The choice of a strongly coupled approach has been necessary to avoid the first order error associated with the loosely coupled time-step, where effectively the structural solution and flow solution are out of sync. TAU is run strongly coupled through initialisation of the variables from two separate streams. One contains the latest solution, the other contains the variables from the (up to) two previous completed time-steps. When TAU initialises the solver for each solution step it reads the variables in the stream from time-level k to $k-1$ and $k-1$ to $k-2$ (if the old variables at $k-1$ are present in the stream). This step is done only if a deformed grid movement is activated. This step is performed using the stream that contains the data from the last completed time step and then the grid movement is turned off and the latest solution is read in, which overwrites

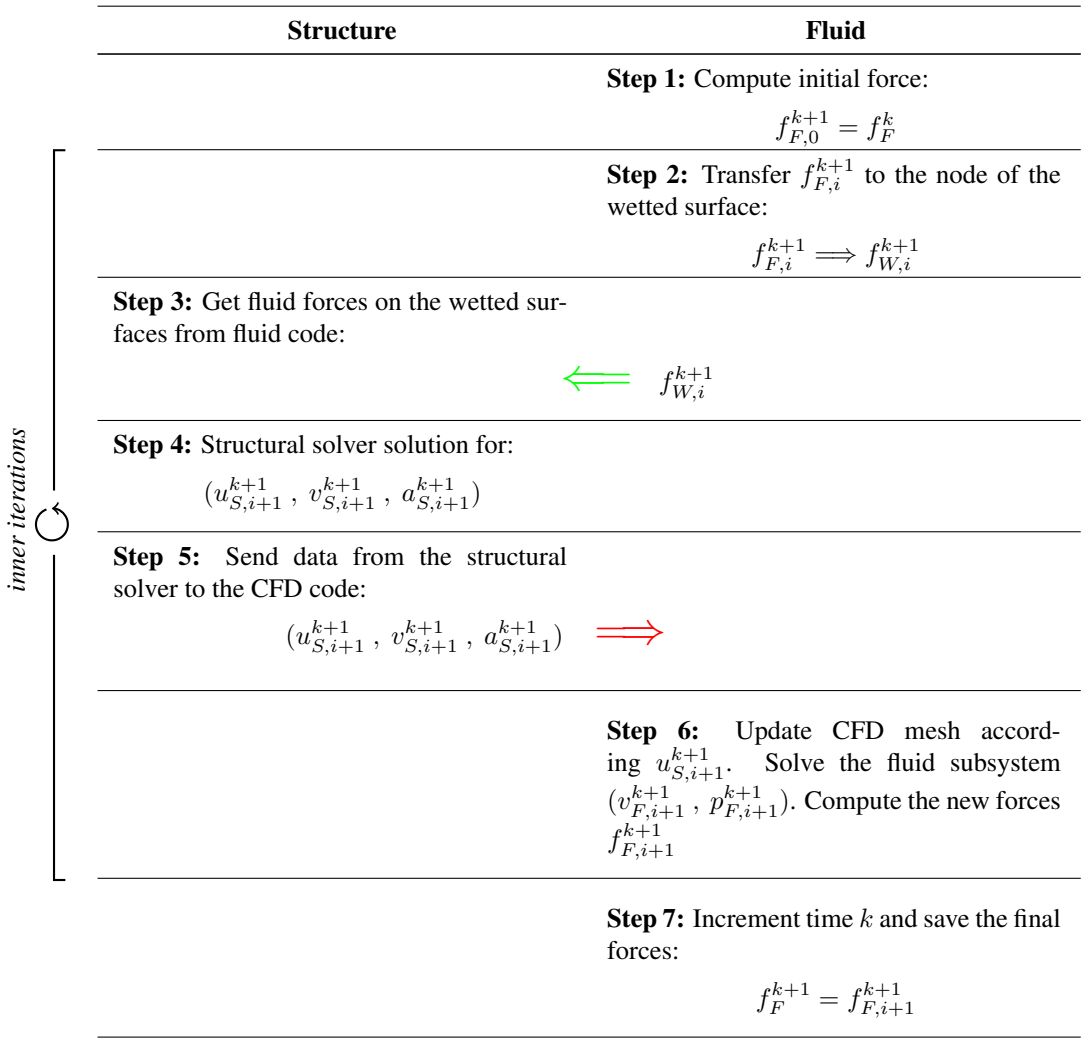

Figure 4.2: Implicit Fluid Structure coupling solution scheme.

the values in level k (but not those in $k-1$ or $k-2$, as grid movement is turned off). In this way the values at $k-1$ and $k-2$ are the values from the last completed time step and the values in k are those from the latest solution. The use of the solution stream used by TAU to previously restart unsteady simulations has been achieved through modification of the python scripting rather than the code itself and should allow future applications of the AlpesFSI as a tool. Furthermore, this technique has now been adopted by DLR in the new TAU release.

4.1.2 AlpesFSI Interface

The OpenFSI interface is available within the nonlinear solution sequence (SOL400) of the finite element structural solver MSC Nastran [103]. This interface is created using the MSC

Software Service Development Kit (SDK). Once implemented the code can be called inside the Nastran bulk data file, allowing a multi-physics analysis FEM/CFD to be performed. An overview of the AlpesFSI interface solution process is given in Figure 4.3.

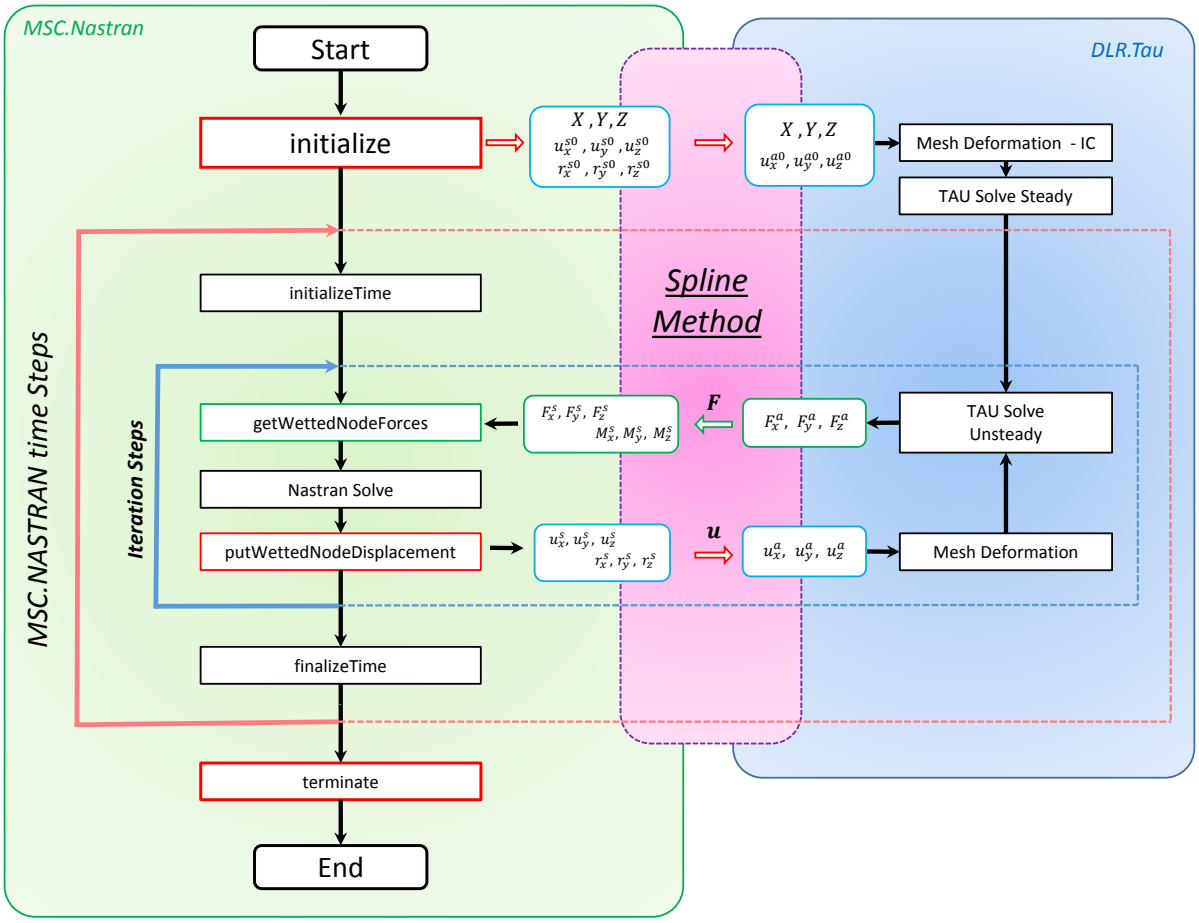

Figure 4.3: AlpesFSI interface for coupled FEM/CFD simulations.

To perform a coupled analysis using this interface it is necessary that the FEM and CFD models are coincident in their geometrical undeformed (stress-free) configuration. In fact, the displacements computed by the FEM solver are always evaluated with respect to that configuration. More details on how the difference in the mesh grid resolution is handled will be discussed in the following sections.

Three main steps can be identified in the solution process:

Initialisation step: at the beginning of the analysis the FEM code sends the CFD information regarding the initial configuration, so that it is possible to prescribe an initial deformation to the models.

Iteration step: the CFD solver sends the computed forces to the FEM solver which will calculate the structural deformation and the associated displacements to apply to the CFD mesh. Two solution approaches have been implemented in the AlpesFSI interface:

Explicit Method: the information is exchanged only once per time step. The forces are read at the beginning of the time step and the displacements are sent at the end of it. During the time step a Newton-Raphson iterative process is used to compute the displacements.
Implicit Method: the information is exchanged inside the Newton-Raphson loop more than once, before exiting from the time step.

Finalise step: at the end of the iterative process a termination message is sent to the structural and to the fluid dynamic solver, so that the analysis is terminated and the results file is created [104].

4.1.3 Newton-Raphson iteration method

In presence of a nonlinear element the equilibrium of the applied load, constrained forces and nodal forces is not immediately reached: therefore an iterative scheme such as the Newton-Raphson method is required [105, 106]. Considering the equilibrium equation given by:

$$\mathbf{f_p} + \mathbf{f_q} - \mathbf{f_n} = 0 \tag{4.1}$$

where $\mathbf{f_p}$ is the vector of applied loads, $\mathbf{f_q}$ the vector of constraint forces and $\mathbf{f_n}$ the vector of element nodal forces: these being nonlinear functions of the displacements for nonlinear elements. Since the error vanishes at constrained points and the constraint forces vanish at free points, the unbalanced forces acting at nodal points at any iteration step are conveniently defined as an error vector by:

$$\mathbf{r} = \mathbf{f_p} - \mathbf{f_n} \tag{4.2}$$

Based on Newton's method, the linearized system of equations given by Eq. 4.1 and 4.2 is solved for incremental displacements by Gaussian elimination in succession. The Jacobian of the error vector emerges as the tangential stiffness matrix $\mathbf{K}_T$. The equation to solve for the

displacement at the i-th iteration is given by:

$$\mathbf{K}_T \, \Delta \mathbf{u}^i = \mathbf{r}^{i-1} \tag{4.3}$$

where the tangential stiffness matrix is given by

$$\mathbf{K}_T = - \left. \frac{\partial \mathbf{r}}{\partial \mathbf{u}} \right|_{u=u'} = \left. \frac{\partial \mathbf{f_n}}{\partial \mathbf{u}} \right|_{u=u'} \tag{4.4}$$

while the incremental displacement

$$\Delta \mathbf{u}^i = \mathbf{u}^i - \mathbf{u}^{i-1} \tag{4.5}$$

and the residual error is

$$\mathbf{r}^i = \mathbf{f_p} - \mathbf{f_n}(\mathbf{u}^i) \tag{4.6}$$

The iteration continues until the residual error $\mathbf{r}$ and the incremental displacement Δu become negligible, which is signified by the convergence criteria.

The tangential stiffness, introduced above, consists of the geometric stiffness in addition to the material stiffness, without regard to the coordinate transformation

$$\mathbf{K}_T = \mathbf{K}^m + \mathbf{K}^d \tag{4.7}$$

where $\mathbf{K}^m$ and $\mathbf{K}^d$ refer to the material and the differential stiffness, respectively. Then the residual load error is automatically carried over to the next increment process. The merit of the Newton-Raphson methods is the quadratic rate of convergence:

$$\left\| u^* - u^{i+1} \right\| \leq q \left\| u^* - u^i \right\|^2 \tag{4.8}$$

where u^* is a true value of $\mathbf{u}$, q is a constant, and $\| \ \|$ represent a vector norm. From a practical standpoint however, determination of the tangential stiffness and its inverse at each iteration entails a considerable amount of computation. In Figure 4.4 a schematic representation of the iteration sequence for the Newton-Raphson method is shown. The tangential stiffness is evaluated for three points before the convergence is reached.

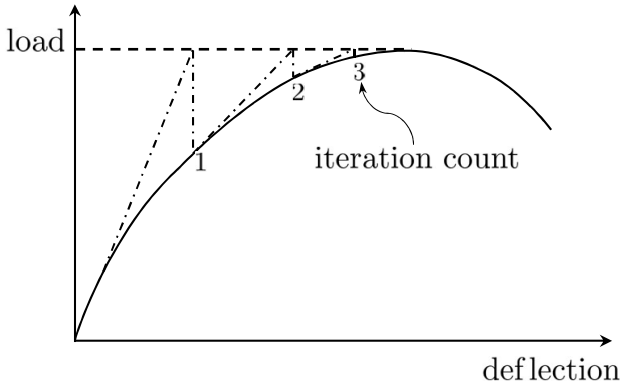

Figure 4.4: Newton-Raphson iteration method

4.1.4 Damping definition in transient analysis

Damping is a mathematical approximation used to represent the energy dissipation observed in a structure. Damping is difficult to model accurately since it is caused by many mechanisms including: viscous effects, external friction, internal friction and structural nonlinearities [106]. Because these effects are difficult to quantify, damping values are often computed based on the results of a dynamic test. Two types of damping are generally used for linear-elastic materials: viscous and structural. Referring for simplicity to a single degree of freedom system, the viscous damping force, which is proportional to the velocity, can be expressed as:

$$f_v = b\,\dot{u} \tag{4.9}$$

where b is the viscous damping coefficient and $\dot{u}$ is the velocity. The structural damping force is instead proportional to the displacement and given by:

$$f_s = i\,G\,k\,u \tag{4.10}$$

where G is the structural damping coefficient, k is the stiffness, u the displacement and $i = \sqrt{-1}$ is the imaginary unit.

Since in the transient response analysis the results are real values, it is not possible to use a complex coefficient. Therefore, structural damping has to be defined by means of an equivalent viscous damping. To appreciate the impact of this on the solution, a relation between structural and equivalent viscous damping must be defined.

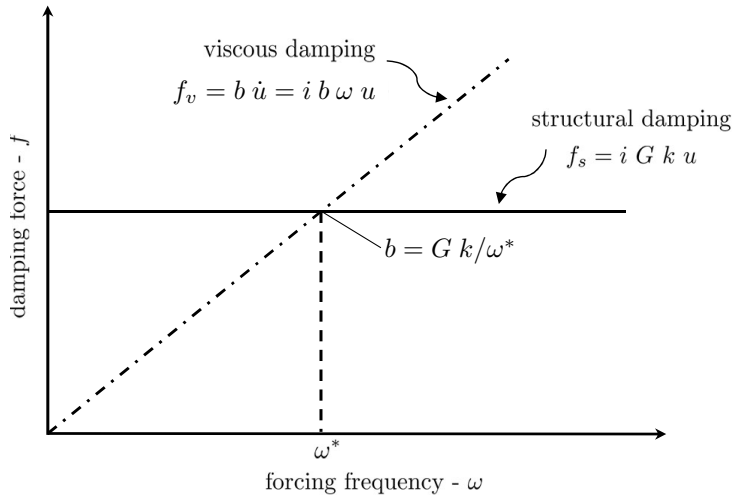

Figure 4.5: Structural damping and viscous damping force for constant amplitude sinusoidal displacement.

For a sinusoidal displacement response of constant amplitude, the structural damping force is constant and the viscous damping force is proportional to the forcing frequency. Figure 4.5 shows this as well as that for constant sinusoidal motion the two damping forces are equal at a single frequency. At this frequency

$$Gk = b\omega^* \Rightarrow b = \frac{Gk}{\omega^*} \tag{4.11}$$

where ω^* is the frequency at which the structural and viscous damping forces are equal for a constant amplitude of sinusoidal motion. If the frequency ω^* is the circular natural frequency ω_n

$$b = \frac{G\,k}{\omega_n} = G\,\omega_n\,m \tag{4.12}$$

where considering the definition of critical damping b_{cr}:

$$b_{cr} = 2\sqrt{k\,m} = 2\,m\,\omega_n \tag{4.13}$$

In correspondence of the resonance, $\omega = \omega_n$ for a constant amplitude sinusoidal displacement:

$$\frac{b}{b_{cr}} = \zeta = \frac{G}{2} \Rightarrow G = 2\,\zeta \tag{4.14}$$

Two parameters are used to convert structural damping to equivalent viscous damping in a

transient analysis. An overall structural damping coefficient can be applied to the entire system stiffness matrix defining the circular frequency at which damping is to be made equivalent. Additionally the structural damping coefficient is defined according to Eq. (4.14). In order to have comparable result with the gust response analysis performed in frequency domain, where a 2% critical damping is considered for all the range of frequency, g has been chosen to be equal to 0.04.

4.1.5 Nonlinear solution sequence in MSC Nastran, SOL 400

The nonlinear solution sequence available in MSC Nastran, identified as SOL 400 [105], allows the performance of several analysis type combinations. Of particular interest for this research is the nonlinear coupled physics analysis. This is activated when a nonlinear analysis is requested in the case control section of the input file. Two nonlinear solutions are available:

- Nonlinear static analysis: NLSTAT.
- Nonlinear transient analysis: NLTRAN.

In these solutions it is possible to account for structural large displacements effects. However, it is even possible to deactivate these effects: in such case the structural analysis is performed with linear methods, maintaining the functionality to perform multi physics analysis. Since in the present work the FSI analyses have been used to compare the results with a linear method (DLM), the structural model has been solved deactivating the large displacement effects.

Traditionally, most of the pre-existing coupled fluid structure interaction analysis using an OpenFSI application, in MSC Nastran, have been focussed on the investigation of unsteady problems such as flutter or gust response [107]. The OpenFSI interface is activated in the AlpesFSI, developed in this project, for both these cases. Additionally, the AlpesFSI interface has implemented the capability to perform multi-step analysis. Here, a nonlinear static calculation precedes a nonlinear unsteady calculation. Thus, within the same interface, the NLSTAT analysis can be used to perform static aeroelastic analysis (e.g. analyse the static aeroelastic deformation of an aircraft, trim analysis), while the NLTRAN analysis can be used to investigate the unsteady response of the structure to a gust disturbance or the two can be combined.

In the case of a nonlinear static solution sequence the forces are read at the beginning of the structural solution. They are then transferred to the structure in a series of steps (defined by the user), where the external load increase from 0% to 100%. This is necessary to avoid problems with convergence of the FEM solver, (e.g. in the presence of "large displacements"). It is also possible to introduce a relaxation factor to facilitate the convergence to the steady deformation.

4.1.6 Interpolation method

One of the most important aspects for a fluid structure analysis is how information is transferred between the different models. Usually each solver (fluid and structure) uses a different mesh due to the different characteristics of the models. The CFD fluid mesh is refined compared to the structural one, and most of the time the two meshes do not coincide at the fluid-structure interface. However, to be able to perform a calculation it is fundamental to transmit the load from the CFD nodes (aerodynamic model) to the wetted finite element nodes (structural model), so that a deformation may be computed and used to update the position of the aerodynamic grid. In order to transfer the forces and displacements from the CFD mesh to the FEM, and vice versa, it is necessary to use a transformation matrix.

The AlpesFSI interface is independent of the method used to compute the fluid-structure interpolation matrix. This is read during the initialisation step and only matrix-vector multiplications are performed during the analysis step. For this, the forces on the structural grid are obtained via:

$$\mathbf{f}_{str} = \mathbf{H}_{sa}\, \mathbf{f}_{aero} \tag{4.15}$$

where $\mathbf{H}_{sa}$ is the force interpolation matrix. The aerodynamic displacements are given as:

$$\mathbf{u}_{aero} = \mathbf{H}_{as}\, \mathbf{u}_{str} \tag{4.16}$$

where $\mathbf{H}_{as}$ is the displacement interpolation matrix.

Two different methodologies have been used to obtain the interpolation matrices. The first is an interpolation scheme based on radial basis functions, developed by Rendall and Allen within the CFD Group at the University of Bristol [30, 71]. The second method is based on the 3D beam and 3D surface available in MSC Nastran via SPLINE6 and SPLINE7 [108].

Since the method developed by Rendall and Allen uses radial basis functions (RBFs) it works on totally arbitrary point clouds of any form, allowing the removal of all dependency relating to the volume mesh, structural mesh and flow solver type. This can be achieved because all connectivity requirements are removed. This is true for both the coupling and mesh motion problems. Detailed information regarding the implementation are discussed by Rendall and Allen in reference [30].

One of the advantages of this method is that it can be applied to both structured and unstructured CFD meshes. Moreover, it is not affected by poor quality meshes where the aerodynamic and structural surface may cross. Despite the totally general formulation and applicability to any mesh type and structural elements, this method can be computationally expensive, since it operates with global coupling matrices of big dimensions: $N_s \times N_a$ (where N_s and N_a are respectively the number of surface structural and aerodynamic points). A further improvement of this method from Rendall and Allen [71] has increased the efficiency by using a pointwise partition of unity (PPoU), which has allowed the matrix size to be reduced substantially, without compromising the aerodynamic surface smoothness. In the improved formulation of this method the forces are transferred only to structural points near each aerodynamic point.

Even though this method allows the conservation of moments and forces, in its current form it is only able to transfer three degrees of freedom. For this reason its use is more suitable in the presence of a three dimensional structural model, (e.g. a wing box structure).

The second method used to obtain the coupling has been based on two routines available within the Nastran code, namely SPLINE6 and SPLINE7 which define a six degree of freedom surface and beam spline, respectively. This method is particularly suitable for the situation where the FEM model is represented by beam stick elements. In this particular case the coupling matrix has been obtained using the “Hybrid Static Aeroelasticity Toolkit” [70] developed by MSC Software Toulouse. This toolkit, available in the pre-processor MSC Patran Flight Loads, allows a six degree of freedom spline to be generated for fluid structure coupling.

4.2 Test Cases

This section presents the results achieved with the AlpesFSI interface for steady and unsteady aeroelastic investigations, which verify its efficacy.

First a standard academic literature case is considered, the flutter behaviour of the AGARD 445.6 wing [109].

The subsequent test cases are for the FFAST wing [110], a representative wing model of a civil airliner. For this application a nonlinear static analysis is used to identify the aeroelastic steady deformation. From this trim configuration a nonlinear unsteady analysis for the gust response has been performed.

4.2.1 AGARD 445.6 weakened model

The AGARD 445.6 wing model has been chosen as the first aeroelastic test for the AlpesFSI interface. The flutter behaviour of this wing was experimentally investigated by Yates [109] and numerical computations reported in many publications [111, 107, 112, 113].

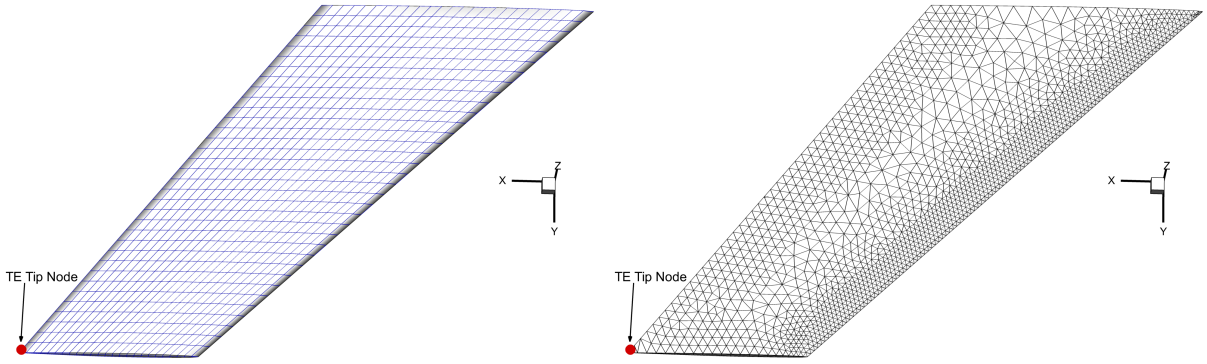

(a) FE model. (b) CFD model.

Figure 4.6: AGARD 445.6 wing model.

The specific configuration selected here is the 2.5 ft “weakened model” number 3 [109]. The definition “weakened model” refers to the fact that the original solid homogeneous laminated mahogany model was reduced in stiffness by drilling holes through the wing normal to the chord plane [114]. This modification was necessary to obtain flutter throughout the tunnel Mach number and density range. To ensure aerodynamic continuity the holes were filled using

a rigid foam plastic, which did not alter the stiffness of the perforated wing. This model is characterised by a 45° quarter chord sweep angle, a panel aspect ratio of 1.65, a taper ratio of 0.66 and chordwise sections of the wing are given by the NACA 65A004 aerofoil. The structural model consist of solid elements, and the material parameters have been designed to give the first four eigenfrequencies. In particular, the first three eigenfrequencies fit those reported in [109] very well, as reported in Table 4.2.

Mode number	Mode name	FEM, Hz	Experimental, Hz
1	1^{st} wing bending	9.57	9.60
2	1^{st} wing torsion	38.11	38.10
3	2^{nd} wing bending	50.84	50.70
4	2^{nd} wing torsion	98.67	98.50

Table 4.2: AGARD wing natural modes frequency comparison: FEM vs Test.

The coupling surfaces of the aerodynamic and structural mesh are shown in Figure 4.6. The aerodynamic surface has 3047 grid points leading to 9141 parameters, while the structural one has 1750 surface grid points leading to 5250 parameters. This model has been analysed in the subsonic case for Mach number $M_{\infty} = 0.901$, with a constant density $\rho_{\infty} = 0.099477\ kg/m^3$ and an initial dynamic pressure of $p_{\infty} = 3265\ N/m^2$. For all the analysis Euler equations are used to solve the aerodynamics.

Initially a time step size of $\Delta t = 0.0005\ s$ has been used. The dynamic response of the structure has been studied following an initial deflection, proportional to the first bending mode, with a maximum displacement at tip trailing edge of $1\ cm$.

Figure 4.7 shows a comparison of the vertical displacement of the TE at the wing tip highlighted in Figure 4.6, with varying time step size in a weakly coupled method (1 inner time step). A reference solution calculated using a strongly coupled analysis is also included. It is evident that the dynamic behaviour in a loosely coupled method is quite sensitive to the time step size used for the simulation. In particular it can be seen that as the time step size is reduced, the response is gradually converging to the response obtained with a strongly coupled analysis (this reference case is indicated by the dashed black line).

In Figure 4.8 it is possible to observe that there is little time step influence on the strongly coupled responses. For this specific case, 2 inner iterations are also shown to be sufficient to get

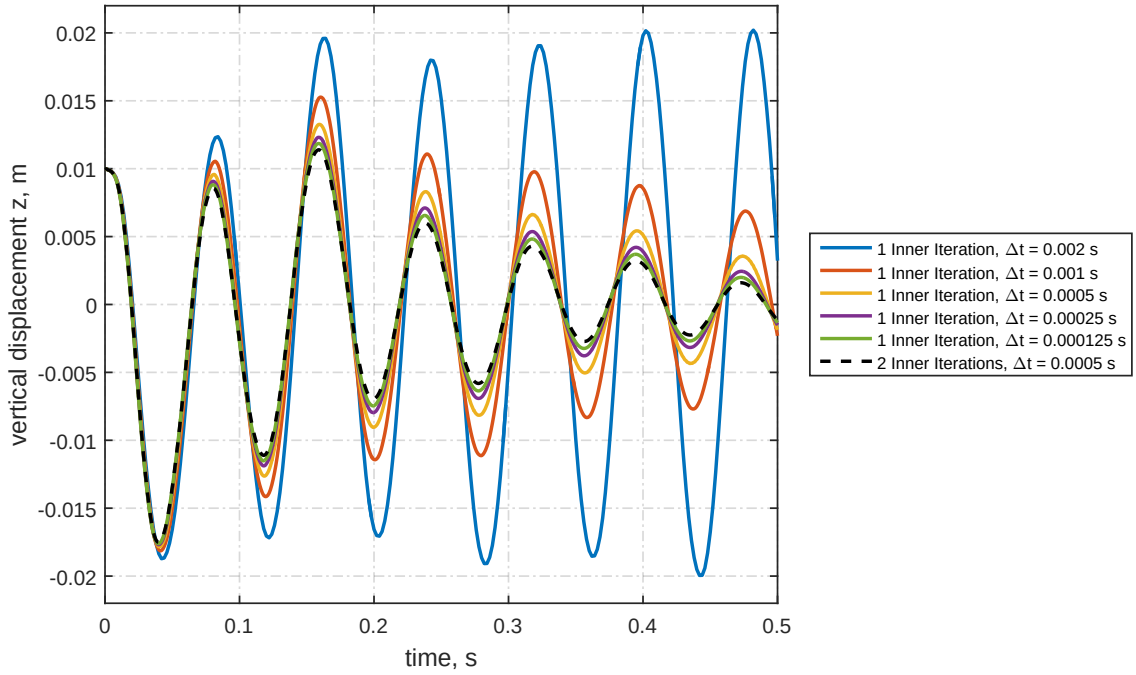

Figure 4.7: AGARD 445.6 wing tip TE vertical displacement varying time step size, Δt, in a weakly coupled method.

convergence between the aerodynamics and structural codes.

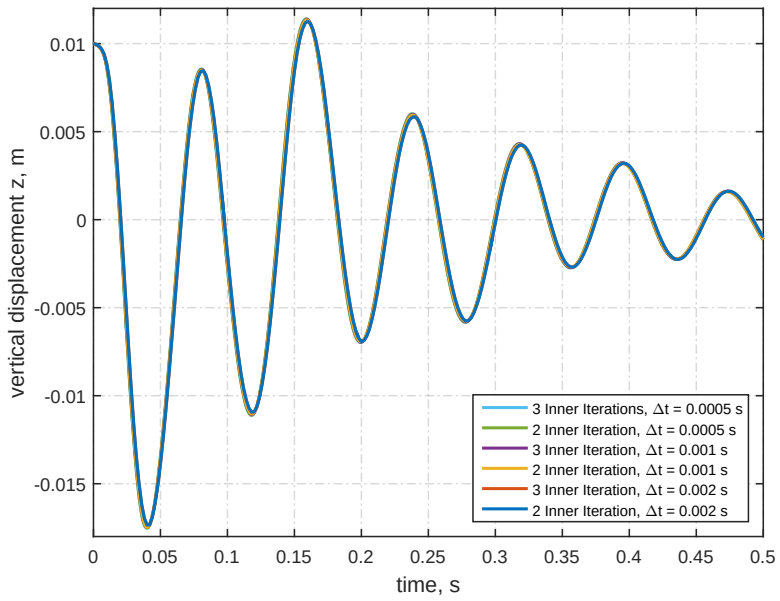

Figure 4.8: AGARD 445.6 wing tip TE vertical displacement varying time step size, Δt, in a strongly coupled method.

Figure 4.9 shows details of TE wing tip vertical displacement for different time step sizes.

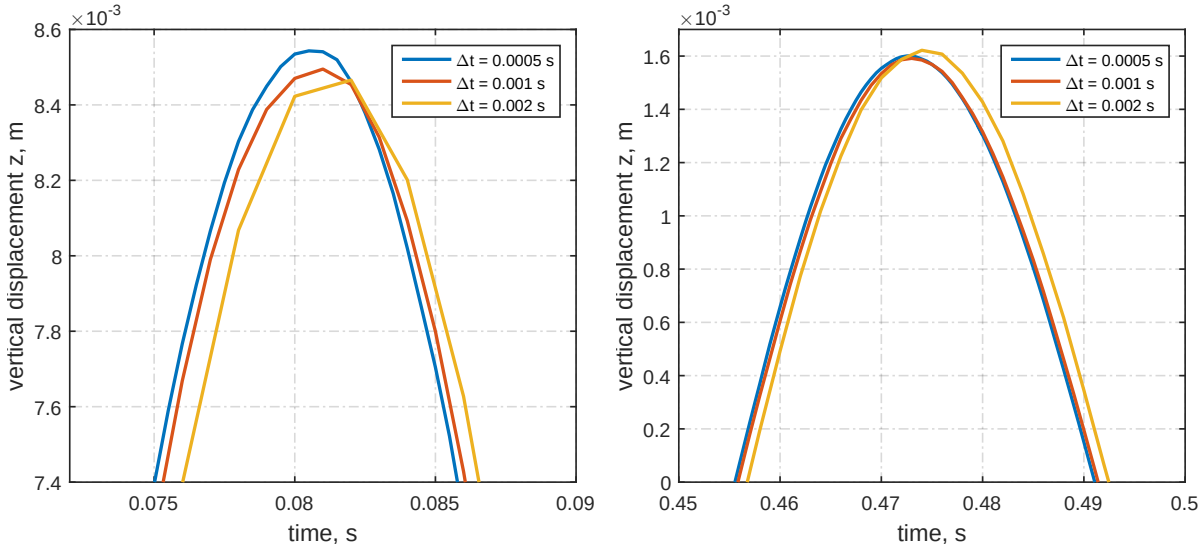

Figure 4.9: Comparison of TE wing tip vertical displacements, for different Δt using a strongly coupled method with two inner iterations.

4.3 FFAST Wing model

The second test case considered uses a geometry representative of large civil aircraft, the FFAST wing. The suitability of the method to investigate steady aeroelastic analysis was first considered, before an additional unsteady load analysis was performed. A full aircraft model was developed as part of the FFAST project [110] to be representative of a single-aisle civil jet airliner. The structural model of the aircraft is a beam stick FE model with lumped masses, as shown in Figure 4.10.

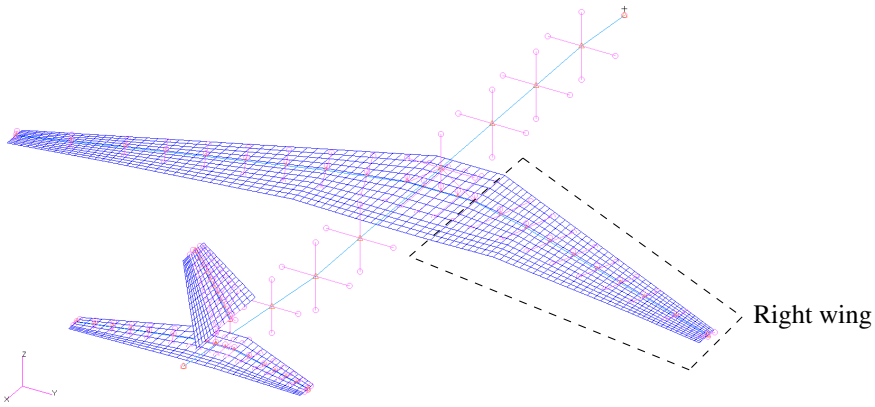

Figure 4.10: Full FFAST FE beam stick type and DLM model.

For this analysis just the right wing has been considered cantilevered at the root (fuselage junction). The wing FE model considered, extracted from the wing fuselage junction, includes the pylon structure and mass, while the engine is modelled only in terms of mass. It contains 10 beam elements for a total of 11 structural grid points, Figure 4.11.

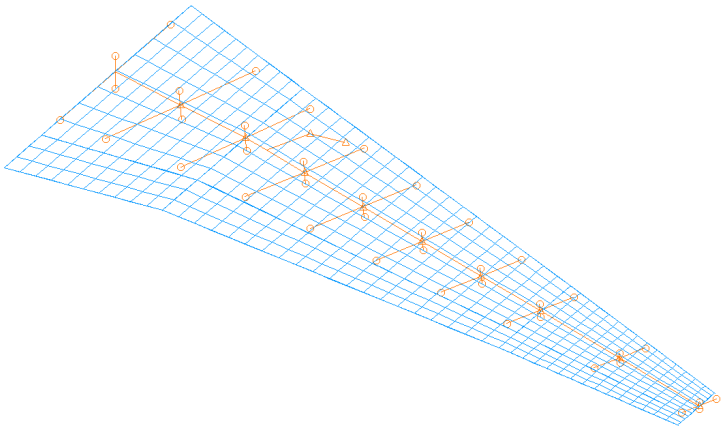

Figure 4.11: FFAST right wing FE and DLM model.

The aerodynamic panel model which will be used in subsequent chapters as the DLM mesh

has 11 boxes in the chord wise direction and 45 boxes in span, for a total of 495 aerodynamic panels. The panel method used in this investigation is the Doublet-Lattice Method available in the commercial solver MSC Nastran.

A CFD model has been created using aerofoil data available for the three sections: root, crank and tip, Figure 4.12. The wing CFD model created does not include the engine and pylon, and has 33227 surface grid points. The CFD model has been solved using Euler equations. The flight condition used in the investigation is a $1g$ condition at an altitude of $11000\ m$, Mach number $M = 0.85$.

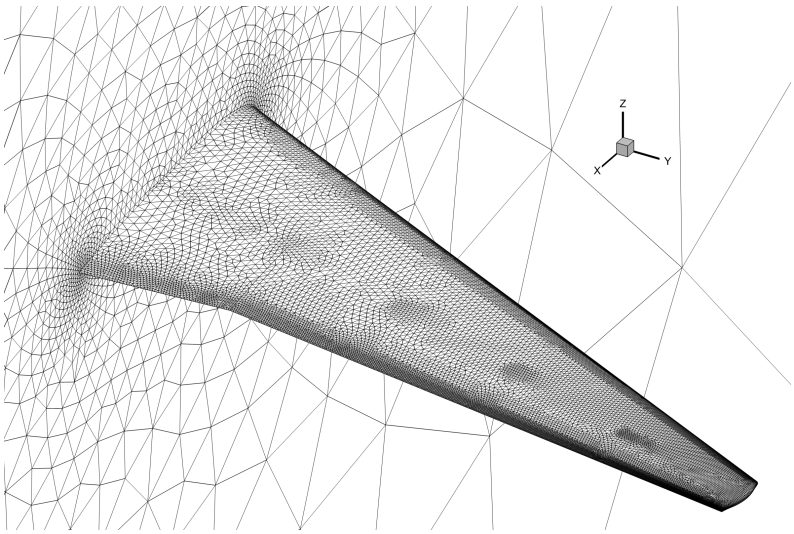

Figure 4.12: FAST right wing CFD model.

4.3.1 Aeroelastic Static Trim analysis

The AlpesFSI interface has been used to identify the trim aeroelastic steady deformation, considering an angle of attack of 2° at the root. The steady deformation of the wing at trim and the convergence of the vertical displacement of the wing tip is shown in Figure 4.13. In this case six iterations are necessary to get to the steady convergence, and no relaxation factor has been applied.

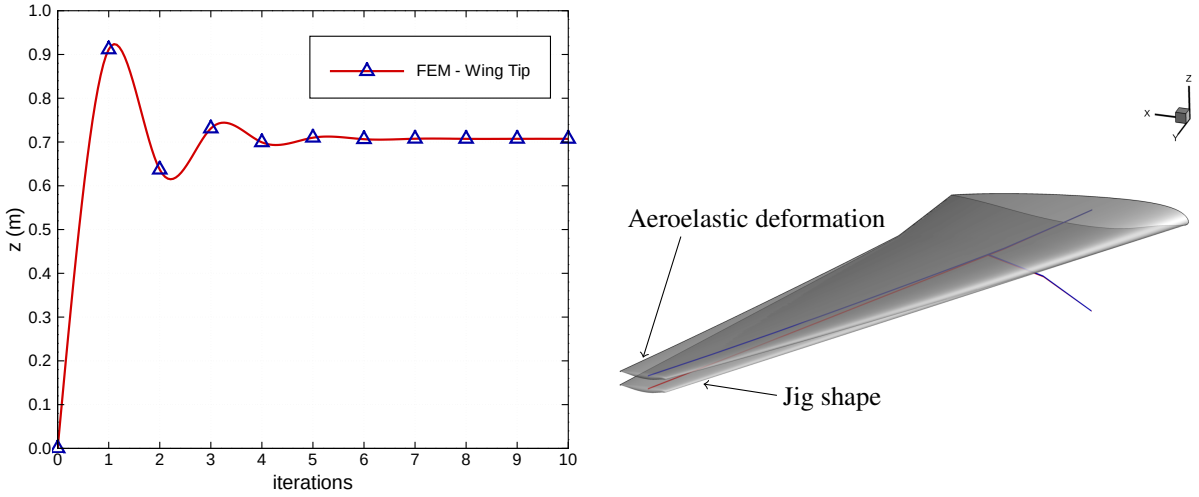

(a) Wing tip node vertical displacement.

(b) Fluid structure aeroelastic deformation at trim.

Figure 4.13: FFAST wing trim analysis.

4.3.2 Unsteady transient analysis for gust

The steady deformation at trim can be used as a starting point for a transient response in a gust analysis. Figure 4.3.2 shows a typical one minus cosine (1MC) gust velocity profile, having a maximum gust velocity of w_{g0} and gust wavelength of L_g. Three reference gust lengths are analysed and their shapes are depicted in Figure 4.14(b).

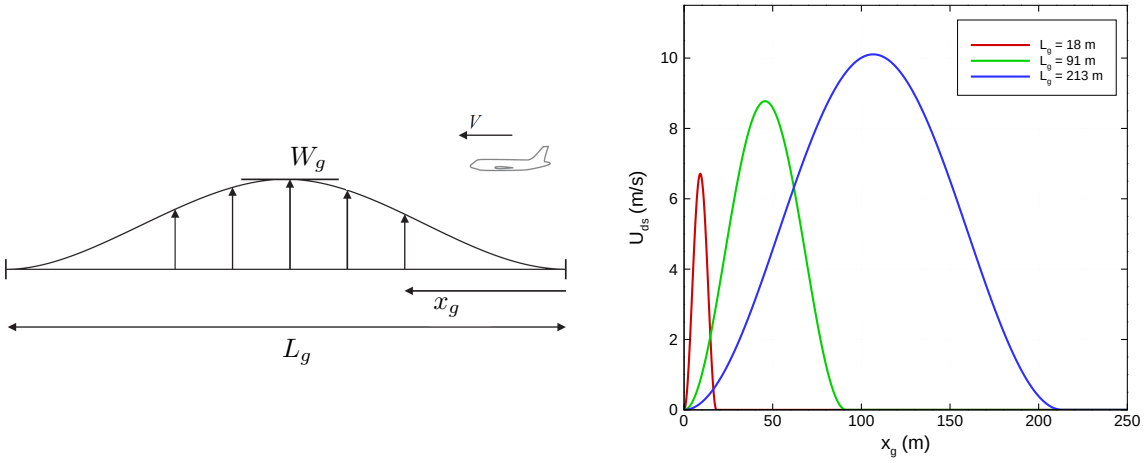

(a) “$1 - \cos$” gust shape [8].

(b) Gust profile analysed.

Figure 4.14: Gust profile.

As prescribed by the “Certification Specification for Large Aeroplanes CS-25” [9], the shape of

the gust has to be taken as:

$$W_g(x) = \begin{cases} \frac{U_{ds}}{2}\left(1 - cos\left(\frac{\pi x}{H}\right)\right) & for \;\; 0 \leq x \leq 2H \\ \\ 0 & otherwise \end{cases} \tag{4.17}$$

where x is the distance penetrated into the gust, H (in m) is the distance parallel to the flight path of the aeroplane for the gust to reach its peak velocity ($H = L_g/2$, half of the gust wavelength) and U_{ds} is the design gust velocity in equivalent air speed (EAS), defined as:

$$U_{ds} = U_{ref} F_g \left(\frac{H}{106.68}\right)^{1/6} \tag{4.18}$$

In Eq. (4.18) where U_{ref} is the reference gust velocity in EAS and F_g is the flight profile alleviation factor. U_{ref} reduces linearly from $17.07\ m/s$ EAS at sea level to $13.41\ m/s$ EAS at $4572\ m$ ($15000\ ft$) and then again to $6.36\ m/s$ EAS at $18288\ m$ ($60000\ ft$). In the following example a value of F_g equal to 1 has been considered. The gust is modelled in TAU, using a field velocity method [115, 77, 80]. It is prescribed to start just outside the computational domain and travel at free stream velocity U_∞. Figure 4.15 shows the time history of the variation of the global lift and pitching moment coefficient due to the three gust lengths.

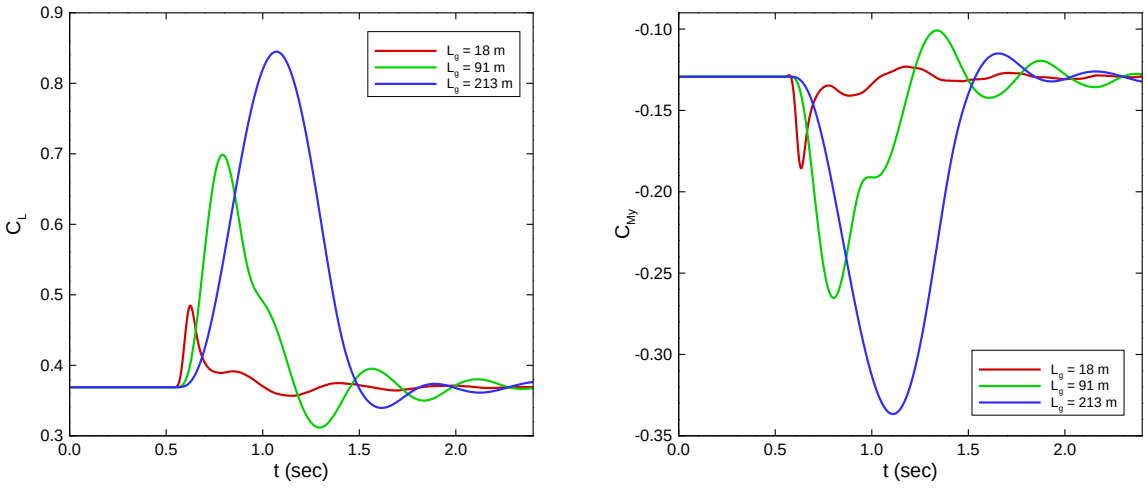

(a) Total wing C_L.

(b) Total wing C_{M_y}.

Figure 4.15: CFD results due to the gust.

Figure 4.16 shows a comparison of the upper wing surface c_p distribution at the trim condition and at the point of maximum lift coefficient after the gust has perturbed the steady state for the three different gust lengths.

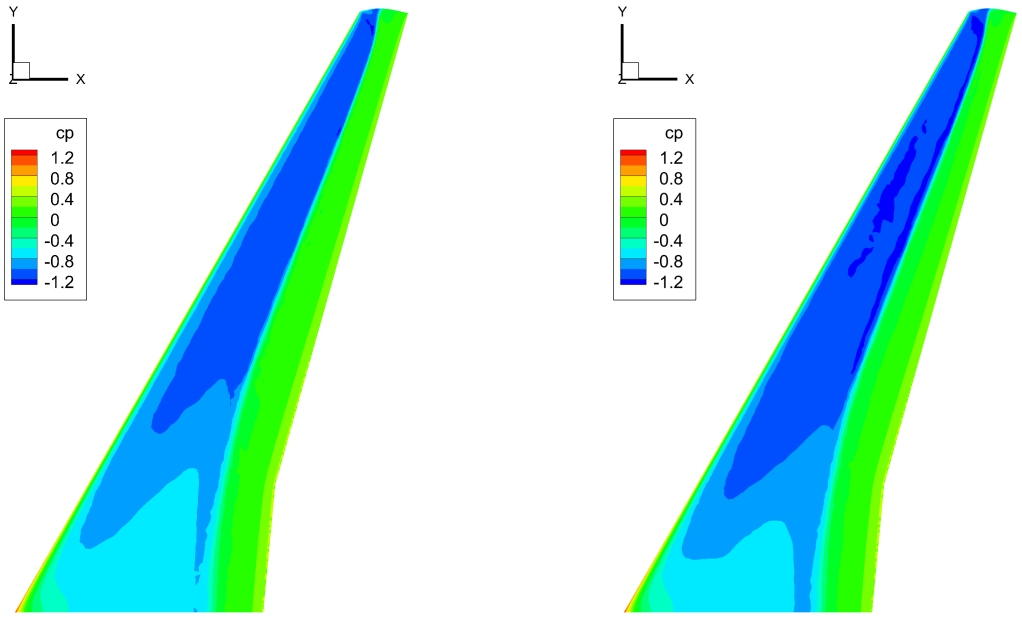

(a) Trim condition.

(b) $L_g = 18\ m$

(c) $L_g = 91\ m$

(d) $L_g = 213\ m$

Figure 4.16: c_p distribution on FFAST right wing upper surface.

The effect of the gust disturbance on the airframe can be analysed in terms of structural displacement and loads. For example it is possible to have an indication of the structural deformation analysing the time history of the wing tip vertical displacement, reported in Figure 4.17 for the three reference gust lengths.

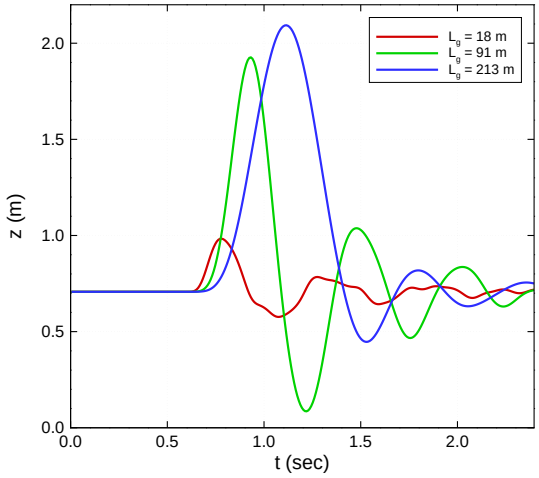

Figure 4.17: FE model loads resultant at wing root.

Since the main objective of a gust loads analysis is to identify the maximum loads acting on the structure, relevant quantities that can be investigated are the wing root vertical force F_z, torsion M_x and bending moment M_y. The time histories for these interest quantities, relevant for the structural sizing, obtained for the different gust lengths are presented in Figure 4.18.

All the simulation presented in this section were performed using the High Performance Computing (HPC) server facility "BlueCrystal Phase 3" available at the Advanced Computing Research Centre (ACRC) at the University of Bristol. Each gust analysis has been performed using 1 node and sixteen 2.6 GHz SandyBridge cores, requiring twelve hours of computing time for 2.4 seconds of simulation time.

The loads evaluated using the AlpesFSI interface in this section, will be used as the reference high fidelity results to compare the doublet-lattice correction method in the following chapter.

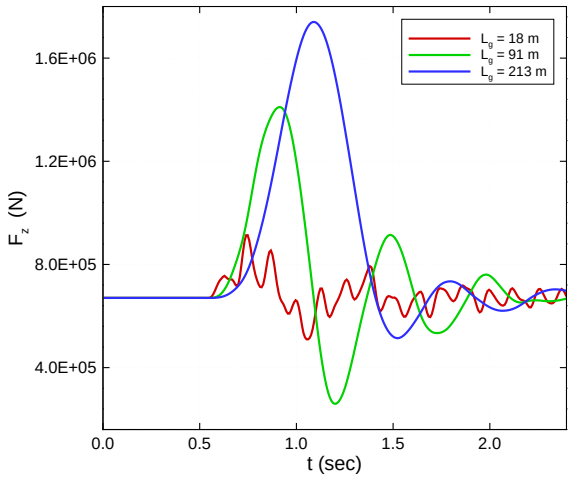

(a) Wing root shear force, F_z.

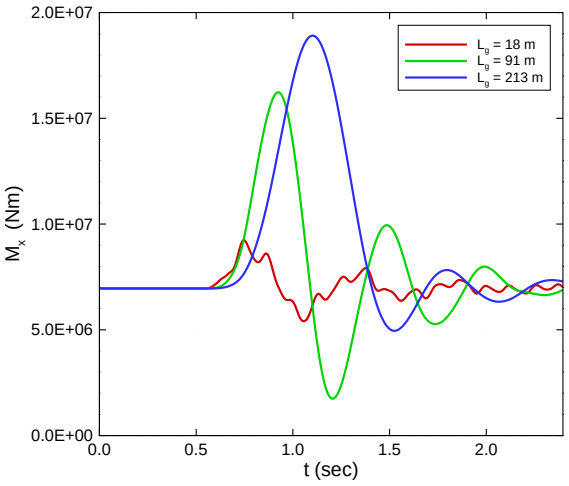

(b) Wing root bending moment, M_x.

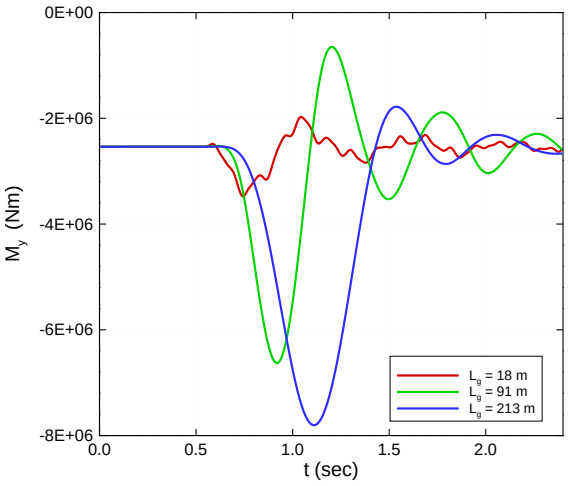

(c) Wing root torque, M_y.

Figure 4.18: FE model loads resultant at wing root.

Figure 4.19, gives an overview of the interaction between the gust disturbance and the wing model. The maximum structural deformation is shown with respect to the gust location for a gust length of $L_g = 91\ m$.

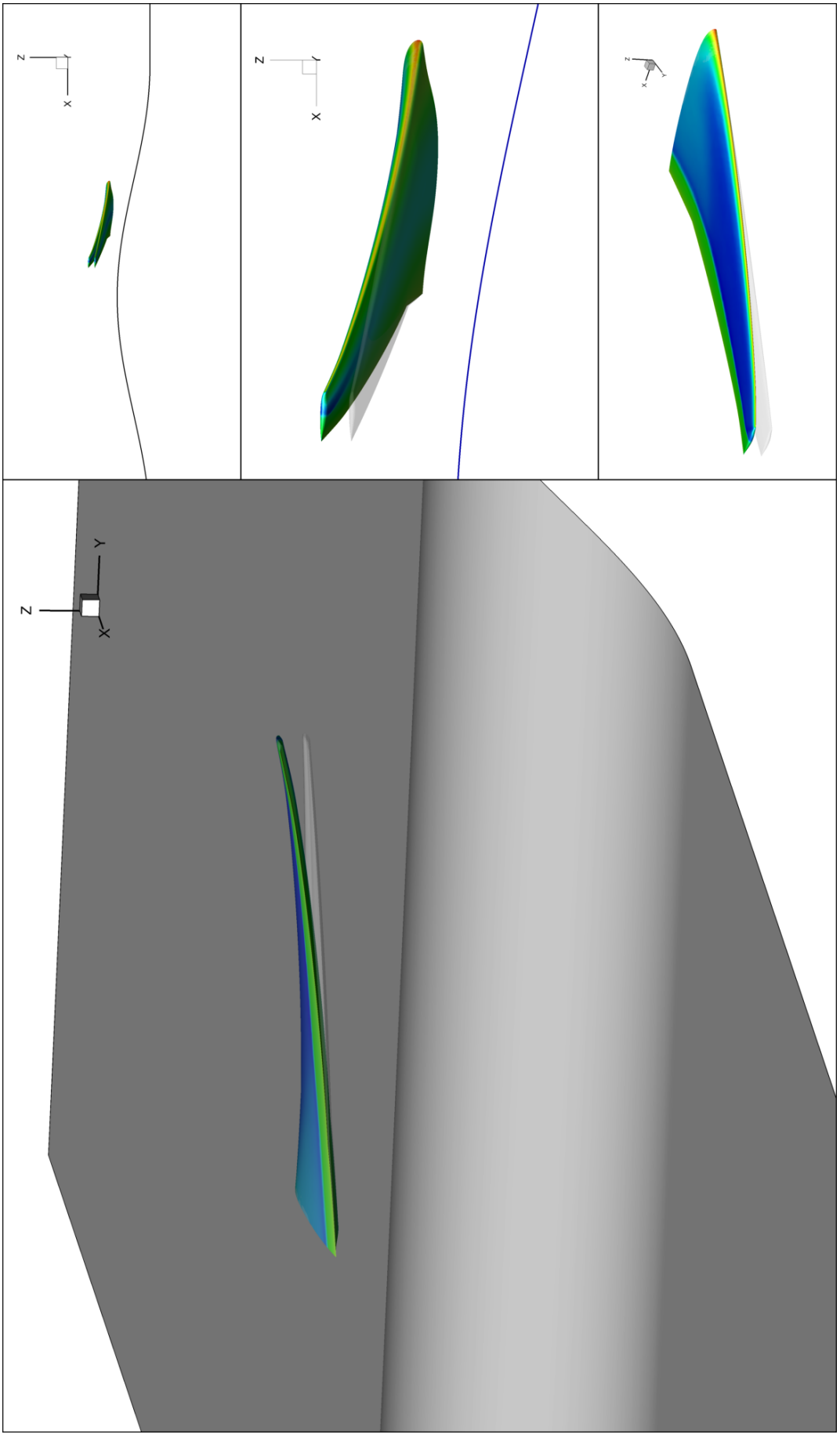

Figure 4.19: Structural deformation due to the gust wing interaction, simulated using the AlpesFSI analysis environment.

CHAPTER 5

A Doublet Lattice Correction Method for Gust Loads Analysis

This chapter presents a new methodology, developed during this research, to correct the air loads computed using the doublet-lattice method for gust loads analysis [20]. This correction technique has been formulated in the frequency domain and calculates a matrix of correction coefficients at selected reduced frequencies. Based on the idea proposed in [24], it makes use of a post multiplying approach, and considers complex correction factors to ensure a good representation of the unsteady aerodynamics. This approach makes use of frequency domain harmonic aerodynamic loads to be used as high fidelity reference loads. These could be evaluated using time domain CFD simulations, however this approach could be very expensive in terms of computational time, hence, linear frequency domain (LFD) analyses have been used to reduce the computational cost necessary to evaluate the reference aerodynamics loads. Additionally a correction factor interpolation method can be performed to reduce the number of reference cases that need to be analysed using the LFD code. In the implementation of the method the LFD solutions are considered via a strip loads approach.

5.1 Doublet-Lattice Method Correction Approach

It is required that the correction approach increases the accuracy of the doublet-lattice method in those situations where the simplifying assumption used in its derivation limit its applicability. One specific example could be a cruise flight condition in the transonic regime, where aerodynamic nonlinearities are relevant and viscous and thickness effects are not negligible.

Typically for an aircraft loads analysis the structural Global Finite Element Model (GFEM) is condensed to a set of discrete points in correspondence of which the loads are evaluated. A comparison of a GFEM model for a commercial aircraft and the set of points used for the generation of the condensed model is shown in Figure 5.1. The reduced model, described in terms of mass and stiffness matrix allows a sensible reduction in the computational time necessary for the loads investigation.

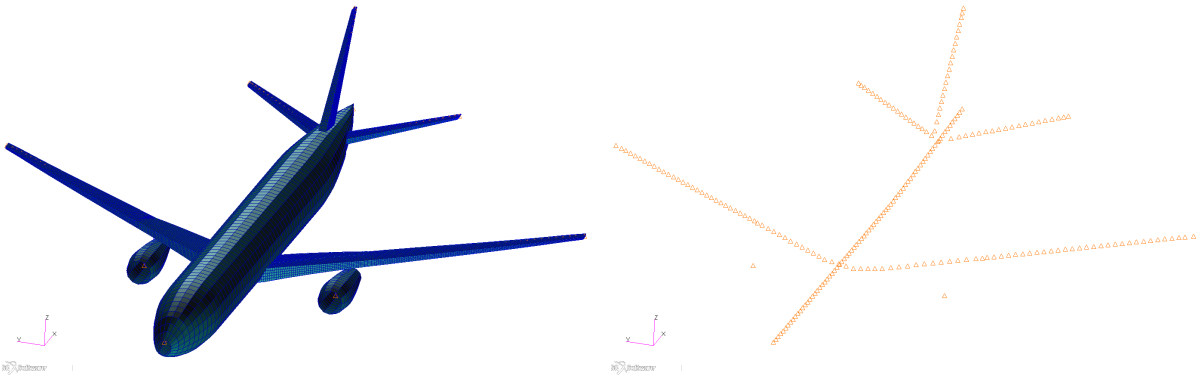

(a) Nasa CRM GFEM Model (b) NASA CRM Condensed Model

Figure 5.1: NASA Common Research Model GFEM and reference point used for condensation.

This implies that the aerodynamic loads have to be integrated over the reduced structural grid to perform an aeroelastic simulation.

On the base of this consideration, the correction method, formulated in the present work, is intended to give a corrected DLM method which is able to compute data comparable to the reference aerodynamic data. These could be either experimental results coming from wind tunnel tests, or numerical results from computational fluid dynamics simulations. Since for this research, no experimental results are available, the reference high fidelity data will be obtained from CFD simulations in all cases. In particular the AlpesFSI interface introduced in Chapter 4 will be used to obtain the aeroelastic reference data, used as target loads.

To achieve this, it has been chosen to define a matrix of correction coefficients, which will correct the downwash evaluated for each panel of the doublet-lattice mesh. This is obtained, introducing a correction matrix which post multiplies the AIC matrices: with the intention to improve the capability to account for the unsteady aerodynamic effect, often not captured by the correction method presented so far [54], for gust loads analysis.

The presented method allows a correction for each of the reduced frequencies at which the AIC matrices are computed to be defined. In this way the unsteady aerodynamic effects are accurately captured. Moreover, the correction is specialized in order to model the unsteady effects of the flow perturbation over the rigid panel mesh and those of the mode shape deformation. This generates two sets of correction coefficient for reduced frequency. Since such a process could become quite expensive in terms of computational cost, LFD analyses are used to evaluate the correction factor and an interpolation of the correction coefficient has been introduced to reduce the number of reference data.

In the following sections the doublet-lattice method formulation for aerodynamic and structural loads discussed in Chapter 2 is specialised for the definition of the correction method proposed. Initially an application for steady aeroelastic loads is provided. Subsequently, the correction of unsteady loads due to sinusoidal gust and to structural deformations are considered.

5.1.1 Integrated loads approach

The correction method formulated in this Chapter is based on the so called “strip loads approach”. Since a good representation of the shock position and movement is not achievable on the corrected DLM mesh, due to the low refinement in the aerodynamic panel discretisation, the correction method targets the integrated aerodynamic loads on a series of strips defined along the wing span.

In order to fit this assumption, both the DLM and the CFD mesh have been divided into a series of strips along the span. An example of the application of this method is shown for the FFAST right wing model in Figure 5.2. In this case a total of 10 strips have been considered along the wing.

The integrated loads computed from the CFD analysis, for each strip, become the target loads

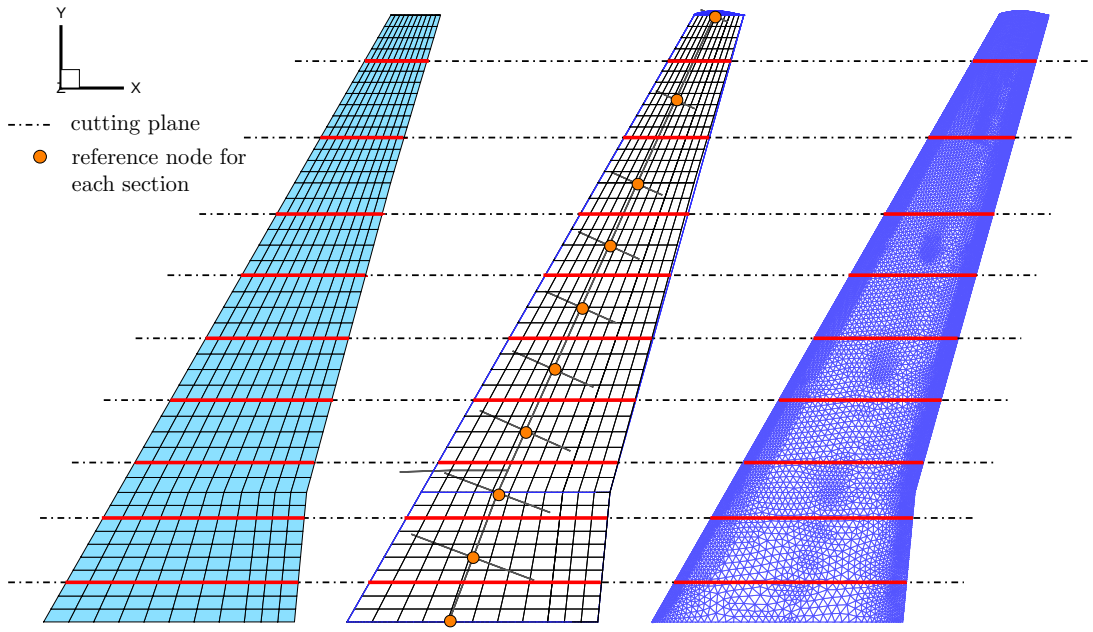

(a) DLM panel model (b) FEM model (c) CFD model

Figure 5.2: Comparison of DLM and CFD mesh, showing the sectional cutting planes and structural nodes along the wing aperture, used as reference points in the moment calculations.

that the low fidelity method should be able to predict. These are obtained integrating the c_p distribution on the wing section considered and specifying a reference point for each strip for the resulting moments calculation. For the DLM data the integrated loads for each strip have been calculated using the "monitor points" functionality available in MSC Nastran. These consist of interpolating matrices which allow the evaluation of the integral loads acting on a list of panels defined by the user. Choosing an appropriate subdivision of the panels (to match the strip definition), it has been possible to obtain the reference aerodynamic loads to compare with the reference data.

5.2 AIC Correction for steady aeroelasticity

The steady aeroelastic integrated loads computed from the baseline doublet-lattice method [116], and introduced in Chapter 2, can be expressed as:

$$\mathbf{F}_a^{DLM_S} = \bar{q}\mathbf{G}_{kr}^T\mathbf{S}_{kj}\mathbf{A}_{jj}^{-1}\mathbf{w}_j^{DLM} \tag{5.1}$$

where $\mathbf{G}_{kr}^{T}$ is the integration matrix over the aerodynamic monitor points discussed in the previous section. A new set is introduced here:

- *r-set*: is the set of the monitor points degree of freedom.

Since the DLM is based on a flat panel mesh, which does not account for the effects of camber or thickness, it produces a null aerodynamic force for an angle of attack equal to 0°. However, it is possible to define a corrected DLM by: introducing a post multiplying diagonal matrix $\mathbf{W}_{jj}^{w}$ of correction coefficients, and adding a second term which accounts for the aerodynamic forces at zero angle of attack. At this point it is possible to write:

$$\widehat{\mathbf{F}}_{a}^{DLM_S} = \bar{q}\mathbf{G}_{kr}^{T}\mathbf{S}_{kj}\mathbf{A}_{jj}^{-1}\ \mathbf{W}_{jj}^{w}\mathbf{w}_{j}^{DLM} + \bar{q}\mathbf{G}_{kr}^{T}\mathbf{S}_{kj}\mathbf{F}_{j}^{e} \tag{5.2}$$

where the second term on the right hand side of the equation takes into consideration the α_0 contribution by means of the matrix $\mathbf{F}_{j}^{e}$.

The aim of the correction approach proposed is to match the reference integrated steady aerodynamic loads acting on the structural nodes, that for the present work are computed by means of CFD simulations:

$$\mathbf{F}_{a}^{CFD_S} = \widehat{\mathbf{F}}_{a}^{DLM_S} \tag{5.3}$$

Thus:

$$\mathbf{F}_{a}^{CFD_S} = \bar{q}\mathbf{G}_{kr}^{T}\mathbf{S}_{kj}\mathbf{A}_{jj}^{-1}\ \mathbf{W}_{jj}^{w}\mathbf{w}_{j}^{DLM} + \bar{q}\mathbf{G}_{kr}^{T}\mathbf{S}_{kj}\mathbf{F}_{j}^{e} \tag{5.4}$$

The correction process aims to find the matrices $\mathbf{W}_{jj}^{w}$ and $\mathbf{F}_{j}^{e}$ such that the sectional loads computed with the DLM method match the CFD loads. The pair of matrices that can be used to correct the DLM are not unique. Therefore the idea is to find two matrices that also minimise the change to the DLM solution. The aim is to find a $\mathbf{F}_{j}^{e}$ as close as possible to zero and a matrix $\mathbf{W}_{jj}^{w}$ as close to the identity matrix as possible. This means minimising the weighted sum of the square of the deviations, where the deviation $\mathbf{W}_{jj}^{w}$ is defined as the difference between the correction factor and unity

$$\mathbf{W}_{jj}^{w} = \begin{bmatrix} \ddots & & \\ & \mathbf{I} + \boldsymbol{\epsilon}^{w} & \\ & & \ddots \end{bmatrix} \tag{5.5}$$

This leads to an under determined problem, with two unknowns to be minimised:

$$\mathbf{F}_a^{CFD_S} = \bar{q}\mathbf{G}_{kr}^T\mathbf{S}_{kj}\mathbf{A}_{jj}^{-1}\lceil\mathbf{I}+\boldsymbol{\epsilon}^w\rfloor\mathbf{w}_j^{DLM} + \bar{q}\mathbf{G}_{kr}^T\mathbf{S}_{kj}\mathbf{F}_j^e \tag{5.6}$$

The previous equation can be rewritten as follows:

$$\mathbf{F}_a^{CFD_S} = \bar{q}\mathbf{G}_{kr}^T\mathbf{S}_{kj}\mathbf{A}_{jj}^{-1}\mathbf{I}\mathbf{w}_j^{DLM} + \bar{q}\mathbf{G}_{kr}^T\mathbf{S}_{kj}\mathbf{A}_{jj}^{-1}\boldsymbol{\epsilon}^w\mathbf{w}^{DLM} + \bar{q}\mathbf{G}_{kr}^T\mathbf{S}_{kj}\mathbf{F}_j^e \tag{5.7}$$

where the first term on the right hand side is the uncorrected DLM:

$$\mathbf{F}_a^{CFD_S} = \mathbf{F}_a^{DLM_S} + \bar{q}\mathbf{G}_{kr}^T\mathbf{S}_{kj}\mathbf{A}_{jj}^{-1}\boldsymbol{\epsilon}^w\mathbf{w}^{DLM} + \bar{q}\mathbf{G}_{kr}^T\mathbf{S}_{kj}\mathbf{F}_j^e \tag{5.8}$$

So defining a delta between the CFD and DLM strip loads:

$$\Delta\mathbf{F}_a^S = \mathbf{F}_a^{CFD_S} - \mathbf{F}_a^{DLM_S} \tag{5.9}$$

$$\Delta\mathbf{F}_a^S = \bar{q}\mathbf{G}_{kr}^T\mathbf{S}_{kj}\mathbf{A}_{jj}^{-1}\boldsymbol{\epsilon}^w\mathbf{w}_j^{DLM} + \bar{q}\mathbf{G}_{kr}^T\mathbf{S}_{kj}\mathbf{F}_j^e \tag{5.10}$$

This under determined problem will be solved using a least squares approach. However, it is necessary to calculate the DLM downwash. Introduced in Eq. (2.30), it can be specialised for a static trim analysis considering two contributions:

$$\mathbf{w}_j^{DLM} = \mathbf{D}_{jk}\mathbf{G}_{ka}\mathbf{u}_a + \mathbf{D}_{jx}\mathbf{u}_x \tag{5.11}$$

The first term on the right hand side of Eq. (5.11) is due to the presence of the structural deformation, while the second is related to the presence of the unity displacement of the aeroelastic extra point. Substituting Eq. (5.11) in Eq. (5.2) it is possible to write the corrected DLM contribution as:

$$\widehat{\mathbf{F}}_a^{DLM_S} = \bar{q}\mathbf{G}_{kr}^T\mathbf{S}_{kj}\mathbf{A}_{jj}^{-1}\ \mathbf{W}_{jj}^w\mathbf{D}_{jk}\mathbf{G}_{ka}\mathbf{u}_a + \bar{q}\mathbf{G}_{kr}^T\mathbf{S}_{kj}\mathbf{A}_{jj}^{-1}\ \mathbf{W}_{jj}^w\mathbf{D}_{jx}\mathbf{u}_x + \bar{q}\mathbf{G}_{kr}^T\mathbf{S}_{kj}\mathbf{F}_j^e \tag{5.12}$$

From Eq. (5.12) it is possible to decompose the expression for the aerodynamic forces into

those for a rigid aeroelastic system:

$$\widehat{\mathbf{F}}_{a_R}^{DLM_S} = \bar{q}\mathbf{G}_{kr}^T\mathbf{S}_{kj}\mathbf{A}_{jj}^{-1}\mathbf{W}_{jj}^w\mathbf{D}_{jx}\mathbf{u}_x + \bar{q}\mathbf{G}_{kr}^T\mathbf{S}_{kj}\mathbf{F}_j^e \tag{5.13}$$

and the contribution of the elastic increment:

$$\widehat{\mathbf{F}}_{a_E}^{DLM_S} = \bar{q}\mathbf{G}_{kr}^T\mathbf{S}_{kj}\mathbf{A}_{jj}^{-1}\mathbf{W}_{jj}^w\mathbf{D}_{jk}\mathbf{G}_{ka}\mathbf{u}_a \tag{5.14}$$

In order to compute the correction coefficients, $\boldsymbol{\epsilon}^w$, and the zero angle of attack contribution, $\mathbf{F}_j^e$, it is necessary to solve Eq. (5.10) for two reference conditions. Typically the aeroelastic deformation at trim in a cruise condition is the result of an aerodynamic optimization, and is a known value. In this case the steady correction will target that specific configuration and the displacement vector is assigned. In the present work the flight shape of the wing is not known, for this reason a first correction step will consider just the rigid aerodynamic forces. From this the elastic deformation will be computed and an additional step will be necessary to converge to the aeroelastic deformation. Considering a wing clamped at the root, without any control surfaces, the only aeroelastic extra point is the angle of attack:

$$\mathbf{u}_x = \{\alpha\} \tag{5.15}$$

At this point Eq. (5.10) can be solved for two flight conditions at different angles of attack: the first considering an angle of attack of $0°$, and the second at the flight incidence of the reference condition at which the loads are required. This allows the following system of equations to be written as:

$$\Delta\mathbf{F}_a^{S_1} = \bar{q}\mathbf{G}_{kr}^T\mathbf{S}_{kj}\mathbf{A}_{jj}^{-1}\boldsymbol{\epsilon}^w\mathbf{D}_{jx}\mathbf{u}_x^1 + \bar{q}\mathbf{G}_{kr}^T\mathbf{S}_{kj}\mathbf{F}_j^e \tag{5.16}$$

$$\Delta\mathbf{F}_a^{S_2} = \bar{q}\mathbf{G}_{kr}^T\mathbf{S}_{kj}\mathbf{A}_{jj}^{-1}\boldsymbol{\epsilon}^w\mathbf{D}_{jx}\mathbf{u}_x^2 + \bar{q}\mathbf{G}_{kr}^T\mathbf{S}_{kj}\mathbf{F}_j^e \tag{5.17}$$

which can be written in a matrix format and solved in a least square sense:

$$\begin{Bmatrix}\Delta\mathbf{F}_a^{S_1}\\ \Delta\mathbf{F}_a^{S_2}\end{Bmatrix} = \begin{bmatrix}\bar{q}\mathbf{G}_{kr}^T\mathbf{S}_{kj}\mathbf{A}_{jj}^{-1}\mathbf{D}_{jx}\mathbf{u}_x^1 & \bar{q}\mathbf{G}_{kr}^T\mathbf{S}_{kj}\\ \bar{q}\mathbf{G}_{kr}^T\mathbf{S}_{kj}\mathbf{A}_{jj}^{-1}\mathbf{D}_{jx}\mathbf{u}_x^2 & \bar{q}\mathbf{G}_{kr}^T\mathbf{S}_{kj}\end{bmatrix}\begin{Bmatrix}\boldsymbol{\epsilon}^w\\ \mathbf{F}_j^e\end{Bmatrix} \tag{5.18}$$

The solution of the minimization problem allows the computation of the rigid and elastic aero-

dynamic integrated loads computed by the corrected DLM using Eq. (5.13) and Eq. (5.14).

5.3 AIC Correction for Gust Response Analysis

The aeroelastic frequency response analysis in modal coordinates, as implemented in the MSC Nastran solver, and introduced in Eq. (2.52), is based on the solution of the following equation:

$$\left[-\omega^2\mathbf{M}_{hh} + i\omega\mathbf{B}_{hh} + (1+ig)\,\mathbf{K}_{hh}\right]\mathbf{u}_h = \bar{q}w_g\mathbf{P}_P(\omega)\mathbf{Q}_{hj}(M,i\kappa)\mathbf{w}_j(\omega) + \bar{q}\mathbf{Q}_{hh}(M,i\kappa)\mathbf{u}_h \tag{5.19}$$

where the two terms at the right hand side of the equation account for the aerodynamic loads. The first gives the aeroloads due to a gust disturbance:

$$\mathbf{Q}_{hj}(M,i\kappa) = \boldsymbol{\phi}_{ah}^T\mathbf{G}_{ka}^T\mathbf{S}_{kj}\;\mathbf{A}_{jj}^{-1} \tag{5.20}$$

and the second, those aeroloads due to a structural deformation:

$$\mathbf{Q}_{hh}(M,i\kappa) = \boldsymbol{\phi}_{ah}^T\mathbf{G}_{ka}^T\mathbf{S}_{kj}\;\mathbf{A}_{jj}^{-1}\;\mathbf{D}_{jk}\mathbf{G}_{ka}\boldsymbol{\phi}_{ah} \tag{5.21}$$

These two contributions are linearly added to evaluate the total aerodynamic load. For this reason, the presented correction method first corrects the rigid gust loads and then the aerodynamic load obtained from a mode shape deformation.

5.3.1 AIC Correction using Sinusoidal Gusts

The aim of this correction approach is to match the integrated aerodynamic loads acting on the structural nodes computed from the CFD code for a sinusoidal gust shape. Following a similar process as seen in the previous section it is possible to write:

$$\mathbf{F}_a^{CFD_G} = \widehat{\mathbf{F}}_a^{DLM_G} \tag{5.22}$$

where the right hand side term, introduced in Eq. (2.50), can be expanded, for the corrected Doublet-Lattice Method [116], as follows:

$$\mathbf{F}_a^{CFD_G} = \bar{q} w_g \mathbf{P}_P(\omega) \mathbf{G}_{kr}^T \mathbf{S}_{kj} \, \mathbf{A}_{jj}^{-1} \mathbf{W}_{jj}^w \mathbf{w}_j(\omega) \tag{5.23}$$

where w_g is the gust scaling factor, $\mathbf{P}_P(\omega)$ is the Fourier transform of the time domain gust disturbance defined by the user and $\mathbf{w}_j$ is the downwash vector. This last term is defined as follows:

$$\mathbf{w}_j(\omega_i) = \cos\gamma_j e^{-i\omega_i(x_j - x_0)/U_\infty} \qquad \text{with } i = 1, \cdots, N_f \tag{5.24}$$

where ω_i is the excitation frequency, or gust frequency, γ_j is the dihedral angle of the j-th aerodynamic element, x_j is the x-location of the j-th aerodynamic element in the aerodynamic coordinate system and x_0 is the reference coordinate for the gust. Defining the generalised aerodynamic influence coefficient matrix relating the downwash to the aerodynamic loads on the monitor points, which correspond to the CFD strips being matched:

$$\mathbf{Q}_{ARJ}^T = \mathbf{G}_{kr}^T \mathbf{S}_{kj} \, \mathbf{A}_{jj}^{-1} \tag{5.25}$$

it is possible to rewrite

$$\mathbf{F}_a^{CFD_G} = \bar{q} w_g \mathbf{P}_P(\omega) \mathbf{Q}_{ARJ}^T \mathbf{W}_{jj}^w \mathbf{w}_j(\omega) \tag{5.26}$$

Considering a time gust disturbance with a sinusoidal shape, the Fourier Transform is a vector with only one non zero component, corresponding to the frequency of the input signal. Expanding Eq. (5.26) for a single frequency, it is a possible to write:

$$\mathbf{F}_a^{CFD_G} = \bar{q} w_g \mathbf{Q}_{ARJ}^T \mathbf{W}_{jj}^w \bar{\mathbf{w}}_j^G \tag{5.27}$$

Considering a diagonal correction matrix, as in Eq. (5.5), Eq. (5.27) can be written as:

$$\mathbf{F}_a^{CFD_G} = \mathbf{F}_a^{DLM_G} + \bar{q} w_g \mathbf{Q}_{ARJ}^T \begin{bmatrix} \ddots & & \\ & \boldsymbol{\epsilon}^w & \\ & & \ddots \end{bmatrix} \bar{\mathbf{w}}_j^G \tag{5.28}$$

so that it is possible to express the change in aerodynamic loads as:

$$\Delta\mathbf{F}_a^G = \bar{q} w_g \mathbf{Q}_{ARJ}^T \begin{bmatrix} \ddots & & \\ & \bar{\mathbf{w}}_j^G & \\ & & \ddots \end{bmatrix} \{\boldsymbol{\epsilon}^w\} \tag{5.29}$$

and with the introduction of the following matrix:

$$\mathbf{Q}_P = w_g \mathbf{Q}_{ARJ}^T \begin{bmatrix} \ddots & & \\ & \bar{\mathbf{w}}_j^G & \\ & & \ddots \end{bmatrix} \tag{5.30}$$

this becomes

$$\Delta\mathbf{F}_a^G = \bar{q}\mathbf{Q}_P\{\boldsymbol{\epsilon}^w\} \tag{5.31}$$

All the matrices and vectors in Eq. (5.31) are complex, so it possible to rewrite it as explicitly complex:

$$\Re(\Delta\mathbf{F}_a^G) + i\Im(\Delta\mathbf{F}_a^G) = \bar{q}[\Re(\mathbf{Q}_P) + i\Im(\mathbf{Q}_P)]\{\Re(\boldsymbol{\epsilon}^w) + i\Im(\boldsymbol{\epsilon}^w)\} \tag{5.32}$$

Using the following notation:

$$\begin{aligned} \Re(\Delta\mathbf{F}_a^G) &= \Delta\mathbf{F}_a{}^{RG} \\ \Im(\Delta\mathbf{F}_a^G) &= \Delta\mathbf{F}_a{}^{IG} \\ \Re(\mathbf{Q}_P) &= \mathbf{Q}_P{}^R \\ \Im(\mathbf{Q}_P) &= \mathbf{Q}_P{}^I \\ \Re(\boldsymbol{\epsilon}^w) &= \boldsymbol{\epsilon}^R \\ \Im(\boldsymbol{\epsilon}^w) &= \boldsymbol{\epsilon}^I \end{aligned} \tag{5.33}$$

it is possible to write Eq. (5.32) as:

$$\begin{aligned} \Delta\mathbf{F}_a^{RG} + i\Delta\mathbf{F}_a^{IG} &= \bar{q}\Big(\mathbf{Q}_P{}^R + i\mathbf{Q}_P{}^I\Big)\Big(\boldsymbol{\epsilon}^R + i\boldsymbol{\epsilon}^I\Big) \\ &= \bar{q}\Big(\mathbf{Q}_P{}^R\boldsymbol{\epsilon}^R + i\mathbf{Q}_P{}^R\boldsymbol{\epsilon}^I + i\mathbf{Q}_P{}^I\boldsymbol{\epsilon}^R - \mathbf{Q}_P{}^I\boldsymbol{\epsilon}^I\Big) \end{aligned} \tag{5.34}$$

and writing it in a purely real matrix format, it is possible to obtain:

$$\begin{Bmatrix} \Delta\mathbf{F}_a^{RG} \\ \Delta\mathbf{F}_a^{IG} \end{Bmatrix} = \bar{q} \begin{bmatrix} \mathbf{Q}_P{}^R & -\mathbf{Q}_P{}^I \\ \mathbf{Q}_P{}^I & \mathbf{Q}_P{}^R \end{bmatrix} \begin{Bmatrix} \boldsymbol{\epsilon}^R \\ \boldsymbol{\epsilon}^I \end{Bmatrix} \tag{5.35}$$

Solving in a least square sense it is possible to determine the correction factors and obtain the correction matrix for each reduced frequency.

5.3.2 Weighted Correction Method

It is possible to use a weighting in the least square solution of Eq. (5.35). As a first approach, it has been decided to use the uncorrected AIC matrix as the weight, as previously described by Rodden in [33]. Introducing a new variable:

$$\boldsymbol{\epsilon} = \mathbf{W}^{\epsilon}\,\widehat{\boldsymbol{\epsilon}} \tag{5.36}$$

where the matrix $\mathbf{W}^{\epsilon}$ is defined as

$$\mathbf{W}^{\epsilon} = \begin{bmatrix} \mathbf{W}^{\epsilon R} & 0 \\ 0 & \mathbf{W}^{\epsilon I} \end{bmatrix} \tag{5.37}$$

where $\mathbf{W}^{\epsilon^R}$ and $\mathbf{W}^{\epsilon^I}$ are the real and imaginary weightings given by

$$\mathbf{W}^{\epsilon R} = \begin{bmatrix} \ddots & & \\ & |\mathbf{A}_{jj}^{-1^R}\,\mathbf{I}| & \\ & & \ddots \end{bmatrix} \qquad \mathbf{W}^{\epsilon I} = \begin{bmatrix} \ddots & & \\ & |\mathbf{A}_{jj}^{-1^I}\,\mathbf{I}| & \\ & & \ddots \end{bmatrix} \tag{5.38}$$

and $\mathbf{I}$ is a vector of ones. Substituting Eq. (5.36) and Eq. (5.37) in Eq. (5.35), the new system to solve, written in real matrix form, becomes:

$$\begin{Bmatrix} \Delta\mathbf{F}_a^{R^G} \\ \Delta\mathbf{F}_a^{I^G} \end{Bmatrix} = \bar{q} \begin{bmatrix} \mathbf{Q}_P{}^R & -\mathbf{Q}_P{}^I \\ \mathbf{Q}_P{}^I & \mathbf{Q}_P{}^R \end{bmatrix} \begin{bmatrix} \mathbf{W}^{\epsilon R} & 0 \\ 0 & \mathbf{W}^{\epsilon I} \end{bmatrix} \begin{Bmatrix} \widehat{\boldsymbol{\epsilon}}^R \\ \widehat{\boldsymbol{\epsilon}}^I \end{Bmatrix} \tag{5.39}$$

5.3.3 AIC Correction using Harmonic Mode Shapes

The aerodynamic strip loads due to an harmonic mode deformation of the structure, in the frequency domain, calculated using the DLM can be expressed as

$$\mathbf{F}_a^{DLM_{MS}} = \bar{q}\mathbf{G}_{kr}^T\mathbf{S}_{kj}\ \mathbf{A}_{jj}^{-1}\mathbf{w}_{ja}^{MS} \tag{5.40}$$

where the downwash due to the mode shape deformation is given by:

$$\mathbf{w}_{ja}^{MS} = (\mathbf{D}_{jk}^1 + i\kappa\mathbf{D}_{jk}^2)\mathbf{G}_{ka}^T\tilde{\mathbf{u}}_a \tag{5.41}$$

For Eq. (5.41) $\tilde{\mathbf{u}}_a$ is the Fourier transform of the structural mode deformation time history, given by the product of the modal amplitude and a vector defining the time history of the harmonic shape variation:

$$\tilde{\mathbf{u}}_a = \mathcal{F}(\mathbf{u}_a(t)) \tag{5.42}$$

Using the same approach as previously used for the gust correction we can introduce a correction matrix to match the mode shape loads calculated with CFD, leading to the equation:

$$\mathbf{F}_a^{CFD_{MS}} = \bar{q}\mathbf{G}_{kr}^T\mathbf{S}_{kj}\ \mathbf{A}_{jj}^{-1}\mathbf{W}_{jj}^w\mathbf{w}_{ja}^{MS} \tag{5.43}$$

Using Eq. (5.25) it is possible to rewrite Eq. (5.43) as:

$$\mathbf{F}_a^{CFD_{MS}} = \bar{q}\mathbf{Q}_{ARJ}^T\mathbf{W}_{jj}^w\mathbf{w}_{ja}^{MS} \tag{5.44}$$

and using the same diagonal definition for $\mathbf{W}_{jj}^w$ as Eq. (5.5), the increment in aerodynamic loads can be expressed as:

$$\Delta\mathbf{F}_a^{MS} = \bar{q}\mathbf{Q}_{ARJ}^T\begin{bmatrix}\ddots & & \\ & \boldsymbol{\epsilon}^w & \\ & & \ddots\end{bmatrix}\{\mathbf{w}_{ja}^{MS}\} = \bar{q}\mathbf{Q}_{ARJ}^T\begin{bmatrix}\ddots & & \\ & \mathbf{w}_{ja}^{MS} & \\ & & \ddots\end{bmatrix}\{\boldsymbol{\epsilon}^w\}. \tag{5.45}$$

Introducing the matrix:

$$\mathbf{Q}_W = \mathbf{Q}_{ARJ}^T \begin{bmatrix} \ddots & & \\ & \mathbf{w}_{ja}^{MS} & \\ & & \ddots \end{bmatrix} \tag{5.46}$$

it is possible to write:

$$\Delta\mathbf{F}_a^{MS} = \bar{q}\mathbf{Q}_W\{\boldsymbol{\epsilon}^w\} \tag{5.47}$$

Proceeding in an analogous way to that presented in Eq.(5.32), and introducing the notation:

$$\begin{aligned} \Re(\mathbf{Q}_W) &= \mathbf{Q}_W{}^R \\ \Im(\mathbf{Q}_W) &= \mathbf{Q}_W{}^I \end{aligned} \tag{5.48}$$

$$\Delta\mathbf{F}_a^{R^{MS}} + i\Delta\mathbf{F}_a^{I^{MS}} = \bar{q}\Big(\mathbf{Q}_W{}^R\boldsymbol{\epsilon}^R + i\mathbf{Q}_W{}^R\boldsymbol{\epsilon}^I + i\mathbf{Q}_W{}^I\boldsymbol{\epsilon}^R - \mathbf{Q}_W{}^I\boldsymbol{\epsilon}^I\Big) \tag{5.49}$$

gives the real matrix equation:

$$\begin{Bmatrix} \Delta\mathbf{F}_a^{R^{MS}} \\ \Delta\mathbf{F}_a^{I^{MS}} \end{Bmatrix} = \bar{q} \begin{bmatrix} \mathbf{Q}_W{}^R & -\mathbf{Q}_W{}^I \\ \mathbf{Q}_W{}^I & \mathbf{Q}_W{}^R \end{bmatrix} \begin{Bmatrix} \boldsymbol{\epsilon}^R \\ \boldsymbol{\epsilon}^I \end{Bmatrix} \tag{5.50}$$

In this case only one mode has been considered, but the system can be extended to multiple mode shape deformations. In particular, tests have demonstrated that the best results are obtained when the flexible contribution correction factors are computed considering both the gust and the mode shape deformation:

$$\begin{Bmatrix} \Delta\mathbf{F}_a^{R^G} \\ \Delta\mathbf{F}_a^{I^G} \\ \Delta\mathbf{F}_a^{R^{MS^n}} \\ \Delta\mathbf{F}_a^{I^{MS^n}} \end{Bmatrix} = \bar{q} \begin{bmatrix} \mathbf{Q}_P{}^R & -\mathbf{Q}_P{}^I \\ \mathbf{Q}_P{}^I & \mathbf{Q}_P{}^R \\ \mathbf{Q}_W{}^{R^n} & -\mathbf{Q}_W{}^{I^n} \\ \mathbf{Q}_W{}^{I^n} & \mathbf{Q}_W{}^{R^n} \end{bmatrix} \begin{Bmatrix} \boldsymbol{\epsilon}^R \\ \boldsymbol{\epsilon}^I \end{Bmatrix} \quad with\ \ n = 1, ..., N^{modes} \tag{5.51}$$

In this case no weighting approach has been considered.

CHAPTER 6

DLM Correction Method Application for the FFAST Right Wing model

The doublet-lattice correction method formulated in Chapter 5 is initially applied to the FFAST right wing model. The doublet-lattice method used in this application is the one available in the commercial software MSC Nastran [116]. High fidelity aerodynamic data are computed using the DLR TAU-Code [55], by means of full order time domain (CFD) analysis. Additionally, a comparison with the equivalent loads computed using linearised frequency domain (LFD) [50, 94] is presented. Using full order time domain unsteady CFD analysis to compute the reference aerodynamic loads didn't make this approach efficient from a computational point of view. However, this has been necessary because the LFD for gusts [117, 118] were not available at the time in which this method was developed. They were released as part of the DLR TAU-Code only at the end of this project. Nevertheless, this offered a good opportunity to compare and validate the time linearised approach results versus the time domain aero loads.

The reference aeroelastic simulations are evaluated by means of the fully coupled solution environment AlpesFSI presented in Chapter 4.

Two reference flight conditions are discussed. The first is at a low Mach number, which has no shock on the wing surface. The second is chosen to be representative of a cruise flight condition in the transonic regime.

A first application of the correction method is used to match the aeroelastic static loads at trim. Afterwards the correction method is used to compute the corrected AIC matrices to match the aeroelastic response to a discrete gust of one minus cosine shape.

6.1 Static aeroelastic correction

The aim of the steady correction approach is to match the aeroelastic loads at trim computed using the AlpesFSI interface [19]. Assuming that the trim flight shape is not known in advance, the correction method has been used to match the aerodynamic loads computed in the undeformed jig shape (Flight Shape 1, FS1). The system given in Eq. (5.18) is solved using the steady CFD reference loads computed at two different angle of attack, $0°$ and $2°$. In Figure 6.1 the integrated vertical force and pitching moment over each of the strips defined in Figure 5.2, for the rigid undeformed CFD model at $\alpha = 2°$, are compared to the baseline (BL) and corrected DLM. Since the strips have been defined around each structural node and following the subdivision of the DLM panels, they are characterized by a different width. In particular the first strip is thinner compared to the second strip, and this is the reason for the discontinuity between the values reported in Figure 6.1. In this case the corrected DLM perfectly matches the rigid CFD strip loads.

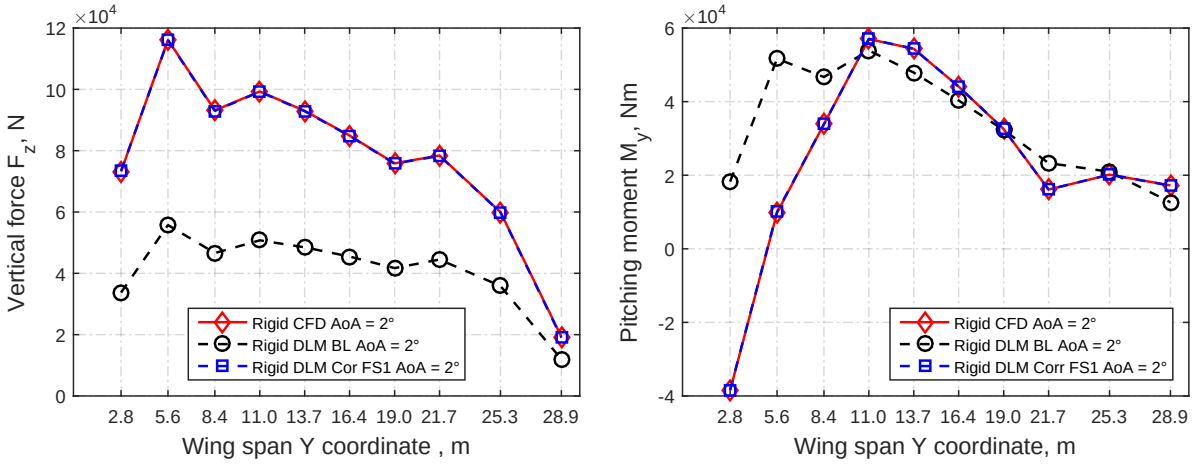

(a) Vertical force, F_z.

(b) Pitching moment, M_y.

Figure 6.1: Rigid strip loads comparison for the undeformed flight shape at $\alpha = 2°$.

However, this initial correction does not give an accurate estimation of the elastic loads at the

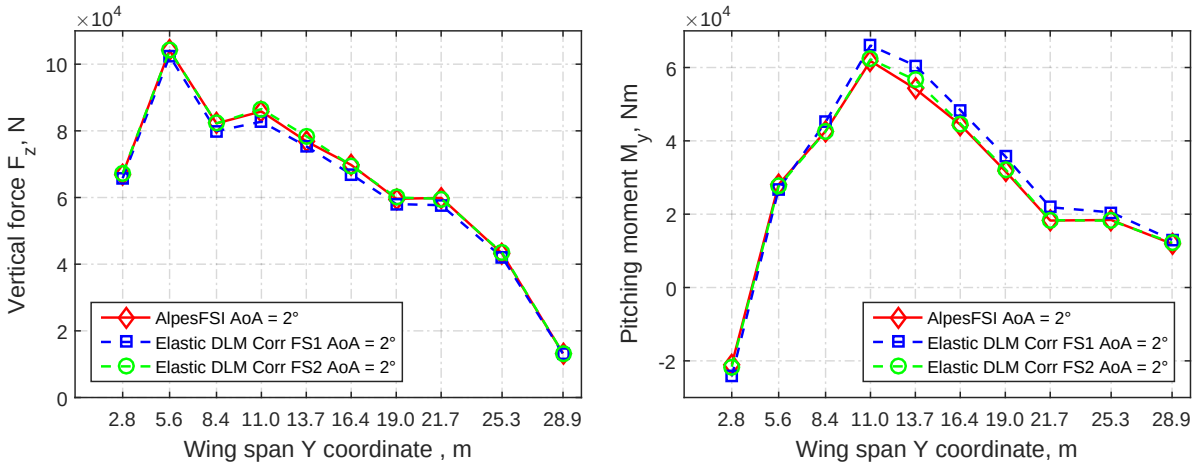

(a) Vertical force, F_z.

(b) Pitching moment, M_y.

Figure 6.2: Aeroelastic strip loads comparison at $\alpha = 2°$.

desired flight condition at $\alpha = 2°$, Figure 6.2. In order to increase the accuracy of the corrected method, a second correction step has been considered: using Eq. (5.10) and computing the strip loads using the CFD deformed at the flight shape computed at the previous step (referenced as Flight Shape 2 or FS2). As shown in Figure 6.2, the corrected DLM for FS2 is very close to the loads computed using the AlpesFSI interface. In case the flight shape is known in advance, only one correction step is sufficient to compute the steady correction. In this case the two sets of reference loads would be obtained by performing a rigid CFD analysis (at two different values of angle of attack) in the flight shape configuration.

6.2 CFD integrated loads in the frequency domain

To compute the gust analysis using the DLM method a range of frequencies from 0 to 30 Hz, has been considered. In this range the FFAST right wing model presents 13 natural modes of vibration, which are shown in Figure 6.3.

Introducing the reduced frequency κ:

$$\kappa = \frac{\omega}{U_\infty} \frac{l_{ref}}{2} \tag{6.1}$$

where l_{ref} is a reference length and U_∞ is the free stream velocity. The AIC matrices have been

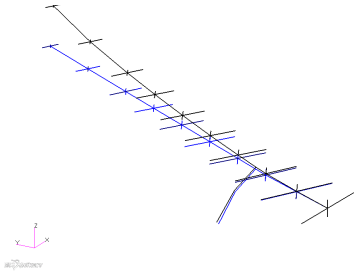

(a) Mode 1 = 1.88 Hz

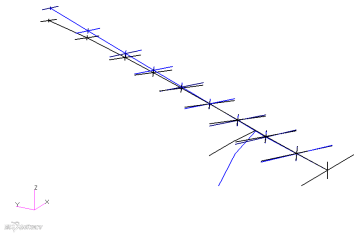

(b) Mode 2 = 2.53 Hz

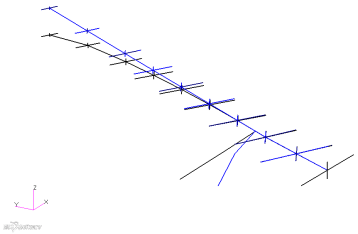

(c) Mode 3 = 2.65 Hz

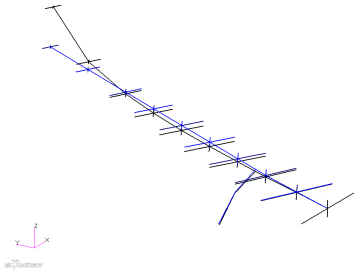

(d) Mode 4 = 4.56 Hz

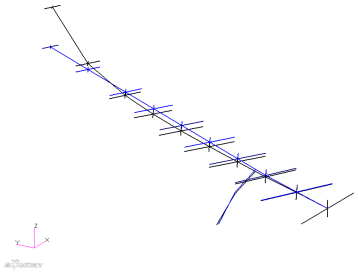

(e) Mode 5 = 4.78 Hz

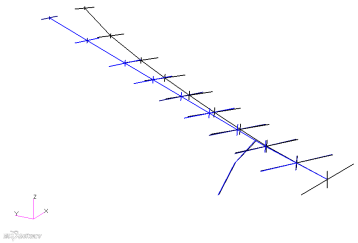

(f) Mode 6 = 6.40 Hz

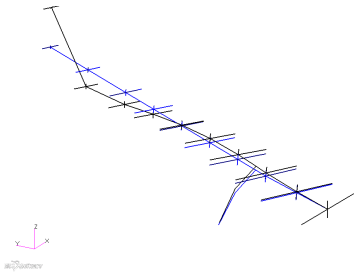

(g) Mode 7 = 8.86 Hz

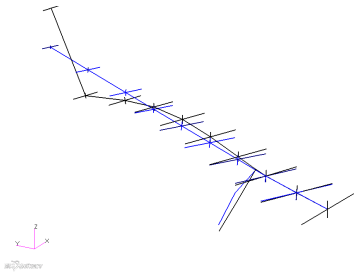

(h) Mode 8 = 11.62 Hz

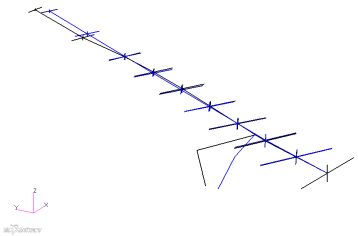

(i) Mode 9 = 13.84 Hz

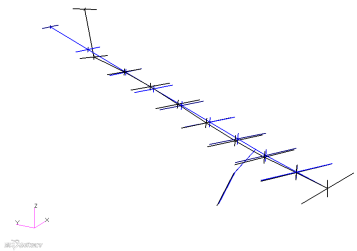

(j) Mode 10 = 15.24 Hz

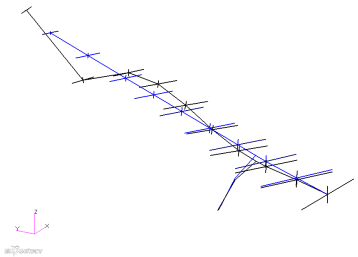

(k) Mode 11 = 16.48 Hz

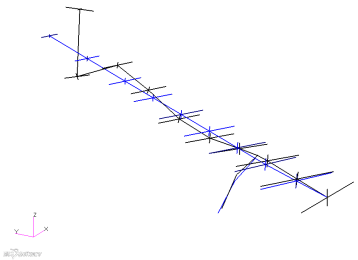

(l) Mode 12 = 26.12 Hz

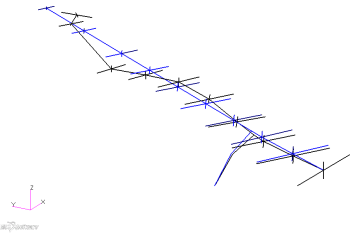

(m) Mode 13 = 29.64 Hz

Figure 6.3: FFAST wing natural mode shapes in the range $0 - 30$ Hz.

evaluated for 25 values of κ in a range between 0.01 and 2.00, as reported in Tleable 6.1.

κ	$f_g\,[Hz]$	$L_g\,[m]$	κ	$f_g\,[Hz]$	$L_g\,[m]$
0.01	0.13	1906.95	0.50	6.58	38.14
0.02	0.26	953.47	0.60	7.89	31.78
0.03	0.39	635.65	0.70	9.21	27.24
0.04	0.53	476.74	0.80	10.52	23.84
0.05	0.66	381.39	0.90	11.84	21.19
0.06	0.79	317.82	1.00	13.15	19.07
0.07	0.92	272.42	1.10	14.47	17.34
0.08	1.05	238.37	1.20	15.78	15.89
0.09	1.18	211.88	1.30	17.10	14.67
0.10	1.32	190.69	1.40	18.41	13.62
0.20	2.63	95.35	1.50	19.73	12.71
0.30	3.95	63.56	2.00	26.30	9.53
0.40	5.26	47.67			

Table 6.1: List of reduced frequency used to perform the gust analysis in the frequency domain, with corresponding gust frequency and gust length.

The correction method has been applied first to compute the correction over the rigid gust aerodynamic loads and then to match the aerodynamic loads due to the mode shape deformation.

6.2.1 Rigid gust correction

To compute the linearised frequency domain loads, the rigid CFD response to a sinusoidal gust input, of amplitude W_g and gust length L_g, has been studied in the DLR TAU-Code, Figure 6.4. To remain in the linear region a small gust amplitude of $1\ m/s$ has been chosen. Introducing

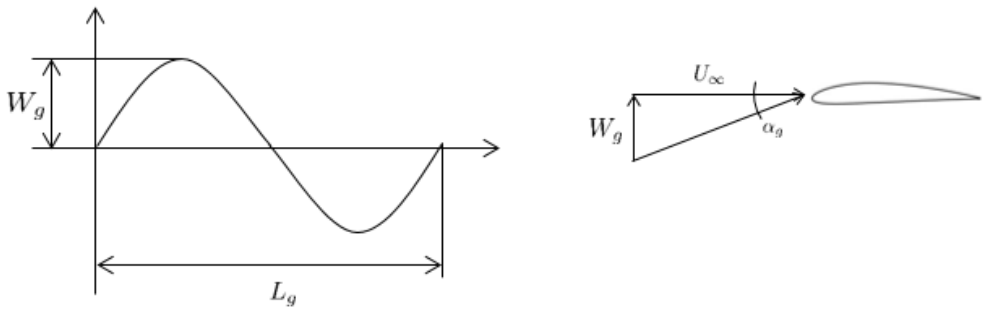

Figure 6.4: Sinusoidal gust shape used to correct the rigid gust loads.

the variation of angle of attack due to a vertical gust as:

$$\alpha_g = \tan^{-1}\left(\frac{W_g}{U_\infty}\right) \tag{6.2}$$

the gust considered for this investigation had an $\alpha_g = 0.25°$. The gust lengths, instead, have been chosen in order to match the desired reduced frequencies, from Eq. (6.1):

$$\kappa = \frac{\omega_g}{U_\infty}\frac{l_{ref}}{2} = \frac{2\pi f_g}{U_\infty}\frac{l_{ref}}{2} \tag{6.3}$$

where f_g is the gust frequency:

$$f_g = \frac{\kappa\, U_\infty}{\pi\, l_{ref}} \tag{6.4}$$

which is related to the gust length:

$$f_g = \frac{U_\infty}{L_g} \implies L_g = \frac{U_\infty}{f_g} \tag{6.5}$$

For each value of reduced frequency reported in Table 6.1, the time history of the integrated loads for the ten strips along the wing has been computed. The input signal has been chosen long enough to reach a stationary harmonic response. At this point a reference period has been selected, and an equivalent periodic signal has been reconstructed, Figure 6.5.

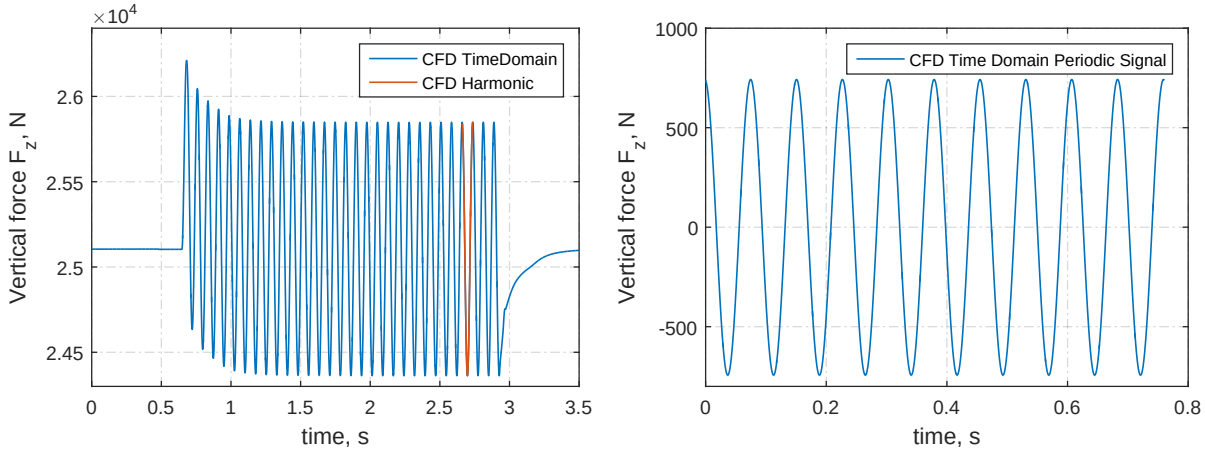

(a) CFD Time Domain Gust Response.

(b) CFD Periodic Signal.

Figure 6.5: Rigid CFD sinusoidal gust response.

From the periodic time domain analysis the frequency equivalent loads have been evaluated us-

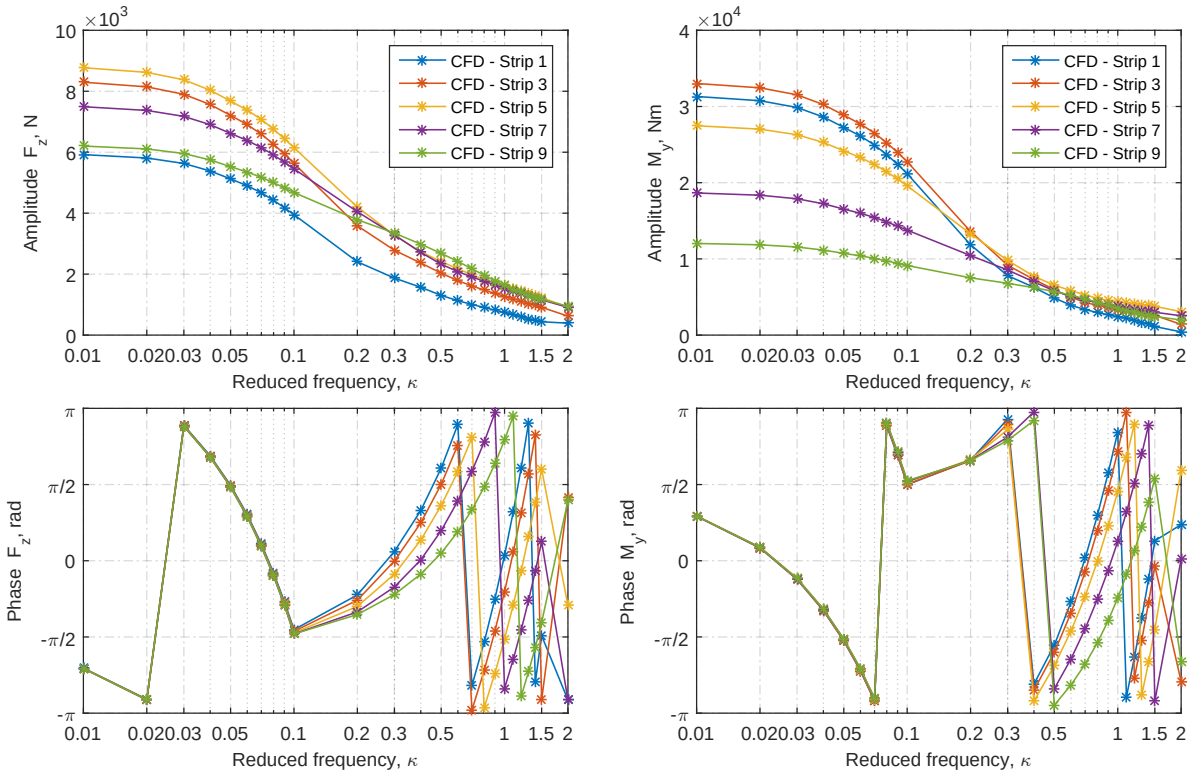

(a) Vertical force, F_z.

(b) Pitching moment, M_y

Figure 6.6: Amplitude and phase comparison versus reduced frequency due to sinusoidal gust encountering for CFD simulation. Vertical force and pitching moment for strip 1, 3, 5, 7 and 9.

ing a Fourier Series. To obtain comparable results to those computed by the DLM implemented in MSC Nastran, the Fourier Series algorithm defined in [116] has been used. In Figure 6.6, amplitude and phase versus the reduced frequency for vertical force and pitching moment is shown for a selection of strips along the wing span. These represent the reference data used to evaluate the rigid gust correction.

The correction factors have been computed solving the system of equations given in Eq. (5.51) for each of the reduced frequencies analysed.

The correction factors distribution over the DLM mesh are reported here for four reference reduced frequency values ($\kappa = 0.01$, $\kappa = 0.10$, $\kappa = 1.00$ and $\kappa = 1.50$) in Figure 6.7. The results for the other frequencies show the same behaviour as these plots.

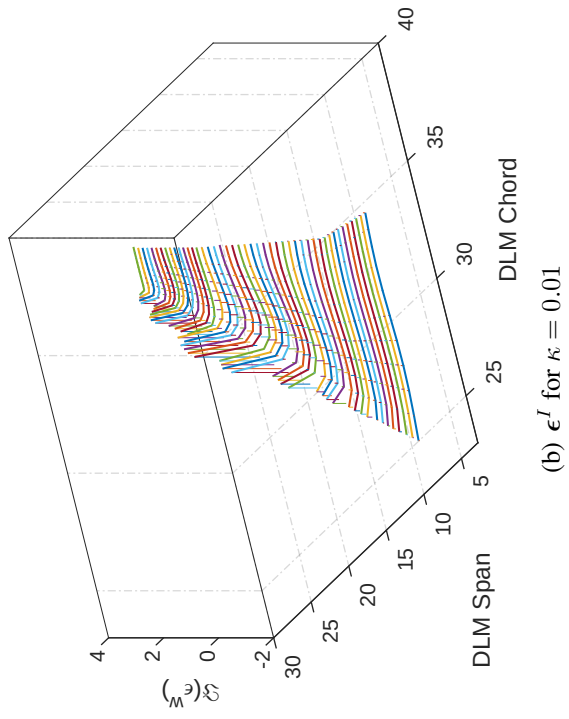

(a) ϵ^R for $\kappa = 0.01$

(b) ϵ^I for $\kappa = 0.01$

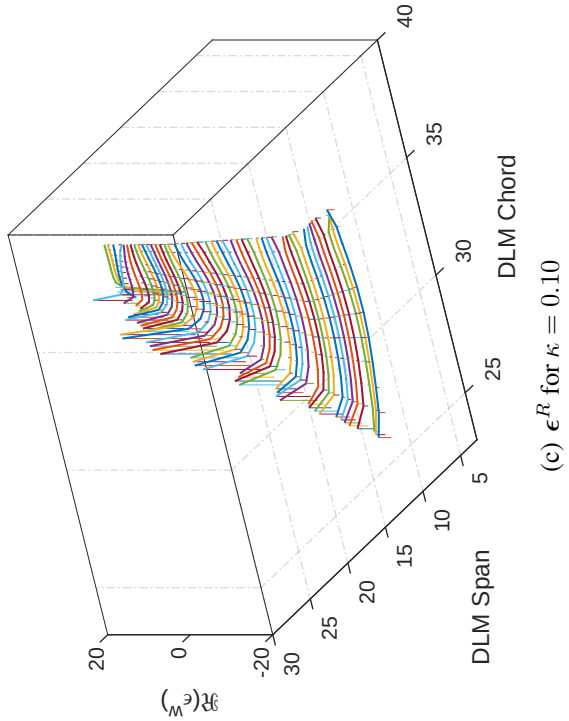

(c) ϵ^R for $\kappa = 0.10$

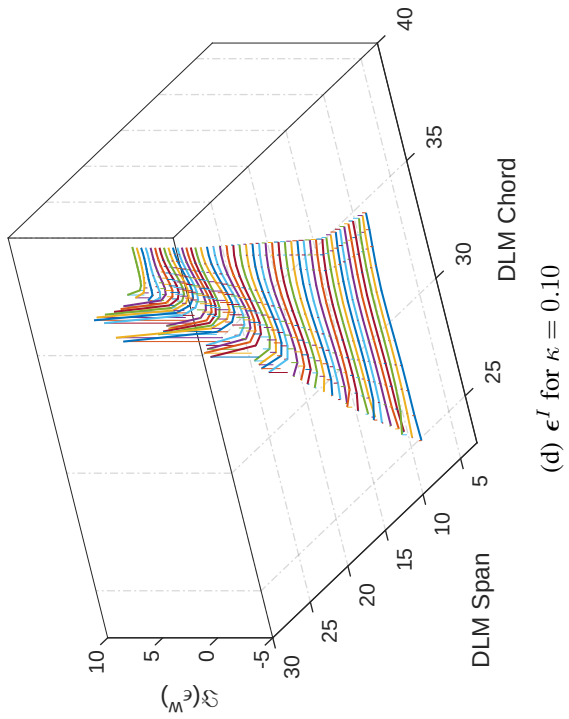

(d) ϵ^I for $\kappa = 0.10$

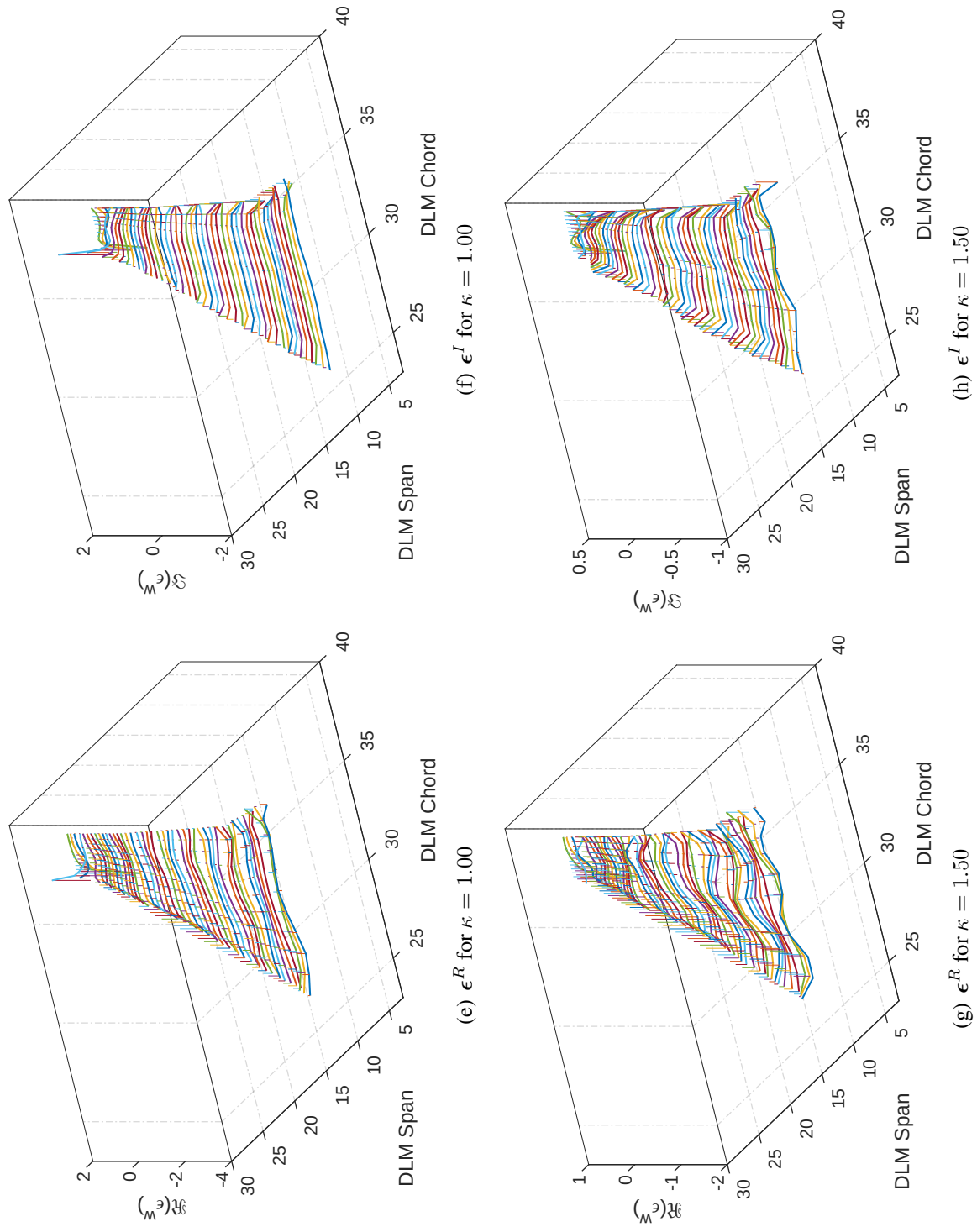

(e) ϵ^R for $\kappa = 1.00$ (f) ϵ^I for $\kappa = 1.00$

(g) ϵ^R for $\kappa = 1.50$ (h) ϵ^I for $\kappa = 1.50$

Figure 6.7: Correction factors distribution over the doublet lattice mesh showing real and imaginary part, for reduced frequency $\kappa = 0.01$, $\kappa = 0.10$, $\kappa = 1.00$ and $\kappa = 1.50$

The correction factors look to be predominant at the leading edge for the lowest reduced frequency of $\kappa = 0.01$ and $\kappa = 0.10$, Figures 6.7(a) to 6.7(d). In these cases the frequency is still quite low and the correction is targeting manly steady effects. The highest correction at the leading edge is related to the presence of effects not well captured by the DLM such as leading edge suction, shock wave location and thickness effects. Considering the higher reduced frequencies, Figure 6.7(e), 6.7(f), the correction starts to involve more the wing tip, probably related to the wing tip vortex. For the reduced frequency of $\kappa = 1.5$ it looks like the correction factors have a quite smooth variation in chordwise direction but the absolute values are lower than the other cases.

6.2.2 Mode shape deformation correction

Two mode shapes have been considered to evaluate the flexible loads contribution. The first wing bending and first wing torsion have been selected as reference flight shapes to be mapped to the fluid mesh surface. The properties of the two modes selected are reported in Table 6.2 and Figure 6.8 depicts the flight shapes mapped over the CFD surface mesh.

Mode number	Mode name	Frequency, Hz
1	1^{st} wing bending	1.88
2	1^{st} wing torsion	2.53

Table 6.2: Wing natural modes used in the correction process.

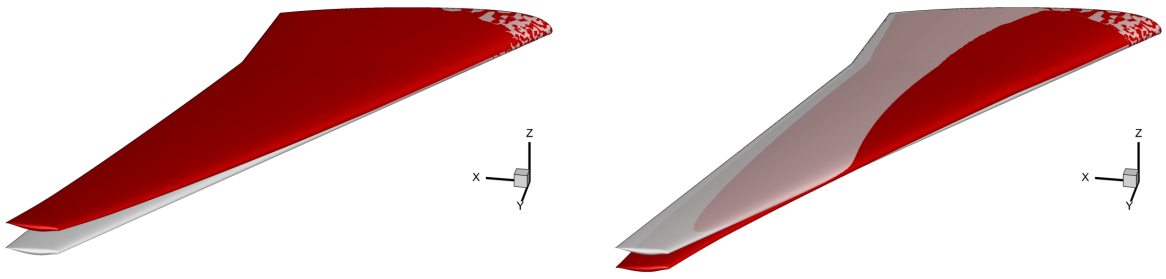

(a) First wing bending. (b) First wing torsion

Figure 6.8: Mode shapes of FFAST wing mapped to CFD surface mesh.

An harmonic sinusoidal mesh deformation has been applied for each of the reduced frequencies reported in Table 6.1. A small amplitude has been considered for the mode deformation: a

maximum displacement at the wing tip of 10 and 5 cm has been considered respectively, for the first and second mode. The aerodynamic integrated loads for each strip along the span have been computed for the listed reduced frequencies. The amplitude and phase versus the reduced frequency of the vertical force and pitching moment for five different strips along the span are reported. Figure 6.9 shows the results for the first mode shape and Figure 6.10 shows results for the second mode shape. These results represent the reference data used to evaluate the mode shape gust correction.

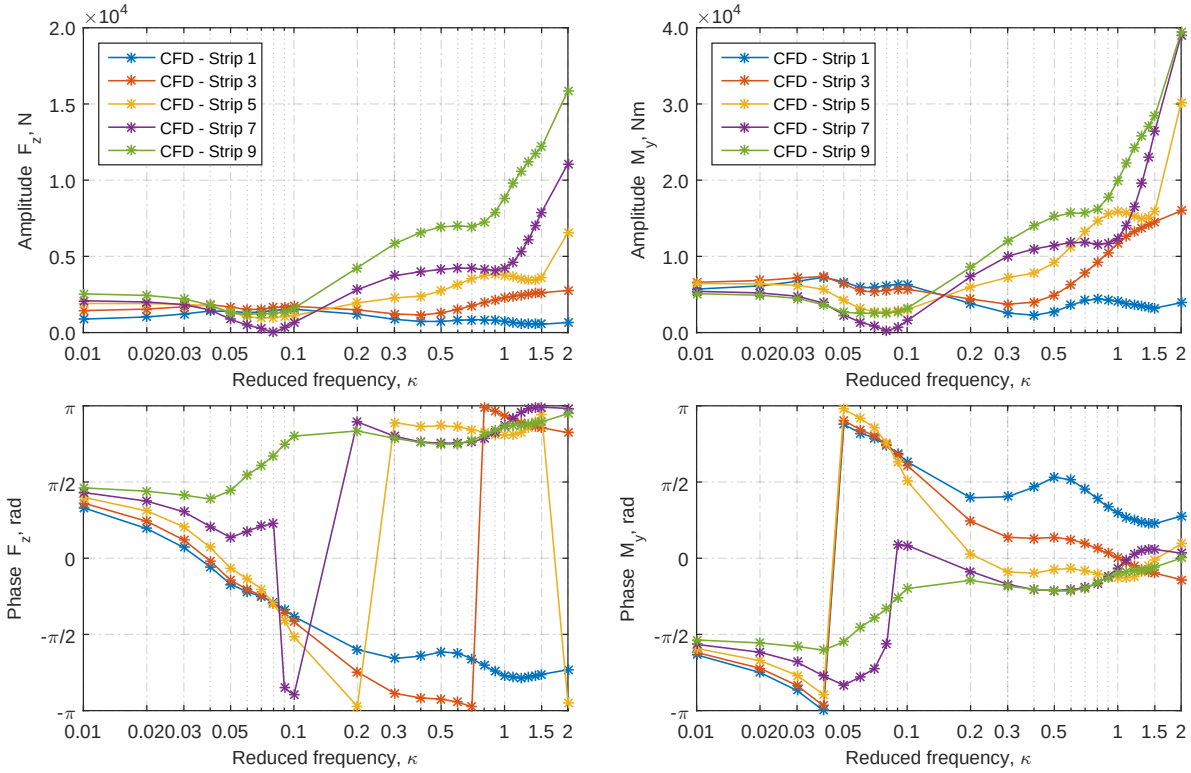

(a) Vertical force, F_z.

(b) Pitching moment, M_y

Figure 6.9: Amplitude and phase comparison versus reduced frequency for first mode shape harmonic motion. Vertical force and pitching moment for strip 1, 3, 5, 7 and 9.

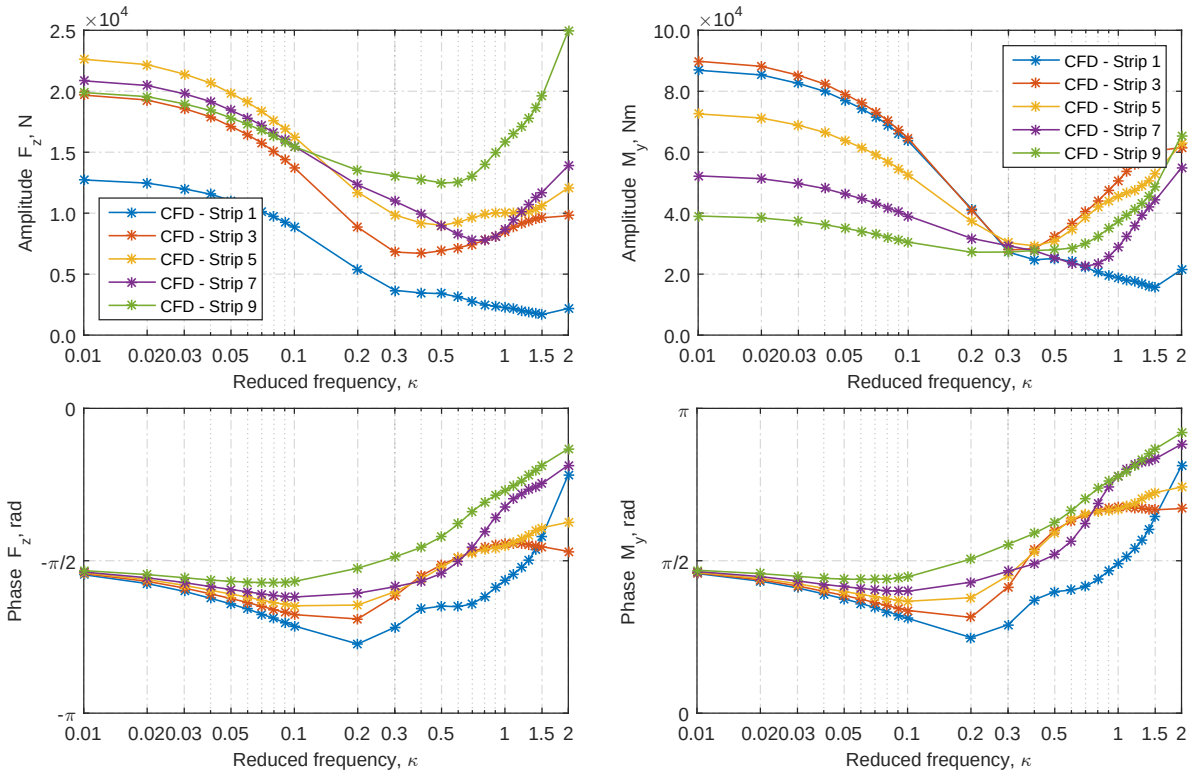

(a) Vertical force, F_z.

(b) Pitching moment, M_y

Figure 6.10: Amplitude and phase comparison versus reduced frequency for second mode shape harmonic motion. Vertical force and pitching moment for strip 1, 3, 5, 7 and 9.

6.3 Discrete Gust Response Analysis

The correction factors computed in the previous sections, have been used to update the AIC matrices computed in the gust response analysis. The corrected AIC matrices evaluated in the pre-processing step have been stored in a ".OP4" format and used to replace the AIC matrices computed by Nastran at run time. From this point, gust analysis can be performed to investigate the response to a typical one minus cosine (1MC) gust velocity profile. The gust shapes considered are those prescribed by the "Certification Specification for Large Aeroplanes CS-25" [9], and described in Eq. 4.17. Five reference gust lengths have been considered and their vertical velocity profiles are shown in Figure 6.11.

Two sets of gusts have been investigated to check the validity of the method for a cruise flight condition at $1g$ and altitude of $11000\ m$, Table 6.3, where $T_g = L_g/U_\infty$.

The first is a low Mach number flight condition, $M = 0.5$. In this situation the flow on the

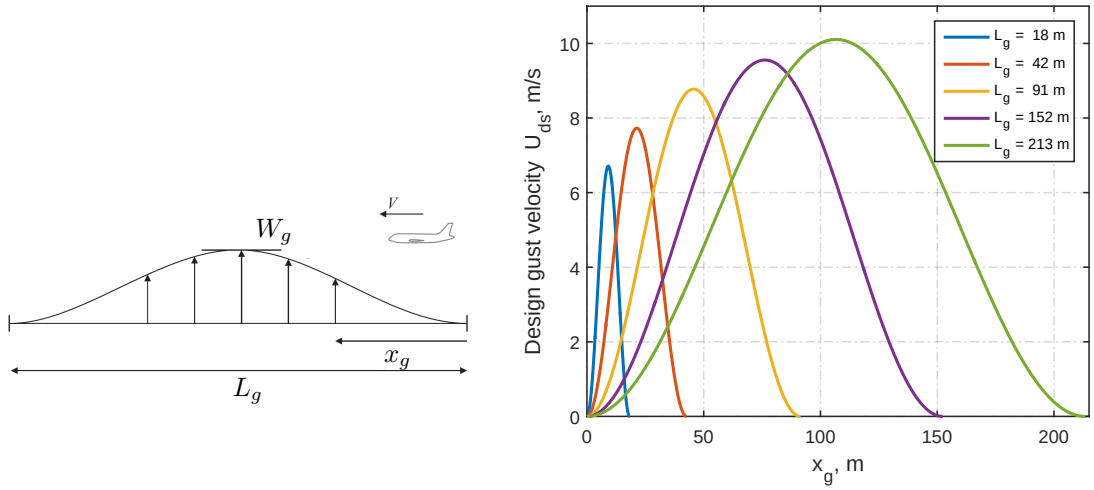

(a) "$1 - \cos$" gust shape [8].

(b) Gust profile analysed.

Figure 6.11: Gust profile.

$AoA,\ deg$	$L_g,\ m$	$W_g^{TAS},\ m/s$	M	$\alpha_g,\ deg$	$T_g,\ s$	M	$\alpha_g,\ deg$	$T_g,\ s$
0.0	18.28	12.29	0.50	4.76	0.124	0.85	2.81	0.073
0.0	42.67	14.15	0.50	5.48	0.289	0.85	3.23	0.170
0.0	91.44	16.07	0.50	6.22	0.620	0.85	3.67	0.365
0.0	152.40	17.50	0.50	6.77	1.033	0.85	3.99	0.608
0.0	213.36	18.51	0.50	7.15	1.446	0.85	4.22	0.851

Table 6.3: One minus cosine gust profiles considered for gust loads response analysis, flight condition at $1g$ and altitude of $11000\ m$.

wing surface is subsonic, as shown in Figure 6.12(a), and it has been verified that no shock forms when the gust reaches the wing. The second case considers a cruise flight condition in the transonic regime, at $M = 0.85$, Figure 6.12(b).

6.3.1 Rigid gust correction

The first step to correct the AIC matrices has been to consider, as reference aerodynamic data, the harmonic loads due to a sinusoidal gust shape and considering the CFD model as rigid. The corrected AIC matrices for each of the reduced frequencies have been used to evaluate the aeroelastic response to a one minus cosine gust shape. The aeroelastic solver, in the commercial software MSC Nastran, evaluates the aerodynamic loads due to the gust disturbance considering a rigid panel model and then sums to these the loads considering the flexibility due to the

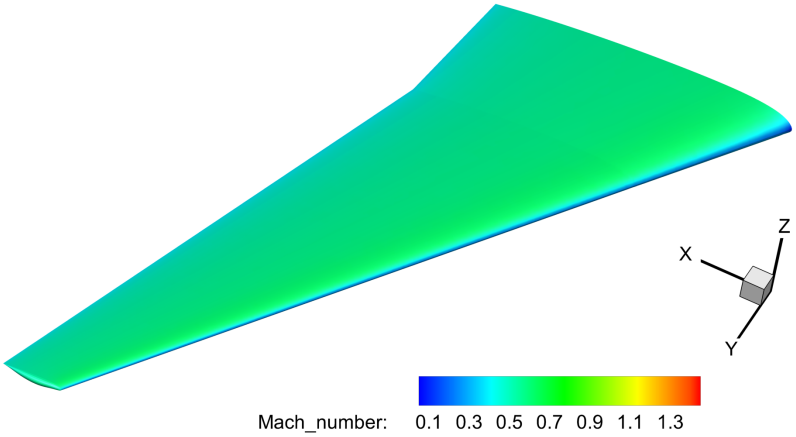

(a) Flight condition $M = 0.50$

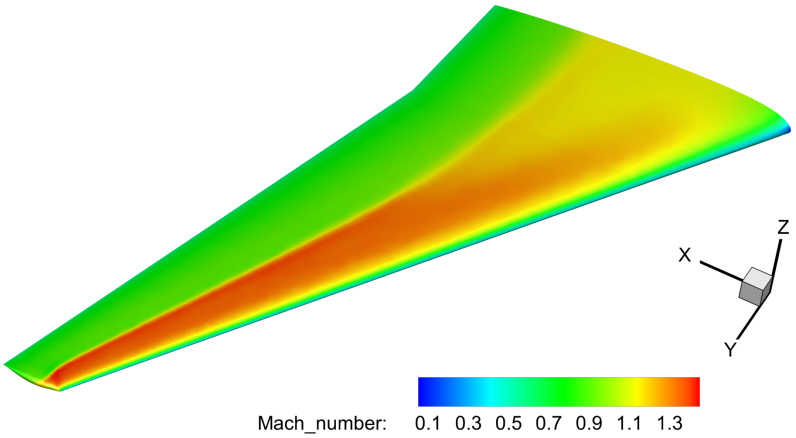

(b) Flight condition $M = 0.85$

Figure 6.12: FFAST wing surface Mach number for the two flight conditions .

structure. As a first comparison, the aerodynamic loads computed considering a rigid CFD simulation for different gust lengths are compared with the rigid gust loads computed with the baseline DLM and the DLM corrected using sinusoidal gusts.

The correction using sinusoidal gusts, are able to match the rigid CFD results very well for both the flight conditions. For this reason only the transonic case is reported for the medium gust length of $91.44\ m$. In Figure 6.13 a comparison for vertical force F_z and pitching moment M_y of five reference strips along the wing span is reported. Some small differences are noticeable for the outboard strips. The reason for this behaviour is associated with the 3D wing tip effects not captured by the panel method.

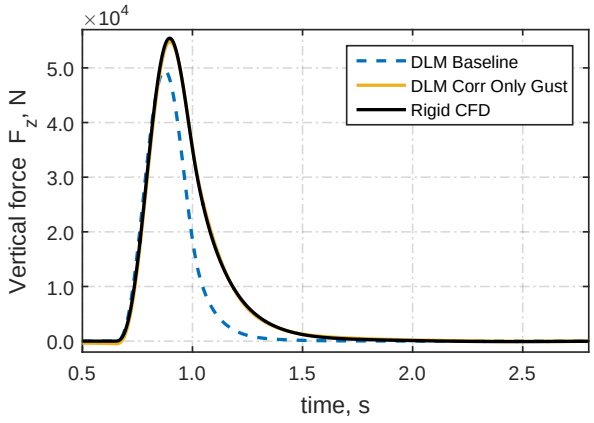

(a) F_z, strip 1.

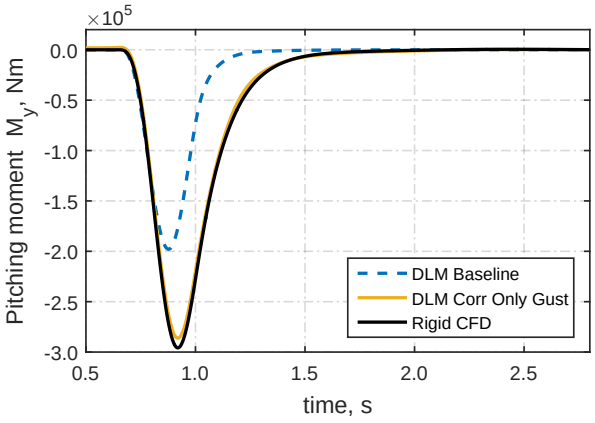

(b) M_y, strip 1.

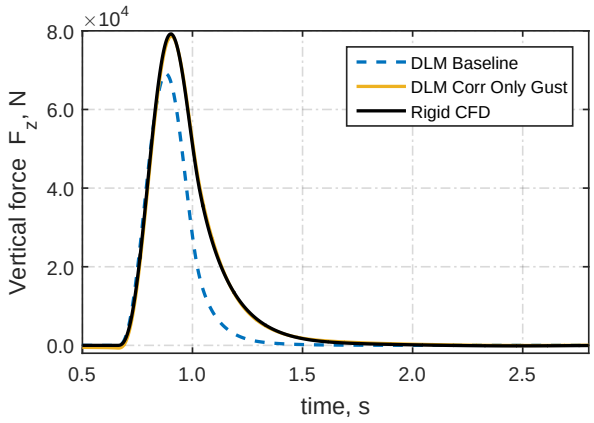

(c) F_z, strip 3.

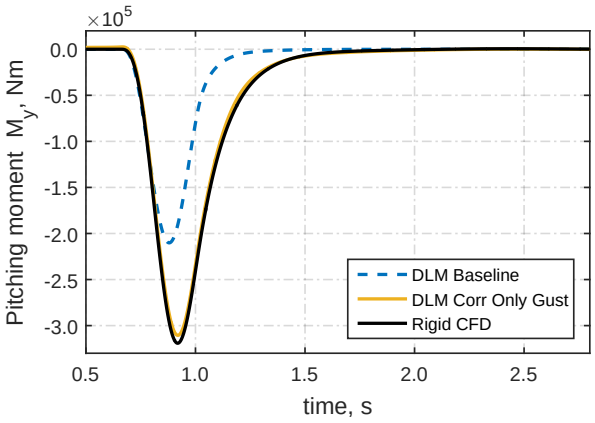

(d) M_y, strip 3.

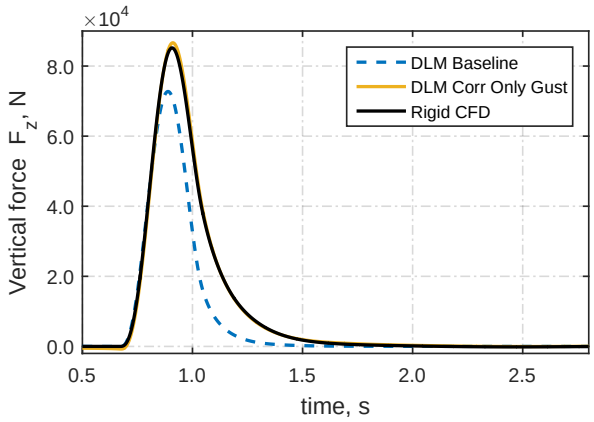

(e) F_z, strip 5.

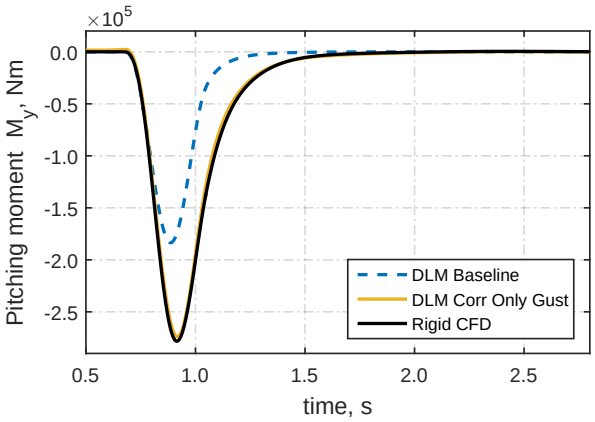

(f) M_y, strip 5.

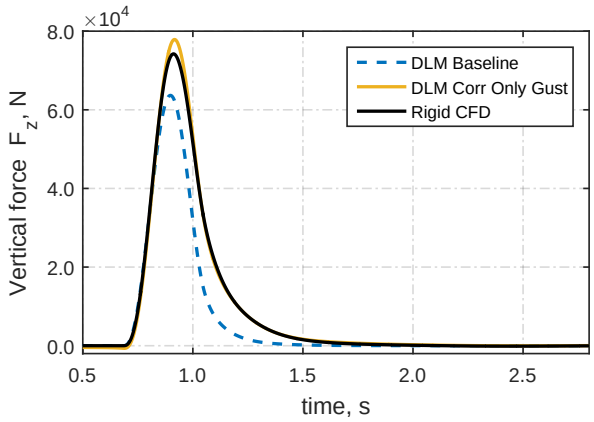

(g) F_z, strip 7.

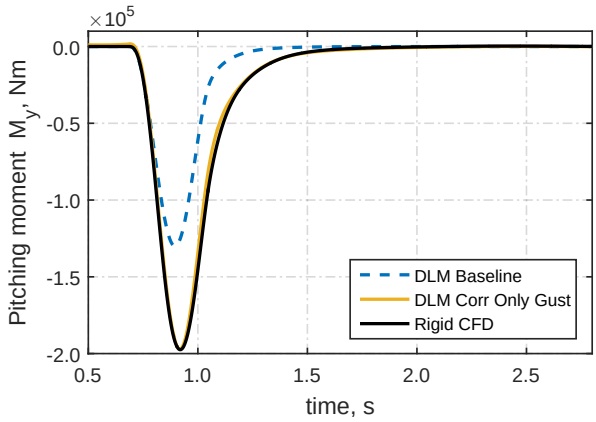

(h) M_y, strip 7.

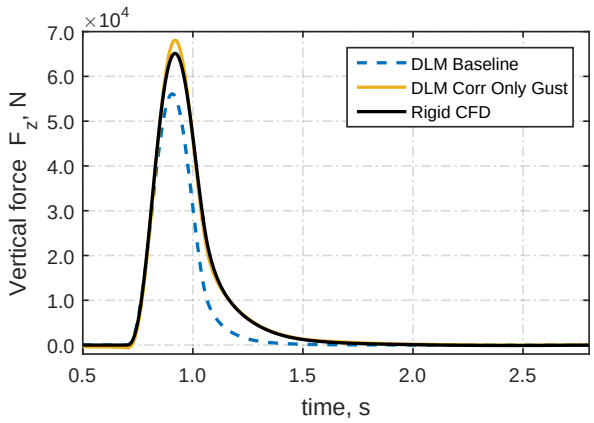

(i) F_z, strip 9.

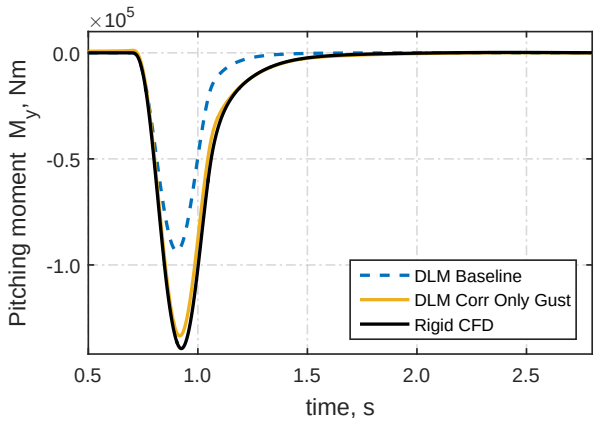

(j) M_y, strip 9.

Figure 6.13: Strip aerodynamic loads computed with Baseline DLM, Corrected DLM and rigid CFD for transonic Mach number, $M = 0.85$, and medium gust length $L_g = 91.44\ m$.

In Figure 6.14 the total wing aerodynamic loads computed using the DLM are compared with the rigid CFD. It is possible to notice that the corrected DLM is able to match quite well the CFD loads. Only for the larger gust length, Figure 6.14(e) and 6.14(f), the corrected DLM tends to overestimate the loads computed with the CFD. This is probably due to the nonlinearities that the correction methods can not account for in the present formulation.

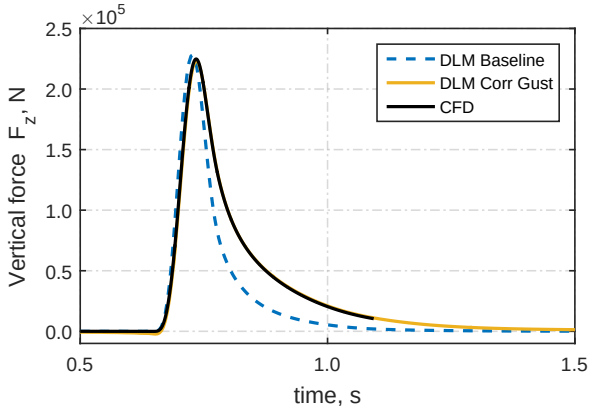

(a) F_z, $L_g = 18.28\ m$.

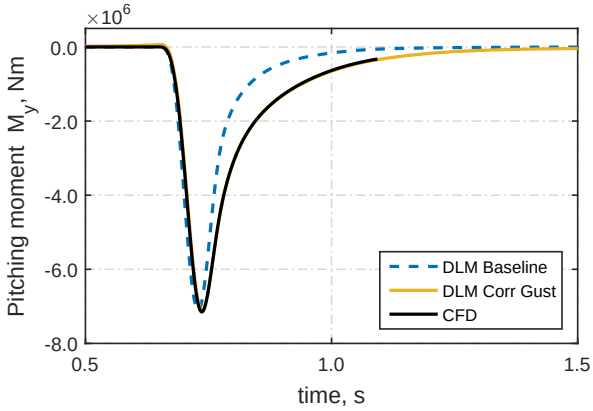

(b) M_y, $L_g = 18.28\ m$.

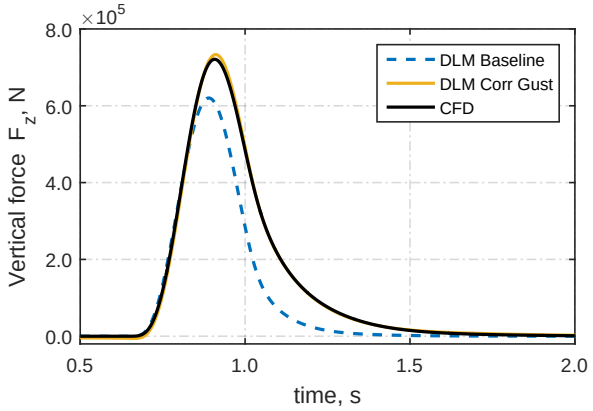

(c) F_z, $L_g = 91.44\ m$.

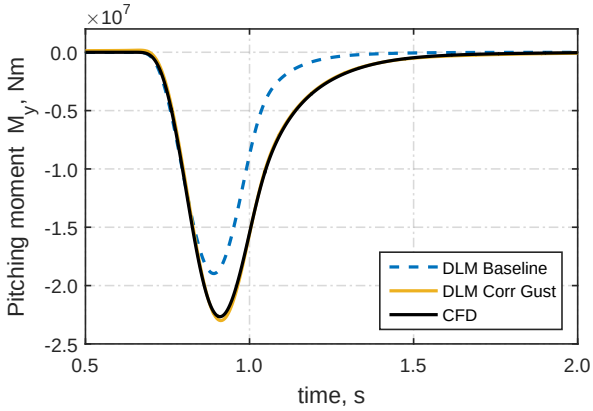

(d) M_y, $L_g = 91.44\ m$.

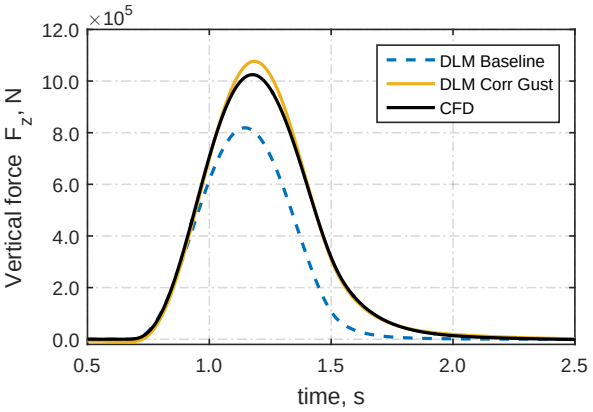

(e) F_z, $L_g = 213.36\ m$.

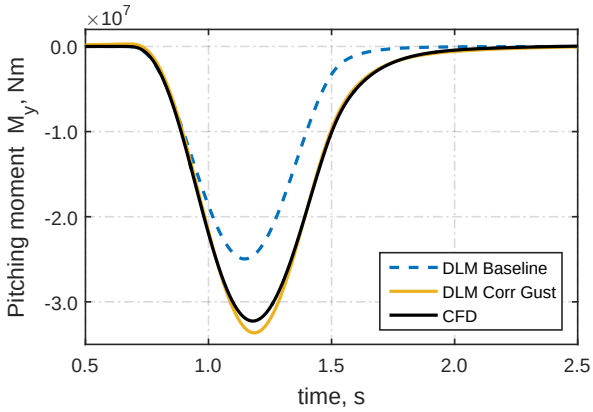

(f) M_y, $L_g = 213.36\ m$.

Figure 6.14: Total aerodynamic loads computed with Baseline DLM, Corrected DLM and rigid CFD for transonic Mach number, $M = 0.85$, and three reference gust lengths.

6.3.2 Flexible mode gust correction

The total aeroelastic loads computed using: the baseline DLM, the DLM corrected only with gust data and the DLM corrected using gust data and mode data, are compared with the results

obtained from the fluid structure interactions simulation. Comparison is made for a series of strips along the wing span for the medium gust length of $91.44\ m$. The vertical force and pitching moment are plotted for five reference strips for the flight condition at $M = 0.5$ in Figure 6.15.

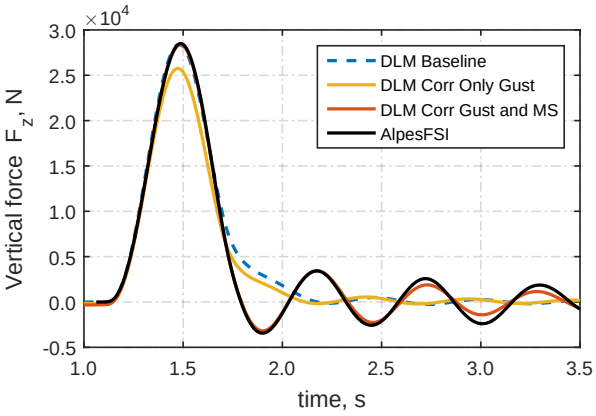

(a) F_z, strip 1.

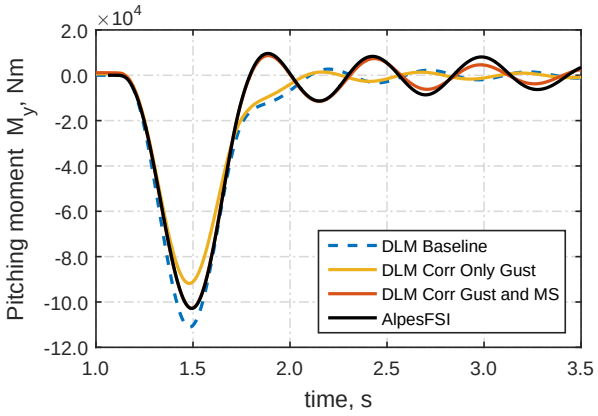

(b) M_y, strip 1.

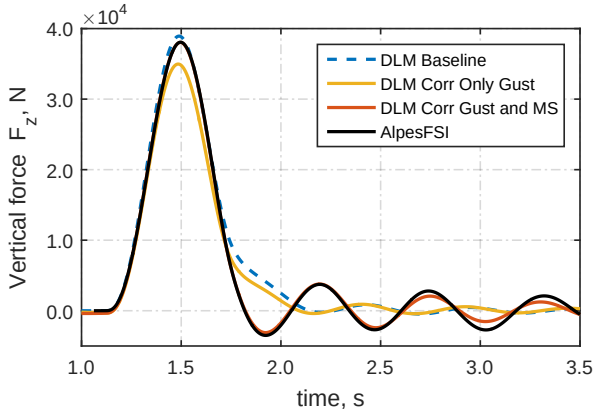

(c) F_z, strip 3.

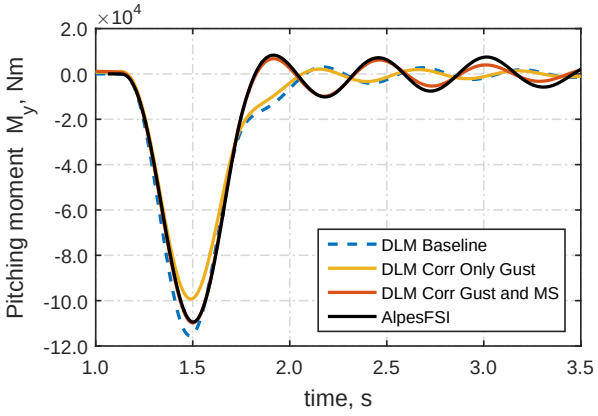

(d) M_y, strip 3.

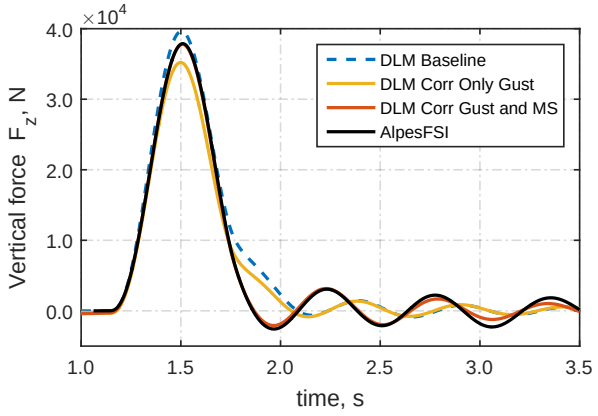

(e) F_z, strip 5.

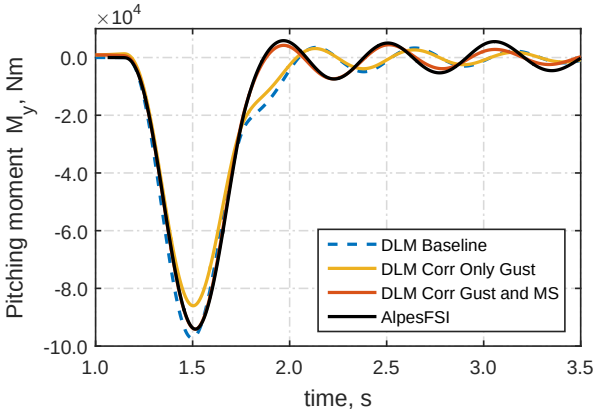

(f) M_y, strip 5.

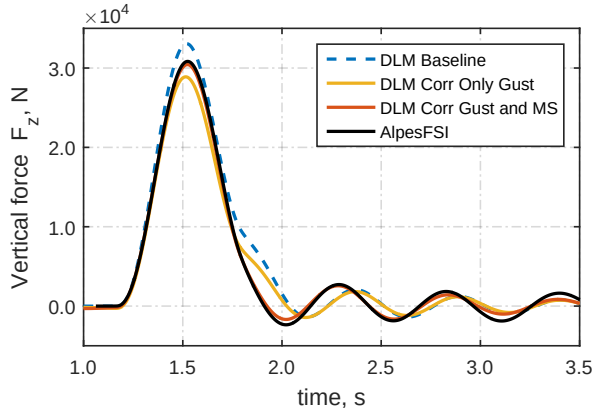

(g) F_z, strip 7.

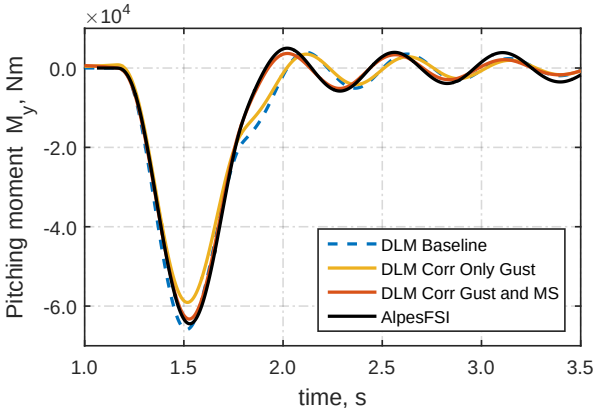

(h) M_y, strip 7.

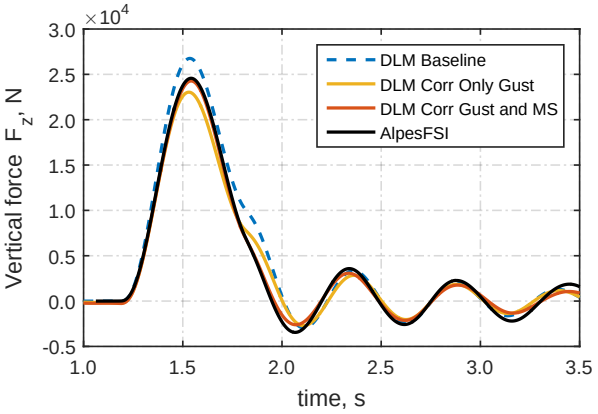

(i) F_z, strip 9.

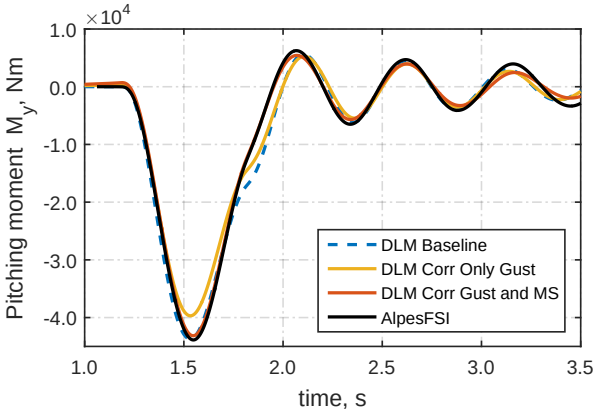

(j) M_y, strip 9.

Figure 6.15: Strip aerodynamic loads computed with Baseline DLM, Corrected DLM and AlpesFSI for $M = 0.50$ and $L_g = 91.44\ m$.

The DLM correction, using only the sinusoidal gusts is not sufficient to get a good prediction of the loads. However, if the correction process takes into consideration the flexible mode shapes, the aeroelastic loads are able to match the fully coupled solution with reasonable accuracy. A

similar behaviour is observed for the transonic flight condition at $M = 0.85$, Figure 6.16.

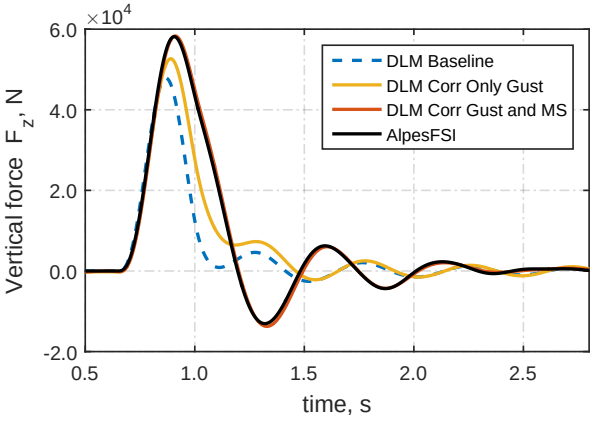

(a) F_z, strip 1.

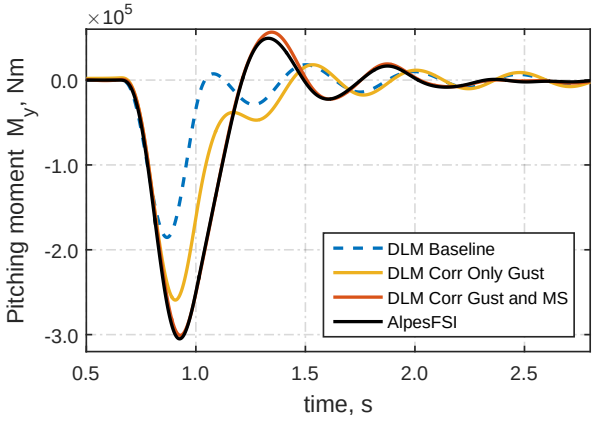

(b) M_y, strip 1.

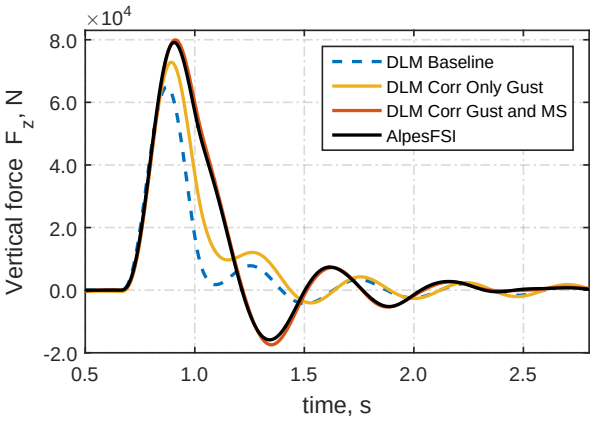

(c) F_z, strip 3.

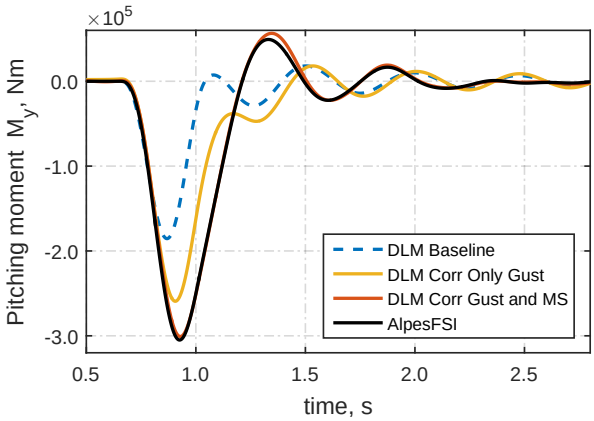

(d) M_y, strip 3.

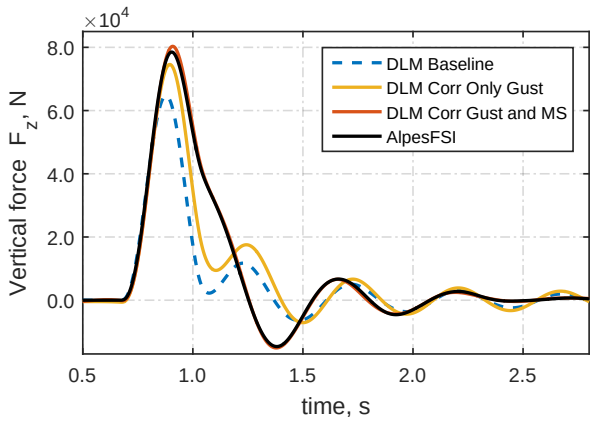

(e) F_z, strip 5.

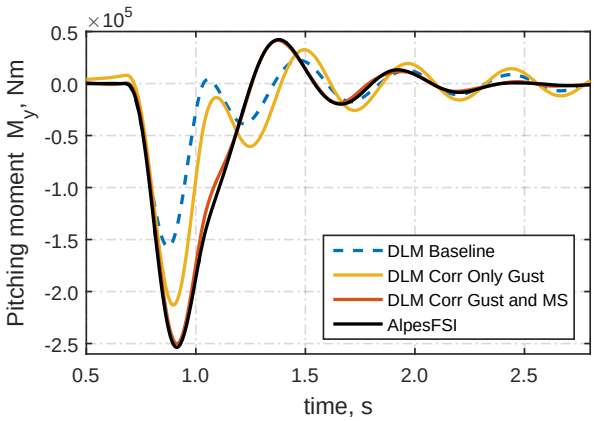

(f) M_y, strip 5.

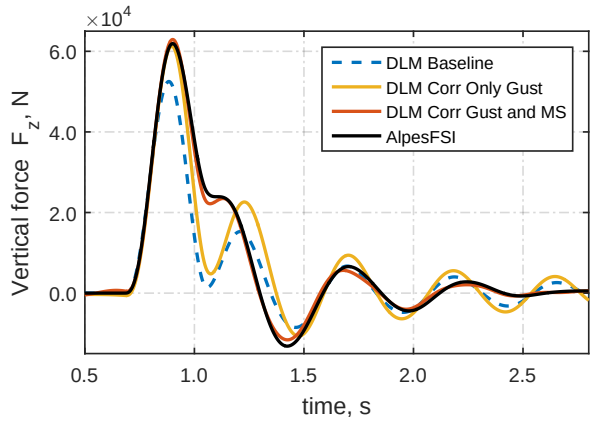

(g) F_z, strip 7.

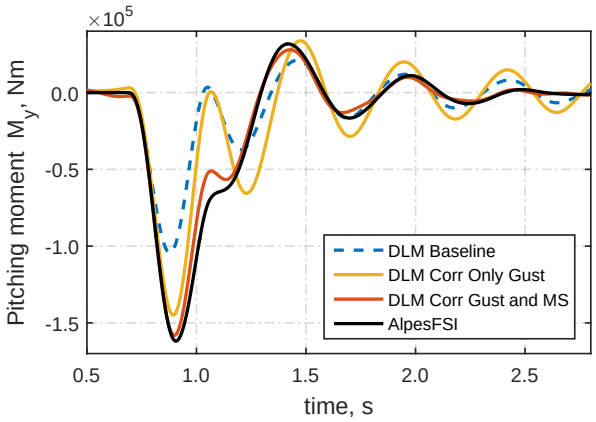

(h) M_y, strip 7.

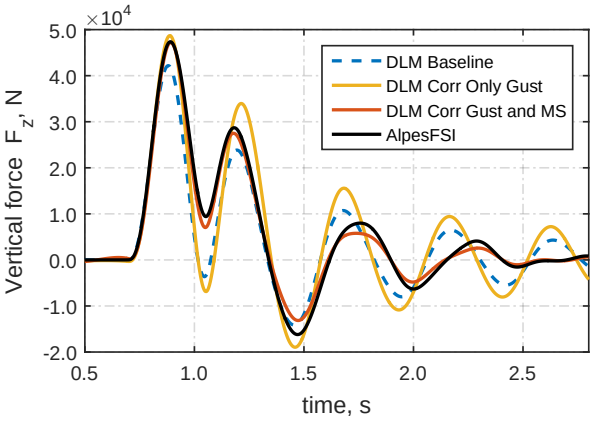

(i) F_z, strip 9.

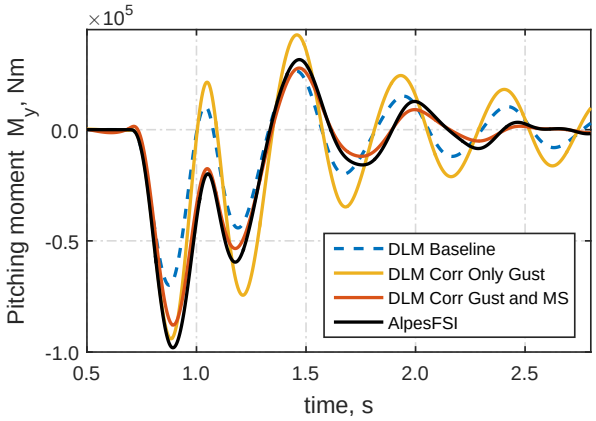

(j) M_y, strip 9.

Figure 6.16: Strip aerodynamic loads computed with Baseline DLM, Corrected DLM and AlpesFSI for $M = 0.85$ and $L_g = 91.44\ m$.

Figure 6.17 shows the total aerodynamic loads for the flight point at $M = 0.50$ for the five gust lengths considered. In general the correction method shows a good behaviour for all of them. However, it is still possible to notice how for the longest gust length, nonlinear effects become relevant and the linear correction approach implemented tends to deviate slightly from the fully coupled analysis. The results for the higher Mach number condition are reported in Figure 6.18.

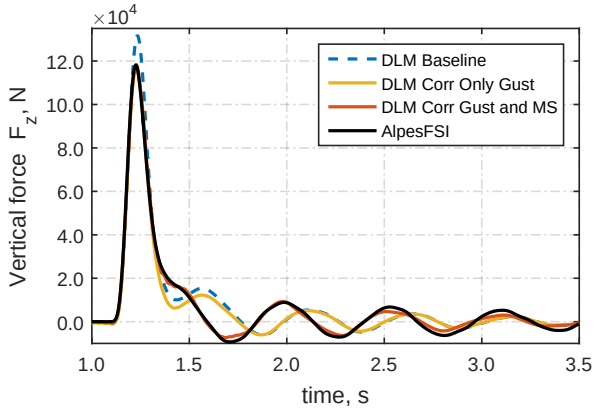

(a) F_z, $L_g = 18.28\ m$.

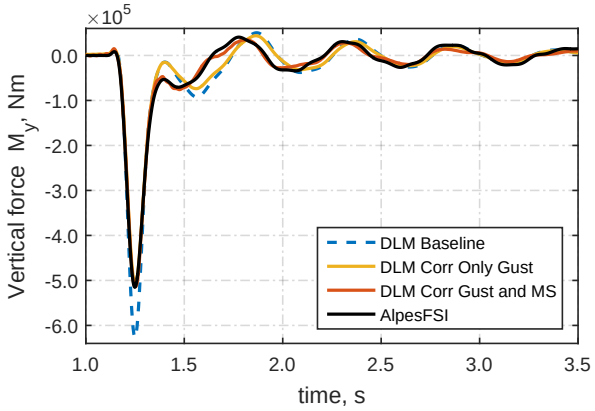

(b) M_y, $L_g = 18.28\ m$.

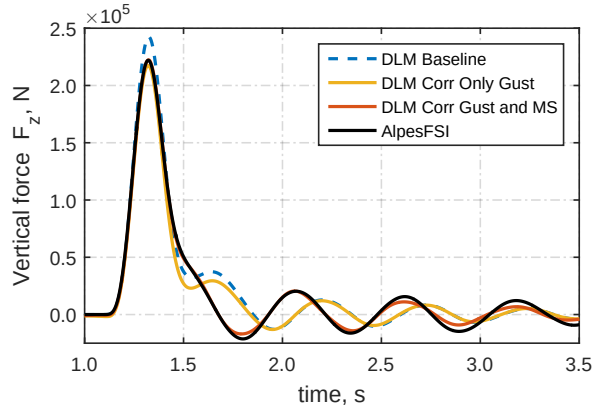

(c) F_z, $L_g = 42.67\ m$.

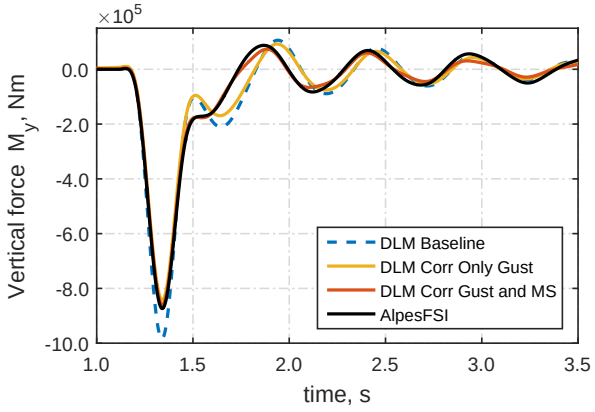

(d) M_y, $L_g = 42.67\ m$.

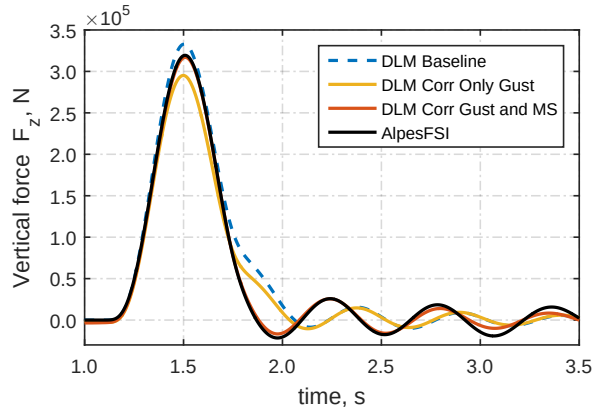

(e) F_z, $L_g = 91.44\ m$.

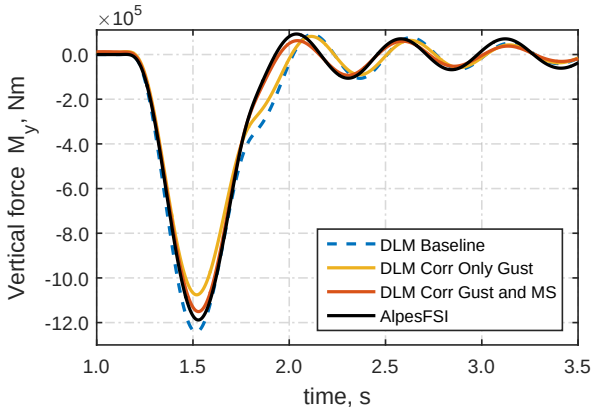

(f) M_y, $L_g = 91.44\ m$.

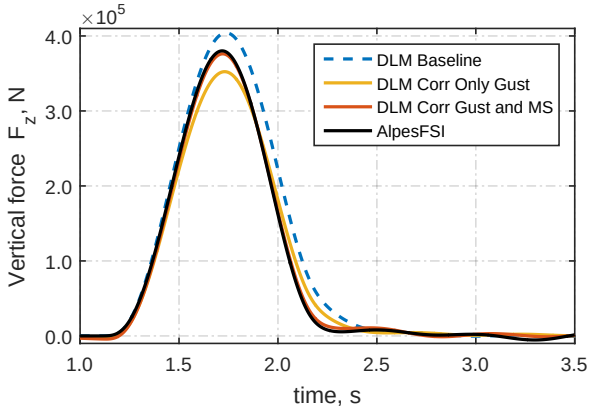

(g) F_z, $L_g = 152.40\ m$.

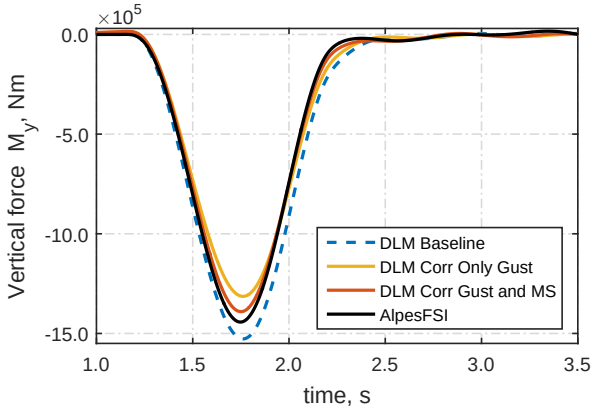

(h) M_y, $L_g = 152.40\ m$.

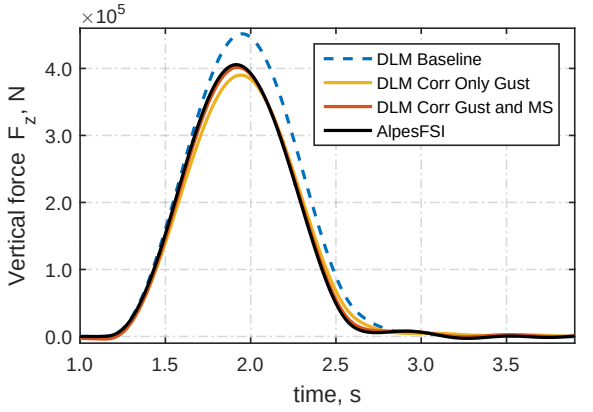

(i) F_z, $L_g = 213.36\ m$.

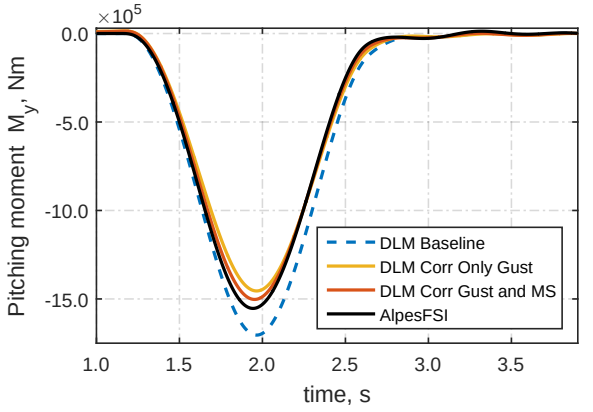

(j) M_y, $L_g = 213.36\ m$.

Figure 6.17: Total aerodynamic loads computed with Baseline DLM, Corrected DLM and AlpesFSI for $M = 0.50$.

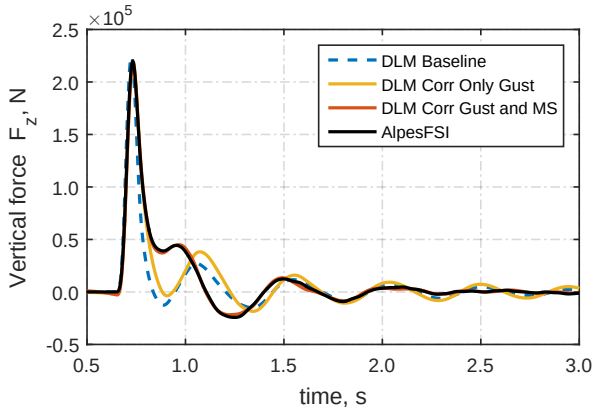

(a) F_z, $L_g = 18.28\ m$.

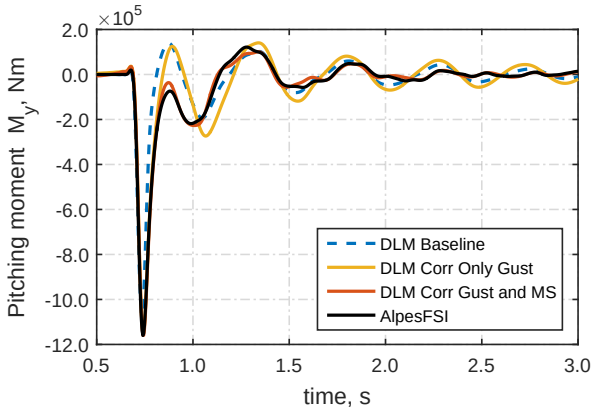

(b) M_y, $L_g = 18.28\ m$.

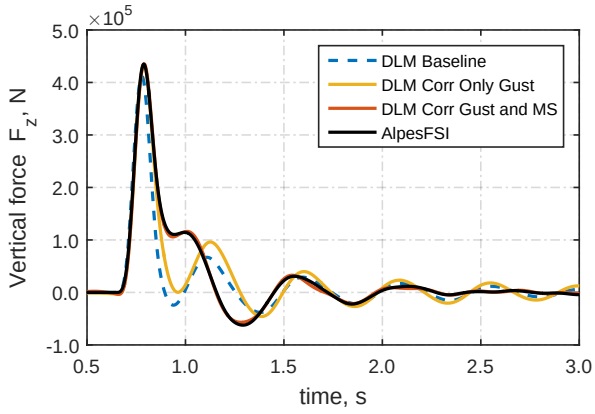

(c) F_z, $L_g = 42.67\ m$.

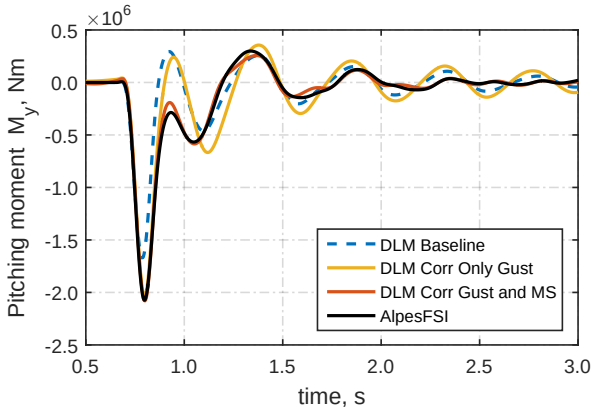

(d) M_y, $L_g = 42.67\ m$.

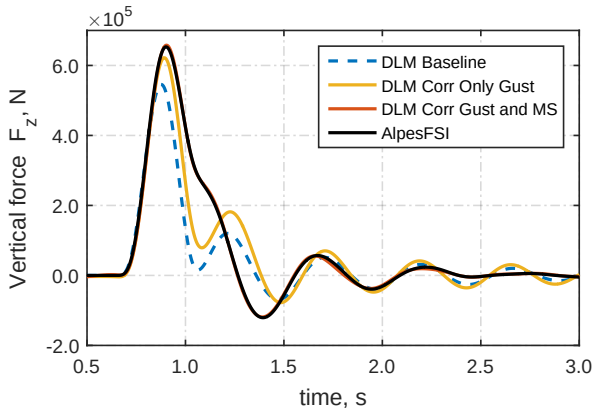

(e) F_z, $L_g = 91.44\ m$.

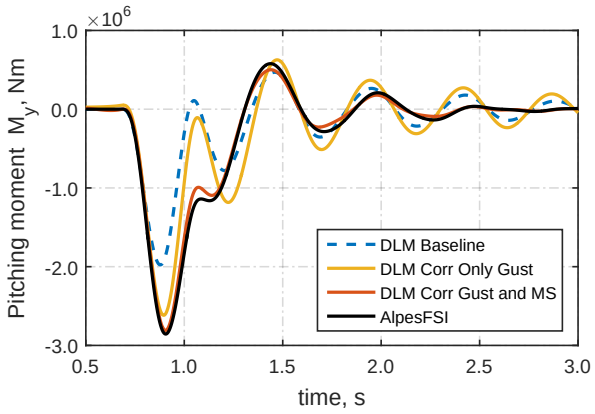

(f) M_y, $L_g = 91.44\ m$.

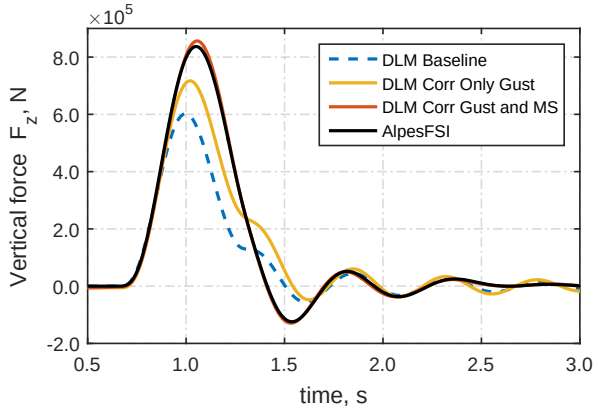

(g) F_z, $L_g = 152.40\ m$.

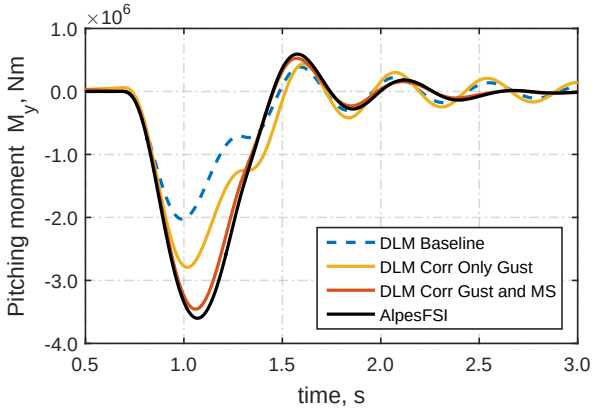

(h) M_y, $L_g = 152.40\ m$.

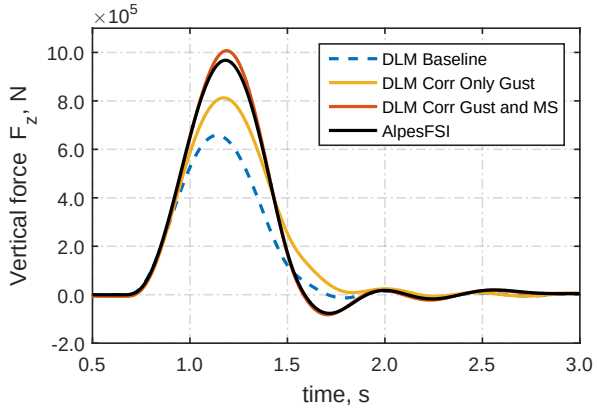

(i) F_z, $L_g = 213.36\ m$.

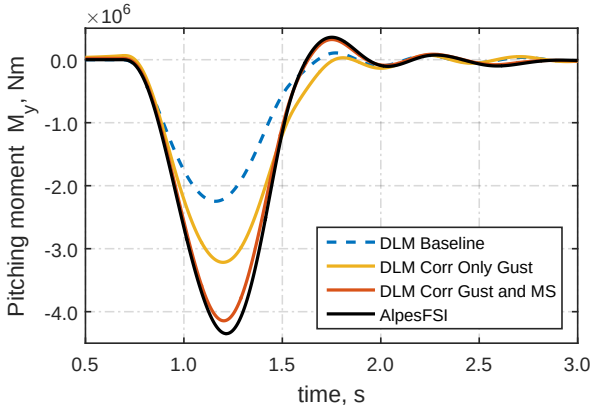

(j) M_y, $L_g = 213.36\ m$.

Figure 6.18: Total aerodynamic loads computed with Baseline DLM, Corrected DLM and AlpesFSI for $M = 0.85$.

As observed in the previous case, the correction method using only sinusoidal gusts does not produce accurate results for the total aeroelastic loads. Including flexible mode information in the correction process the corrected DLM results are in complete agreement with the fluid structure interaction results. It is still possible to observe, however, a slight difference for the longest gust length, where nonlinear aerodynamic behaviour is present and is not captured by the correction method.

6.4 LFD for correction approach

Since Linearised Frequency Domain (LFD) for gust analysis became available in the DLR TAU-Code, the expensive time domain simulations, to compute the reference high fidelity loads, can be replaced by the more efficient LFD analysis. The assumption of small perturbation finds a perfect match with the LFD definition. An initial study has been carried out to check that the LFD results obtained for the strip loads were in agreement with the time domain CFD results. In Figure 6.19, the magnitude and phase due to the sinusoidal gust disturbance is compared for three strips along the wing span.

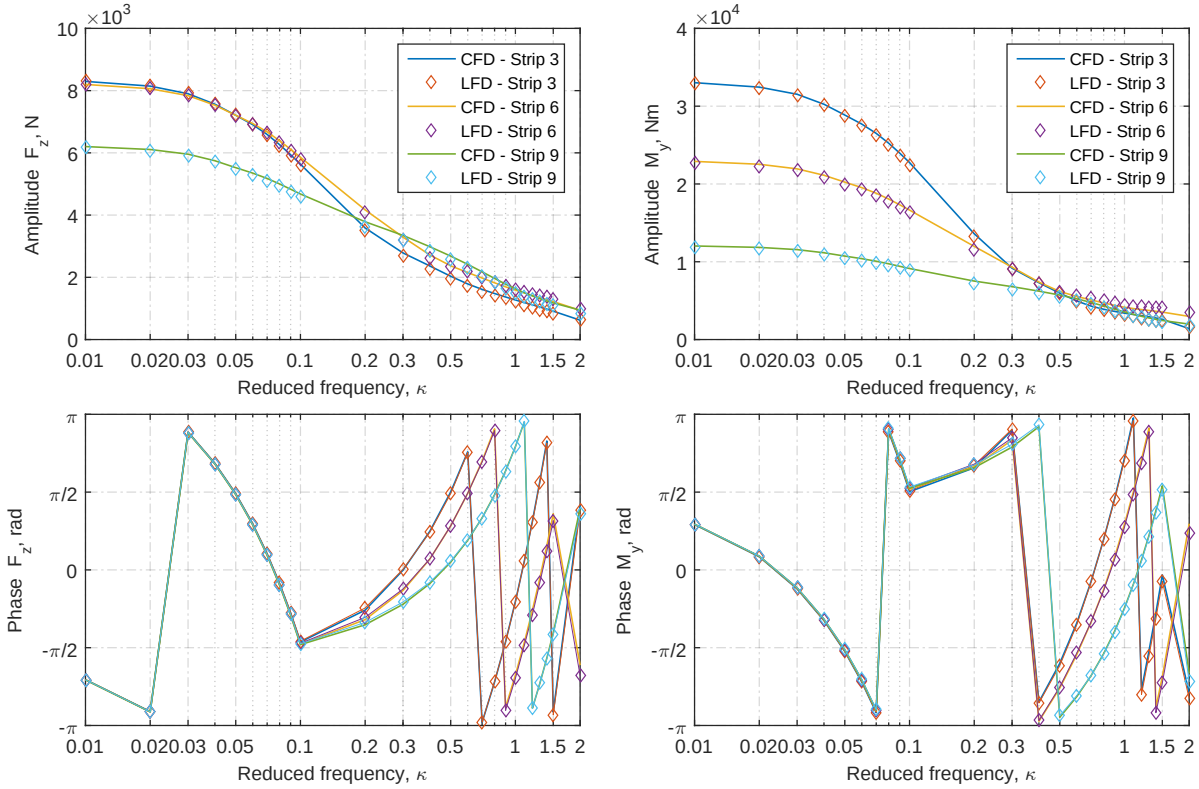

(a) Vertical force, F_z.

(b) Pitching moment, M_y.

Figure 6.19: Amplitude and phase comparison versus reduced frequency due to sinusoidal gust encounter for time domain CFD and LFD. Vertical force and pitching moment for strip 3, 6 and 9.

A comparison between CFD and LFD results for the strip vertical force and pitching moment has been reported in Figure 6.20 for the first mode (first wing bending) and in Figure 6.21 for

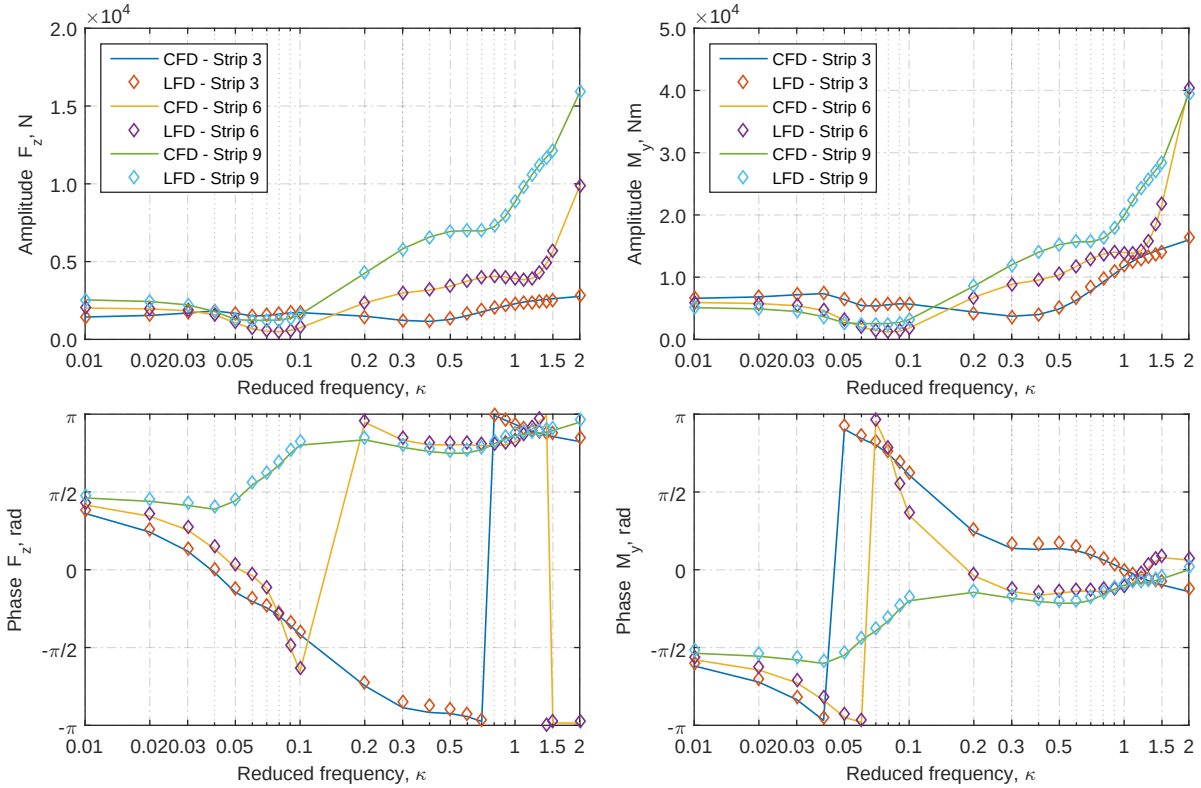

(a) Vertical force, F_z. 1^{st} wing bend.

(b) Pitching moment, M_y. 1^{st} wing bend.

Figure 6.20: Amplitude and phase comparison versus reduced frequency due to the first mode deformation for time domain CFD and LFD, for strip 3, 6 and 9.

the second mode (first wing torsion). These verify a good agreement between the time domain analysis and the linearised frequency approach.

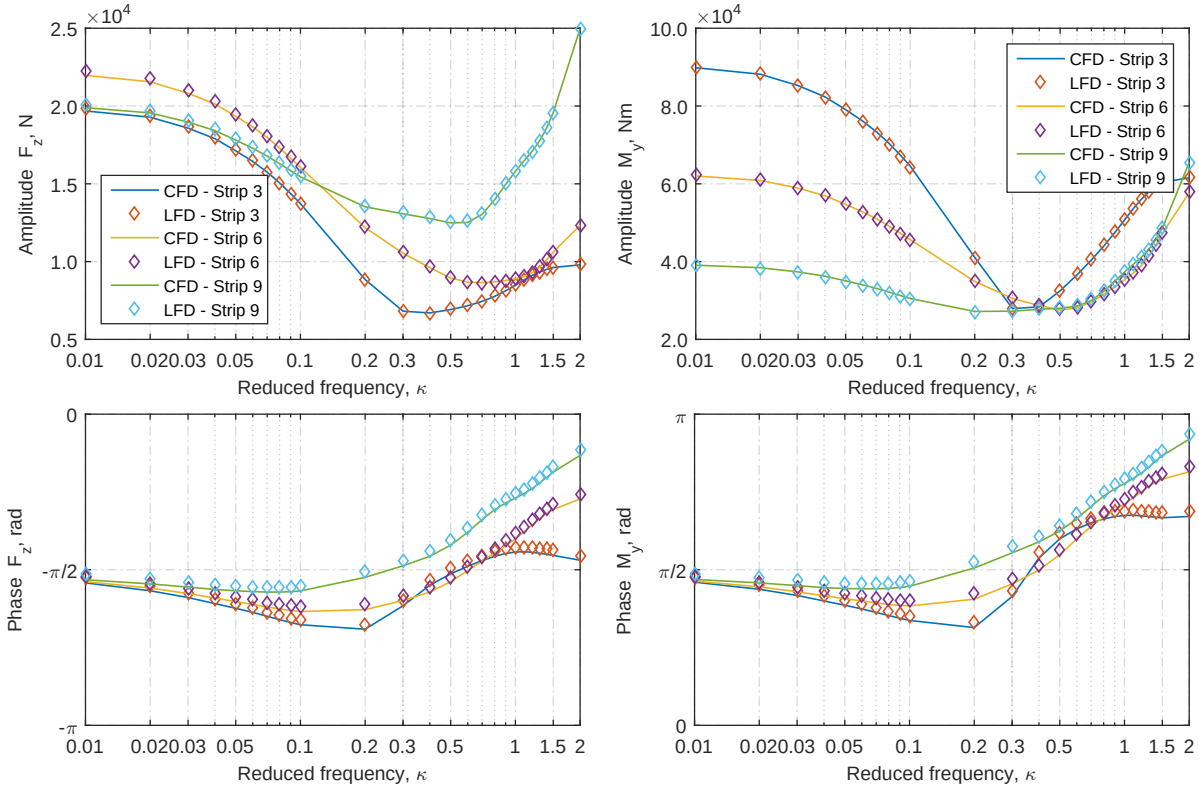

(a) Vertical force, F_z. 1^{st} wing tors.

(b) Pitching moment, M_y. 1^{st} wing tors.

Figure 6.21: Amplitude and phase comparison versus reduced frequency, for vertical force and pitching moment, due to the second mode deformation for CFD and LFD. Strips 3, 6 and 9.

The data obtained from the LFD analysis have been used to compute the correction matrices, as presented in the previous chapter. For the sake of clarity, a comparison of the results obtained with these matrices has been performed versus those obtained using time domain CFD results. The LFD correction matrices have been shown to give a perfect match to the results previously presented, as was expected. The results comparing the total vertical force and pitching moment are reported in Figure 6.22.

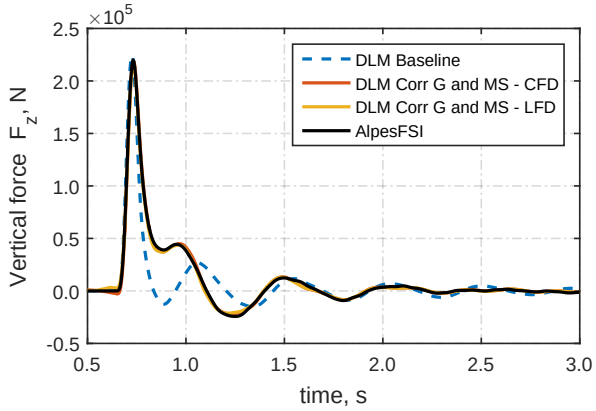

(a) F_z, $L_g = 18.28\ m$.

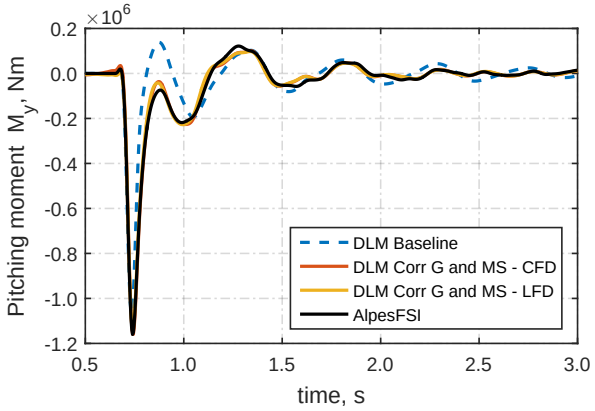

(b) M_y, $L_g = 18.28\ m$.

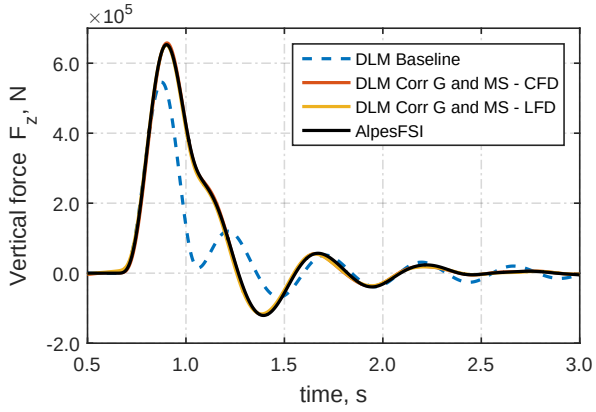

(c) F_z, $L_g = 91.44\ m$.

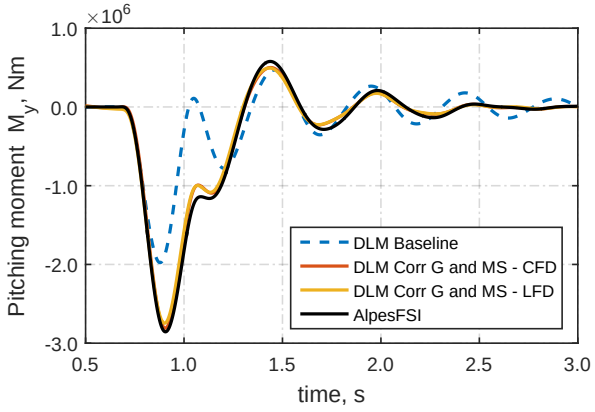

(d) M_y, $L_g = 91.44\ m$.

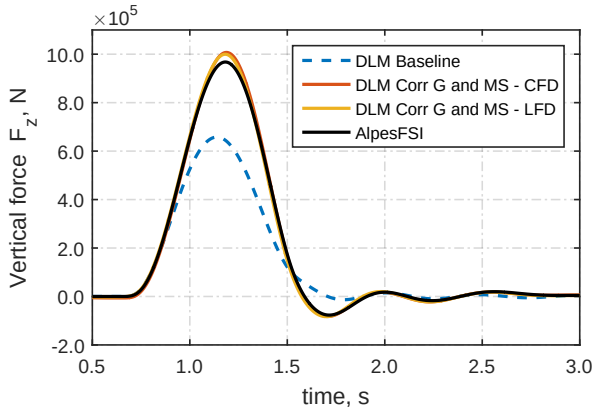

(e) F_z, $L_g = 213.36\ m$.

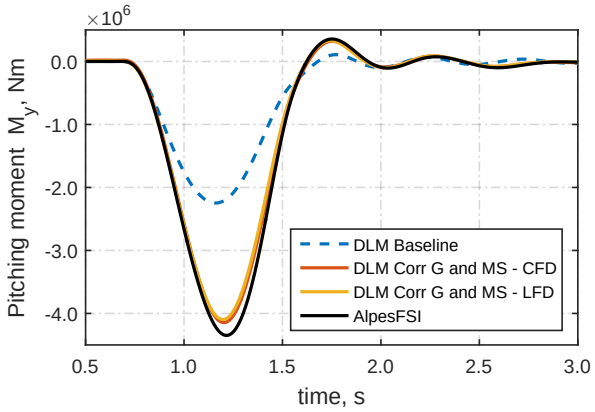

(f) M_y, $L_g = 213.36\ m$.

Figure 6.22: Total aerodynamic loads computed with Baseline DLM, Corrected DLM using CFD time domain data, Corrected DLM using LFD data and AlpesFSI interface for $M = 0.85$.

6.5 Interpolation over the correction factors

In the application of the correction method presented in this chapter, a relatively high number of reference cases have been employed. Previous work has shown how it is not beneficial to reduce the number of reduced frequencies used in the DLM gust solver, because that would produce the effect of having a linear interpolation in frequency. However, plotting the correction coefficients ϵ^W computed as a function of the reduced frequency, for a series of panels, it is possible to notice how they show a smooth variation, Figure 6.23. In this picture each line corresponds to the real and imaginary part of the correction factor over a selected panel of the DLM mesh. On Figure 6.23(a) is shown the correction factor for sinusoidal gust, while on Figure 6.23(b) the correction factor for mode shape deformation is reported. The colour of the lines identify the selected panel. From this observation it appears that in this case it is possible to reduce the

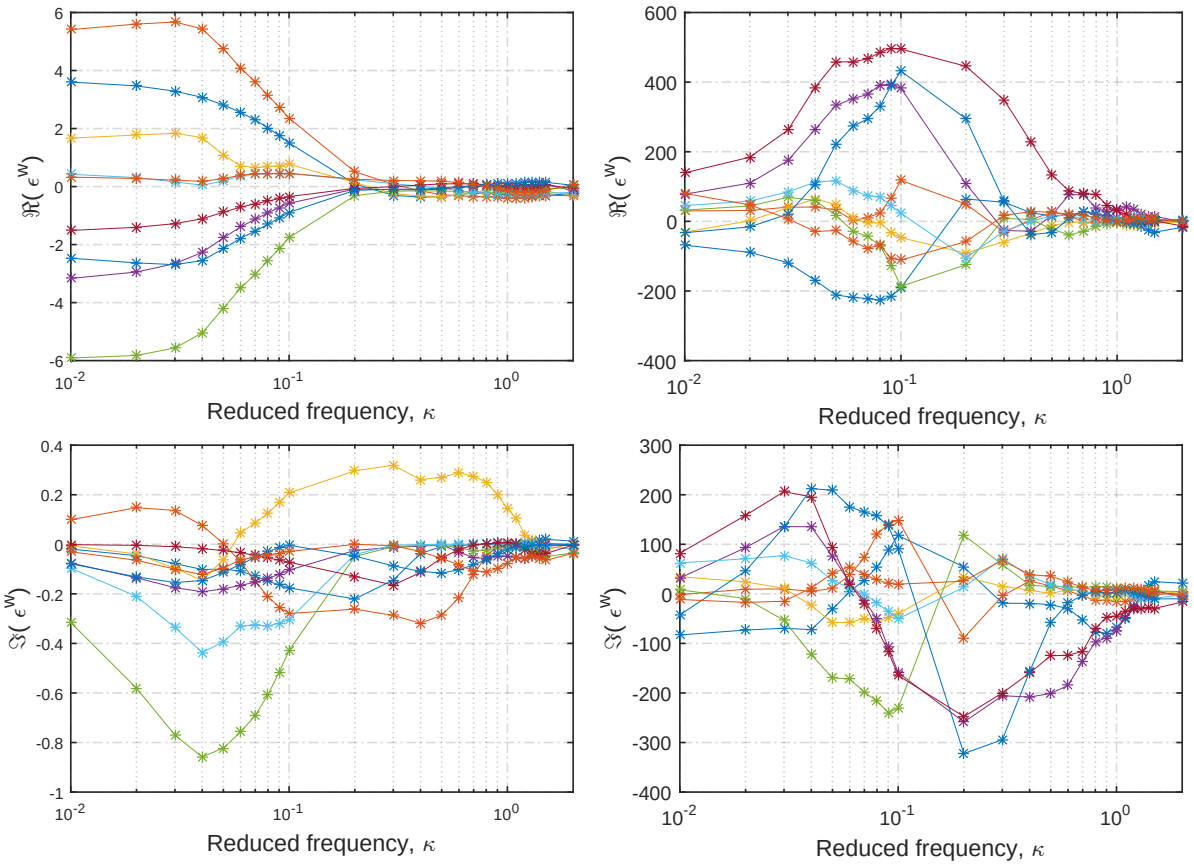

(a) Correction factors for sinusoidal gust.

(b) Correction factors for mode shape deformation.

Figure 6.23: Real and imaginary part of the correction factors ϵ^W in function of the reduced frequency κ, for a selection of panels of the DLM mesh.

sampling points and interpolate the correction factors over the range of frequencies of interest. In this way the LFD simulations can be performed for a selection of reduced frequency values, and then the correction factors can be extended to the full series of κ, Table 6.1, by means of interpolation. In Figure 6.24, the results obtained from the full corrected method, and those obtained computing LFD simulations for only six frequencies ($\kappa = [0.01; 0.05; 0.1; 0.2; 0.5; 2]$) plus linear interpolation are presented for the transonic flight condition, $M = 0.85$.

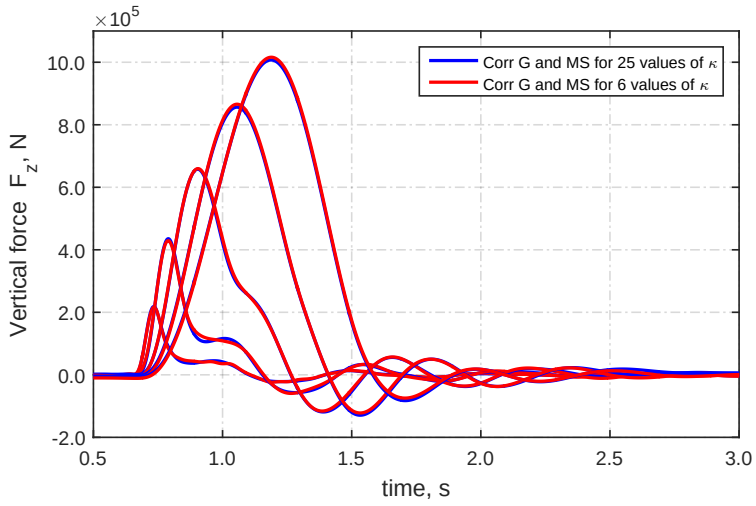

(a) Vertical force, F_z.

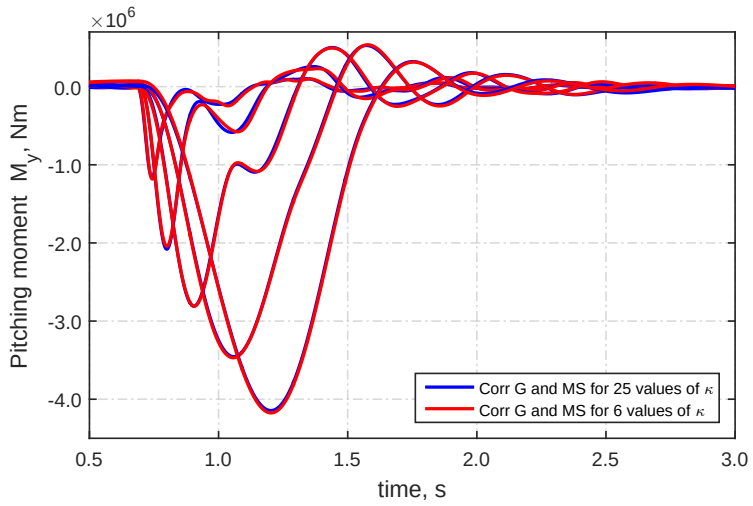

(b) Pitching moment, M_y.

Figure 6.24: Total aerodynamic loads for the five gusts length computed using the DLM corrected for all the reduced frequencies and for only 6 reduced frequencies. Transonic flight condition $M = 0.85$.

It is observed that the aerodynamic loads computed using a reduced number of reference high fidelity cases is very close to the original results. These results are very promising and suggest

that an optimization approach could be designed to identify the most important cases to be calculated with the LFD solver and which could be found via an interpolation technique.

The list of reduced frequencies selected here are capable of covering the full range of corrections, and this highlights how it is not necessary to compute reference data for all the frequencies used in the gust analysis. However, it is mandatory to request the full list of frequency in the gust analysis, and then provide correction factors obtained from an interpolation approach. Omitting the reduced frequencies from the analysis input causes MSC Nastran to skip the calculation of the AIC matrix at those frequencies. But, in order to compute the output for all the range of frequencies, it performs a linear interpolation between AIC matrices, resulting in a poor quality results.

Furthermore, these results highlight how not all the reduced frequencies have the same impact on the final response. And in fact, it might be possible that a direct relationship between the reduced frequency and the frequency of the mode shape most excited by the specific gust length exists. However, no specific investigations have been carried out in the course of this thesis, but they could be of interest for future research activities.

6.6 Structural loads evaluation for gust modelling

To evaluate how the more accurate aerodynamic loads prediction affects the structural response, the wing tip vertical displacement time history, for the range of gust lengths analysed at the transonic flight condition, is shown in Figure 6.25.

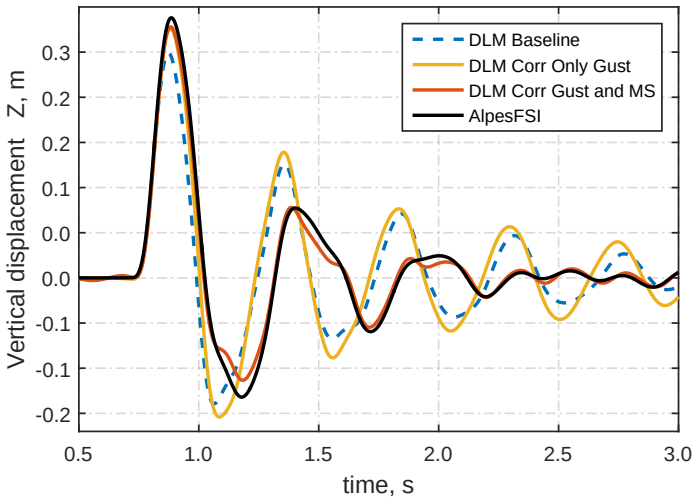

(a) Wing tip vertical displacement, $L_g = 18.28\ m$

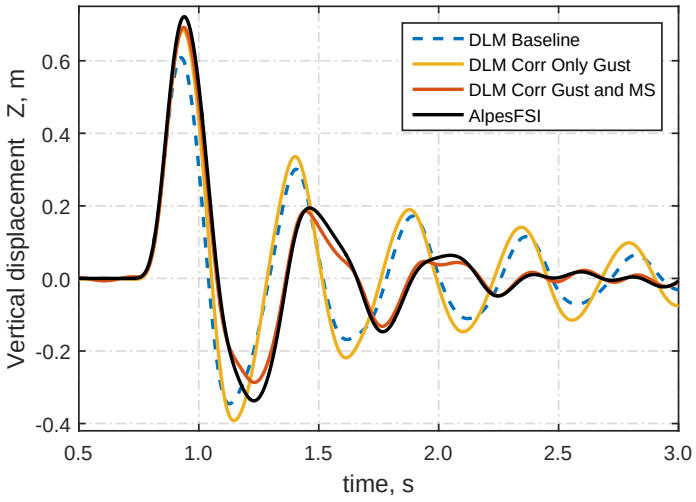

(b) Wing tip vertical displacement, $L_g = 42.67\ m$

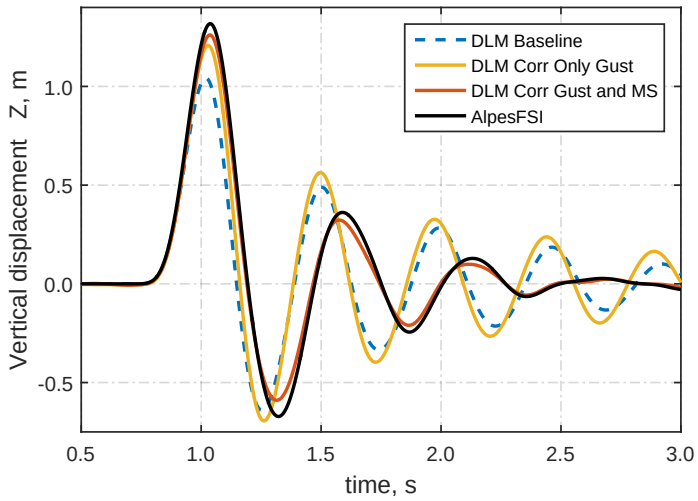

(c) Wing tip vertical displacement, $L_g = 91.44\ m$

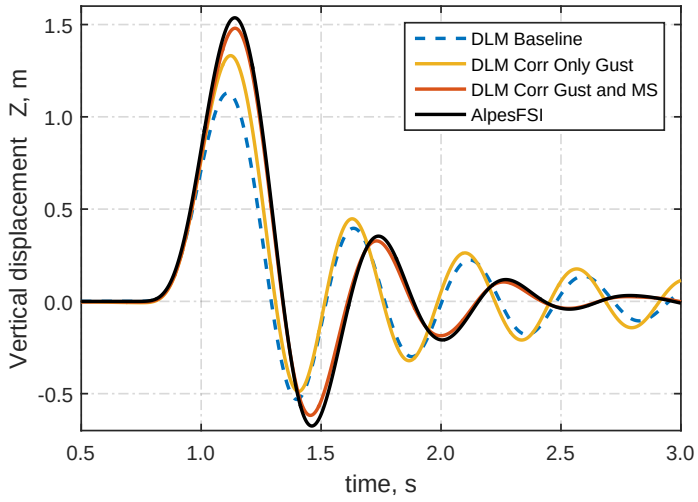

(d) Wing tip vertical displacement, $L_g = 152.40\ m$

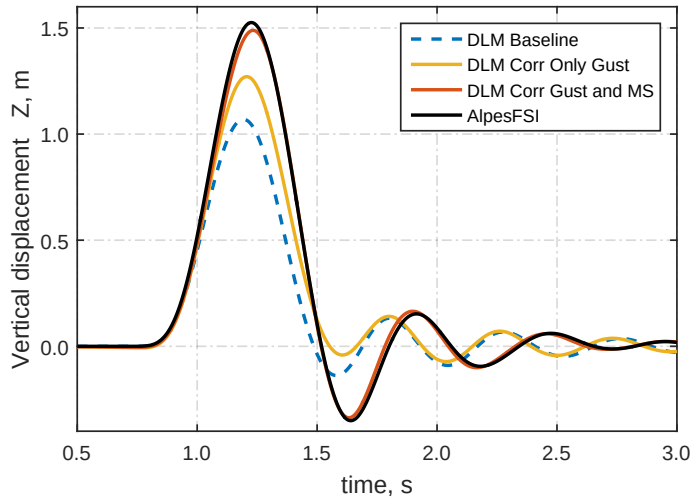

(e) Wing tip vertical displacement, $L_g = 213.36\ m$

Figure 6.25: FFAST wing vertical tip displacement, transonic flight condition $M = 0.85$.

The vertical displacement predicted by the baseline DLM is always far from the reference results. Introducing the correction using the sinusoidal gust allows an improvement in the accuracy of the structural response for the first peak. However, this correction is not capable of giving a good representation of the transient structural response. Including the correction for the mode shapes, the corrected DLM is capable of producing a structural deformation which can predict both the maximum displacement and the transient decay of the oscillation well. A small difference between the DLM corrected with gust and mode shape and the AlpesFSI results, is always present for all the gusts analysed. This is probably related to the different spline methodologies that are used for the two models, which produce a different structural loads distribution.

A more accurate prediction of the structural loads can lead to a better structural sizing. For this reason an important quantity of interest is the loads at the wing root. Figure 6.26 shows the impact of the correction on the wing root shear and torsion. In this case only the delta loads are compared, removing the steady trim contribution from the AlpesFSI results. In this case correcting only using the sinusoidal gust does not allow a good prediction at the wing root due to the gust disturbance. In general a good agreement is found comparing the DLM corrected for gust and mode shape with respect to the fully coupled results. However, small variation could be associated with the different spline methodologies considered to map forces and displacements for the CFD mesh and the DLM mesh.

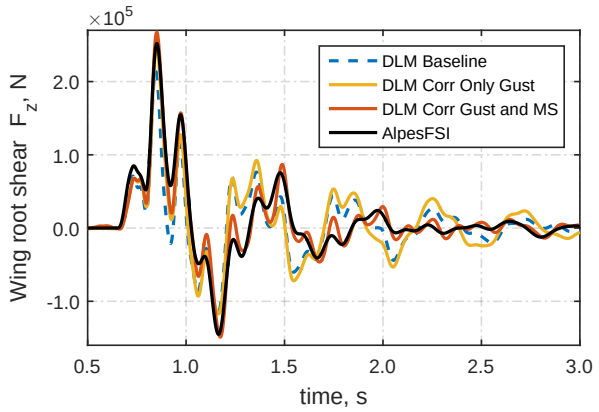

(a) Root shear F_z, $L_g = 18.28\ m$.

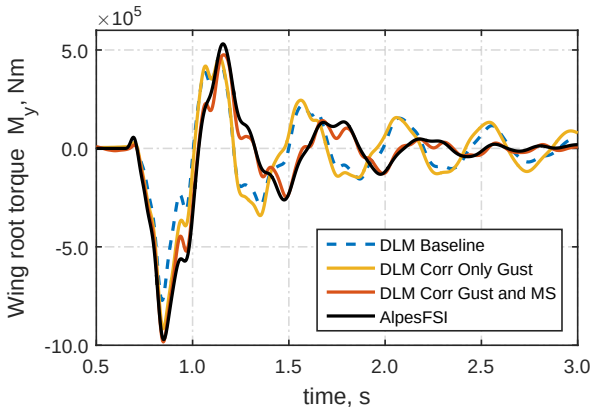

(b) Root torque M_y, $L_g = 18.28\ m$.

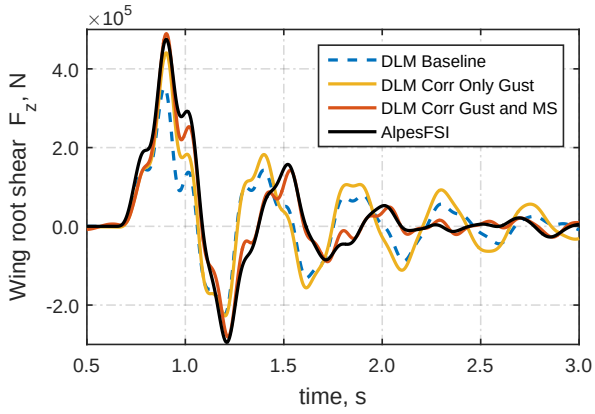

(c) Root shear F_z, $L_g = 42.67\ m$.

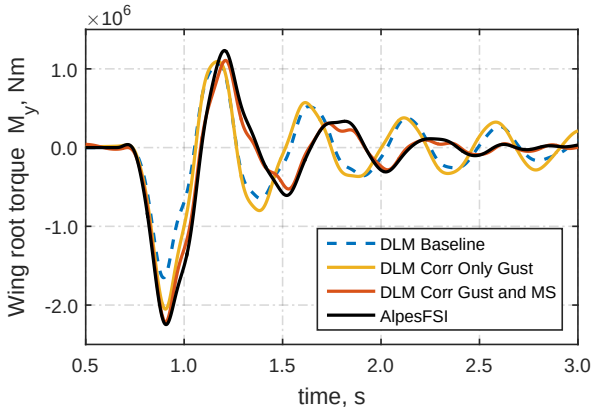

(d) Root torque M_y, $L_g = 42.67\ m$.

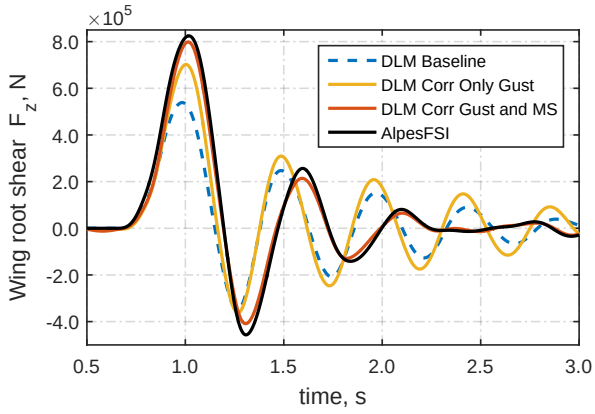

(e) Root shear F_z, $L_g = 91.44m$.

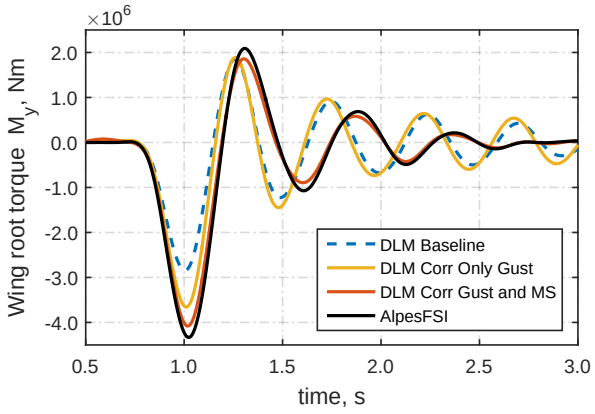

(f) Root torque M_y, $L_g = 91.44\ m$.

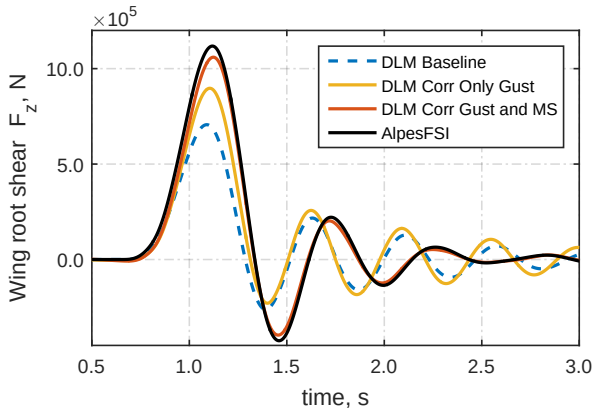

(g) Root shear F_z, $L_g = 152.40\ m$.

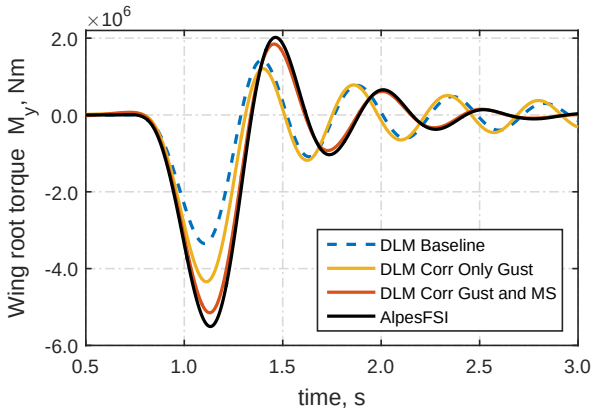

(h) Root torque M_y, $L_g = 152.40\ m$.

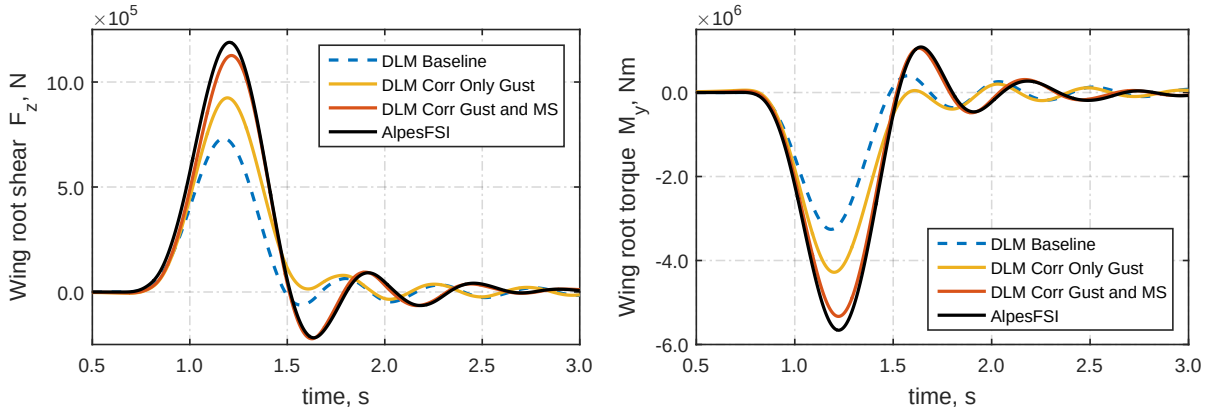

(i) Root shear F_z, $L_g = 213.36\ m$.

(j) Root torque M_y, $L_g = 213.36\ m$.

Figure 6.26: Wing root shear and torque for the reference gust lengths, transonic flight condition $M = 0.85$

6.7 DLM correction comparison

In Figure 6.27 the wing root shear and bending moment obtained with a traditional steady correction approach is compared with the DLM corrected with gust and mode shape, developed in this thesis. As already discussed in Section 5.1, applying the correction computed for a steady case, corresponding to a reduced frequency $\kappa = 0$, to all the AIC matrices does not allow the unsteady effect related to the gust perturbation to be corrected. In fact, the correction matrix computed for the steady case consists of just real terms. It is evident from all the gust lengths how the steady approach is not capable to reproduce the dynamic behaviour related to the structure deformation. Additionally in terms of peak loads the steady correction tends to over predict the loads for the shorter gust lengths, Figures 6.27(a) to 6.27(d). For the longer gust lengths, instead, the steady correction tends to under-predicted the peak loads as shown in Figures 6.27(e) to 6.27(j).

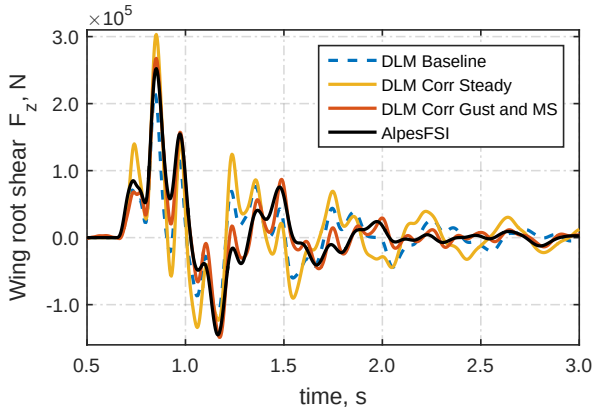

(a) Root shear F_z, $L_g = 18.28\ m$.

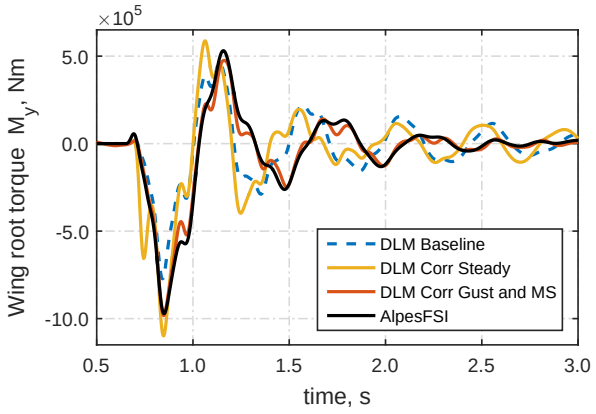

(b) Root torque M_y, $L_g = 18.28\ m$.

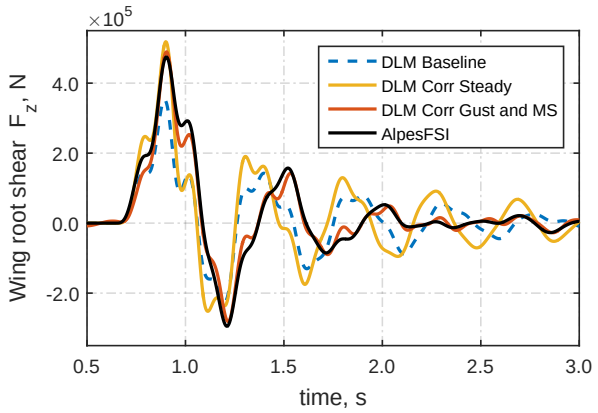

(c) Root shear F_z, $L_g = 42.67\ m$.

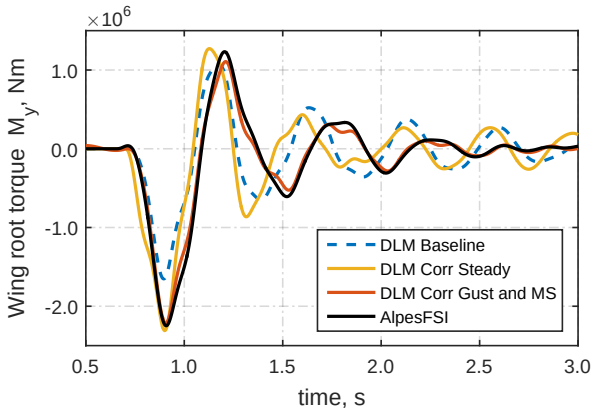

(d) Root torque M_y, $L_g = 42.67\ m$.

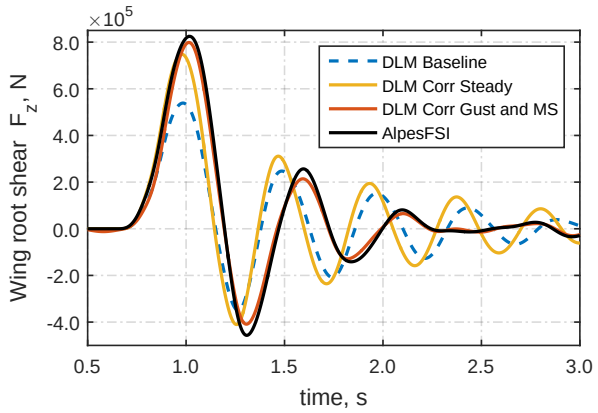

(e) Root shear F_z, $L_g = 91.44m$.

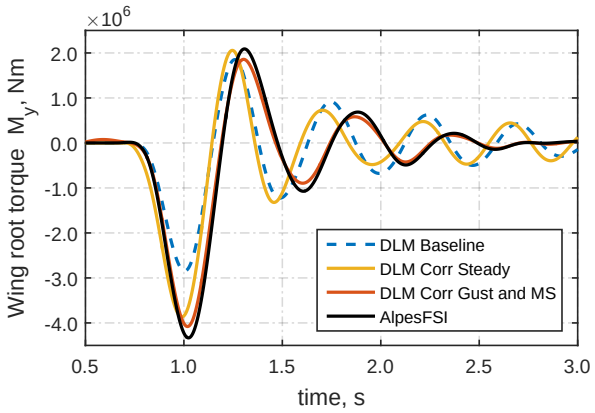

(f) Root torque M_y, $L_g = 91.44\ m$.

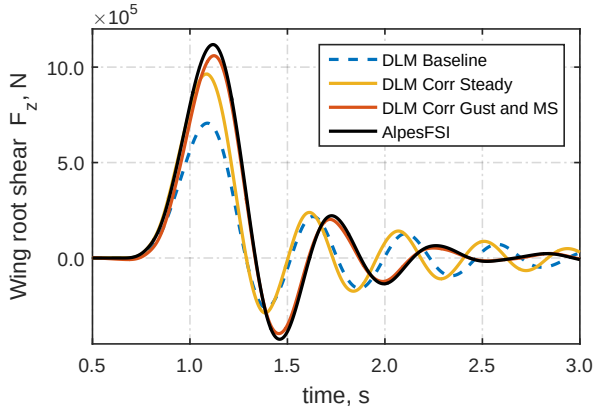

(g) Root shear F_z, $L_g = 152.40\ m$.

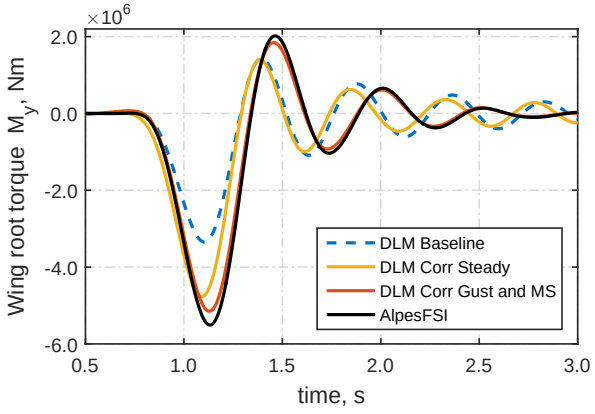

(h) Root torque M_y, $L_g = 152.40\ m$.

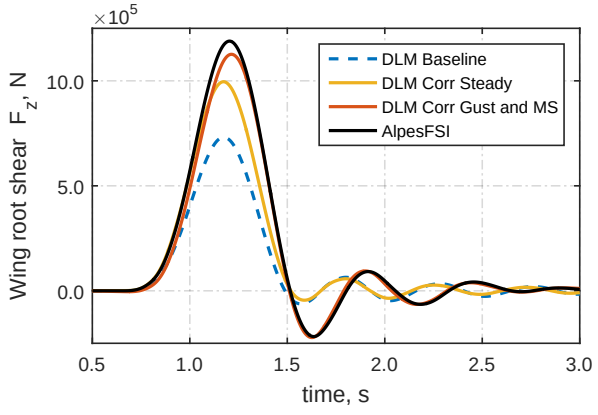

(i) Root shear F_z, $L_g = 213.36\ m$.

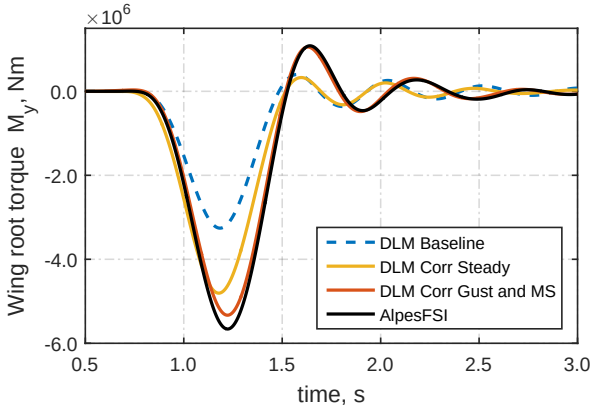

(j) Root torque M_y, $L_g = 213.36\ m$.

Figure 6.27: Wing root shear and torque for the reference gust lengths for a transonic flight condition $M = 0.85$. Comparison of a steady correction approach and the correction method considering gust and mode shapes.

6.8 Computational cost

All the analysis presented in this chapter has been performed via the Advanced Computing Research Centre (ACRC) at the University of Bristol using the High Performance Computing (HPC) BlueCristal Phase 3 (BCP3) [119]. All the AlpesFSI, CFD and LFD simulations have been performed employing the parallelization capability based on domain decomposition with MPI communication (Message Passing Interface) available in the DLR TAU-code, as described in Section 3.1. Several tests have been performed in order to identify the best option between computational efficiency and transfer of information, in addition to queuing time for job submission. The best trade off has been to submit the simulation on 1 node including 16×2.6GHz Intel SandyBridge cores on BCP3. The simulations using MSC Nastran were always submitted to BCP3 but using a single core per job. In Table 6.4 a comparison of the computation cost for the different types of simulation is shown. The high fidelity AlpesFSI simulations are by far the most expensive analyses to perform, with about 12 hours of running time for each gust length and 4 sec of simulation. The rigid CFD analysis requires about 8 minutes to converge to a residual of 10^{-8}. Each LFD simulation requires about 4 minutes. The MSC Nastran gust analysis about 2 minutes.

Simulation type	Simulation platform, cores	Time, minutes
AlpesFSI	16×2.6 GHz	720
TAU CFD	16×2.6 GHz	8
TAU LFD	16×2.6 GHz	4
MSC Natran SOL146	1×2.6GHz	2

Table 6.4: Computational cost comparison.

Correction type	Analyses, number	Time, minutes
DLM Corr Steady	2 CFD	16
DLM Corr Only Gust	25 LFD	100
DLM Corr Gust and MS	100 LFD	400
DLM Corr Gust and MS Interpolated	24 LFD	96

Table 6.5: Computational cost to generate the correction methods.

CHAPTER 7

A doublet-lattice method correction approach application using RANS simulations

In the present chapter the correction technique will be applied to a full aircraft model, representative of a large civil aircraft. The computational fluid dynamic model, in this case is a half aircraft model, and accounts for viscous effects by solution of the RANS equations.

7.1 NASA Common Research Model

The model chosen to apply the correction method is a test case representative of a large transportation aircraft, the NASA Common Research Model (NCRM) [120]. This model configuration consists of a half CFD model including wing, fuselage and horizontal tail plane and is shown in Figure 7.1. Vertical tail plane, pylon and engine are not modelled in this test case. The reference aerodynamic geometry is based on the publicly available model developed for the AIAA 4th Drag Prediction Workshop by DLR [120]. The simulations were carried out using the coarse Solar mesh which consist of a hybrid structured-unstructured mesh, which has approx 3.7 millions volume points, and 100014 grid points on the surface (as shown in Figure 7.1). A hemispheric far field boundary is defined with a radius of $757\ m$. Symmetry boundary conditions are defined in the x-z plane at the middle of the fuselage.

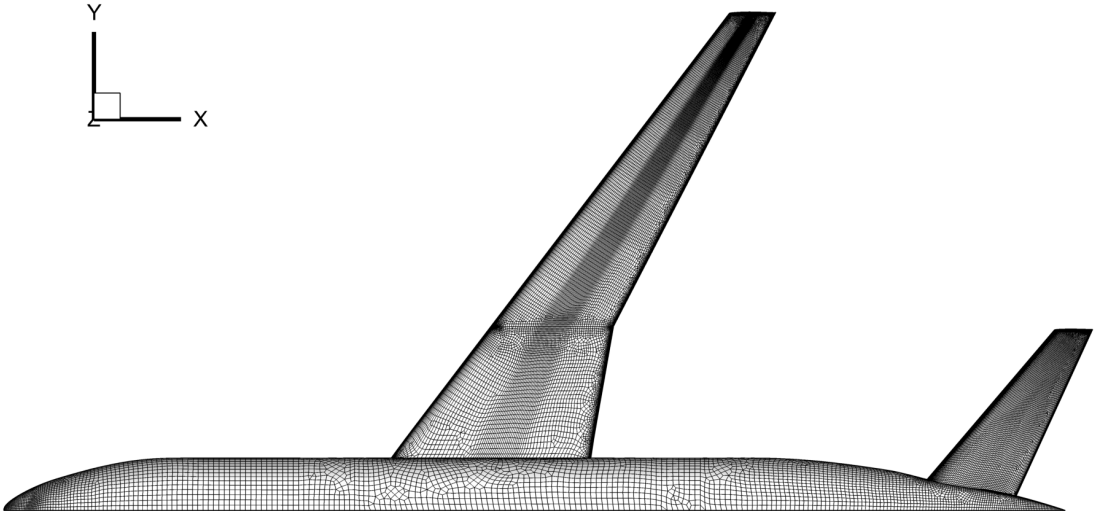

Figure 7.1: NCRM CFD Mesh Top view.

The model has been investigated considering a reference cruise flight condition at $1g$ and in order to compare the results with DLM method available in Nastran an angle of attack of 0 degrees has been chosen. In Table 7.1 the flight parameters used for the investigation are given. All the simulations have been performed using the negative Spalart-Allmaras turbulence model [121].

Parameter	Value
Angel of attack	0 deg
Mach number	0.86
Velocity	260.71 m/s
Altitude	9142 m
Density	0.4587 kg/m^3
Temperature	228.723 K
Reference length	7.0 m
Reynolds number	$56.3 \cdot 10^6$

Table 7.1: Flight parameters used to identify the steady aeroelastic flight shape.

The structural model used in the analysis is given in a dynamically condensed form, in terms of mass and stiffness matrices, known as the FERMAT FEM [122]. Two mass configuration are available for this model, but in the present investigation only the maximum take-off weight case has been used. The aeroelastic static deformation has been identified using the fully coupled CFD/FEM analysis by means of the AlpesFSI interface. Including the effect of the gravity in the analysis, a wing tip vertical displacement of 6.09 cm from the given flight shape has been

found. Figure 7.2 shows the c_p distribution over the trimmed aeroelastic surface mesh.

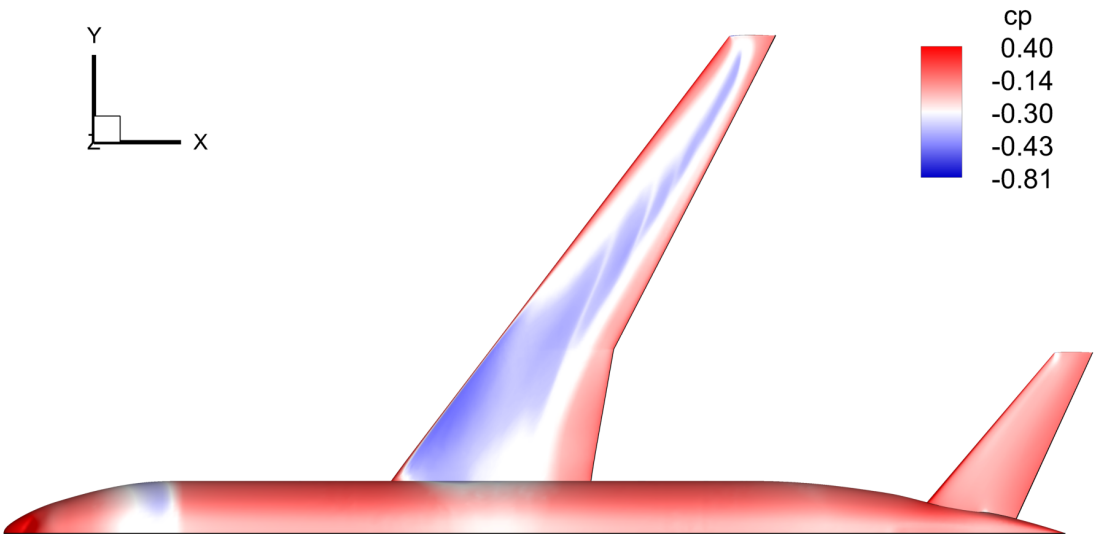

Figure 7.2: NCRM CFD Mesh Top view, cp distribution at trim.

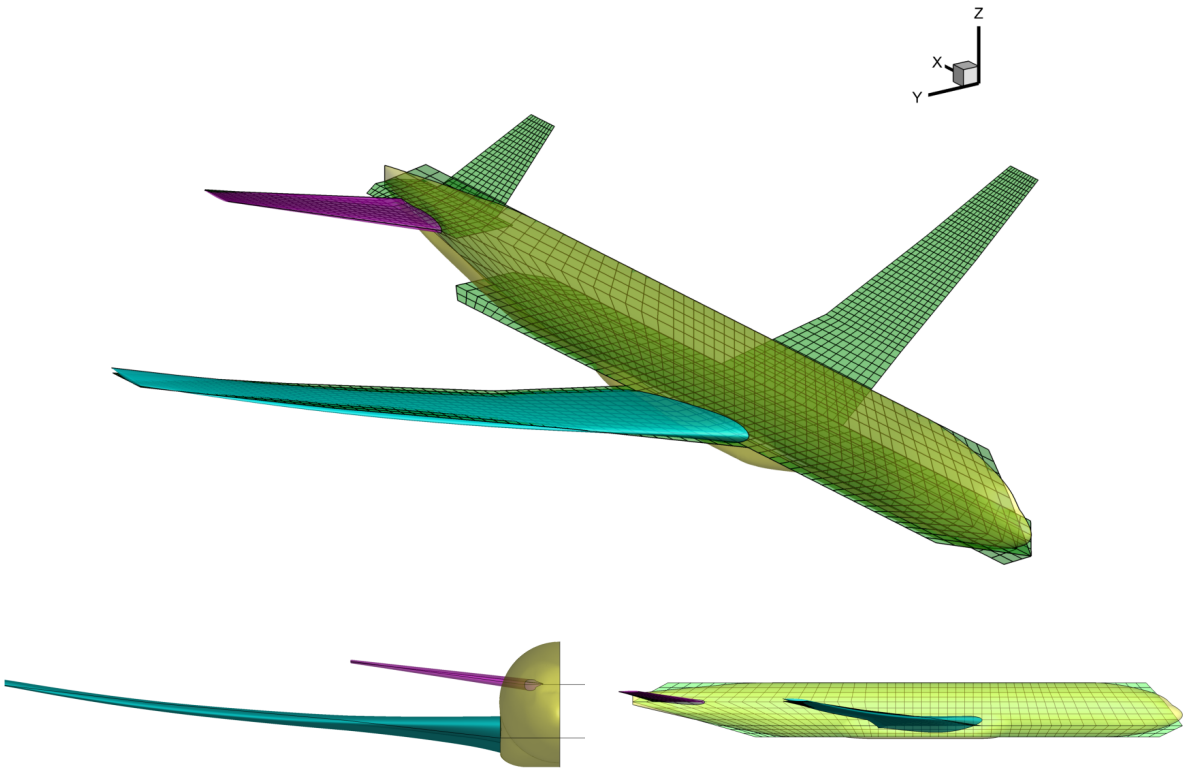

Figure 7.3: Comparison of DLM and CFD mesh for NASA Common Research Model.

A new doublet-lattice mesh has been created, including the fuselage and a comparison of the CFD and DLM model is shown in Figure 7.3. In order to match with the full structural model,

both right and left parts of the aircraft have been modelled in the panel aero mesh. However the corrections have been evaluated considering only the left wing and then symmetrised on the right side. For the wing DLM mesh 12 panels have been considered in the chord-wise direction, and 52 along the span for a total of 624 panels.

7.2 Aeroelastic gust response

The aeroelastic response to a discrete gust, with a one minus cosine shape, has been studied. Three different discrete gust lengths have been considered, being representative of a "short", "medium" and "long" gust length. Table 7.2 summarises the parameters used for the gust investigations. Initially nominal gust amplitudes have been considered matching that specified by the regulations CS-25.

$AoA,\ deg$	$L_g,\ m$	$W_g^{TAS},\ m/s$	M	$\alpha_g,\ deg$	$T_g,\ sec$	$f_g,\ Hz$
0.0	18.28	11.24	0.86	2.46	0.070	14.29
0.0	91.44	14.70	0.86	3.22	0.350	2.86
0.0	213.36	16.94	0.86	3.71	0.818	1.22

Table 7.2: One minus cosine gust profiles with nominal CS-25 amplitude.

The model has been considered clamped at the center of the fuselage and only the wing flexibility has been accounted for. As will be clear in the following section, it is worth stating that for higher gust amplitudes (in particular for the longer gust) significant structural deformations are found for these clamped cases. A free free aircraft model would not experience the same level of deformation. As explained in Chapter 4, the AlpesFSI interface is not able to account for rigid body modes in the formulation used for the present work. The large structural deformations produce a nonlinear aeroelastic response, which is outside the range of applicability of the time-linearised aerodynamic simulation used to compute the corrections for the DLM method. For this reason additional comparisons have been performed by scaling the gust amplitude to 50% and 75% of the nominal ones, in order to test the applicability of the correction methodology to gusts prescribed by the CS-25 regulations. The corresponding parameters are given in Table 7.3 and 7.4 respectively.

$AoA,\ deg$	$L_g,\ m$	$W_g^{TAS},\ m/s$	M	$\alpha_g,\ deg$	$T_g,\ sec$
0.0	18.28	5.62	0.86	1.23	0.070
0.0	91.44	7.35	0.86	1.61	0.350
0.0	213.36	8.47	0.86	1.86	0.818

Table 7.3: One minus cosine gust profiles with 50% of CS-25 amplitude.

$AoA,\ deg$	$L_g,\ m$	$W_g^{TAS},\ m/s$	M	$\alpha_g,\ deg$	$T_g,\ sec$
0.0	18.28	8.43	0.86	1.85	0.070
0.0	91.44	11.02	0.86	2.42	0.350
0.0	213.36	12.70	0.86	2.79	0.818

Table 7.4: One minus cosine gust profiles with 75% of CS-25 amplitude.

7.3 LFD results for NCRM

To perform the correction process a range of reduced frequencies between 0.01 and 4.0 has been selected, corresponding to frequencies between 0.077 Hz and 30.88 Hz. To compute the reference aerodynamic loads, 13 strips have been selected along the wing span. Figure 7.4 shows the strip subdivision along the wing span.

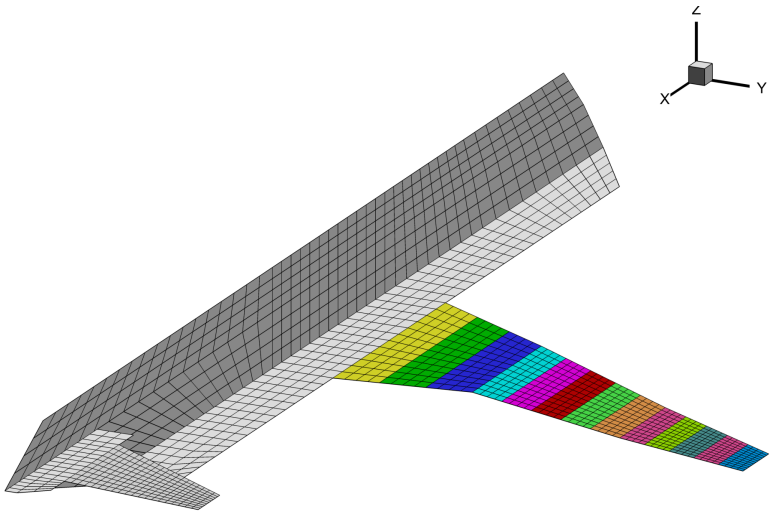

Figure 7.4: NCRM right wing DLM mesh strip suddivision.

The first step in the correction procedure has involved the computation of the reference aerodynamic loads, due to a sinusoidal gust for the range of reduced frequencies, κ, selected. Table 7.5 lists the reduced frequencies at which the aerodynamic loads have been computed.

Vertical forces and pitching moments are reported in terms of amplitude and phase as a function

κ	Frequency, Hz	Wave length, m	κ	Frequency, Hz	Wave length, m
0.01	0.08	2199.11	1.00	7.72	21.99
0.05	0.39	439.82	1.20	9.27	18.33
0.10	0.77	219.91	1.50	11.58	14.66
0.20	1.54	109.96	2.00	15.44	11.00
0.30	2.32	73.30	2.50	19.30	8.80
0.50	3.86	43.98	3.00	23.16	7.33
0.60	4.63	36.65	3.50	27.02	6.28
0.80	6.18	27.49	4.00	30.88	5.50

Table 7.5: Reduced frequency list considered for DLM correction

of the reduced frequency, for the thirteen strips. Figure 7.5 shows the vertical force F_z and pitching moment M_y, for these strips as a function of the reduced frequency κ.

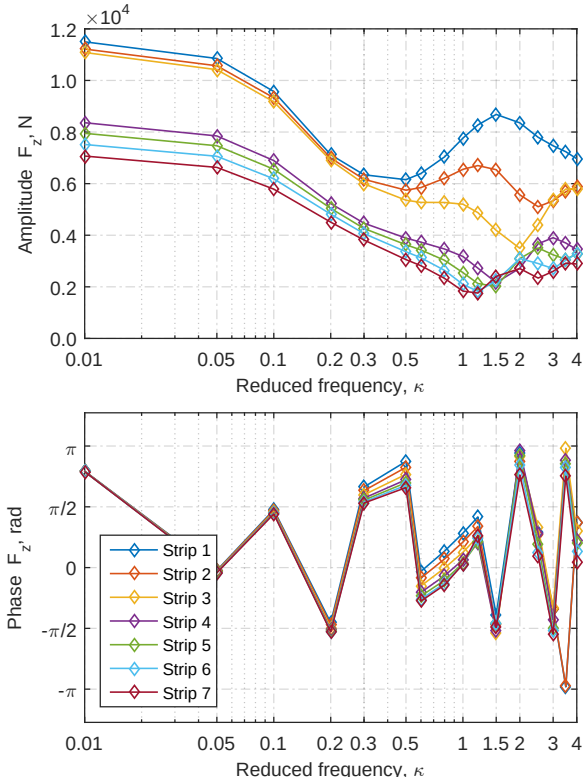

(a) LFD vertical force for strip 1 to 7.

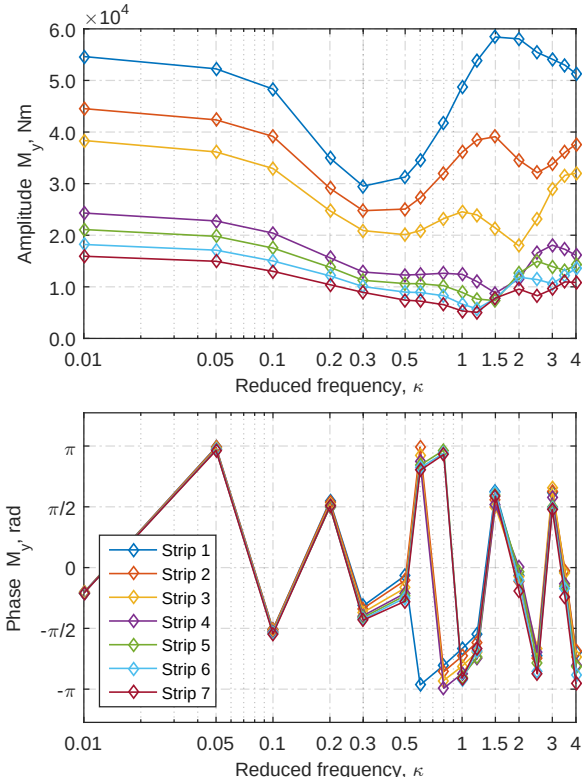

(b) LFD pitching moment for strip 1 to 7.

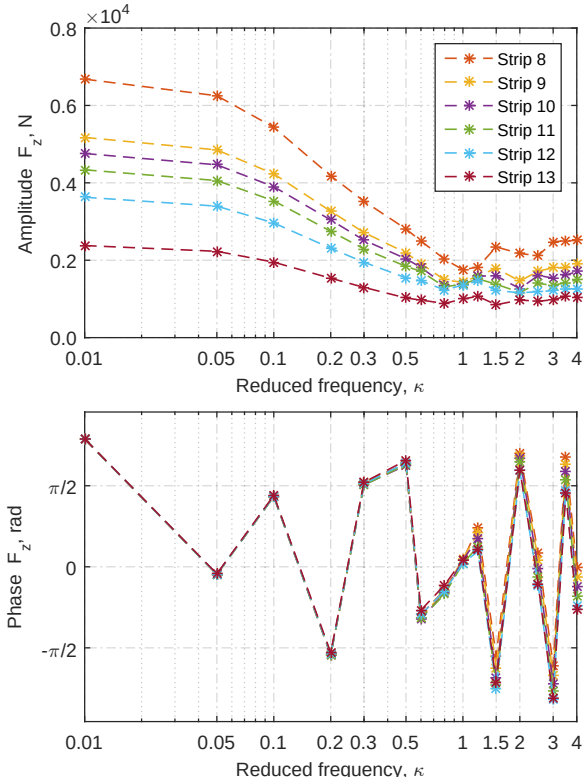

(c) LFD vertical force for strip 8 to 13.

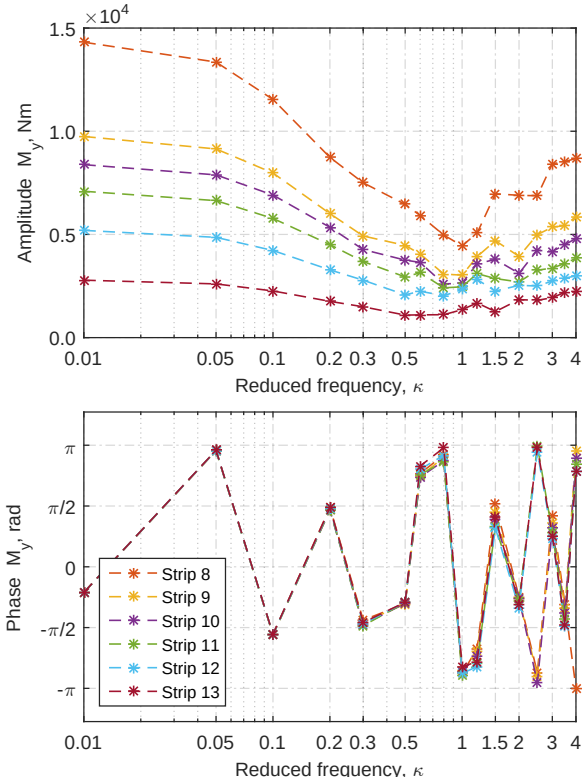

(d) LFD pitching moment for strip 8 to 13.

Figure 7.5: LFD vertical force and pitching moment for sinusoidal gust.

To compute the correction accounting for structural flexible effects, three deformations of the wing have been considered: the first and second wing bending, Figure 7.6 and 7.7, together with the first wing torsion Figure 7.8. The structural mode shape deformation has been obtained by running a normal modes analysis and then mapping to the CFD mesh surface. The properties of the three modes selected are reported in Table 7.6.

Mode number	Mode name	Frequency, Hz
2	Right wing 1^{st} wing bending	0.99
8	Right wing 2^{nd} wing bending	2.71
21	Right wing 1^{st} wing torsion	10.59

Table 7.6: Wing natural modes used in the correction process.

In order to remain in the linear region, the linear frequency domain analysis for mode shape deformation has been computed considering a small wing tip deflection. The normal modes deformation mapped to the CFD mesh surface have been scaled to 10% of the maximum deformation.

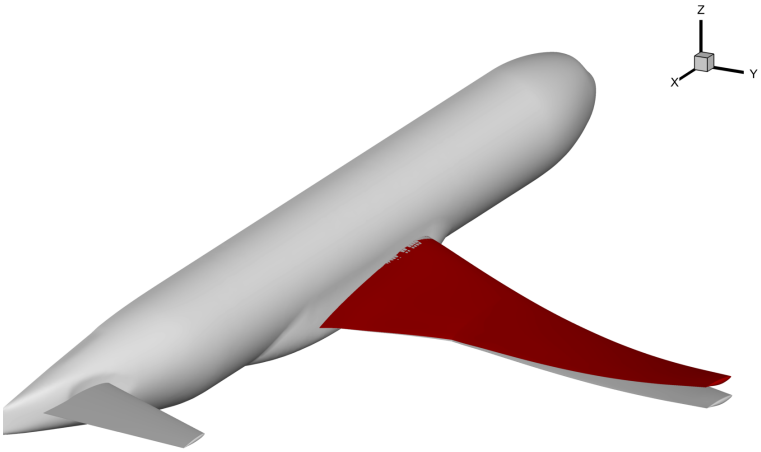

Figure 7.6: NCRM first wing bending mode shape mapped to the CFD surface mesh.

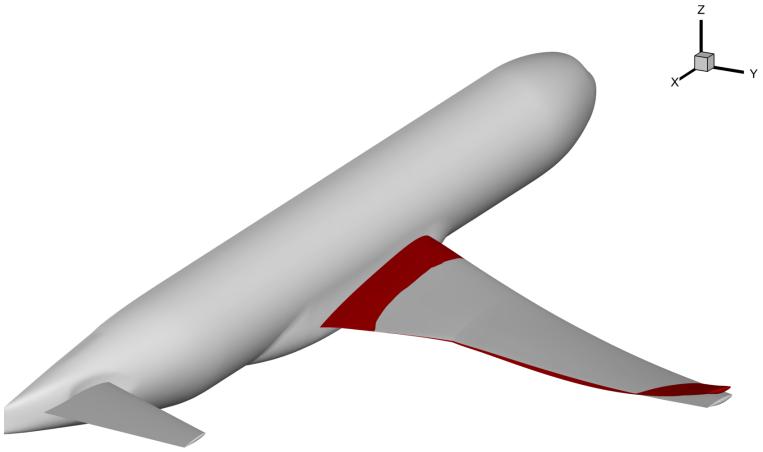

Figure 7.7: NCRM second wing bending mode shape mapped to the CFD surface mesh.

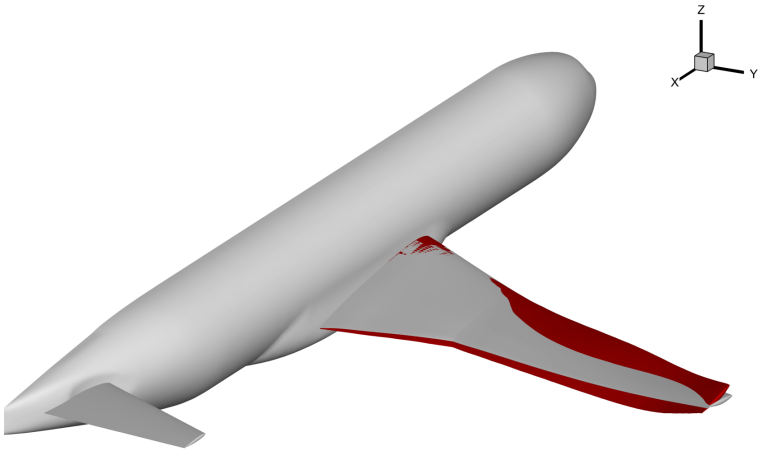

Figure 7.8: NCRM first wing torsion mode shape mapped to the CFD surface mesh.

In Figure 7.9 the LFD results of vertical force and pitching moment, due to the 1^{st} wing bending deformation, are plotted as a function of the reduced frequency for the 13 strips along the wing. In a similar way, Figure 7.10 and Figure 7.11 report the LFD results for the 2^{nd} wing bending and 1^{st} wing torsion.

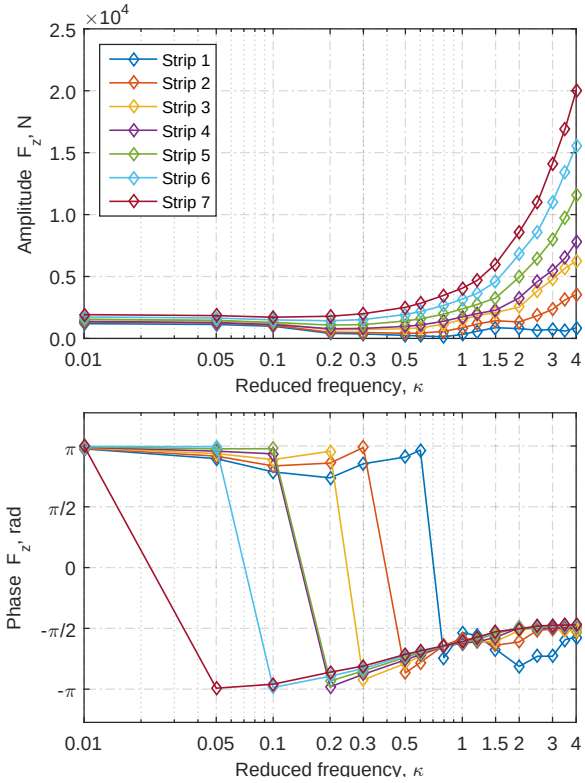

(a) Vertical force strip from 1 to 7.

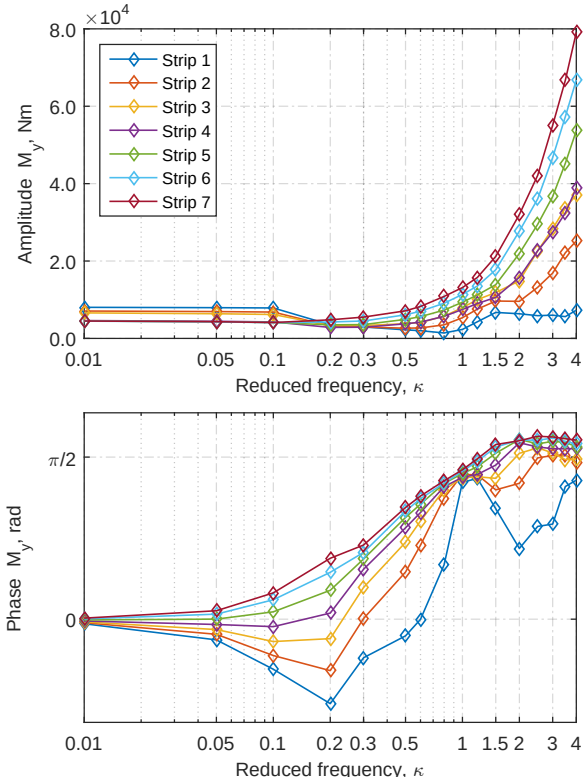

(b) Pitching moment strips from 1 to 7.

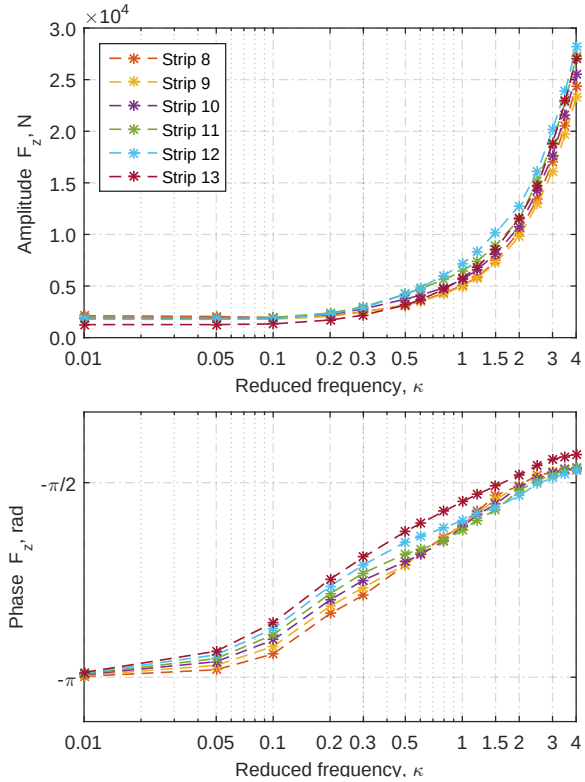

(c) Vertical force strip from 8 to 13.

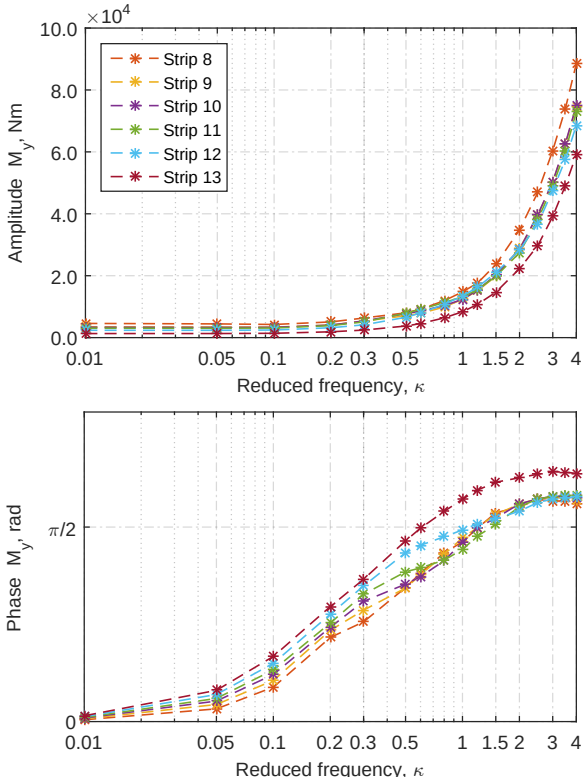

(d) Pitching moment strips from 8 to 13.

Figure 7.9: LFD vertical force and pitching moment for Mode 1: 1^{st} wing bending

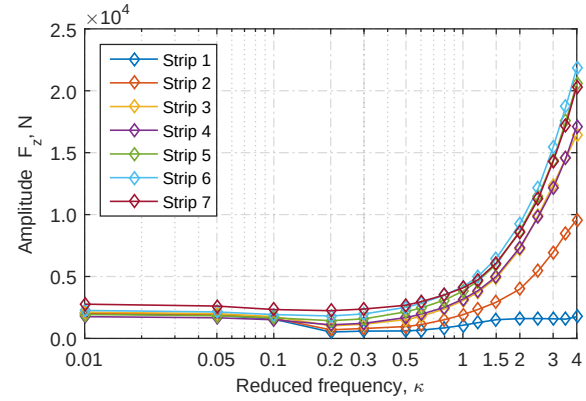

(a) Vertical force strip from 1 to 7.

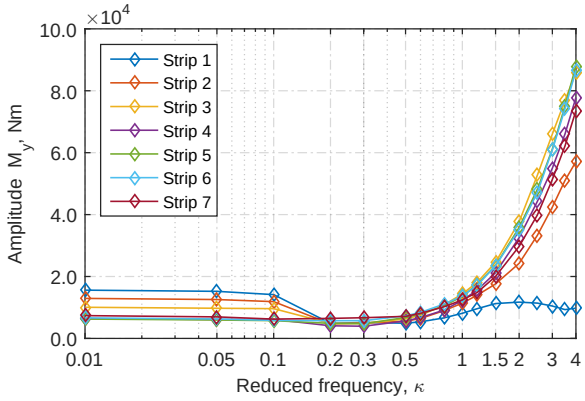

(b) Pitching moment strips from 1 to 7.

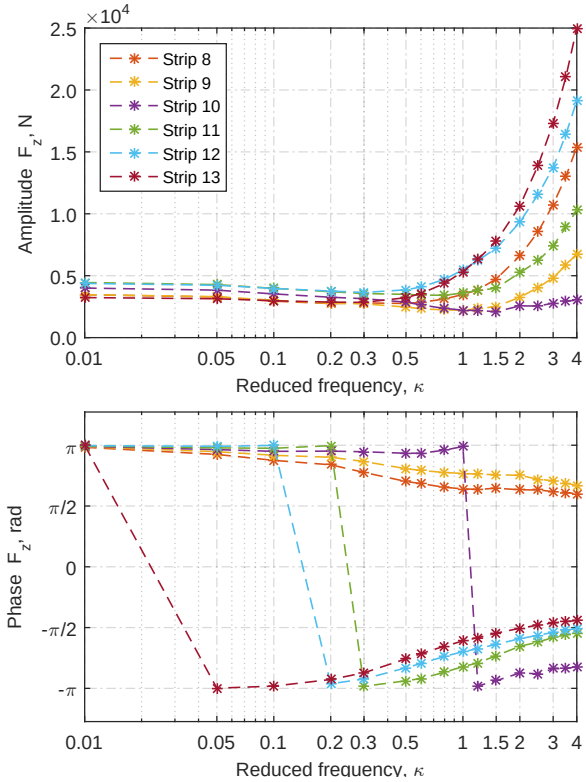

(c) Vertical force strip from 8 to 13.

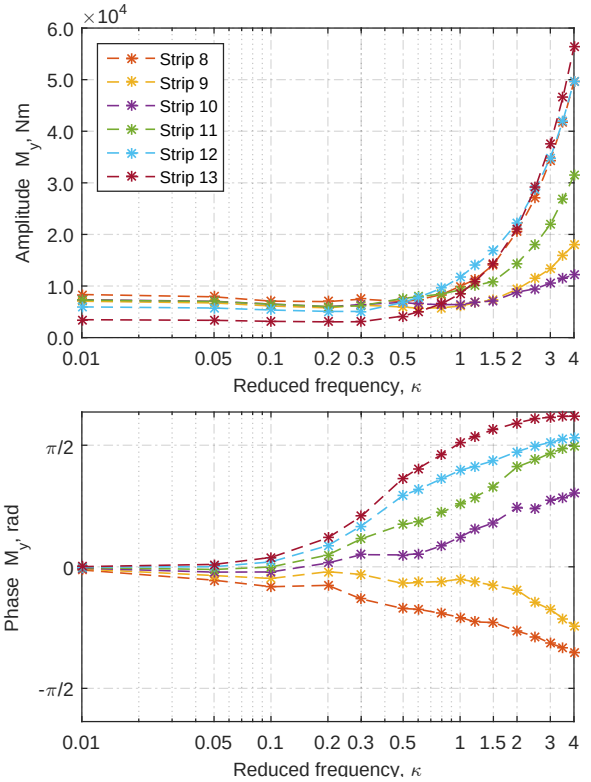

(d) Pitching moment strips from 8 to 13.

Figure 7.10: LFD vertical force and pitching moment for Mode 2: 2^{nd} wing bending

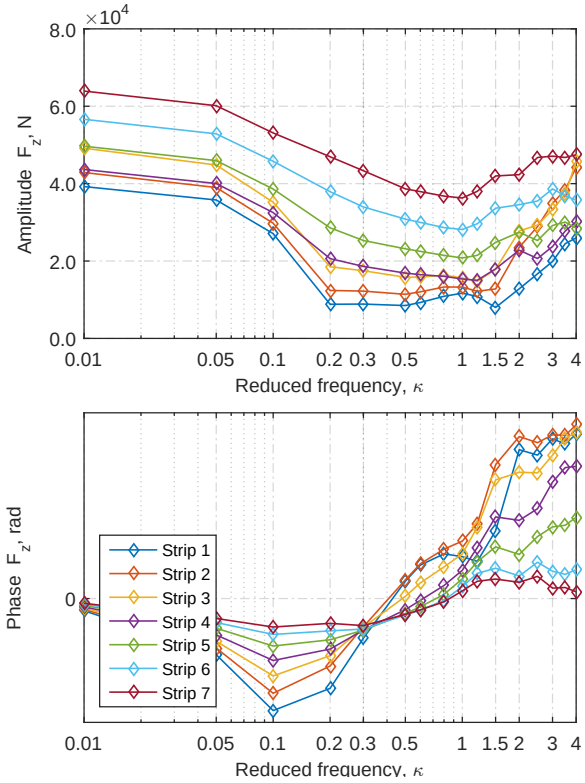

(a) Vertical force strip from 1 to 7.

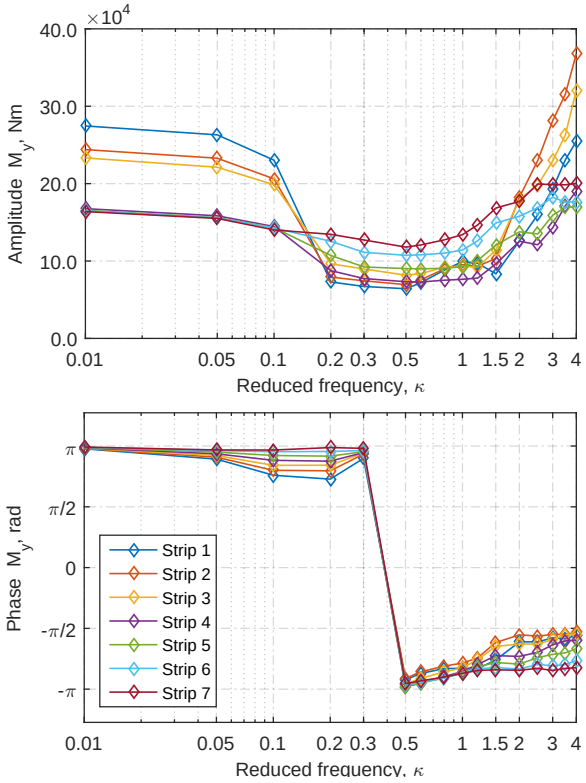

(b) Pitching moment strips from 1 to 7.

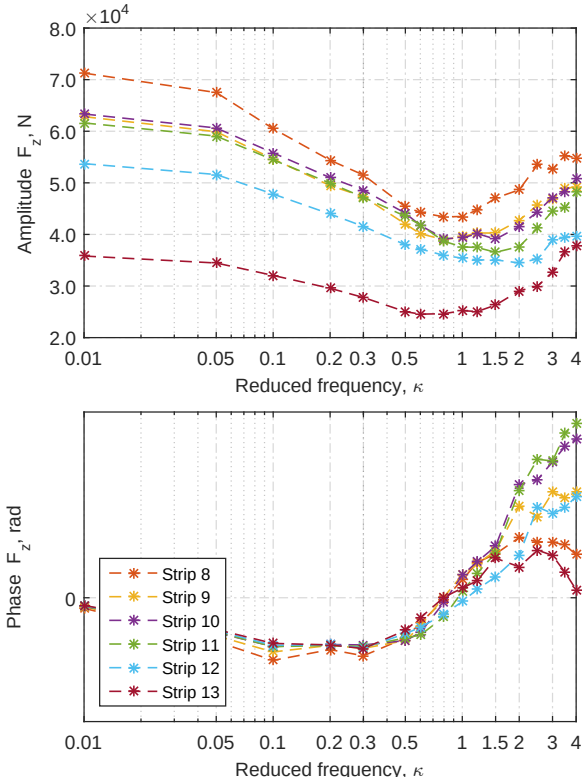

(c) Vertical force strip from 8 to 13.

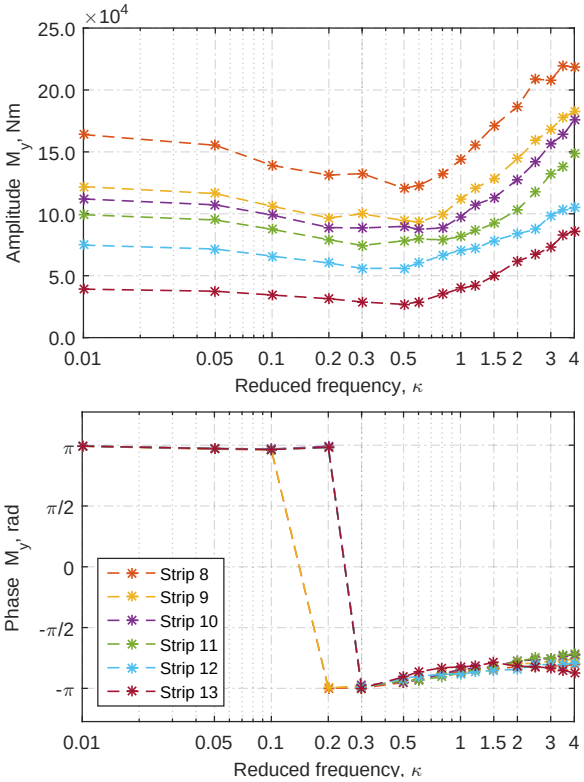

(d) Pitching moment strips from 8 to 13.

Figure 7.11: LFD vertical force and pitching moment for Mode 3: 1^{st} wing torsion

7.4 Rigid Gust Loads Correction

The total wing vertical forces and pitching moments are plotted for the different gust lengths in Figure 7.12, considering only the rigid gust loads.

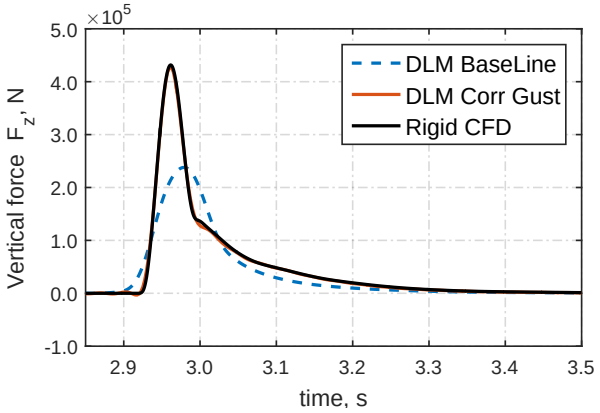

(a) Vertical force F_z, $L_g = 18.28\ m$.

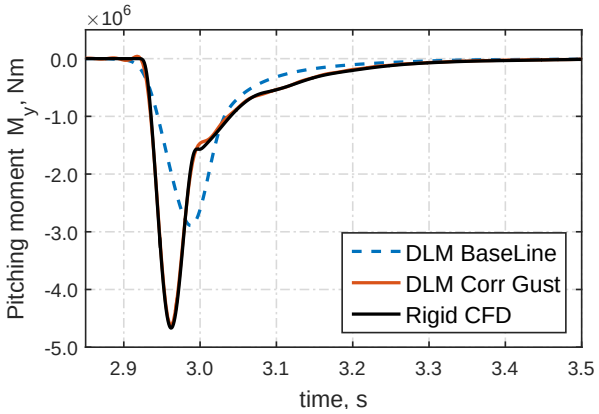

(b) Pitching moment M_y, $L_g = 18.28\ m$.

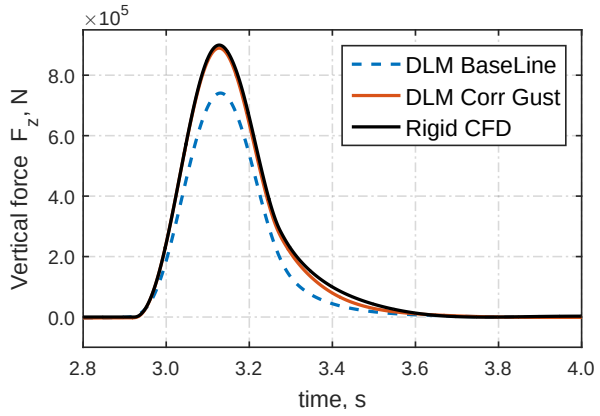

(c) Vertical force F_z, $L_g = 91.44\ m$.

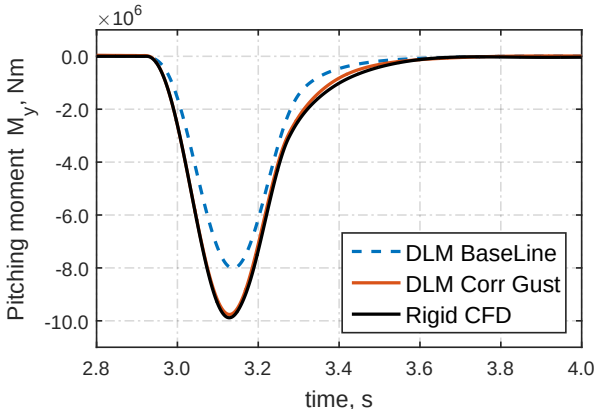

(d) Pitching moment M_y, $L_g = 91.44\ m$.

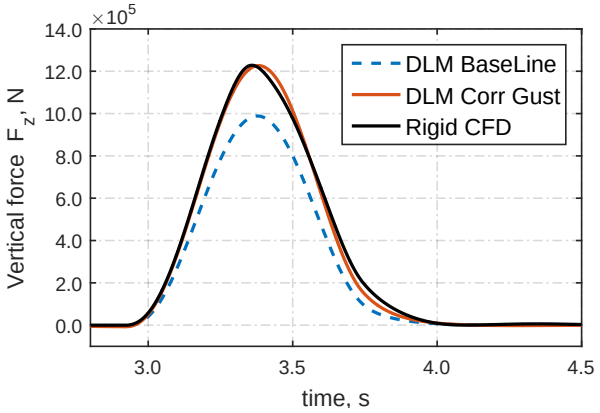

(e) Vertical force F_z, $L_g = 213.36\ m$.

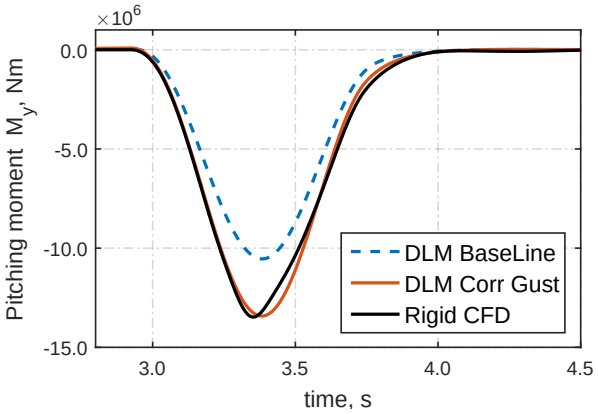

(f) Pitching moment M_y, $L_g = 213.36\ m$.

Figure 7.12: Aerodynamic loads computed with Baseline DLM, Corrected DLM rigid CFD, for the NASA common research model.

The correction approach using LFD for the sinusoidal gusts is able to produce a good approximation of the gust loads for the short and medium gust length. However for the longest gust case nonlinear effects become relevant and the correction method, based on linear assumptions, shows a slight difference from the CFD analysis.

7.5 Aeroelastic gust simulations for NCRM

The aeroelastic high fidelity gust response aerodynamic loads have been computed using the strongly coupled CFD/FEM analysis environment, AlpesFSI. For the structural part of the simulation, geometric nonlinear effects due to large displacement and rotation have been neglected, since such effects can not be accounted for in the frequency domain simulation. In the coupled simulation, the fuselage has been considered constrained and only the aerodynamic wing loads have been applied to the structure. The total wing aerodynamic loads have been integrated from the c_p grid value given by the CFD TAU-Code.

To compare the effect of large structural deformation, a comparison of the fully coupled gust loads results for different gust amplitude, 50%, 75% and 100% of the prescribed vertical velocity defined by the regulation, is reported in Figure 7.13.

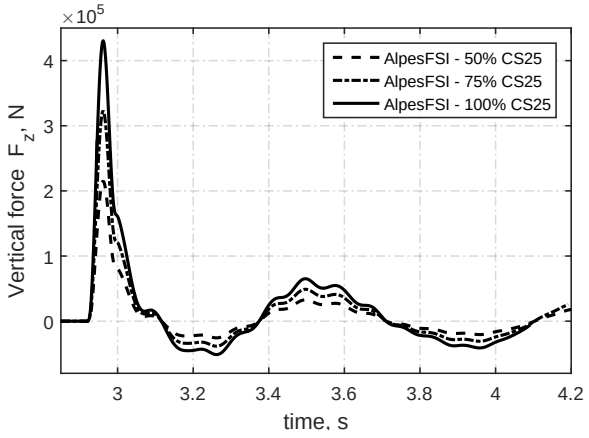

(a) Vertical force F_z, $L_g = 18.28\ m$.

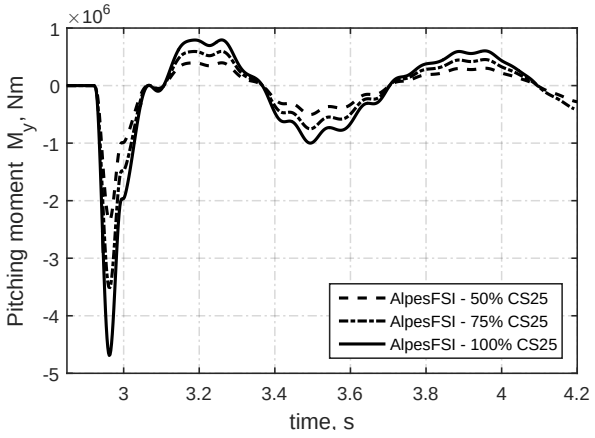

(b) Pitching moment M_y, $L_g = 18.28\ m$.

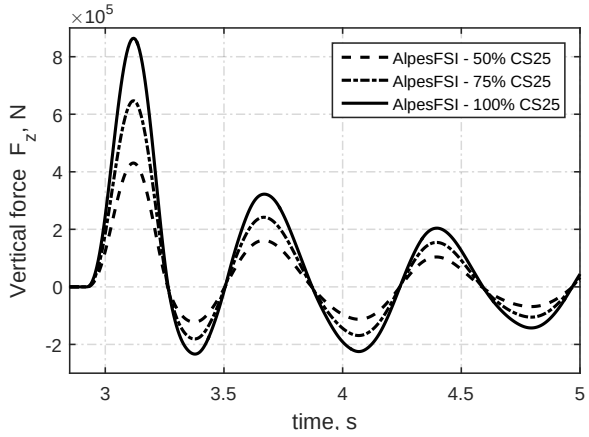

(c) Vertical force F_z, $L_g = 91.44\ m$.

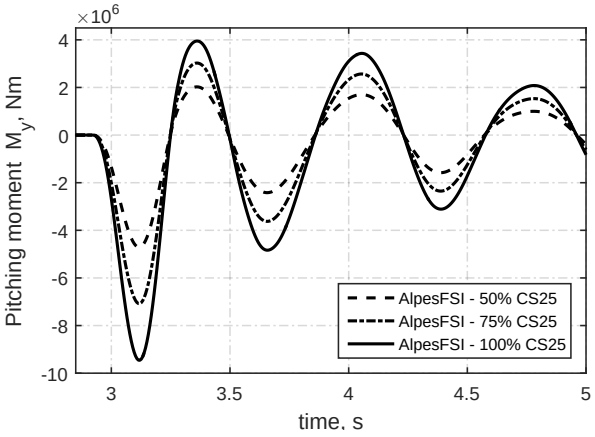

(d) Pitching moment M_y, $L_g = 91.44\ m$.

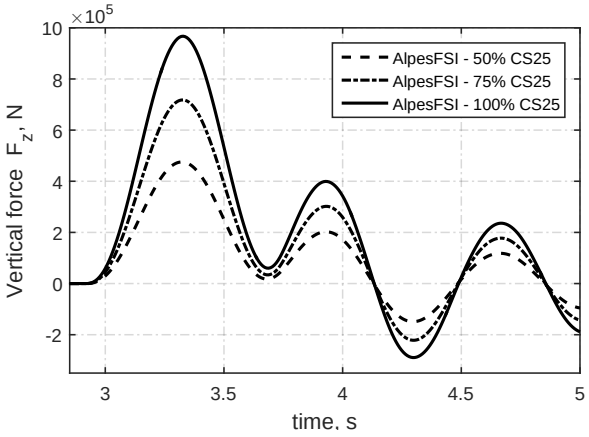

(e) Vertical force F_z, $L_g = 213.36\ m$.

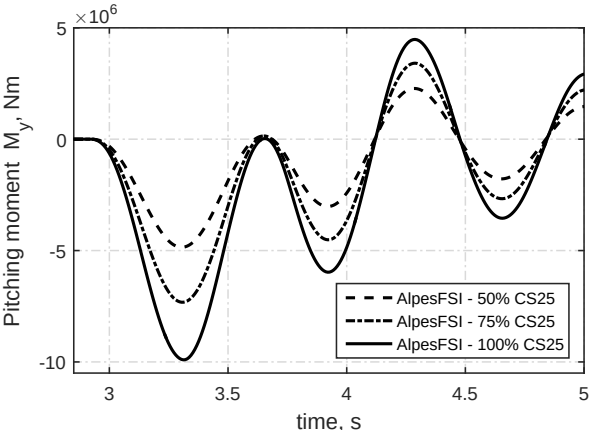

(f) Pitching moment M_y, $L_g = 213.36\ m$.

Figure 7.13: Comparison of total wing vertical force and pitching moment computed with AlpesFSI for the NASA common research model, scaling the gust amplitude to 50% and 75% versus the nominal gust amplitude prescribed by CS-25 regulation.

The fully coupled analysis environment does not show evidence of nonlinear behaviour for the flight point considered. A comparison of the wing tip deformation is reported in Figure 7.14, for

the three gust lengths considering the nominal gust amplitude as prescribed by the regulation.

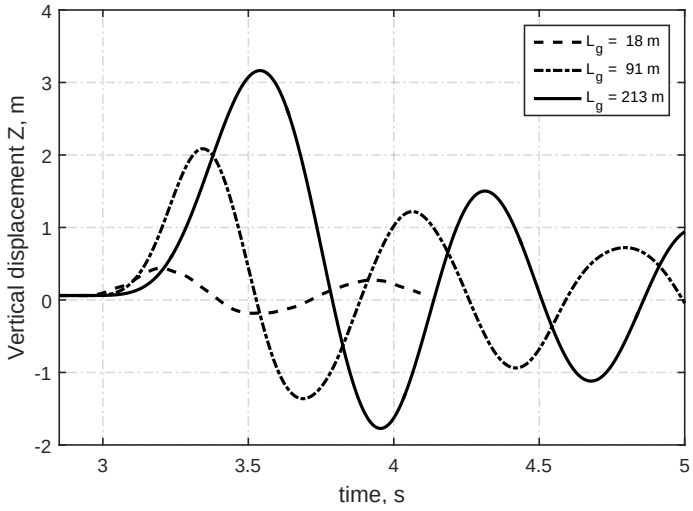

Figure 7.14: Wing tip displacement for the three gust length and nominal gust amplitude.

7.5.1 Corrected DLM using LFD simulations for gust and mode shapes

Using the corrected AIC matrices computed using only LFD simulations for sinusoidal gusts does not give an accurate estimate of the aeroelastic gust response, for a flexible aircraft structure, as shown in Figure 7.15. In this case for the shortest gust length it is possible to observe an oscillatory response in the corrected DLM which may be caused to exciting of a specific mode of vibration. The oscillatory response, in fact, has a frequency of about 9.52 Hz, very close to the frequency of the correction computed at the reduced frequency $\kappa = 1.2$ of 9.27 Hz, as given from Table 7.5.

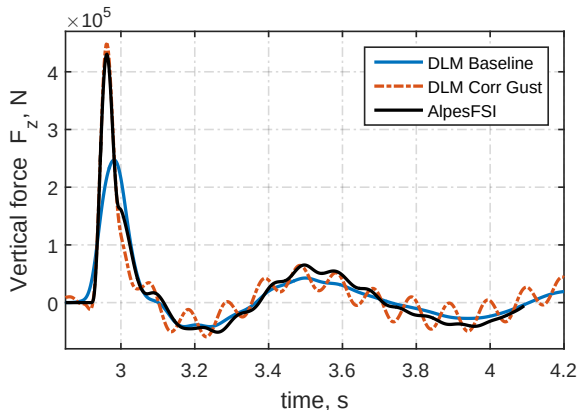

(a) Vertical force F_z, $L_g = 18.28\ m$.

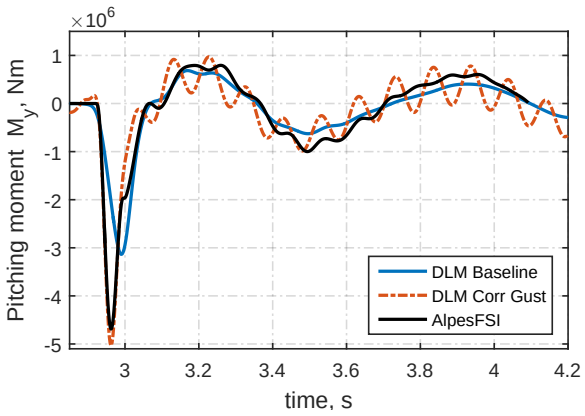

(b) Pitching moment M_y, $L_g = 18.28\ m$.

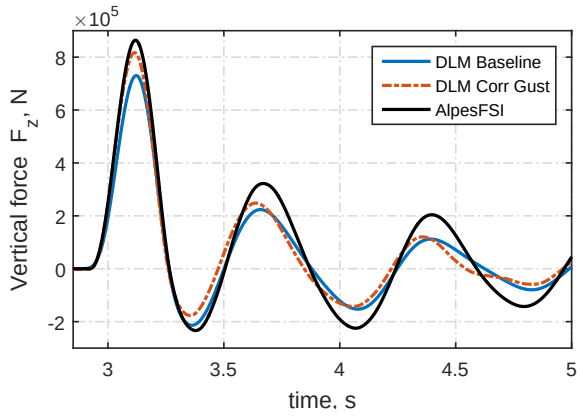

(c) Vertical force F_z, $L_g = 91.44\ m$.

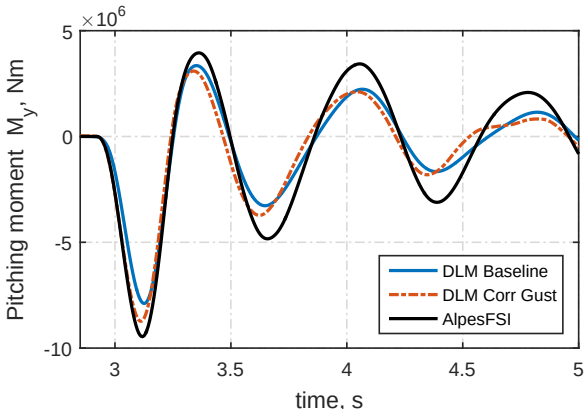

(d) Pitching moment M_y, $L_g = 91.44\ m$.

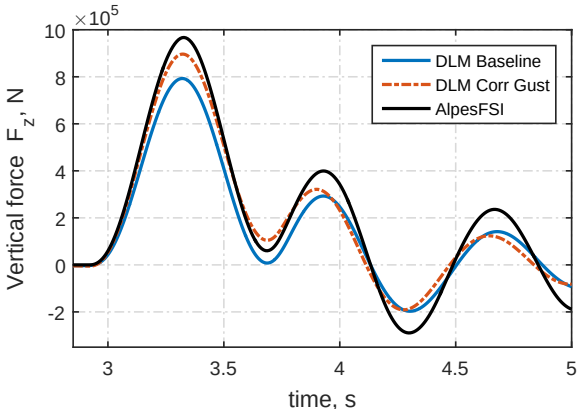

(e) Vertical force F_z, $L_g = 213.36\ m$.

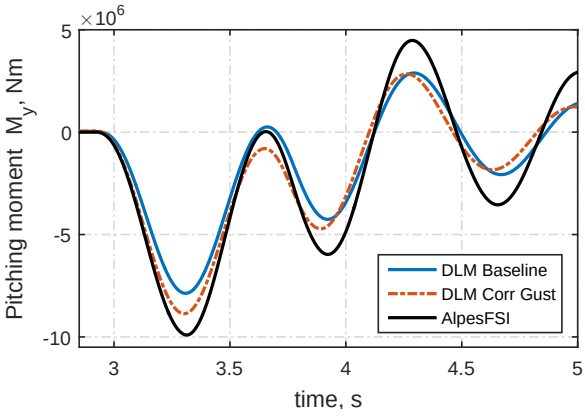

(f) Pitching moment M_y, $L_g = 213.36\ m$.

Figure 7.15: Comparison of vertical force and pitching moment for AlpesFSI, uncorrected DLM and corrected DLM using sinusoidal gust.

It is worth recalling that a different idealization for the structural damping is adopted in the AlpesFSI analysis compared to the DLM simulation. In the analysis in the frequency domain, a modal damping equal to the 2% of the critical damping is considered, while in the time domain simulation an equivalent viscous damping is adopted since the coefficient of the dynamic equation can not be complex.

To account for the structure flexibility, it is necessary to correct the AIC matrices considering the aerodynamic loads due to flexible mode deformations. In Chapter 6, for the FFAST wing test case, a unique choice of flexible modes that worked at the best for all the gust lengths was found. In the present test case a different choice of the mode selection has been necessary to get the optimal correction results. In fact, for the short gust length, $L_g = 18.28\ m$, the second wing bending and first wing torsion mode shape have been used. The resulting total wing aerodynamic vertical force, F_z, and pitching moment, M_y, are shown in Figure 7.16.

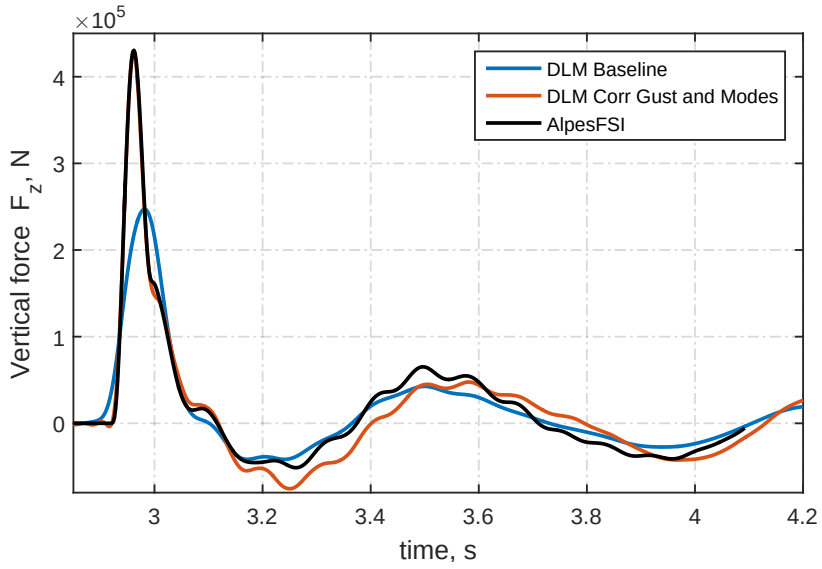

(a) Vertical force F_z, $L_g = 18.28\ m$.

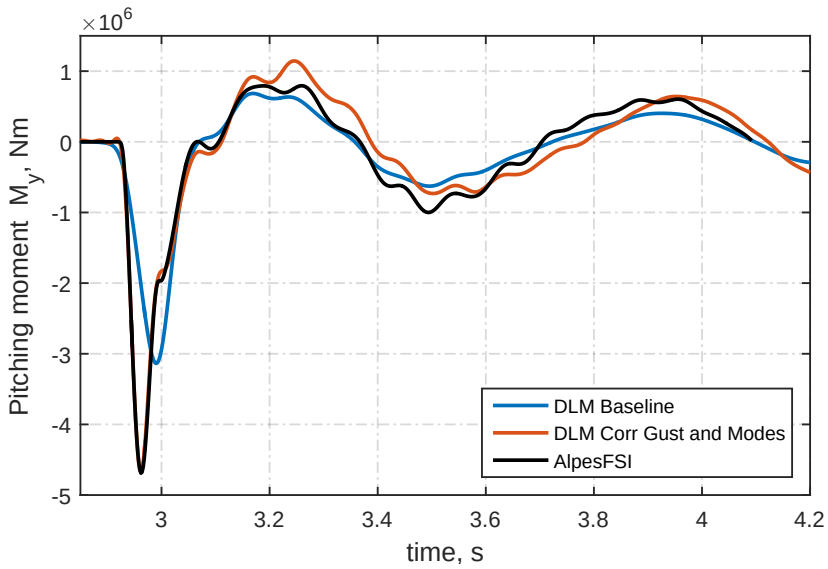

(b) Pitching moment M_y, $L_g = 18.28\ m$.

Figure 7.16: Comparison of vertical force and pitching moment for AlpesFSI, uncorrected and corrected DLM, for short gust length and nominal amplitude.

On the other hand, for the medium and long gust length the best results have been obtained using the first wing bending and first wing torsion modes, in the correction coefficient evaluation. The comparison of the uncorrected and corrected DLM versus the FSI analysis are shown in Figure 7.17 and Figure 7.18.

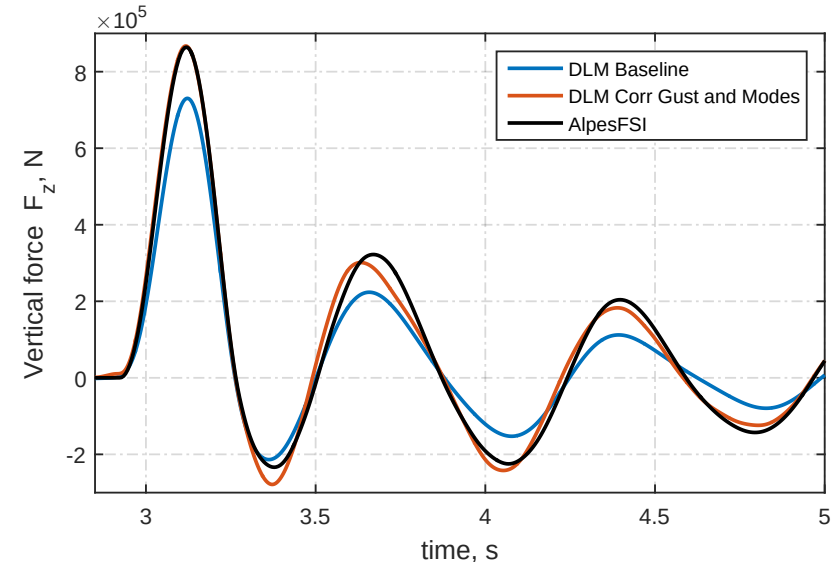

(a) Vertical force F_z, $L_g = 91.44\ m$.

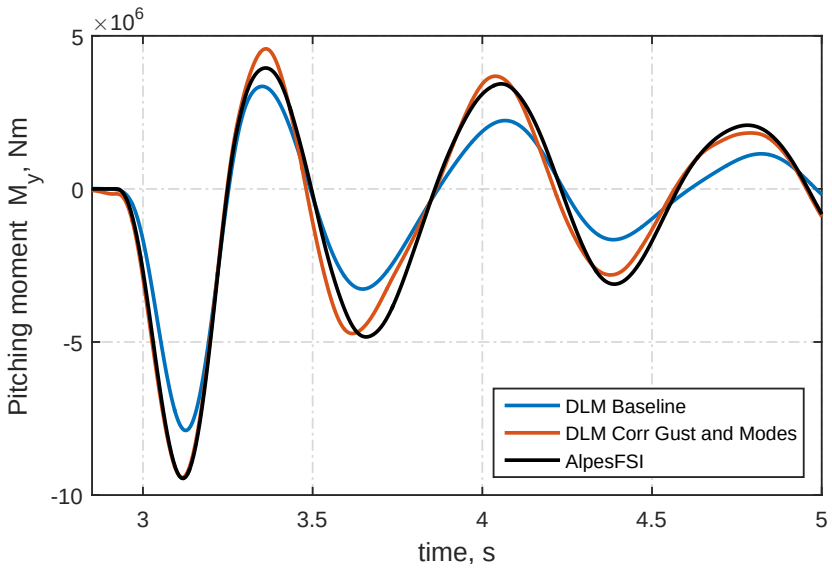

(b) Pitching moment M_y, $L_g = 91.44\ m$.

Figure 7.17: Comparison of vertical force and pitching moment for AlpesFSI, uncorrected and corrected DLM, for medium gust length and nominal amplitude.

The correction method presented is capable of capturing the maximum loads due to the gust perturbation very well, for all the gust lengths. The dynamic behaviour of the flexible structure is represented with very good accuracy, even though some more conservative results are estimated for the loads driven by the structural deformation.

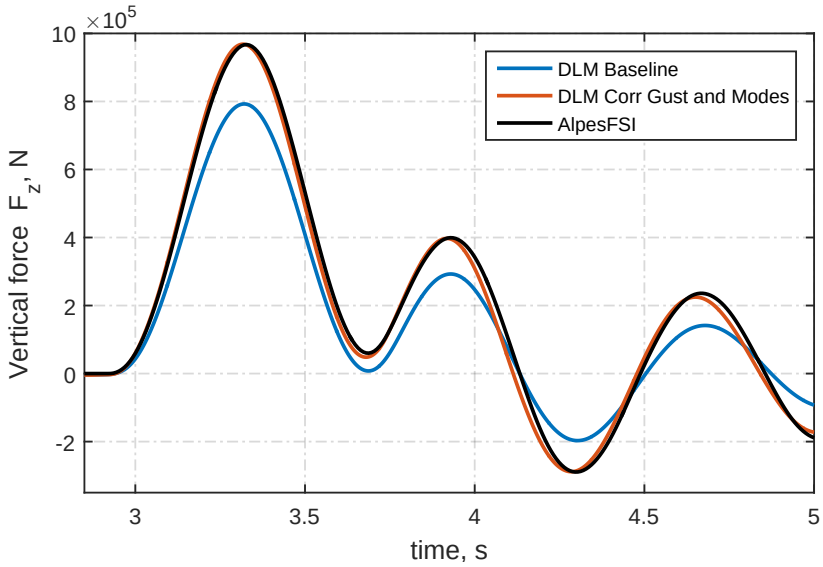

(a) Vertical force F_z, $L_g = 213.36\ m$.

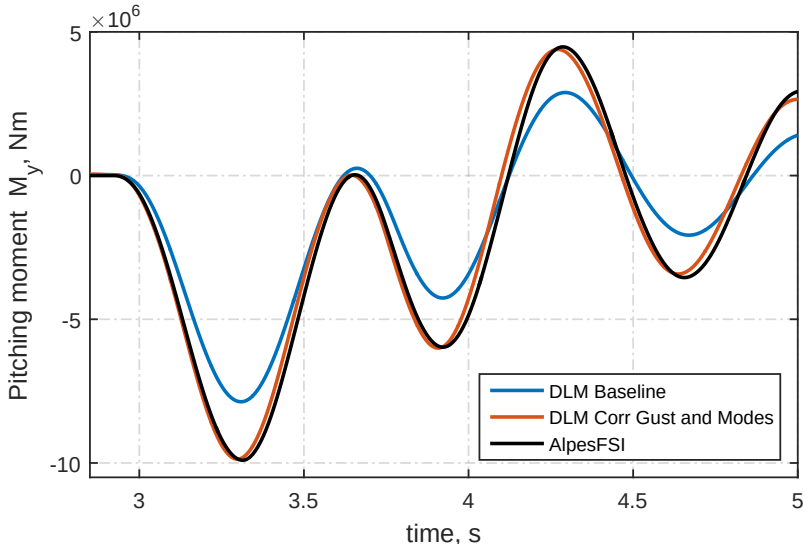

(b) Pitching moment M_y, $L_g = 213.36\ m$.

Figure 7.18: Comparison of vertical force and pitching moment for AlpesFSI, uncorrected and corrected DLM, for long gust length and nominal amplitude.

The reasons for the slight deviation of the corrected method compared to the fully coupled analysis are not clear. One of the possible reasons is related to the interpolation methodology used to map the forces and displacement in the two different models, CFD and DLM. The six degree of freedom splines that were implemented interpolate the deformations on a three dimensional aerodynamic shape of the CFD model, compared to the flat panel model of the DLM.

7.5.2 Modal participation factor for mode shape selection

The correction method presented has demonstrated a very good capability to account for unsteady effects in the transonic regime. An essential part of the correction as been accounting for the mode shape deformation, which has permitted better capture of the interaction between the flow and the deforming structure, improving the dynamic response of the model. In this regard, the application of the method to a full aircraft solved with RANS equations, has highlighted how the selection of the appropriate mode shapes to correct is a key aspect to achieve a good correction. In the present formulation of the correction method, several mode shapes can be used to correct the flexible loads increment. However since each of the modes will be treated with the same importance the minimization algorithm used to computed the correction factor does not lead to an optimal solution. To solve this problem it would be necessary to:

- identify the flexible modes shapes more excited by a certain gust shape;
- formulate the minimization problem, that leads to the calculation of the correction factors, to allow a weighting factor for each mode considered.

During the final stage of this thesis preliminary studies have highlighted how the modal participation factor could guide in the selection of the flexible modes to correct. Gusts with different wavelength and amplitude excite different modes, so it may be appropriate to select different sets of modes to use in the correction according to the gust disturbance of interest. However, the integration of this functionality has not been possible in the time frame of the thesis, but it could be an interesting point for future works.

7.6 DLM correction methods comparison

In this section the correction method considering gust and mode shapes is compared with a traditional approach where the correction factors computed for the steady aeroelastic deformation (at $\kappa = 0$) are used to correct all the reduced frequencies. The general trend of the steady corrections is to scale the uncorrected results, with a poor capacity to capture the interaction between the deforming structure and the gust disturbance. In particular for the short and long

gust length, Figure 7.19 and 7.21, the steady correction tends to underestimates the peak loads while for the medium gust length, Figure 7.20, it overestimates the load due to the gust.

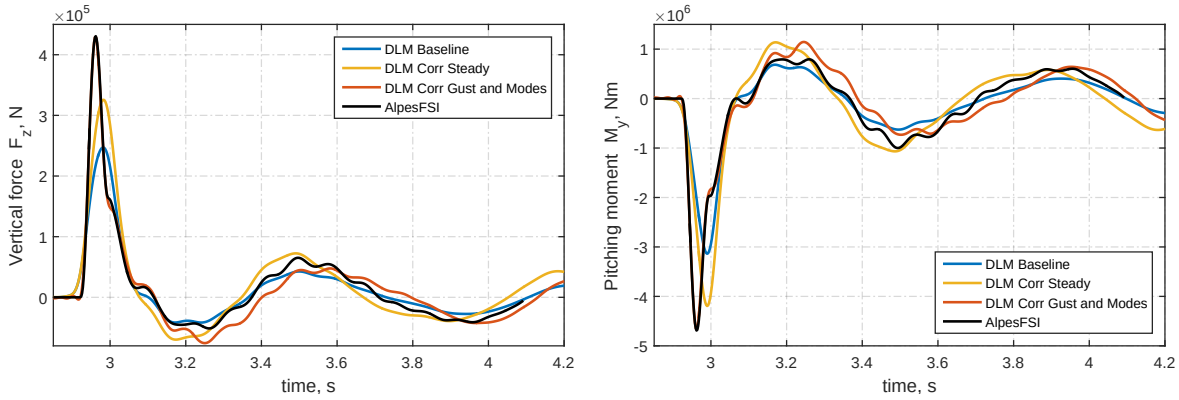

(a) Vertical force F_z, $L_g = 18.28\ m$. (b) Pitching moment M_y, $L_g = 18.28\ m$.

Figure 7.19: Comparison of vertical force and pitching moment for AlpesFSI, uncorrected and corrected DLM, for short gust length and nominal amplitude.

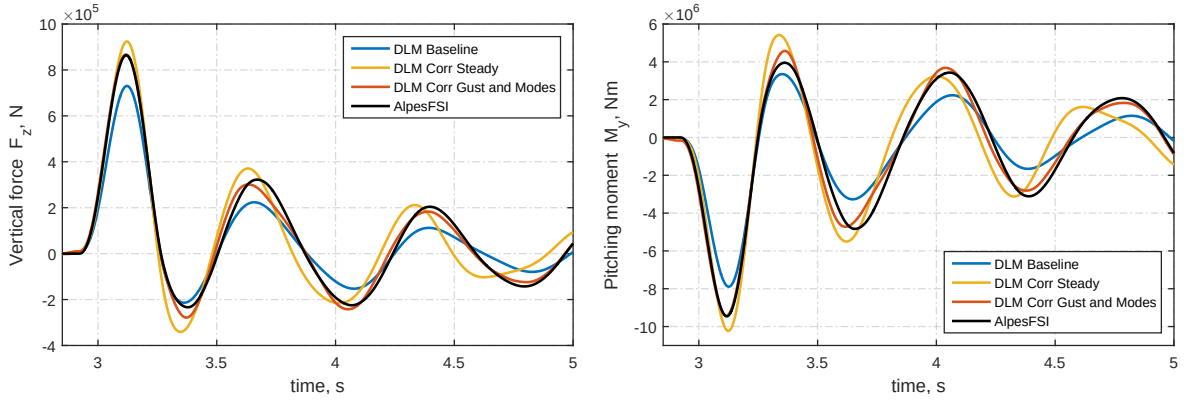

(a) Vertical force F_z, $L_g = 91.44\ m$. (b) Pitching moment M_y, $L_g = 91.44\ m$.

Figure 7.20: Comparison of vertical force and pitching moment for AlpesFSI, uncorrected and corrected DLM, for medium gust length and nominal amplitude.

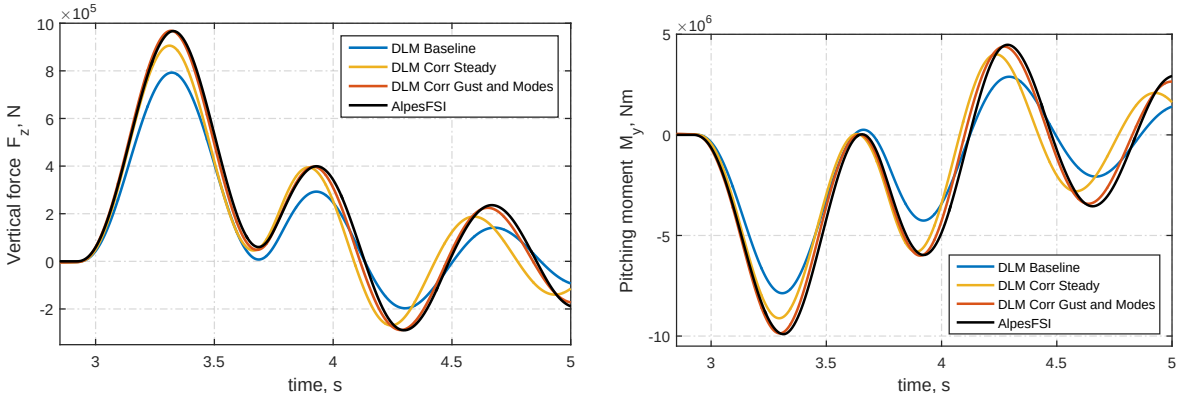

(a) Vertical force F_z, $L_g = 213.36\ m$.

(b) Pitching moment M_y, $L_g = 213.36\ m$.

Figure 7.21: Comparison of vertical force and pitching moment for AlpesFSI, uncorrected and corrected DLM, for long gust length and nominal amplitude.

7.7 Computational cost

The higher complexity of the RANS simulations requires more computing power to complete the CFD and LFD analysis, in a reasonable time frame. All the simulations have been performed on the BlueCrystal Phase 3 server at the University of Bristol, but in this case 32 cores were used to solve the fluid dynamic model. Table 7.7 shows the computational cost of the single simulations, while Table 7.8 indicates the time necessary to generate the correction method for the NASA Common Research Model.

Simulation type	Simulation platform, cores	Time, minutes
AlpesFSI	32×2.6 GHz	2880
TAU CFD	32×2.6 GHz	20
TAU LFD	32×2.6 GHz	12
MSC Natran SOL146	1×2.6GHz	2

Table 7.7: Computational cost comparison for the NCRM.

Correction type	Analyses, number	Time, minutes
DLM Corr Steady	2 CFD	40
DLM Corr Only Gust	16 LFD	192
DLM Corr Gust and MS	48 LFD	576

Table 7.8: Computational cost to generate the correction methods for the NCRM.

CHAPTER 8

Conclusions and Future Work

8.1 Conclusions

This thesis has presented a novel methodology to correct the aeroloads computed using the Doublet-Lattice Method for gust loads analysis. The proposed approach corrects the downwash for each aero box defining a matrix of correction coefficients which post-multiply the aerodynamic influence coefficient matrices. Furthermore, the correction factors are computed for the full range of frequency analysed and consist of complex numbers which are able to represent the unsteady effects associated with the gust response problem. The proposed method has been applied initially considering reference Computational Fluid Dynamics (CFD) results obtained by time domain simulation. However, these are highly computationally expensive: for this reason Linearised Frequency Domain (LFD) analysis has been used to evaluate the reference loads.

In order to validate the results provided by the correction approach, a fully coupled fluid structure interaction analysis environment has been created. The AlpesFSI interface, coupling the CFD TAU-Code and the FEM MSC Nastran solver, has been used to perform steady aeroelastic simulations, as well as transient time marching analysis.

A first application of the correction techniques has investigated the response to a one minus cosine gust disturbance of a wing constrained at the root. The FFAST right wing model has

been studied considering different gust lengths as described by the certification authority for large aircraft, EASA CS-25. Two different flight conditions have been analysed to validate the method proposed. A low Mach number ($M = 0.50$) has been considered first, where no shock was observed on the surface of the wing. Additionally, a flight point representative of a transonic cruise flight condition for a civil transport aircraft ($M = 0.85$) has been considered. Correcting the DLM using only sinusoidal gust loads gave very good agreement with the rigid CFD gust response. However, it was not able to capture the effect related to the elastic structural deformation. Including in the correction process the reference CFD results obtained from two mode shape deformations gave very good agreement with the reference aeroelastic gust response evaluated using the AlpesFSI interface. Additionally it was shown that the correction coefficients were characterised by a fairly smooth trend with respect to the reduced frequency. This allowed a reduction in the number of reference data to be investigated with the LFD solver, and extending the correction to the entire range of reduced frequency (necessary for the analysis) by linear interpolation.

Lastly the method proposed was applied to a full aircraft model, representative of a large civil aircraft: the NASA Common Research Model. Also in this case the rigid gust loads evaluated by the DLM, corrected with sinusoidal gust, were in good agreement with the rigid CFD results. Again the correction method needed two reference mode shapes to account well for the flexibility of the structure, and agree with the fluid structure aeroelastic results. Additionally, for this application it was observed that different reference mode shapes were necessary to accurately correct different gust lengths.

The corrected method presented, thanks to the interpolation approach over the correction factor, represents a valid alternative to reduced order models (ROM). The latter, in fact, would require a much higher number of sampling points to be computed with LFD simulations:

$$LFD_{ROM} = \text{Nr. } \kappa \times (\text{Nr. Flexible Modes} + 1)$$

Interpolating the correction factors over the range of frequency analysed and selecting the appropriate mode shapes for the flexible correction, the method presented offers a great improvement compared to traditional correction methods, keeping the computational cost limited.

Moreover, the way in which this method has been formulated would allow a seamless integra-

tion in the current tools and methods used to correct the DLM method in the industrial context. In fact, once the correction factor matrices have been evaluated, they would fit with very small modification in all the DLM based gust analysis methods.

8.2 Recommendations for Future Work

The DLM correction method presented in this work has been compared to reference loads computed with the AlpesFSI interface, however this implementation did not include the capability to account for rigid body modes of the model. A future research project could investigate the effect on the correction process of a free-free flight condition.

As demonstrated in this work, interpolating the correction factor above the reduced frequency is a valid approach to reduce the number of reference LFD simulations to be performed. Future activities could investigate how to identify apriori the specific values of frequency which need to be simulated. Similarly it could be studied how to select the structural mode shapes to correct. A preliminary study has already been conducted on how an index such as the Modal Participation Factor could give an indication of which structural modes are influencing the structural response to a certain gust length. With this it can be studied how to define a weight for different modes.

The present correction method has been applied to a discrete number of flight points. But the entire flight envelope for aircraft loads analysis requires thousand of combinations of mass case and flight conditions to be analysed, including high lift and air brakes deployment configurations.

Ideally a correction data base should be created including all the possible configurations of interest. Since this could be very expensive, a surrogate model, based on a data fitting approach, could allow the extension of the correction method to cover the entire flight envelope. An optimization approach could help to identify the combinations of mode shapes and reduced frequencies for which the reference data have to be computed. The interpolation process can then be adopted to extrapolate this result over different reduced frequencies and flight points.

The method presented in this thesis has been formulated on the constitutive equations of the doublet-lattice method. However, being based on the correction of the downwash generated by the aero box of the panel method, it may be extended to other potential methods formulated in

the frequency domain.

One last opportunity for future work, could be to extend the corrections to account for nonlinear structural deformation. Many recent works in the literature are addressing the possibility to define nonlinear modes for a high aspect ratio wing, with large displacement. This information could be used to identify the mode shapes for which to compute the LFD analysis and account for geometrical non linearities in the correction coefficients evaluation.

References

[1] M. Darecki, C. Edelstenne, T. Enders, E. Fernandez, P. Hartman, J.-P. Herteman, M. Kerkloh, I. King, P. Ky, M. Mathieu, G. Orsi, G. Schotman, C. Smith, and J.-D. Wörner. Flightpath 2050 Europe's Vision for Aviation. Technical report, 2011.

[2] G. Marsh. Airbus A350 XWB update. *Reinforced Plastics*, 54(6):20–24, 2010.

[3] M. Kamlet. NASA Tests New Alloy to Fold Wings in Flight. https://www.nasa.gov/centers/armstrong/feature/nasa-tests-new-alloy-to-fold-wings-in-flight.html. Accessed: 2018-02-25.

[4] A. Castrichini, V. Hodigere Siddaramaiah, D. E. Calderon, J. E. Cooper, T. Wilson, and Y. Lemmens. Nonlinear Folding Wing Tips for Gust Loads Alleviation. *Journal of Aircraft*, 53(5):1391–1399, 2016.

[5] C. Howcroft, D. Calderon, L. Lambert, M. Castellani, J. E. Cooper, M. H. Lowenberg, and S. Neild. Aeroelastic Modelling of Highly Flexible Wings. *15th Dynamics Specialists Conference*, (January):1–26, 2016.

[6] R. Cook, D. Calderon, M. H. Lowenberg, S. Nield, J. E. Cooper, and E. Coetzee. Worst Case Gust Prediction of Highly Flexible Wings. *58th AIAA/ASCE/AHS/ASC Structures, Structural Dynamics, and Materials Conference*, (January), 2017.

[7] W. Krüger. Fully coupled aeroelastic gust and manoeuvre simulations. http://www.dlr.de/ae/en/desktopdefault.aspx/tabid-9646/16577_read-40509/. Accessed: 2018-02-26.

[8] J. R. Wright and J. E. Cooper. *Introduction to Aircraft Aeroelasticity and Loads*. John Wiley & Sons, Ltd, 2007.

[9] Easa. Certification Specifications for Large Aeroplanes CS-25. Technical Report 19 September, 2007.

[10] Joint Aviation Authorities. Joint Aviation Regulations - 25, Airworthiness Standards: Transport Category Airplanes, volume Subpart C - Structure. Technical report.

[11] T. Kier. Comparison of Unsteady Aerodynamic Modelling Methodologies with Respect to Flight Loads Analysis. *AIAA Atmospheric Flight Mechanics Conference and Exhibit*, (August):1–14, 2005.

[12] J. G. Leishman. Subsonic unsteady aerodynamics caused by gusts using the indicial method. *Journal of Aircraft*, 33(5):869–879, 1996.

[13] E. Albano and W. P. Rodden. A doublet-lattice method for calculating lift distributions on oscillating surfaces in subsonic flows. In *AIAA 6th Aerospace Sciences Meeting*. American Institute of Aeronautics and Astronautics, Feb 1968.

[14] W. P. Rodden. *Theoretical and Computational Aeroelasticity*. The Americas Group, 2011.

[15] G. Yang and S. Obayashi. Numerical Analyses of Discrete Gust Response for an Aircraft. *Journal of Aircraft*, 41(June):1353–1359, 2004.

[16] L. Reimer, M. Ritter, R. Heinrich, and W. Krüger. CFD-based Gust Load Analysis for a Free-flying Flexible Passenger Aircraft in Comparison to a DLM-based Approach. In *22nd AIAA Computational Fluid Dynamics Conference AIAA*, number June, pages 1–17, 2015.

[17] R. Palacios, H. Climent, A. Karlsson, and B. Winzell. Assessment of strategies for correcting linear unsteady aerodynamics using CFD or experimental results. In *International Forum on Aeroelasticity and Structural Dynamics (IFASD)*, 2001.

[18] R. G. Annes Da Silva, O. A. F. Mello, J. L. F. Azevedo, P. C. Chen, and D. D. Liu. Investigation on Transonic Correction Methods for Unsteady Aerodynamics and Aeroelastic Analyses. *Journal of Aircraft*, 45(6):1890–1903, 2008.

[19] C. Valente, D. Jones, A. Gaitonde, J. E. Cooper, and Y. Lemmens. OpenFSI Interface For Strongly Coupled Steady And Unsteady Aeroelasticity. In *IFASD 2015 International Forum on Aeroelasticity and Structural Dynamics*, pages 1–16, Saint Petersburg, Russia, 2015.

[20] C. Valente, C. Wales, D. Jones, A. Gaitonde, J. E. Cooper, and Y. Lemmens. A Doublet-Lattice Method Correction Approach for High Fidelity Gust Loads Analysis. In *58th AIAA/ASCE/AHS/ASC Structures, Structural Dynamics, and Materials Conference*, Grapevine, Texas, 9 -13 January 2017.

[21] C. Valente, C. Wales, D. Jones, A. Gaitonde, J. . E. Cooper, and Y. Lemmens. An Optimized Doublet-Lattice Method Correction Approach for a Large Civil Aircraft. In *International Forum on Aeroelasticity and Structural Dynamics IFASD 2017*, pages 1–15, 25-28 June 2017.

[22] M. Blair. A Compilation of the Mathematics Leading to the Doublet Lattice Method. Technical Report WL-TR-92-30280, 1992. Wright Laboratory.

[23] M. Landahl. Kernel Function for Nonplanar Oscillating Surfaces in a Subsonic Flow. *AIAA Journal*, 5(5):1045–1046, may 1967.

[24] E. Albano and W. P. Rodden. A Doublet-Lattice Method for Calculating Lift Distributions on Oscillating Surfaces in Subsonic Flows. *AIAA Journal*, 7(2):279–285, 1969.

[25] Zona technology Inc. ZAERO Theoretical Manual. Technical report, 2017.

[26] ZONA Technology Inc. ZONAIR User's Manual - Engineering Software for Aerodynamics and Flight Loads. Technical report, 2016.

[27] P. C. Chen and D. Sarhaddi. Transonic-Aerodynamic-Influence-Coefficient Approach for Aeroelastic and MDO Applications. *Journal of Aircraft*, 37(1), 2000.

[28] P. C. Chen, D. Sarhaddi, D. D. Liu, and M. Karpel. Unified Aerodynamic-Influence-Coefficient Approach for Aeroservoelastic and Multidisciplinary Optimization Applications. *Journal of Aircraft*, 37(2), 2000.

[29] T. Kier. Comparison of Unsteady Aerodynamic Modelling Methodologies with Respect to Flight Loads Analysis. *AIAA Atmospheric Flight Mechanics Conference and Exhibit*, (August):1–14, 2005.

[30] T. C. S. Rendall and C. B. Allen. Unified fluid–structure interpolation and mesh motion using radial basis functions. *International Journal for Numerical Methods in Engineering*, 74(October 2007):1519–1559, 2008.

[31] MSC Software Corporation. *MSC Nastran 2013.1 Dynamic Analysis User ' s Guide*. MSC Software, Newport Beach, CA 92660, U.S.A., 2013.

[32] H. Tijdeman. *Investigations of the Transonic Flow Around Oscillating Airfoils*. National Aerospace Laboratory NLR.

[33] J. P. Giesing, T. P. Kalman, and W. P. Rodden. Correction Factor Techniques for Improving Aerodynamic Prediction Methods. Technical Report NASA CR-144967, 1976.

[34] D. Dimitrov and R. Thormann. DLM-Correction Method for Aerodynamic Gust Response Prediction. *International Forum on Aeroelasticity and Structural Dynamics (IFASD)*, pages 1–10, 2013.

[35] K. Dau. A Semi-Empirical Method for Calculating Pressures on Oscillating Wings in Unsteady Transonic Flow, Rept. DA-EF24-B08/92. Technical report, Deutsche Airbus, Bremen, Germany, 1992.

[36] H. C. Garner. A Practical Framework for Evaluation of Oscillating Aerodynamic Loadings on Wings in Supercritical Flows. *Unsteady Airloads in Separated and Transonic Flow*, 1977.

[37] S. Emil, J. Glaser, and R. Coll. Aerodynamic derivatives factoring scheme for the MSC/NASTRAN doublet lattice program, 1990.

[38] D. D. Liu, Y. F. Kao, and K. Y. Fung. An Efficient Method for Computing Unsteady Transonic Aerodynamics of Swept Wings with Control Surfaces. *J. Aircraft*, 25(1):25–31, 1988.

[39] P. C. Chen, D. Sarhaddi, and D. D. Liu. Transonic-Aerodynamic-Influence-Coefficient Approach for Aeroelastic and MDO Applications. *Journal of Aircraft*, 37(1):85–94, 2000.

[40] D. P. Bertsekas. *Constrained optimization and Lagrange multiplier methods*. Academic press, 2014.

[41] M. L. Baker. CFD Based Corrections for Linear Aerodynamic Methods. In *AGARD SMP Meeting on " Numerical Unsteady Aerodynamic and Aeroelastic Simulation"*, Aalborg, Denmark, 1997.

[42] I. Jadic, D. Hartley, and J. Giri. An enhanced correction factor technique for aerodynamic influence coefficient methods. *MSC's proceedings for 1999 Aerospace Users Conference.*, (March 1999), 1999.

[43] J. Brink-Spalink and J. M. Bruns. Correction of unsteady aerodynamic influence coefficients using experimental or CFD data. In *41st AIAA Conference Atlanta, GA*, 2000.

[44] D. M. Pitt and C. E. Goodman. Flutter calculations using Doublet Lattice aerodynamics modified by the full potential equations. In *28th AIAA Str*, volume 4, Monterey, CA, 1987.

[45] W. E. McCain. Measured and Calculated Airloads on a Transport Wing Model. *Journal of Aircraft*, 22(4):336–342, 1985.

[46] W. Luber and H. Schmid. Flutter investigations in the transonic flow regime for a fighter type aircraft. Technical report, AGARD, 1983.

[47] R. G. Annes Da Silva, J. L. F. Azevedo, and O. Mello. Navier-Stokes-Based Study into Linearity in Transonic Flow for Flutter Analysis. *Journal of Aircraft*, 40(5):997–1000, 2003.

[48] D. J. Ewins. *Modal testing: theory and practice*, volume 15. Research studies press Letchworth, 1984.

[49] R. Thormann and D. Dimitrov. Correction of aerodynamic influence matrices for transonic flow. *CEAS Aeronautical Journal*, 5(4):435–446, 2014.

[50] R. Thormann and M. Widhalm. Linear-Frequency-Domain Predictions of Dynamic-Response Data for Viscous Transonic Flows. *AIAA Journal*, 51(11):2540–2557, 2013.

[51] D. Quero Martin. DLM Unsteady Correction using non linear CFD gust aerodynamics. In *DRLK Conference*, volume 350, Augsburg, Germany, 2014.

[52] D. Quero Martin, G. Rabádan, and W. Krüger. On an Innovative Approach to account for Gust Aerodynamic Nonlinearities. In *AIAA SciTech*, number 5-9 January 2015, Kissimmee, Florida, pages 1–17, 2015.

[53] E. H. Dowell, S. R. Bland, and M. H. Williams. Linear/Nonlinear Behavior in Unsteady Transonic Aerodynamics. *AIAA Journal*, 21(1):38–46, 1983.

[54] D. Friedewald. Quasi-steady doublet-lattice correction for aerodynamic gust response prediction in attached and separated transonic flow. *CEAS Aeronautical Journal*, 9(1):53–66, 2018.

[55] D. Schwamborn, T. Gerhold, and R. Heinrich. The DLR TAU-Code: Recent Applications in Research and Industry. *European Conference on Computational Fluid Dynamics, ECCOMAS CFD 2006*, pages 1–25, 2006.

[56] T. Gerhold, M. Galle, O. Friedrich, and J. Evans. Calculation of complex three-dimensional configurations employing the DLR-tau-code. *35th Aerospace Sciences Meeting and Exhibit*, m(January), 1997.

[57] D. Schwamborn, T. Gerhold, and V. Hannemann. On the Validation of the DLR-TAU Code. In W. Nitsche, H.-J. Heinemann, and R. E. Hilbig, editors, *New Results in Numerical and Experimental Fluid Mechanics II*. 1999.

[58] CentaurSoft, CENTAUR. http://www.centaursoft.com/. Accessed: 2018-02-25.

[59] D. G. Martineau, S. Stokes, S. J. Munday, A. P. Jackson, B. J. Gribben, and N. Verhoeven. Anisotropic hybrid mesh generation for industrial RANS applications. *AIAA Paper*, 534(2006):39, 2006.

[60] T. Gerhold. What is TAU. Technical report. Deutscher Luft- und Raumfahrtkongress.

[61] N. Kroll, T. Gerhold, S. Melber, R. Heinrich, T. Schwarz, and B. Schöning. Parallel Large Scale Computations for Aerodynamic Aircraft Design with the German CFD System MEGAFLOW. In *Parallel Computational Fluid Dynamics - Practice and Theory*, pages 227–236. B.V., Elsevier Science, 2002.

[62] P. Aumann, H. Barnewitz, H. Schwarten, K. Becker, R. Heinrich, B. Roll, M. Galle, N. Kroll, T. Gerhold, D. Schwamborn, and M. Franke. MEGAFLOW: Parallel complete aircraft CFD. *Parallel Computing*, 27(4):415–440, 2001.

[63] A. Beckert, T. Gerhold, D. Schwamborn, and K. Weinman. Applications of the DLR-TAU Code to Fluid-Structure Interaction on Hybrid Grids. In *ECCOMAS 2000*, Barcelona, Spain, 2000.

[64] A. Schütte, G. Einarsson, B. Schöning, M. Wulf, J. Neumann, J. Arnold, T. Alrutz, J. Heinecke, T. Forkert, and H. Schumann. Prediction of the Unsteady Behavior of Maneuvering Aircraft by CFD Aerodynamic, Flight-Mechanic and Aeroelastic Coupling. *RTO Organisation Conference, Budapest*, 2005.

[65] A. Schütte, G. Einarsson, A. Raichle, B. Schöning, W. Mönnich, M. Orlt, J. Neumann, J. Arnold, and T. Forkert. Numerical Simulation of Maneuvering Aircraft by Aerodynamic, Flight Mechanics and Structural Mechanics Coupling. *Journal of Aircraft*, 46(1):53–64, 2009.

[66] H. Barnewitz and B. Stickan. *Improved Mesh Deformation*, pages 219–243. Springer Berlin Heidelberg, Berlin, Heidelberg, 2013.

[67] B. Stickan, A. Rempke, S. Helm, and H. Bleecke. High-Fidelity Cfd-Csm Interaction in the Industrial Context. *International Forum on Aeroelasticity and Structural Dynamics IFASD*, (June):1–16, 2017.

[68] U. Burggraf, M. Kuntz, and B. Schöning. *Implementation of the Chimera Method in the Unstructured DLR Finite Volume Code Tau*, pages 93–100. Vieweg+Teubner Verlag, Wiesbaden, 1999.

[69] M. D. Buhmann. *Radial Basis Functions: Theory and Implementations*. Cambridge Monographs on Applied and Computational Mathematics. Cambridge University Press, 2003.

[70] MSC Software Corporation, F. G. Di Vincenzo, and A. Castrichini. *MSC Nastran Hybrid Static Aeroelasticity Integrated , Accurate Static Aeroelastic Analysis with CFD data*. 2013.

[71] T. C. S. Rendall and C. B. Allen. Improved radial basic function fluid-structure coupling via efficient loacalized implementation. *International Journal for Numerical Methods in Engineering*, 78(January):1188–1208, 2009.

[72] B. Stickan, H. Bleecke, and S. Schulze. NASTRAN Based Static CFD-CSM Coupling in FlowSimulator. In *Numerical Fluid Mechanics and Multidisciplinary Design*, volume 123, pages 223–234. 2013.

[73] S. Helm, M. Haupt, B. Stickan, and H. Bleecke. Advancements of CFD-CSM Coupling by Means of Multibody Simulation. In *Deutscher Luft- und Raumfahrtkongress 2015*, volume 0, pages 1–7, 2015.

[74] A. Lurgo and R. Jung. Static Fully Coupled Simulation of a Transport Aircraft High-Lift System. *International Forum on Aeroelasticity and Structural Dynamics IFASD*, (June):1–19, 2017.

[75] N. Kroll, R. Heinrich, W. Krueger, and B. Nagel. Fluid-Structure Coupling for Aerodynamic Analysis and Design: A DLR Perspective (Invited). In *46th AIAA Aerospace Sciences Meeting and Exhibit*, pages 1–31, Reston, Virgina, Jan 2008. American Institute of Aeronautics and Astronautics.

[76] R. Heinrich and L. Reimer. Comparison of Different Approaches for Modeling of Atmospheric Effects Like Gusts and Wake-Vortices in the Cfd Code Tau. (June):1–13, 2017.

[77] G. Jeyakumar and D. Jones. Aerofoil gust responses in viscous flows using prescribed gust velocities. Technical Report AENGM3100. University of Bristol. 2013.

[78] L. Tang and J. D. Baeder. Adaptive Euler simulations of airfoil–vortex interaction. *International Journal for Numerical Methods in Fluids*, 53(5):777–792, 2007.

[79] J. Sitaraman and J. D. Baeder. Field Velocity Approach and Geometric Conservation Law for Unsteady Flow Simulations. *AIAA Journal*, 44(9):2084–2094, 2006.

[80] C. Wales, D. Jones, and A. Gaitonde. Prescribed Velocity Method for Simulation of Aerofoil Gust Responses. *Journal of Aircraft*, pages 1–13, 2014.

[81] D. S. Whitehead and J. R. Grant. Force and Moment Coefficients of High Deflection Cascades. In *2nd International Symposium on Aeroelasticity in Turbomachinery*, 1981.

[82] J. M. Verdon. Development of a Linear Unsteady Aerodynamic Analysis for Finite-Deflection Subsonic Cascades. *AIAA Journal*, 20(9):1259–1267, 1982.

[83] J. M. Verdon and J. R. Caspar. A linearized unsteady aerodynamic analysis for transonic cascades. *Journal of Fluid Mechanics*, 149:403–429, 1984.

[84] K. C. Hall and W. S. Clark. Linearized Euler Predictions of Unsteady Aerodynamic Loads in Cascades. *AIAA Journal*, 31(3):540–550, 1993.

[85] K. C. Hall, W. S. Clark, and C. B. Lorence. A Linearized Euler Analysis of Unsteady Transonic Flows in Turbomachinery. *Journal of Turbomachinery*, 116(3):477–488, jul 1994.

[86] G. D. Mortchéléwicz. Application des Equations D'Euler Linéarisées a la Prevision du Flottement. In *AGARD SMP Meeting on "Numerical Unsteady Aerodynamic and Aeroelastic Simulation"*, Aalborg, Denmark, 1997.

[87] C. Weish. Small Disturbance Euler Simulations for Delta Wing Unsteady Flows due to Harmonic Oscillations. 41(4), 2004.

[88] W. S. Clark and K. C. Hall. A Time-Linearized Navier–Stokes Analysis of Stall Flutter. *Journal of Turbomachinery*, 122(July):467–476, 2000.

[89] A. N. Pechloff and B. Laschka. Small Disturbance Navier-Stokes Method: Efficient Tool for Predicting Unsteady Air Loads. *Journal of Aircraft*, 43(1):17–29, 2006.

[90] A. Pechloff and B. Laschka. Small Disturbance Navier-Stokes Computations for Low-Aspect-Ratio Wing Pitching Oscillations. *Journal of Aircraft*, 47(3):737–753, 2010.

[91] R. Thormann and M. Widhalm. Forced Motion Simulations Using a Linear Frequency Domain Solver for a Generic Transport Aircraft. *International Forum on Aeroelasticity and Structural Dynamics*, pages 1–16, 2013.

[92] C. Kaiser, R. Thormann, D. Dimitrov, and J. Nitzsche. Time-Linearized Analysis of Motion-induced and Gust-induced Airloads with the DLR TAU Code. In *Deutscher Luft- und Raumfahrtkongress 2015*, pages 1–9, 2015.

[93] P. Bekemeyer and S. Timme. Reduced Order Transonic Aeroelastic Gust Response Simulation of Large Aircraft. *35th AIAA Applied Aerodynamics Conference*, June 2017.

[94] P. Bekemeyer, R. Thormann, and S. Timme. Frequency-Domain Gust Response Simulation Using Computational Fluid Dynamics. *AIAA Journal*, 55(7):2174–2185, 2017.

[95] P. Bekemeyer, R. Thormann, and S. Timme. Rapid gust response simulation of large civil aircraft using computational fluid dynamics. *The Aeronautical Journal*, 121(1246):1795–1807, dec 2017.

[96] W. Weigold, B. Stickan, I. Travieso-alvarez, C. Kaiser, and P. Teufel. Linearized Unsteady CFD for Gust Loads with TAU. In *International Forum on Aeroelasticity and Structural Dynamics (IFASD)*, June 2017.

[97] M. Widhalm, R. P. Dwight, R. Thormann, and A. Hubner. Efficient computation of dynamic stability data with a linearized frequency domain solver. In *V European Conference on Computational Fluid Dynamics*, pages 14–17, June 2010.

[98] C. Valente. *Aerodynamic Loads Models for the Aeroelastic TRIM Analysis of an UAV*. PhD thesis, University of Rome "La Sapienza", 2012.

[99] F. Coppola. *An Integrated Computaitonal Environment for the Fluid Structure Interaction Analysis of Aeronautical Non Linear Systems*. PhD thesis, University of Rome "La Sapienza", 2010.

[100] Fraunhofer Institute for Algorithms and Scientific Computing SCAI. MpCCI CouplingEnvironment.

[101] Technische Universitat Braunschweig. Cooperate project "AeroStruct": Development of a FlowSimulator-OpenFSI interface.

[102] K. Lindhorst. Prototype of FS-OpenFSI-Interface - Milestone report. Technical report, 2012.

[103] MSC Software Corporation. *MSC Software Development Kit 2014 User's Guide*. Newport Beach, CA 92660, U.S.A., 2014.

[104] MSC Software Corporation. *MSC Nastran 2014 User Defined Services User's Guide*. MSC Software, Newport Beach, CA 92660, U.S.A., 2014.

[105] MSC Software Corporation. *MSC Nastran 2014.1 Nonlinear User's Guide SOL 400*. MSC Software, Newport Beach, CA 92660, U.S.A., 2014.

[106] MSC Software Corporation. *MSC Nastran 2014 Dynamic Analysis User's Guide*. Newport Beach, CA 92660, U.S.A., 2014.

[107] K. Lindhorst, M. Haupt, and P. Horst. Usage of time domain surrogate model approaches for transient, nonlinear aerodynamics within aero-structural coupling schemes. In *42nd AIAA Fluid Dynamics Conference and Exhibit*, pages 1–14, New Orleans, Louisiana, June 2012.

[108] MSC Software Corporation. *MSC Nastran Quick Reference Guide 2014*. Newport Beach, CA 92660, U.S.A., 2014.

[109] E. C. Yates. *AGARD Standard Aeroelastic Configurations for Dynamic Response. Candidate configuration I - Wing 445.6*. Number 765. AGARD, 1987.

[110] D. Jones and A. Gaitonde. Future Fast Methods for Loads Calculations : The FFAST Project. Technical report.

[111] R. Unger, M. Haupt, and P. Horst. Coupling techniques for computational non-linear transient aeroelasticity. *Proceedings of the Institution of Mechanical Engineers, Part G: Journal of Aerospace Engineering*, 222(4):435–447, 2008.

[112] E. M. Lee-Rausch and J. T. Batina. Calculation of AGARD Wing 445.6 flutter using Navier-Stokes aerodynamics. In *AIAA 11th Applied Aerodynamics Conference*, number 93-3476, Monterey, California, USA, 1993.

[113] R. Kamakoti and W. Shyy. Fluid-structure interaction for aeroelastic applications. *Progress in Aerospace Sciences*, 40(8):535–558, 2004.

[114] N. S. Land and J. Abbott, Frank T. Method of Controlling Stiffness Properties of a Solid-Construction Model Wing. NACA TN 3423. Technical report, 1955.

[115] R. Heinrich and L. Reimer. Comparison of different approaches for gust modeling in the CFD code TAU. In *IFASD 2013 International Forum on Aeroelasticity and Structural Dynamics*, pages 1–12, Bristol, UK, 2013.

[116] E. H. Johnson. *MSC Nastran Version 68 Aeroelastic Analysis User's Guide*. MSC Software, Newport Beach, CA 92660, U.S.A., 1994.

[117] P. Bekemeyer and S. Timme. Reduced Order Gust Response Simulation using Computational Fluid Dynamics. In *57th AIAA/ASCE/AHS/ASC Structures, Structural Dynamics, and Materials Conference*, pages 1–13, San Diego, California, USA, January 2016. American Institute of Aeronautics and Astronautics.

[118] P. Bekemeyer, R. Thormann, and S. Timme. Rapid Gust Response Simulation of Large Civil Aircraft using Computational Fluid Dynamics. In *Applied Aerodynamics Conference*, pages 1–12, Bristol, UK, 19-21 July 2016.

[119] Advanced Computing Research Centre - University of Bristol. http://www.bristol.ac.uk/acrc/.

[120] DLR German Aerospace Center. 4th AIAA CFD Drag Prediction Workshop. http://aiaa-dpw.larc.nasa.gov/Workshop4/workshop4.html. Accessed: 2017-06-05.

[121] S. R. Allmaras, F. T. Johnson, and P. R. Spalart. Modifications and clarifications for the implementation of the Spalart-Allmaras turbulence model. *Seventh International Conference on Computational Fluid Dynamics*, (ICCFD7-1902), 2012.

[122] T. Klimmek. Development of a Structural Model of the CRM Configuration for Aeroelastic and Loads Analysis. In *IFASD2013 International Forum on Aeroelasticity and Structural Dynamics*, 2013.